

Statistical Image Recovery Techniques for Optical Imaging Systems

by
Saowapak Sotthivirat

A dissertation submitted in partial fulfillment
of the requirements for the degree of
Doctor of Philosophy
(Electrical Engineering: Systems)
in The University of Michigan
2003

Doctoral Committee:

Associate Professor Jeffrey A. Fessler, Chair
Professor David J. Anderson
Assistant Professor Brian D. Athey
Professor Emmett N. Leith
Professor Andrew E. Yagle

© Saowapak Sotthivirat 2003
All Rights Reserved

I dedicate this dissertation to my mother and father.

ACKNOWLEDGEMENTS

I would like to express my deepest gratitude to my advisor, Prof. Jeffrey A. Fessler, for the excellent guidance and opportunities he has provided me during my graduate study at the University of Michigan. Beyond intellectual support, his understanding, encouragement, and patience greatly assisted all aspects of my successful passage through this difficult journey. Without him, I would not have been able to accomplish this work. I am greatly indebted to him.

I would like to express my sincere gratitude to Prof. Emmett N. Leith for helping me understand holography. He was always available and willing to answer any questions I may have. I would like to thank Prof. Brian D. Athey for his guidance and assistance on confocal microscopy as well as Jim Beals for helping me obtain confocal microscopy data. I also thank Prof. Andrew E. Yagle and Prof. David J. Anderson for serving on my committee and sharing ideas.

I thank the Thai government and the Department of Cell and Developmental Biology at the University of Michigan for their financial support.

Living alone in the U.S. was made possible by the support of my friends in the U.S. and in Thailand. Special thanks to Kanda Runapongsa for her sincere friendship, concern, and emotional support. She is always there for me and I can always trust her. I thank Pasut Ratanabanangkoon for encouragement and giving me strength. I also thank Piraporn Limpaphayom and Suthep Thanapathomsinchai for their genuine friendship and assistance on anything I needed. Thanks to Pat-

tarin Kosubpaisarn, Poth Boontor, Panita Pongpaibool, and Vorapas Thunyalukul for their concern, advice, and support, especially during difficult times. I further extend my gratitude to my colleagues: Sangtae Ahn, Selin Aviyente, John Choi, Idris Elbakri, Hakan Erdoğan, Jeongtae Kim, Jia Li, Bing Ma, Web Stayman, Dung-An Wang, Hua Xie, Anastasia Yendiki, and Dan Yu for their friendship over the years.

Finally, I would like to thank my family for their unconditional love, support, and encouragement and for always being there for me despite the distance. My father was especially supportive both emotionally and financially and always ensured that I had the best educational opportunities. My mother, who has always taken care of me, always made sure I was happy and safe during my stay in America. My life in the U.S. was also more enjoyable because of my sister, Sutthilug Sotthivirat, who still lives in Kansas. She is also my best friend with whom I can talk, laugh, and cry. I also want to thank my brother, Pahol Sotthivirat, for taking care of my mother and father while I was in America. I am very fortunate to have such a wonderful family.

TABLE OF CONTENTS

DEDICATION	ii
ACKNOWLEDGEMENTS	iii
LIST OF FIGURES	ix
LIST OF TABLES	xvi
LIST OF APPENDICES	xviii
CHAPTER	
I. Introduction	1
1.1 Motivation	1
1.2 Proposed Solutions for Image Recovery Problems	3
1.3 Original Contributions	6
1.4 Dissertation Organization	7
II. Background on Optical Imaging Systems	8
2.1 Confocal Scanning Microscopy	8
2.1.1 Design and Operation	9
2.1.2 Resolution and Limiting Factors	12
2.1.3 Theoretical PSF and Its Transfer Function	13
2.1.4 Existing Image Restoration Techniques	17
2.2 Image Plane Holography	20
2.2.1 Conventional Holography	21
2.2.2 Digital Holography	24
2.2.3 Image Plane Holography with Incoherent Light	25
2.2.4 Theoretical PSF of Image Plane Holography	29
2.2.5 Comparison between Confocal Microscopy and Im- age Plane Holography	30
2.2.6 Existing Reconstruction Techniques	32
III. Statistical Techniques for Image Recovery	36

3.1	Models for Confocal Microscopy and Other Incoherent Imagery	37
3.1.1	Physical and Measurement Models	37
3.1.2	Statistical Models	39
3.2	Models for Image Plane Holography and Other Digital Holography	44
3.2.1	Physical and Measurement Models	44
3.2.2	Statistical Model	47
3.3	Maximum Likelihood Estimates	48
3.3.1	Expectation-Maximization Algorithm	49
3.4	Penalized-Likelihood Estimates	52
3.4.1	Penalty Functions	53
3.5	Iterative Algorithms for Optimization Problems	57
3.5.1	Conditions for Convergence	58
3.5.2	Examples of Gradient-Based Algorithms	59
3.5.3	Classification of Gradient-Based Algorithms	61

IV. Partitioned-Separable Paraboloidal Surrogate Coordinate Ascent Algorithm 64

4.1	Introduction	64
4.2	The Problem	67
4.3	Optimization Transfer Functions	68
4.4	Existing Algorithms	70
4.4.1	Separable Paraboloidal Surrogates (SPS) Algorithm	70
4.4.2	Coordinate Ascent Algorithm with 1D Newton-Raphson Step (CA-NR)	73
4.4.3	Coordinate Ascent Algorithm with Parabola Surrogates (CA-PS)	74
4.4.4	Paraboloidal Surrogates Coordinate Ascent (PSCA) Algorithm	75
4.4.5	“Naive” Parallel Coordinate Ascent Algorithm	76
4.5	PPCA Algorithm	76
4.5.1	Overview	77
4.5.2	Derivation	77
4.6	Convergence Analysis	81
4.7	Convergence Rate	84
4.8	Application to Image Restoration for Confocal Microscopy	85
4.8.1	The Likelihood Part	86
4.8.2	The Penalty Part	88
4.9	Results	90
4.9.1	2-D Simulation Results	90
4.9.2	3-D Simulation Results for Confocal Microscopy	95
4.10	Conclusions for the PPCA Algorithm	97

V. Relaxed Ordered-Subset Algorithm For Image Restoration . . .	101
5.1 Introduction	101
5.2 Measurement Model	104
5.3 The Algorithms	105
5.3.1 Ordered-Subset Technique	106
5.3.2 Ordered-Subset, Separable Paraboloidal Surrogate Algorithm	108
5.3.3 Relaxed Ordered-Subset Separable Paraboloidal Sur- rogate Algorithm	109
5.3.4 Blind Restoration	110
5.4 Subset Design	111
5.5 Implementation Techniques and Complexity	113
5.5.1 Space-Variant Systems	114
5.5.2 Space-Invariant Systems with Convolution	114
5.5.3 Space-Invariant Systems with Use of Fast Fourier Transforms	116
5.6 Simulation and Real Results	119
5.6.1 2-D Simulation Results	119
5.6.2 Subset Design Analysis	124
5.6.3 Limitation on the Number of Subsets	126
5.6.4 Real Confocal Data	127
5.7 Conclusions for the Relaxed OS-SPS Algorithm	130
VI. Computational Comparison of Iterative Algorithms	137
6.1 Comparison of Algorithm Complexity	137
6.2 Comparison of Convergence Rates and Overall Computational Complexity	141
6.3 Conclusions for Computational Comparison	148
VII. Statistical Image Reconstruction for Digital Holography . . .	150
7.1 Introduction	150
7.2 Measurement Model of Digital Holography	153
7.3 Numerical Holographic Reconstruction Methods	155
7.3.1 Conventional Filtering Approach	155
7.3.2 Iterative Reconstruction	156
7.4 Statistical Model	157
7.5 The Algorithm	159
7.5.1 Optimization Transfer	159
7.5.2 Paraboloidal-Surrogate Functions	160
7.5.3 The Separable-Paraboloidal-Surrogate Algorithm . . .	164

7.5.4	Maximum-Likelihood Estimation	165
7.5.5	Penalty Surrogate Function and Penalized-Likelihood Estimation	167
7.5.6	The Conjugate Gradient Method	170
7.5.7	Number of Data Sets Used	172
7.6	Simulation Results	173
7.6.1	Effect of Numbers of Data Sets	174
7.6.2	Real Object Constraint	176
7.7	Conclusions for Holographic Image Reconstruction	177
VIII. Conclusions and Future Work		182
8.1	Conclusions	182
8.2	Future Work	185
APPENDICES		188
BIBLIOGRAPHY		206

LIST OF FIGURES

Figure

2.1	Point illumination, point detection, scanning and a confocal lens system are the basic requirements for confocal scanning microscope. The pinhole is placed in front of the photodetector to suppress out-of-focus signals from other planes.	10
2.2	Confocal technique eliminates the out-of-focus signals from other planes by placing the confocal aperture in front of the photomultiplier tube such that only the signals from the focal plane are detected at the photodetector.	11
2.3	Theoretical PSFs of confocal and nonconfocal fluorescence microscopes in the xz plane. “Confocal” means that the pinhole is totally closed, whereas “nonconfocal” means that the pinhole is totally open (conventional microscope).	16
2.4	Schematic representation of the support region of the OTFs for confocal and nonconfocal microscopes. The missing cone region, where the frequency response is zero, decreases the resolution of the images, especially in the axial direction.	16
2.5	Two processes required in holography are recording and reconstructing processes. The recording process records the interference pattern between the object beam and the reference beam onto the recording medium. The reconstructing process produces the primary image behind the hologram and the conjugate image in front of the hologram by illuminating the hologram with the reference beam.	22
2.6	The object beam is coherent only with the reference beam that comes from the same point source. If plane P_1 is the in-focus plane, then x_1 will be coherent with x'_1 only and x_2 will be coherent with x'_2 only. Thus only plane P_1 will appear on the hologram.	26

2.7	The fringe pattern is finer when the angle between the object beam and the reference beam is wider. The fringe direction is determined from the angle that bisects both beams.	28
2.8	Experimental setup for recording an image plane hologram	29
2.9	Configuration of transmission confocal microscopy and image plane holography systems and their PSFs.	31
2.10	Holographic reconstruction using a filtering method.	34
3.1	Diagram of incoherent imagery	37
3.2	Diagram of digital holography	45
3.3	Illustration of the first-order and second-order neighborhood on one pixel of a 2-D image. The solid lines represents the pairs of penalized pixels in the first-order neighborhood. The solid plus dash lines illustrate the second-order neighborhood.	54
3.4	Illustration of different potential functions. For the Huber and Lange nonquadratic functions, $\delta = 5$	57
4.1	Illustration of a surrogate function	69
4.2	A “naive” parallel coordinate ascent algorithm. Each parallel processor performs the CA algorithm on each subset of pixels separately.	76
4.3	Schematic of the PPCA algorithm	78
4.4	2-D simulation and restoration using a 4-PPCA algorithm with $\beta = 0.01$ and $\delta = 1.5$	92
4.5	Partitioned set patterns of a 2-D image.	94
4.6	Performance on parallel processors in elapsed time for the PPCA algorithms using a 512×512 image and a 15×15 PSF.	94
4.7	Comparison of objective function increase versus number of iterations using monotonic algorithms on a 2-D image.	95
4.8	Comparison of objective function increase versus elapsed time using monotonic algorithms on a 2-D image.	95

4.9	Comparison of objective function increase versus number of iterations using nonmonotonic algorithms on a 2-D image.	96
4.10	Comparison of objective function increase versus elapsed time using nonmonotonic algorithms on a 2-D image.	96
4.11	Results for a 3D simulated spherical shell using a 4-PPCA algorithm for 20 iterations with $\beta = 0.1$ and $\delta = 10$. Lateral and axial medial sections through the image are in the left and right, respectively. For display purpose, the axial sections were scaled in z to obtain a 1:1 aspect ratio.	98
4.12	Performance on parallel processors in elapsed time for the PPCA algorithms using a $256 \times 256 \times 64$ image and a $15 \times 15 \times 15$ PSF.	99
4.13	Comparison of objective function increase versus number of iterations using PSCA and PPCA algorithms on a 3D image.	99
4.14	Comparison of objective function increase versus elapsed time of PSCA and PPCA algorithms on a 3D image.	100
5.1	Illustration of how the OS algorithms work. Assume that $\nabla\Phi(x) = \nabla f_1(x) + \nabla f_2(x)$. When x is far from the solution, the “subset-gradient-balance” conditions hold and an order-of-magnitude acceleration can be achieved in the early iterations. However, for later iterations or when x is near the optimal solution, those conditions are no longer valid and a limit-cycle behavior is observed.	107
5.2	These subsets tend to satisfy the “subset-gradient-balance” conditions. The first number in quotation marks is the number of subsets in each column, and the second number is the number of subsets in each row. The total number of subsets is the product of these two numbers. The pixel label m belongs to the respective set S_m	112

5.3	Investigation of the “subset-gradient-balance” conditions in the OS-SPS algorithm. Four subsets with a “2×2 configuration” were used. The second and third columns show the gradients of the sub-objective functions from the downsampling approach with use of subset 1 and subset 4, respectively, and their differences compared with the gradient of the objective function. Similarly, the last two columns are from the subblock approach. The gradients of the sub-objective functions in the downsampling approach were multiplied by 4 to compensate for the downsampled data. However, this scaling factor is not needed in the subblock approach, because a block of contiguous pixels is used.	113
5.4	These subsets tend to violate the “subset-gradient-balance” conditions. The first number in quotation marks is the number of subblocks in each column, and the second number is the number of subblocks in each row.	114
5.5	Illustration for computing $\hat{l}_i, \forall i \in S_m$ ($M = 2$), using all the information of x and h . The asterisk represents convolution. The white blocks denote elements of x belonging to subset $m = 1$, and the striped blocks denote elements of x belonging to subset $m = 2$	115
5.6	Illustration of computing $\hat{L}_j, \forall j$ ($M = 2$), using some information of ψ_i but all the information of h	116
5.7	2-D theoretical confocal PSF in the xz plane.	120
5.8	Simulated images and restoration using the relaxed OS-SPS algorithm with $\beta = 10^{-6}$ and $\delta = 100$. The PSF in the noisy blurry image was simulated from the 2D PSF of the confocal microscope only in the xz direction, where x is along the horizontal axis and z is along the vertical axis, to show elongation in the z direction. This elongation is reduced in the restored image with CLS but mostly disappears in the restored image with relaxed OS-SPS.	121
5.9	Zoom-in versions	122
5.10	Comparison of objective function increases of DPEM, SPS, OS-SPS, and relaxed OS-SPS algorithms. OS-SPS-8 stands for the OS-SPS algorithm with 8 subsets. Both nonrelaxed and relaxed OS-SPS algorithms have order-of-magnitude acceleration over the DPEM and SPS algorithms.	124

5.11	Comparison of objective function increase versus elapsed time of relaxed OS-SPS with different numbers of subsets. The 16-subset relaxed OS-SPS algorithm yielded the fastest convergence rate. . . .	125
5.12	Restored image using 5 iterations of relaxed OS-SPS-8.	125
5.13	Comparison of different choices of subsets with use of the relaxed OS-SPS algorithm. The subset unbalance of relaxed OS-SPS with the subblock approach causes an unpredictable behavior of the objective function increase at the beginning of iterations but the algorithm eventually converges as a result of relaxation. The relaxed OS-SPS algorithms with the downsampling approach converge at almost the same rate for different choices of subsets.	126
5.14	Illustration of limitation on the number of subsets when using different initial images. (a) When the initial image is far from the solution, the 16-subset case provides the fastest convergence. (b) When the initial image is close to the solution, the 4-subset case converges faster than the 8-subset and 16-subset ones.	128
5.15	Bead image	129
5.16	The $21 \times 21 \times 21$ measured PSF at different slices. The central slice is at slice 11.	132
5.17	The $21 \times 21 \times 21$ Measured PSF at different y locations. The central slice is at slice 11.	133
5.18	Noisy and restored images at $z = 2.38 \mu m$ for xy images and at $x = 7 \mu m$ for yz images. (a) Noisy cell images. Restored images using (b) CLS, (c) the iterative algorithm from Volocity software, (d) 2-D relaxed OS-SPS, and (e) 3-D relaxed OS-SPS.	134
5.19	Profiles of noisy and restored images in the z direction at $x = 7 \mu m$ and $y = 7 \mu m$. (a) Noisy cell images. Restored images using (b) CLS, (c) the iterative algorithm from Volocity software, (d) 2-D relaxed OS-SPS, and (e) 3-D relaxed OS-SPS.	135
5.20	Profiles of noisy and restored images in the z direction at $x = 7 \mu m$ and $y = 28.14 \mu m$. (a) Noisy cell images. Restored images using (b) CLS, (c) the iterative algorithm from Volocity software, (d) 2-D relaxed OS-SPS, and (e) 3-D relaxed OS-SPS.	136

6.1	Comparison of objective function increase versus number of iterations using EM, SPS, PSCA, PPCA, and relaxed OS-SPS for 50 iterations. Note that the relaxed OS-SPS algorithm with 8 subsets achieves the fastest initial convergence.	142
6.2	Comparison of objective function increase versus normalized complexity using EM, SPS, PSCA, PPCA and relaxed OS-SPS with convolution to achieve the same objective function increase obtained from relaxed OS-SPS-8 after only 5 iterations.	144
6.3	Comparison of objective function increase versus normalized complexity using EM, SPS, PSCA, PPCA and relaxed OS-SPS with FFT to achieve the same objective function increase obtained from relaxed OS-SPS-8 after only 5 iterations.	144
6.4	Comparison of objective function increase versus normalized complexity using EM, SPS, PSCA, PPCA, and relaxed OS-SPS with convolution to achieve the same objective function increase that approaches the optimal solution.	146
6.5	Comparison of objective function increase versus normalized complexity using EM, SPS, PSCA, PPCA, and relaxed OS-SPS with FFTs to achieve the same objective function increase that approaches the optimal solution.	146
6.6	Restoration comparison at early and later iterations. (a) Original image. (b) Degraded image. (c) Restored image using relaxed OS-SPS-8 for 5 iterations. (d) Restored image using relaxed OS-SPS-8 for 29 iterations.	147
7.1	The magnitude of the Fourier transform of a hologram.	156
7.2	Illustration of the marginal cost, $h_i(l^R, 0)$, and surrogate functions as a function of l^R . The solid line is the original marginal cost function. The other two lines lying above the cost function are the surrogate functions. The function with the dashed line is called the paraboloidal surrogate function which has the same first derivative and the same point as the original cost function at $l = l^n$	161
7.3	A plot of curvature c_i^R as a function of l^R at two different values of y_i .	163

7.4	Holographic reconstruction of a complex object. The top image of each pair represents the magnitude of the image and the bottom image represents the phase of the image, except for the hologram data. (a) Original image. (b) Two different hologram data. (c) Conventional reconstruction using an apodizing Gaussian filter (NRMSE=40.0%). (d) Half-size statistical reconstruction using one data set (NRMSE=17.5%). Linear interpolation in the vertical direction to the same size as the original image is performed for display. (e) Full-size statistical reconstruction using one data set (NRMSE=17.3%). (f) Full-size statistical reconstruction using two data sets (NRMSE=14.1%).	178
7.5	Profiles of the magnitude of the numerical reconstructed images across the second row of circles.	179
7.6	Profiles of the phase of the numerical reconstructed images across the second row of circles.	179
7.7	Contours of the marginal objective functions at one pixel when (a) using one data set and (b) using two data sets for full-size reconstruction. The “x” mark is the optimal solution at $20 + i110$ and the “o” marks indicate the updates of the estimates starting at $150 + i150$.	180
7.8	Statistical reconstruction of a real object using the real object constraint. (a) Original image. (b) and (c) Hologram data. (d) Conventional reconstruction using an apodizing Gaussian filter (NRMSE=43.8%). (e) Half-size statistical reconstruction using one data set (NRMSE=22.8%). (f) Full-size statistical reconstruction using one data set (NRMSE=21.1%). (g) Full-size statistical reconstruction using two data sets (NRMSE=17.2%).	181
B.1	Light propagation through the object path	194
C.1	Example of groups in GCA algorithm. Pixels with the same group index are updated simultaneously.	200

LIST OF TABLES

Table

2.1	Comparison of the differences between conventional confocal microscopy and image plane holography	32
4.1	Acronyms and description of different algorithms. “Speed” refers qualitatively to the combination of number of iterations and execution time per iteration.	67
4.2	The PPCA Algorithm Outline.	81
4.3	Algorithm Outline of the PPCA Algorithm for Confocal Microscopy.	91
4.4	Comparison of wall times and number of iterations to converge using monotonic for a 512×512 pepper image.	93
4.5	Comparison of wall times and number of iterations to converge using nonmonotonic algorithms for a 512×512 pepper image.	94
4.6	Comparison of wall times of PSCA, and PPCA algorithms for a 3D image.	97
5.1	The Relaxed OS-SPS Algorithm Outline.	111
5.2	Multiplication complexity ratio for computing \hat{l}_i (with the use of FFTs) of OS-SPS and non-OS algorithms with different numbers of subsets	118
5.3	Restoration improvement using FWHM	123
5.4	Comparison of elapsed times per iteration and number of FLOPs for DPEM, SPS, and OS-SPS algorithms	123

6.1	Per-iteration complexity comparison of EM, SPS, PSCA, PPCA and relaxed OS-SPS algorithms for the space-variant case. The letter “P” after the name of the algorithm means that the precomputed curvature was used in the algorithm.	139
6.2	Per-iteration complexity comparison of EM, SPS, PSCA, PPCA and relaxed OS-SPS algorithms for the convolution-based space-invariant system. The letter “P” after the name of the algorithm means that the precomputed curvature was used in the algorithm.	140
6.3	Per-iteration complexity comparison of EM, SPS, PSCA, PPCA and relaxed OS-SPS algorithms for the FFT-based space-invariant system. The letter “P” after the name of the algorithm means that the precomputed curvature was used in the algorithm.	140
6.4	Quantitative comparison of the complexity per iteration of different algorithms in a 2-D case where $N = N_f = 256^2$, $N_h = 15^2$, $K = 4$, and $M = 8$	140
6.5	Quantitative comparison of the complexity per iteration of different algorithms in a 3-D case where $N = N_f = 256^3$, $N_h = 15^3$, $K = 4$, and $M = 8$	141
6.6	Comparison of convergence rates and overall computational complexity of EM, SPS, PSCA, PPCA, and relaxed OS-SPS algorithms to achieve the same objective function increase obtained from relaxed OS-SPS-8 after only 5 iterations. The overall computational complexity was measured by the total number of numerical operations to converge.	143
6.7	Comparison of convergence rates and overall computational complexity of EM, SPS, PSCA, PPCA and relaxed OS-SPS algorithms to achieve the same objective function increase that approaches the optimal solution. The overall computational complexity was measured by the total number of numerical operations to converge. . . .	145
7.1	The SPS algorithm outline for holographic reconstruction	170
7.2	The CG outline for holographic reconstruction	172

LIST OF APPENDICES

Appendix

A.	Theoretical PSF Derivation for Confocal Microscopy	189
	A.1 Single Lens System	189
	A.2 Reflection and Transmission Confocal Microscopes	190
	A.3 Confocal Fluorescence Microscope	192
B.	Theoretical PSF Derivation for Image Plane Holography	194
C.	The Grouped Coordinated Ascent Algorithm (GCA)	200
D.	Curvature Proof	203
E.	Derivation of a Closed-Form Curvature	205

CHAPTER I

Introduction

1.1 Motivation

Image recovery is a technique for recovering an approximation of an original object distribution from observed data and other prior information. Regardless of the observed data, image recovery can refer to both image restoration and image reconstruction because they both aim toward the same goal. For image restoration, the observed data are in the form of images that are often corrupted by blur and noise during formation and acquisition processes in optical or electronic systems. For image reconstruction, the observed data come in different forms that need to be reconstructed to view images, and these data are degraded as well. Image recovery techniques are very attractive for many applications, such as microscopy, astronomy, and medical imaging, because they can be performed easily on a computer to improve the quality of the image without needing to alter the optical system itself, such as a microscope.

Image recovery techniques involve a mathematical procedure that exploits the information available in degraded data to achieve an image that is as close as possible to the original object distribution. In some applications, time is an important factor. Therefore, one desires to use image recovery techniques that produce good quality

images and are computationally fast. Many image recovery techniques have been proposed to achieve these goals. However, the tradeoff between the image quality and computation time always arises when evaluating existing recovery techniques. Based on the noise information used to solve recovery problems, we can categorize image recovery techniques into deterministic and statistical approaches. Deterministic techniques require little or no information about noise, while statistical techniques require knowledge of the characteristics of noise in order to estimate the original object distribution. Examples of deterministic techniques include nearest neighbors [2, 3, 31, 67], inverse filter [3, 56, 67, 71, 88], and constrained least squares [24, 67, 70, 78]. Although these techniques are very fast and simple, they either lack noise models or have fixed noise models that may not agree with the actual physical system. This is a concern because using inaccurate knowledge of the degradation process can reduce the quality of the recovered image.

Unlike deterministic techniques, statistical techniques can be based on the physical model of the system, so that a good combination of the statistical and physical models can produce superior recovery. As a result, statistical techniques tend to provide better image quality than do deterministic techniques. Examples of statistical techniques include maximum likelihood (ML) [39, 65, 67], penalized-likelihood (PL) [36, 49, 59, 125], maximum *a posteriori* (MAP) [13, 55, 62, 63], and Wiener filter [3, 8, 56, 71, 88]. Even though the Wiener filter incorporates a statistical model of the system, it uses a stationary noise model, and this is unrealistic for an object, thus resulting in poor restoration. The nonlinear ML, PL, and MAP methods have been shown to dramatically improve the quality of images compared with deterministic approaches [24, 27, 67]. The drawbacks of these methods compared with deterministic methods are high complexity and large computation time. Therefore, one of

the main goals in this dissertation is to develop statistical techniques for which these drawbacks are minimized.

Although the statistical image recovery techniques developed in this dissertation can be generalized for use with many applications, here we specifically apply them to confocal microscopy and image plane holography [7, 83, 84, 86, 116]. Both of these systems can provide the optical sectioning property for viewing a three-dimensional (3-D) image of a thick object without the need for dissection. However, images acquired by these systems are compromised by poor spatial resolution due to out-of-focus contributions from other planes and by unavoidable optical noise. As described above, statistical image recovery techniques have been shown to produce high quality recovered images. While these techniques have been developed for confocal microscopy, statistical image recovery techniques for image plane holography (as well as digital holography) have barely been explored. Thus another goal of this dissertation is to develop a statistical image reconstruction technique suitable for use in digital holography.

1.2 Proposed Solutions for Image Recovery Problems

In this dissertation we use nonlinear statistical image recovery techniques, including ML and PL estimation, to circumvent the resolution and noise problems of confocal microscopy and image plane holography. Due to the ill-posed nature of recovery problems, the resulting image using the ML method is improved as the solution is approached iteratively, but noise is also amplified. To suppress noise, we add a roughness penalty function to the log-likelihood function to compensate between the smoothness and accuracy of the data fit. This technique is called PL estimation, which is the focus of this dissertation. Because closed-form solutions for ML/PL

estimation are usually unavailable, iterative algorithms are needed [28, 65, 73, 80, 98]. As long as different iterative algorithms are based on the same objective function and are convergent, they do not affect the final image quality. Thus, one desires to have efficient iterative algorithms that converge quickly to the right solution.

Many algorithms for ML/PL image recovery have been constructed; however, no existing algorithm has all the properties of an “ideal” algorithm, including fast convergence rate, quick computation time, stability, simplicity, and parallelizability. Therefore, our first goal is to find new algorithms that overcome the drawbacks of existing algorithms. In this dissertation, we first propose a new, fast-converging, parallelizable algorithm called partitioned-separable paraboloidal surrogate coordinate ascent (PPCA) [108, 109] to overcome the convergence rate and parallelizability tradeoff of existing algorithms. This algorithm is based on paraboloidal surrogate functions and a concavity technique. The paraboloidal surrogates simplify the optimization problem. The idea of the concavity technique is to partition pixels into subsets that can be updated in parallel to reduce the computation time. For fast convergence, pixels within each subset are updated sequentially using a coordinate ascent (CA) algorithm. Unlike the CA algorithm, the PPCA algorithm converges rapidly while remaining parallelizable. We originally develop this algorithm based on the long-term interest in space-variant systems; however, in the applications of confocal microscopy and image plane holography, space-invariant systems are usually assumed for simplicity, and the fast Fourier transform (FFT) can be integrated for further acceleration.

To be compatible with the FFT, we adapt another fast converging algorithm called relaxed ordered-subset separable paraboloidal surrogate (OS-SPS) that was first introduced in image reconstruction for tomography [4] to the problem of pixel-

based image recovery [110, 111]. This algorithm has been shown in tomographic reconstruction to converge to the optimal point while providing fast convergence. Because data acquisition is different in image restoration than in tomography, we need to employ a different strategy for choosing subsets, using pixel locations rather than projection angles. As in tomography, the relaxed OS-SPS algorithm for pixel-based image recovery can provide an order-of-magnitude acceleration over the nonordered-subset version at the early iterations, thus increasing the convergence rate. The proposed PPCA and relaxed OS-SPS algorithms are generalizable to a variety of applications. In this dissertation, we demonstrate them through confocal microscopy problems and achieve good restoration with faster convergence and less computation time than existing iterative algorithms.

For image plane holography, a naive approach to trying to improve degraded holographic images would be to apply image restoration techniques to reconstructed holographic images as input data; however, such reconstructed images are further degraded, in addition to degradation from the recording process, by a spatial filtering technique commonly used in numerical conventional reconstruction. Using such a two-step is unlikely to yield good restored images. A better approach is to directly reconstruct holographic images from hologram intensity data using a statistical technique. In the last part of this dissertation, we develop a novel statistical image reconstruction technique based on Poisson models for image plane holography, as well as general digital holography [112]. Because holography can record both the amplitude and phase of the entire optical wave field, a full recovery of the object can be expected, unlike in confocal microscopy for which only the amplitude is available. In this holographic problem, we use PL estimation to reconstruct the *complex-valued* wave of the object from the *real-valued* hologram intensity data. Specifically, we de-

velop a Poisson statistical model for this problem and derive an optimization transfer algorithm that monotonically decreases the cost function each iteration and ensures convergence to a local minimizer. This approach provides the benefits of improving reconstructed holographic images relative to the conventional reconstruction technique, and can be generalized to many applications of digital holography as well as phase retrieval problems.

1.3 Original Contributions

This dissertation provides several original contributions to the fields of image recovery, microscopy, and holography. These contributions are summarized as follows:

- Development of a fast converging parallelizable algorithm (PPCA) that overcomes the tradeoff between the convergence rate and parallelizability.
- Implementation of parallel code using message-passing interface (MPI) and its portable version (MPICH) to run parallelizable algorithms on parallel processors.
- Adaptation of another fast converging algorithm (relaxed OS-SPS), which is used widely in projection-based image reconstruction for tomography, to the problem of pixel-based image recovery.
- Comparison of the computational complexity and convergence rates of the two proposed, iterative algorithms and other converging iterative algorithms.
- Construction of a statistical model and development of a new statistical reconstruction technique for digital holography, specifically image plane holography, by statistically reconstructing a holographic image directly from hologram intensity data.

- Analysis of the 3-D PSF of image plane holography, a system that allows for optical sectioning.
- Development of a new choice of curvatures for parabolic surrogate functions to simplify the optimization problem and to ensure the convergence of the algorithm.

1.4 Dissertation Organization

This dissertation begins by reviewing background information of optical systems and statistical techniques, and then presents new methods in later chapters. Chapter II reviews some background of confocal microscopy and image plane holography, and examines their limiting factors that cause resolution and noise problems. Chapter III describes statistical image restoration techniques, such as ML and PL estimation, and reviews some existing algorithms. Statistical models for incoherent imagery (e.g., confocal microscopy) and digital holography (e.g., image plane holography) are presented as well. Chapter IV presents a new fast converging parallelizable algorithm (PPCA) based on optimization transfer and concavity techniques. Chapter V presents another fast converging algorithm (relaxed OS-SPS) that is used conventionally in tomographic image reconstruction for use in image restoration. Chapter VI compares our proposed iterative algorithms with other existing converging algorithms for space-variant and space-invariant systems by determining their computational complexity and convergence rates. Chapter VII presents a new statistical image reconstruction technique for digital holography, specifically image plane holography. Finally, Chapter VIII summarizes the entire thesis and presents future work.

CHAPTER II

Background on Optical Imaging Systems

In this dissertation, we apply new statistical image recovery techniques to two specific optical imaging systems: confocal microscopy and image plane holography. The former system is available commercially, while the latter system is still at the research stage. Although both of these systems have nice optical sectioning properties for viewing a 3-D image of a thick object without the need for dissection, they operate differently and have different requirements. Under ideal conditions, both confocal microscopy and image plane holography can produce sharp images. In practice, however, most images produced by these techniques contain out-of-focus signals and noise that arise from the limitations of the systems. Thus, in this chapter we review these systems to understand how they work and their limitations so that a better image recovery technique can be developed to overcome these limitations.

2.1 Confocal Scanning Microscopy

Conventional optical microscopes are inapplicable for viewing a true 3-D image of a thick object because of their finite depth of focus and limited resolution. Even though they can view a 3-D object, their optical sectioning is very poor. The image at each plane contains a lot of noise and an incredibly large amount of out-of-focus

contributions from other planes. In other words, the spatial resolution is very poor, especially in the axial direction . To overcome this problem, the idea of confocal microscopy was first proposed by Minsky in 1957 [30, 60, 93, 94, 97] and then highly developed in the late 1970s [15, 16, 30, 60, 97, 101, 103] for the further improvement and production of useful images. The details of confocal microscopy are discussed next.

2.1.1 Design and Operation

A confocal microscope is excellent for directly visualizing 3-D objects due to its optical sectioning ability, which is also called confocal effect and depth discrimination property. The basic requirements for confocal scanning microscope are point illumination, point detection, a scanned image and a confocal lens system (two lenses sharing a common focus). Confocal means the image of the illumination or excitation pinhole and the backprojection of the detector pinhole have a common focus in the object [16]. Confocal microscopy can be operated in three different modes: reflection, transmission, and fluorescence. The fluorescence mode is used widely since the biological samples are usually labeled with fluorescent materials so that only specific parts of the samples appear on the microscope. A schematic diagram of confocal fluorescence microscope is illustrated in Figure 2.1.

In the fluorescence mode, light originating from the excitation pinhole is focused by an objective lens onto a point in the object and the emitted light focused onto a photodetector via a dichroic mirror. The Krypton/Argon mixed gas laser produces primary wavelengths of 488 nm (blue), 568 nm (yellow/green), and 647 nm (red). The 488 nm line can be used to excite a single fluorophore, fluorescein isothiocyanate (FITC), producing an emission spectrum centered at 520 nm (green) [23]. There-

Confocal Fluorescence Microscope

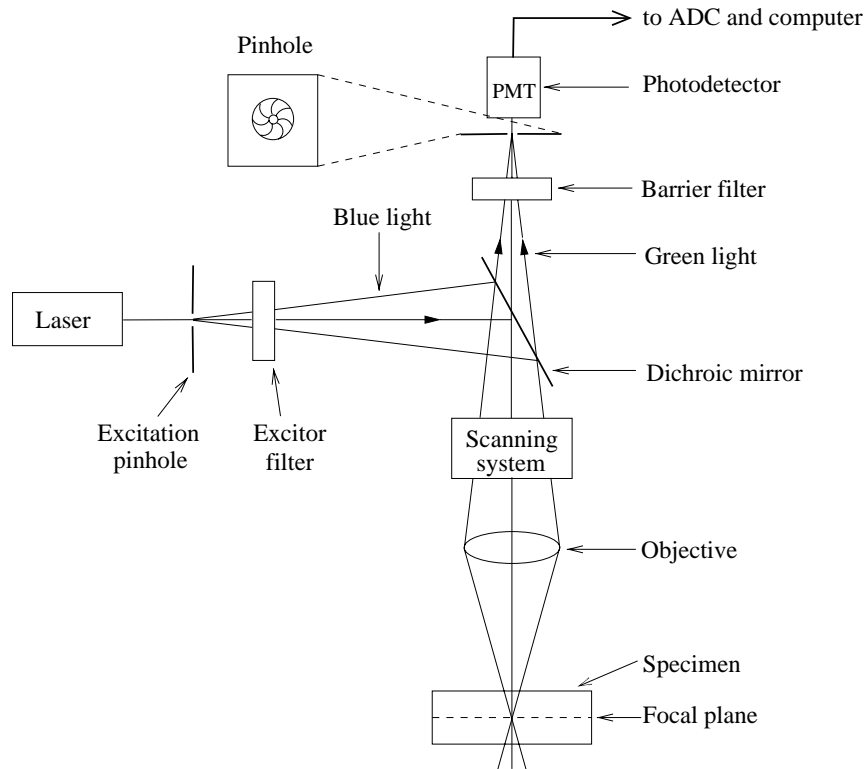


Figure 2.1: Point illumination, point detection, scanning and a confocal lens system are the basic requirements for confocal scanning microscope. The pinhole is placed in front of the photodetector to suppress out-of-focus signals from other planes.

fore, the excitation filter is needed to transmit only the 488 nm wavelength. When the fluorescent molecules absorb the 488 nm wavelength, they emit light at a longer wavelength due to loss in energy as heat. In this way, the green light for FITC is detected. The dichroic mirror deflects the excitation light as well as the reflected light and lets the fluorescently emitted light pass through. The barrier filter further attenuates the excitation and reflected light that passes through the dichroic mirror but transmits the emitted light into the direction of the photodetector, such as a photomultiplier tube (PMT) and a charged-coupled-device (CCD) camera. A confocal aperture or a detector pinhole is placed in front of the photodetector so that the

out-of-focus light will be largely obstructed by the pinhole. Light emitted from below the focal plane focuses in front of the detector pinhole, while light emitted from above the focal plane focuses behind. Therefore, most of that light is not detected at the photodetector: only light from the in-focus plane is detected (Figure 2.2).

Out-Of-Focus and In-Focus Paths of Confocal Microscope

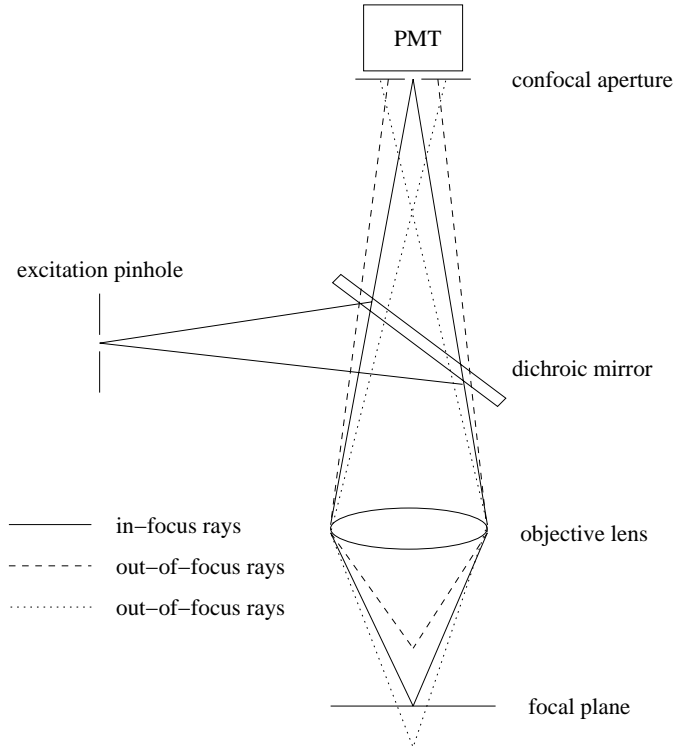


Figure 2.2: Confocal technique eliminates the out-of-focus signals from other planes by placing the confocal aperture in front of the photomultiplier tube such that only the signals from the focal plane are detected at the photodetector.

To construct a 3-D image, the microscope is focused onto a single plane to collect a 2-D image of that plane. Then it is refocused to the next plane. This scanning and refocusing process is repeated until the entire specimen is scanned. The point-by-point scanning is responsible for the confocal property obtained at each plane.

2.1.2 Resolution and Limiting Factors

For an ideal confocal case of an infinitesimal pinhole, the lateral resolution in the focal plane is proportional to the wavelength and inversely proportional to the numerical aperture (NA), whereas the axial resolution along the optical axis is proportional to the wavelength and the refractive index of the lens, yet inversely proportional to the square of the NA [23,30,114]. The NA of a lens system is defined as the relationship between the objective light collection angle (α) and the refractive index (n) of the medium between the objective and specimen: $\text{NA} = n \sin \alpha$. A rough estimate for the lateral or transverse resolution Δxy of a confocal microscope in terms of the full width at half maximum (FWHM) is [23]:

$$\Delta xy = \frac{0.61\lambda}{\sqrt{2}(\text{NA})}$$

where λ is the wavelength of the illuminating light. This resolution is about 40% better than in a conventional microscope. The axial resolution Δz is roughly estimated in terms of the FWHM as [23]:

$$\Delta z = \frac{1.5n\lambda}{(\text{NA})^2}.$$

The factor of 1.5 depends on the ratio of the excitation and emission wavelengths. Even in the ideal case, the axial resolution is not as good as the lateral resolution. The axial FWHM is about 2-3 times larger than the lateral FWHM. However, when the detector pinhole is opened up, the resolution becomes even worse, especially in the axial direction.

The degree of confocal effect depends on the NA of the objective lens and the size of detector pinhole, thus strongly relating to the resolution. The higher the NA is, the thinner the optical section and the higher the resolution will be. When the

detector pinhole is very small, the contributions from out-of-focus regions above and below the focal plane are effectively suppressed, due to the confocal property. In this way, the system behaves as an ideal confocal microscope. However, for a large pinhole, it is similar to the conventional microscope (nonconfocal microscope): the out-of-focus contributions from other planes superimpose on the in-focus plane.

Although a small pinhole provides a good resolution, it allows only a small amount of light to pass through. This would reduce the signal-to-noise ratio (SNR) and the contrast of the image. Therefore, there exists a tradeoff between the resolution and signal-to-noise ratio (SNR). The larger the aperture size, the higher the SNR, but with a degradation of resolution. In many biological studies, weakly fluorescent specimens require a larger pinhole to increase the strength of the signal and the SNR at the expense of resolution.

The resolution of the image can be analyzed from the study of a point spread function (PSF) of a microscope system. The PSF is the response of the system when using a point object as an input. Because the PSF plays a very important role in image recovery, we examine its characteristics in the next section.

2.1.3 Theoretical PSF and Its Transfer Function

In the reflection and transmission modes, a confocal microscope is coherent if a point detector and a point source are used [60]. However, introducing a finite-sized detector pinhole leads to a partially-coherent system. Furthermore, the coherence of the system is completely destroyed when a specimen is labeled with fluorescent materials [60, 102]. Therefore, a confocal fluorescence microscope with any size of a detector pinhole is an incoherent system. While a coherent system is linear in field, and its associated PSF is regarded as an amplitude PSF, an incoherent system is

linear in intensity, and its associated PSF is regarded as an intensity PSF.

When a point source and a point detector are used, the theoretical 3-D amplitude PSF in the reflection and transmission modes is given by:

$$h(\mathbf{x}, \mathbf{y}, \mathbf{z}) = h_1(\mathbf{x}, \mathbf{y}, \mathbf{z})h_2(\mathbf{x}, \mathbf{y}, \mathbf{z})$$

where h_1 is the 3-D amplitude PSF of the objective lens, and h_2 is the 3-D amplitude PSF of the collector lens (or the same objective lens). For circular lenses, this amplitude PSF has an Airy disk pattern and is circularly symmetric at each \mathbf{z} location, but the size of the PSF increases with the distance from the focal plane. Thus, there is elongation in the \mathbf{z} (axial) direction, and this produces poor resolution in the axial direction.

Because the frequency domain of the PSF can provide additional information of the PSF characteristics, we often study its Fourier transform as well. The Fourier transform of the amplitude PSF is called the coherent transfer function (CTF), and the Fourier transform of the intensity PSF is called the optical transfer function (OTF). The 3-D CTF of the reflection confocal microscopy system is the auto-convolution of the 3-D CTF of a conventional coherent microscopy system [60], which produces twice the frequency bandwidth as the CTF for conventional coherent microscopy. As a result, the reflection confocal microscope can provide a better resolution than the conventional microscope can. However, the CTF in the transmission mode is the same as the 3-D OTF of the nonconfocal microscope (See Appendix A. This CTF exhibits a missing cone around the origin. As a result, theoretically, the transmission mode of a confocal microscope does not have an optical sectioning property as in the reflection mode [60].

For an incoherent system, the 3-D intensity PSF of the confocal fluorescence

microscope with a point source and a point detector is given by [60, 75, 76]:

$$h(\mathbf{x}, \mathbf{y}, \mathbf{z}) = |h_1(\mathbf{x}, \mathbf{y}, \mathbf{z})h_2(\mathbf{x}, \mathbf{y}, \mathbf{z})|^2.$$

Similar to the behavior of the amplitude PSF in the reflection and transmission modes, the intensity PSF for confocal fluorescence microscopy also exhibits elongation in the axial direction. The 3-D OTF of a confocal fluorescence microscope is the auto-convolution of the 3-D OTF of a nonconfocal microscope. With a point detector pinhole, the former OTF does not exhibit a missing cone region as in the nonconfocal microscope.

In practice, the detector is not a single point but has a finite size that is adjusted by the pinhole in front of the detector. When a finite-sized circular detector is considered, the intensity PSF in any mode is

$$h(\mathbf{x}, \mathbf{y}, \mathbf{z}) = |h_1(\mathbf{x}, \mathbf{y}, \mathbf{z})|^2[|h_2(\mathbf{x}, \mathbf{y}, \mathbf{z})|^2 **D(\mathbf{x}, \mathbf{y})]$$

where $D(\mathbf{x}, \mathbf{y})$ is the intensity sensitivity of the detector and $[**]$ represents the 2-D convolution operator. Figure 2.3 shows the theoretical PSFs of the confocal and nonconfocal fluorescence microscopes. Elongation in the \mathbf{z} direction appears in both systems; however, the nonconfocal PSF exhibits highly dispersed tails that lead to very poor resolution in the axial direction. Detailed mathematical expressions for the PSFs, CTFs, and OTFs are given in Appendix A.

Due to a finite-sized detector pinhole, the OTF of any microscope is a band-limited function which vanishes outside a prescribed region. When a point detector is used, there exists no missing cone region of the OTF. However, as the detector size (the circular pinhole size) increases, the bandwidth of the 3-D OTF decreases, and a missing cone region appears on the spatial frequency axis around the origin, where

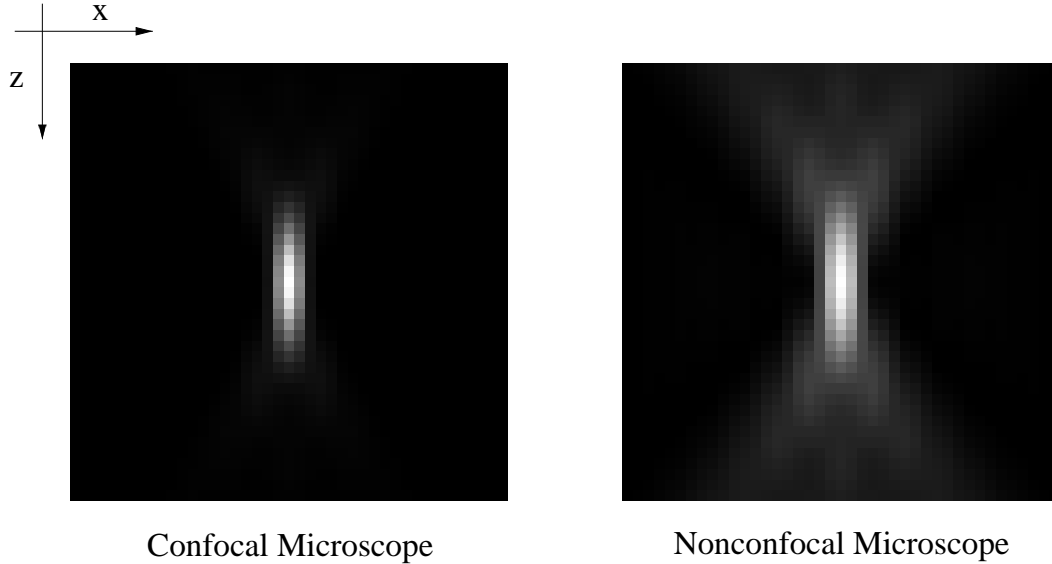


Figure 2.3: Theoretical PSFs of confocal and nonconfocal fluorescence microscopes in the xz plane. “Confocal” means that the pinhole is totally closed, whereas “nonconfocal” means that the pinhole is totally open (conventional microscope).

the Fourier components are zero. The support region of the 3-D OTFs of confocal and nonconfocal microscopes are shown in Figure 2.4.

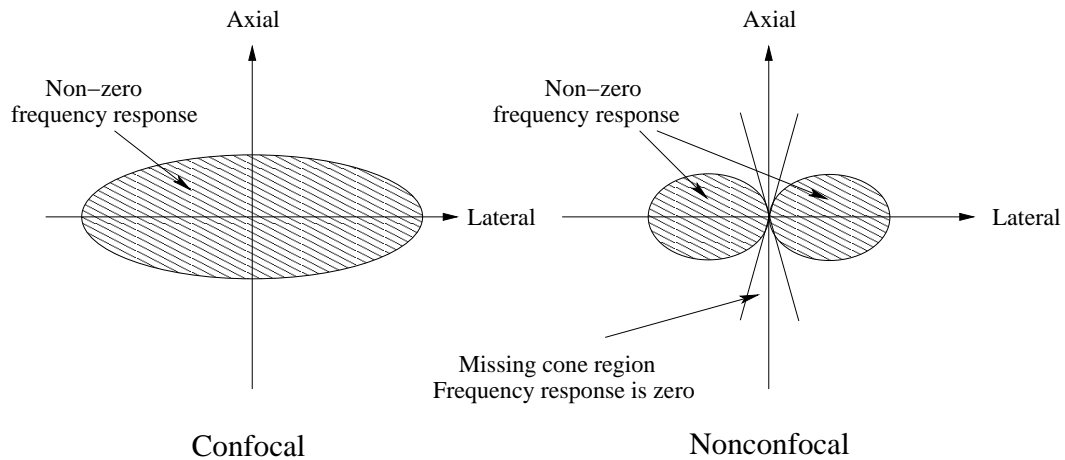


Figure 2.4: Schematic representation of the support region of the OTFs for confocal and nonconfocal microscopes. The missing cone region, where the frequency response is zero, decreases the resolution of the images, especially in the axial direction.

When enlarging the pinhole to increase the SNR of the signal, the bandwidth of

the OTF is reduced and the resolution of the image is degraded. The poor resolution in the axial direction is caused by elongation of the PSF and the missing cone region of the OTF. Because of these limitations in the system, restoration techniques are often used to remedy the compromised image resolution (even in the closed pinhole case).

2.1.4 Existing Image Restoration Techniques

Ideal confocal images are sharp and have high resolution. However, most obtainable images contain low resolution and noise due to an increase in size of the detector pinhole so that more signal can be detected. This reduces the resolution, especially in the axial direction. Therefore, many image restoration techniques have been applied to increase the resolution of and reduce the noise in the image, even in the closed pinhole case. Some people may refer to image restoration as deconvolution. However, we consider deconvolution as a deblurring process without attention to noise. In this section, we will discuss some common image restoration techniques for confocal microscopy. The PSF is assumed to be known in this discussion. Image restoration with an unknown PSF is called as blind restoration [29, 61, 66, 77, 90, 121, 133], in which the PSF needs to be estimated somehow in the restoration process.

Nearest Neighbors Method

In the nearest neighbors method [2, 3, 31, 67], the restored image at each plane is obtained by subtracting the degraded image on that plane with the blurring version of the 2-D degraded images from other planes and then convolving the result with the 2-D inverse filter from the in-focus plane. The explicit expression for this method is shown as follows:

$$\hat{x}_p = \{y_p - c[y_{p-1} + y_{p+1}] ** h_1\} ** g \quad (2.1)$$

where \hat{x} is the restored image, y_p is the degraded image at plane p , h_1 is the 2-D PSF of adjacent planes, g is the 2-D inverse filter of the PSF at the in-focus plane, and c is an empirically determined constant. The nearest neighbors method assumes that out-of-focus light affect only intermediate adjacent planes. Although this method is quick and easy, it is not able to restore the missing cone information and the nonnegativity of the image is not guaranteed.

Linear Filtering Methods

Linear filters include inverse filter, constrained least-squares, and Wiener filter. These filters are simple to implement and require little computation time.

The inverse filtering method simply deblurs the image by using a spatial filter as follows:

$$\hat{x} = y *** h_r \quad (2.2)$$

where h_r is the PSF of the inverse filter and $***$ represents the 3-D convolution. Inverse filter, in fact, considers only the blurring function and ignores noise in the degradation model; therefore, it cannot operate properly in the presence of noise. To avoid the pitfalls of an inverse filter in a noisy case, the pseudo-inverse filter is used instead and has the following form [3, 67]:

$$H_r = \frac{|H|}{|H|^2 + \gamma}$$

where H is the overall transfer function of the system and γ is an empirical constant to prevent the blowup of the inverse filter.

The constrained least-squares (CLS) or Tikhonov-Miller method [8, 120] is based on minimizing the squared difference between a degraded image and a blurred estimate of the original image with the use of regularization to overcome an ill-posed

problem of image restoration. The CLS method assumes that the acquired image is distorted by an additive Gaussian noise. The estimate of the original image \hat{x} is obtained by minimizing the following cost function:

$$\Phi(\hat{x}) = \|y - A\hat{x}\|^2 + \alpha\|C\hat{x}\|^2$$

where A is the system matrix, which represents the 3-D convolution between the PSF and the original for a space-invariant system, α is the regularization parameter, and C is a regularization matrix. By setting the derivative of $\Phi(\hat{x})$ with respect to \hat{x} to zero, the estimate \hat{x} is determined from the following expression:

$$\hat{x} = (A^T A + \alpha C^T C)^{-1} A^T y.$$

If $\alpha C^T C = \gamma$, then CLS becomes a pseudo-inverse filter. If $C^T C = R_f^{-1} R_n$ where R_f and R_n are the correlation matrices of the object and noise, then CLS becomes a Wiener filter, which is a linear optimal filter in the mean square error sense.

Similar to the nearest neighbors method, these linear filtering methods can only restore frequencies inside the bandwidth of the OTF; therefore, they are not capable of restoring the missing cone information. Moreover, nonnegativity is not guaranteed in the image.

Jansson-van Citter Method

The Jansson-van Citter method [3,67,72] is an iterative nonlinear technique. The n th iteration update of the unknown parameters is expressed as follows:

$$x^{n+1} = [x^n + \gamma(y_h^n)(y - y_h^n)]_+ \quad (2.3)$$

where the nonnegativity constraint $[t]_+ = t$ if $t \geq 0$ and 0 elsewhere. The parameter y_h^n is updated at every iteration: $y_h^n = x^n *** h$, where h is the 3-D PSF of the

microscope. The term $\gamma(y_h^n)$ is defined as $\gamma(y_h^n) = 1 - \frac{(y_h^n - \zeta)^2}{\zeta^2}$, where ζ is the maximum value of $y/2$. The Jansson-van Citter method can partially restore the missing cone information; however, its results are not as good as the ML method because no particular noise model is considered in the restoration technique [26].

Maximum Likelihood Method

Unlike all of the above methods which belong to the class of deterministic methods, the ML method is a statistical method that estimates the unknown image or an approximation of the original image by maximizing its log-likelihood function. It is based on a Poisson noise model which is the dominant source of noise in confocal microscopy. The detail of the ML method is given in Chapter III. This nonlinear method was shown to be able to partially restore the missing Fourier components in the missing cone region [24, 65, 67, 122]. Moreover, the nonnegativity constraint can be enforced easily in the ML method. Another advantage of ML estimation is that one can extend the noise model easily for further improvement by including additional effects, such as dark current, detector quantum efficient and photobleaching. The ML solution turns out to be equivalent to the Richardson-Lucy method [89, 98]; however, their mathematical optimization criterion and derivation are different [67]. Because of the ill-posed nature of restoration problems, ML estimation can produce noisy images if iterated too long. Therefore, some form of regularization is necessary, which will be discussed in Chapter III.

2.2 Image Plane Holography

Although confocal microscopy can provide the optical sectioning property for viewing a 3-D image, its point-by-point scanning required to achieve this property slows down the acquisition process and disrupts the real-time visualization. Unlike

the conventional confocal microscope which operates on a scanning principle, image plane holography is capable of capturing the same images one slice at a time while retaining the optical sectioning property. This technique significantly reduces the acquisition time necessary to obtain the image and can be beneficial in real-time imaging. We start this section by reviewing the concept behind conventional holography. Later, we introduce image plane holography and study its concept and limiting factors.

2.2.1 Conventional Holography

Holography is a process of recording both the amplitude and phase of a wave field so that the entire wave field can be regenerated. The holographic process consists of two processes: recording and reconstruction (Figure 2.5). The recording of the interference pattern between the object and reference beams is regarded as a hologram. The interference of two beams produces a fringe pattern, which is a sequence of light and dark areas corresponding to the constructive and destructive interferences, respectively. The fringe spacing depends on the angle between those two beams: the larger the angle, the finer the fringe pattern. The fringes are formed in the direction that bisects the angle between the two interfering waves within the medium [57]. Since photographic film is insensitive to the shape of the wave front, which is essentially the phase, the holographic process using the reference beam converts phase variations into amplitude variations through an interference process. The photographic material used to record the interference pattern is assumed to linearly map an intensity in the detection process into an amplitude in the reconstruction process. In the reconstruction process, the hologram is illuminated by a wave that is similar to the reference wave. The holographic process creates two images: the

primary (virtual) and conjugate (real) images.

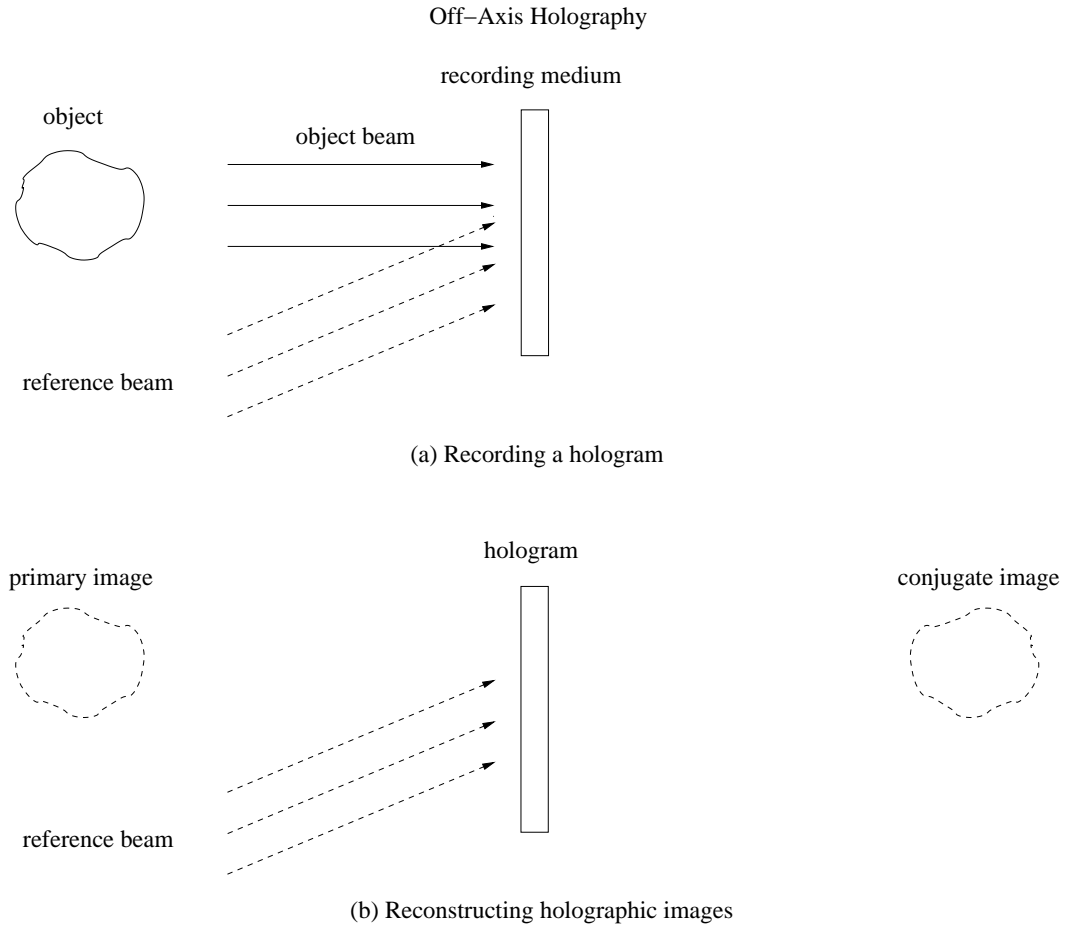


Figure 2.5: Two processes required in holography are recording and reconstructing processes. The recording process records the interference pattern between the object beam and the reference beam onto the recording medium. The reconstructing process produces the primary image behind the hologram and the conjugate image in front of the hologram by illuminating the hologram with the reference beam.

In-line holography, the first holography invented by Gabor [50–52], creates a low contrast image due to the superimposition of the primary and conjugate images, i.e., they form on the same optical axis. In this holography, the object is generally a transparency in which the major portion of the incident wave is transmitted without scattering. Since the reference beam is in the same direction as the object beam, a twin-image problem arises: the primary and conjugate images are superimposed,

causing a strong ambient background which reduces the image contrast.

To eliminate the twin image problem, off-axis holography was first introduced by Leith and Upatnieks [85]. In this technique, the reference beam impinges on the recording surface at some angle with respect to the object beam. Thus, the primary and conjugate images are formed at angularly different locations and are separated from other undesired components. Let u_o be the field of the object beam and u_{ref} be the field of the reference beam including incident illumination at angle θ with respect to the optical axis. The total field incident on the recording plane is given by:

$$u(\vec{r}) = u_o(\vec{r}) + u_{\text{ref}}(\vec{r})$$

where \vec{r} denotes spatial coordinates. A common example of an off-axis reference beam is a plane wave: $u_{\text{ref}} = \mathbf{U}_{\text{ref}} e^{-i2\pi\vec{r}\vec{\alpha}}$ where \mathbf{U}_{ref} is the amplitude of the reference beam, and $\vec{\alpha} = \frac{\sin\theta}{\lambda}$ is the spatial carrier frequency of the reference beam. Thus, the intensity distribution across the recording plane is

$$\begin{aligned} I(\vec{r}) &= |u(\vec{r})|^2 \\ &= |u_o(\vec{r})|^2 + \mathbf{U}_{\text{ref}}^2 + u_o(\vec{r})\mathbf{U}_{\text{ref}}e^{i2\pi\vec{r}\vec{\alpha}} + u_o^*(\vec{r})\mathbf{U}_{\text{ref}}e^{-i2\pi\vec{r}\vec{\alpha}} \end{aligned} \quad (2.4)$$

where $*$ stands for the complex conjugate. The third term, which is proportional to $u_o(\vec{r})$, generates the primary image. Similarly, the fourth term generates the conjugate image. To view the primary image, we illuminate the hologram with an exact duplicate of the original reference wave, in which case the primary image appears behind the photographic plate at exactly the same location where the object was originally located. To view the conjugate image, we illuminate the hologram with a wave that is the complex conjugate of the original reference wave. In this case, the conjugate image appears in front of the photographic plate. Both conventional in-line and off-axis holography records a hologram on photographic film; therefore,

one needs to use time-consuming chemical processing. This inconvenient process can be avoided when a digital detector is used as a recording medium.

2.2.2 Digital Holography

Instead of recording a hologram on photographic film, digital holography uses a digital detector, such as a CCD array, thus reducing some additional tasks required when using photographic film. Digital holography has become attractive for imaging living cells due to its rapid acquisition time and accessibility to a computer [22, 82]. With the digital detector, the reconstruction of the hologram can be performed on a computer. According to (2.4), the frequency domain of the hologram intensity turns the spatial-frequency spectrum of the recorded interference pattern into an angular spectrum of diffracted waves. In conventional numerical reconstruction, one often performs a mask in the frequency domain to extract the frequency components that relate to either the primary image or the conjugate image, thus eliminating the twin image problem.

In addition to the possibility to numerically reconstruct a holographic image, digital holography overcomes some limitations of conventional holography. In conventional holography, exposure time for recording a hologram is limited by stability time of an object motion. The stability time for living tissue is quite short for hologram recording time. The problem of short stability time of living tissue is avoided with digital holography because the sensitivity of the digital detector allows the capture of the object with moderate light and short exposure time [22, 82]. Therefore, there is no need for high power light, which can damage living cells. Since the exposure time of each hologram is shorter than the stability time of tissues, many holograms are recorded and averaged to reduce noise and increase SNR. Although

the digital detector has a large dynamic range (14-18 bits) which can image even the low-contrast fringe, its resolution is not as good as the photographic film.

In both conventional and digital holography, one can classify different types of holograms according to the diffraction or imaging conditions that exist between the object and the recording medium [57]. Examples of this class of holograms include Fresnel, Fourier, and image plane holography. When the recording plane lies in the Fresnel zone of the illuminated object, the process is called Fresnel holography. When the recording plane yields the Fourier transform of the object, the process is called Fourier holography. When a hologram records an image of the object, the process is called image plane holography.

2.2.3 Image Plane Holography with Incoherent Light

Although conventional holography with coherent light can generate the entire 3-D image in one exposure, it does not have a confocal effect and, thus imagery will contain out-of-focus scatters from other planes. Image plane holography, recently developed by Leith *et al.*, is illuminated by incoherent light and provides a confocal property that can reject the out-of-focus signals from other planes in a similar manner as confocal microscopy [7, 83, 84, 86, 116]. The confocal process of image plane holography is illustrated in Figure 2.6.

The idea of image plane holography can be explained by the Van Cittert-Zernike theorem. Light from any two points in the field can interfere if they are within the same coherence area. The size of the coherence area is proportional to the distance from the source and inversely proportional to the area of the source. By way of illustration, we assume that the coherence area is very small and the plane P_1 in the object is the plane of interest. Point x_1 is only coherent with point x'_1 because they

Image Plane Holography Process

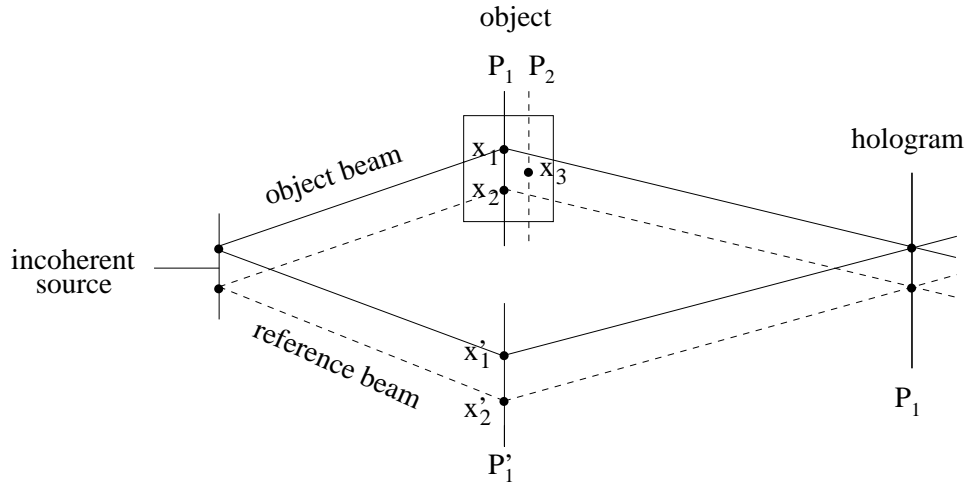


Figure 2.6: The object beam is coherent only with the reference beam that comes from the same point source. If plane P_1 is the in-focus plane, then x_1 will be coherent with x'_1 only and x_2 will be coherent with x'_2 only. Thus only plane P_1 will appear on the hologram.

originate from the same point source and they are equidistant. Likewise point x_2 is only coherent with point x'_2 . Point x_3 on plane P_2 will not be coherent with any points on plane P'_1 ; therefore it will not form the fringe pattern and will not appear on the hologram. With the small coherence area, plane P_2 will not be recorded on the hologram. Therefore, only information on plane P_1 will appear on the hologram and the out-of-focus signals from other planes will get suppressed. Each plane of interest will be recorded on the digital detector at a time, and the scan in the z direction to the next plane is required to obtain the 3-D image. Then numerical reconstruction is performed to view a holographic image.

Even though the entire 3-D image cannot be constructed in one exposure using this technique, a selected plane can be captured at once without scanning, a definite advantage for temporal analysis of specimens and real-time imaging. In addition, the aberrations due to off-axis scanning, which occurs in confocal microscopy, can be avoided. Furthermore, the use of a broad-spectrum source can also support a

multispectral framework. For the current set-up, image plane holography only works in the transmission mode, not in the fluorescence mode. However, it is still useful because the transmission mode in the conventional confocal microscope does not have the confocal property (see pp.60-61 in [60]).

The degree of confocal effect or depth discrimination for image plane holography is directly proportional to the fringe spacing in the fringe pattern, which is, in turn, proportional to the angle between the object and reference beams and the incoherent source illumination [132]. There are two basic regimes of volume-recorded fringes (Figure 2.7). In the first, the two interfering beams impinge from the same side of the recording medium. In this case, the fringe spacing is very coarse, i.e., about the wavelength of the illumination. In the second, the two beams impinge from opposite sides of the recording medium, as in Denisyuk volume reflection holography [132]. In this regime, the fringe pattern is very fine, spacing in the order of $\lambda/2n$, where n is the refractive index of the recording medium. The fringe pattern lies nearly parallel to the emulsion surface. When the object and reference beams are introduced from the opposite side of the recording medium, the angle between these two beams can be wider than when the two beams interfere from the same side, thus better degree of noise suppression. However, a digital detector cannot be used to record such a hologram. To take advantage of a digital detector, we consider only the regime where the two beams impinge on the same side in this dissertation.

In addition to the angle between the object and reference beams, the size of the source also directly effects the fringe localization: the larger the source, the smaller the coherence area, and thus the fringes are more localized. Hence, with a spatially broad source, the fringe localization suppresses light from out-of-focus planes much like the conventional confocal process [7, 115, 116]. A spectrally broad

Two Different Fringe Patterns in Image Plane Holography

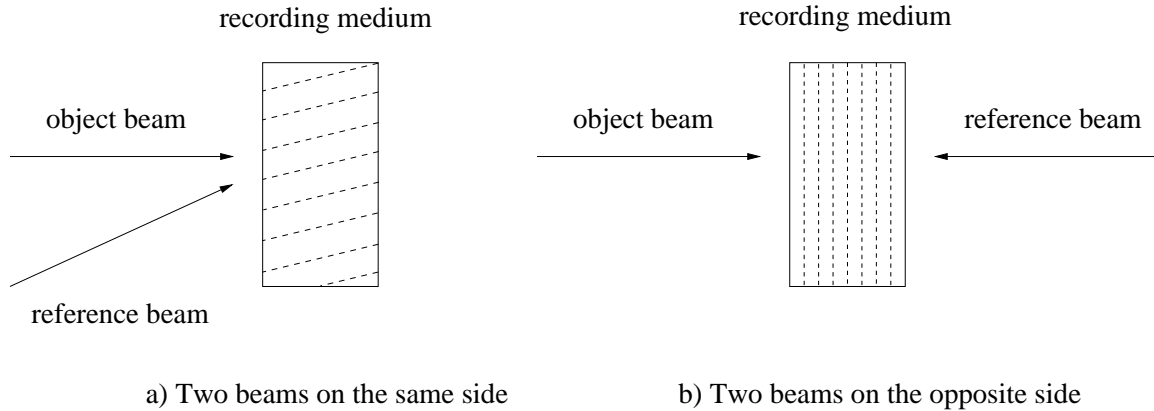


Figure 2.7: The fringe pattern is finer when the angle between the object beam and the reference beam is wider. The fringe direction is determined from the angle that bisects both beams.

source eliminates considerable scattering noise and also leads to fringe localization in depth. The use of simultaneous broad-source and broad-spectrum illumination thus further reduces the out-of-plane scattering noise [116]. For simplicity, here we focus only on the broad-source illumination.

The purpose of broad source illumination is to reduce the coherence in the object beam so that the depth discrimination and improvement in the resolution can be achieved; however, practical sources cannot be arbitrarily large. Furthermore, even for a large source, the coherence will be increased after light passes through a lens. The coherence area increases when a small lens is used. Since lenses in a microscope cannot be too large, an increase in coherence always arises. Moreover, if the source is too big, not only the fringes will be very fine and make it difficult to align the detector properly. Such fine fringes may cause a problem when using a digital detector to record a hologram as well. Because the transverse resolution is determined by the size of the source as seen at the hologram plane and the lateral resolution is determined by the lenses, the resolution is compromised by these limiting factors. As a result,

image recovery techniques can be applied to reduce the blur and noise problems. Due to the important role of the PSF in image recovery, we study the overall system PSF for image plane holography next.

2.2.4 Theoretical PSF of Image Plane Holography

The experimental setup for image plane holography is illustrated in Figure 2.8. The source is adjusted in size by placing rotating ground glass in a diverging laser beam. The source size is determined from the size of the diverging beam where it intersects the ground glass. A quasi-monochromatic and spatially incoherent source generates a partially coherent field. Light from the broad source is split into the object and reference beams via a beam splitter. The lens in the object beam images a selected plane of the object onto the hologram. In the reference path, the matching lens to that in the object path is needed to balance the two beams so that the interference can occur. Then the object and reference beams are brought back to form the fringe pattern at the hologram plane.

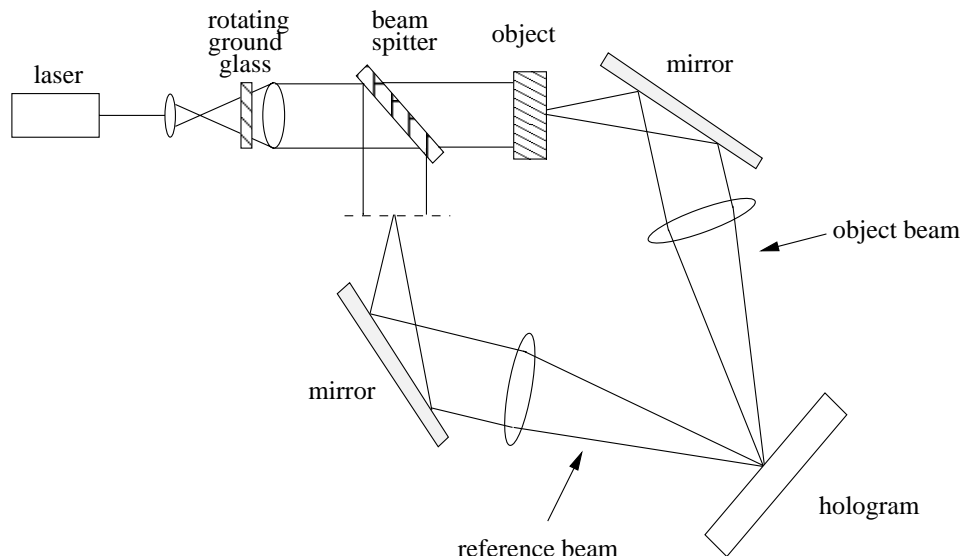


Figure 2.8: Experimental setup for recording an image plane hologram

The amplitude PSF of the overall system according to the above setup is deter-

mined at the output of the reconstruction process. Under an ideal condition where the source size is assumed to be infinitely large, the perfect depth discrimination at each plane is achieved and the corresponding 3-D amplitude PSF can be expressed as follows:

$$h(\mathbf{x}, \mathbf{y}, \mathbf{z}) = h_o(\mathbf{x}, \mathbf{y}, \mathbf{z})h_{\text{ref}}^*(\mathbf{x}, \mathbf{y}, \mathbf{z}) \quad (2.5)$$

where h_o and h_{ref} are the amplitude PSF of the object and reference beams, respectively. The detailed derivation of the PSF for image plane holography is given in Appendix B. This PSF is similar to that of the reflection and transmission confocal microscopes. Because image plane holography can provide the optical sectioning property, its 3-D CTF follows the 3-D CTF of the reflection confocal microscope that has no appearance of the missing cone region in an ideal confocal case. However, when a finite-sized source is used, the amplitude PSF needs to consider the effect of the source into account as well. Thus, the PSF becomes

$$h(\mathbf{x}, \mathbf{y}, \mathbf{z}) = h_o(\mathbf{x}, \mathbf{y}, \mathbf{z})[h_{\text{ref}}^*(\mathbf{x}, \mathbf{y}, \mathbf{z}) ** D(\mathbf{x}, \mathbf{y})] \quad (2.6)$$

where $D(\mathbf{x}, \mathbf{y})$ is the response of the finite-sized source.

2.2.5 Comparison between Confocal Microscopy and Image Plane Holography

In this section, we compare the similarities and differences between image plane holography and conventional confocal microscopy. Conventional confocal microscopy, in general, provides the nice property of optical sectioning, but in fact its transmission mode lacks this property. On the other hand, image plane holography offers the optical sectioning property in the transmission mode. In addition to the confocal effect, the most significant contribution of image plane holography is the absence of the scanning process in the object plane as required in conventional confocal

microscopy. Another advantage of image plane holography over confocal microscopy is the opportunity to capture both the phase and amplitude of a complex object. The latter can view only the amplitude part of an object. Figure 2.9 shows the layout of these two optical systems. If the matching lenses are used in the two systems, and the small pinhole and large source are assumed, then both systems will have the same 3-D amplitude PSF, $h = h_1 h_2^* = h_o h_{\text{ref}}^*$ where h_1 and h_2 are the PSFs of the objective and collector (objective) in transmission confocal microscopy and h_o and h_{ref} are the PSFs of the object and reference beams in image plane holography. Although the overall PSFs are equivalent if they use the same lenses, the configuration of individual PSFs is different, i.e., for transmission confocal microscopy, h_1 and h_2 are in series, while for image plane holography, h_o and h_{ref} are in parallel.

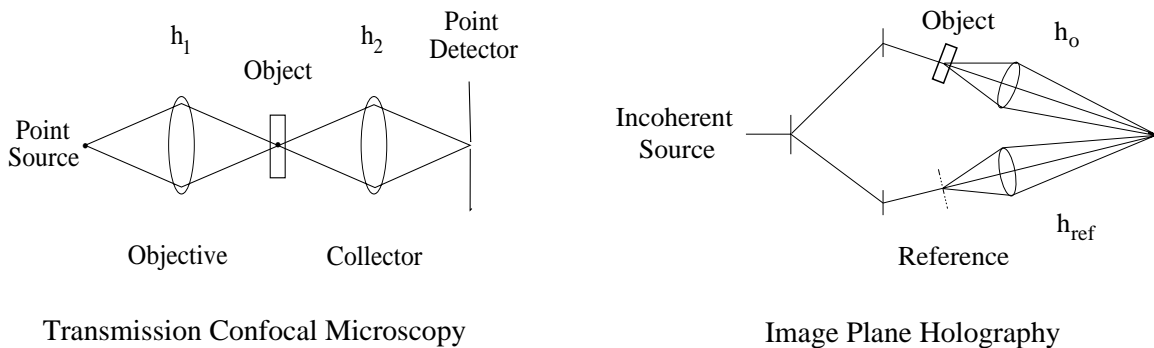


Figure 2.9: Configuration of transmission confocal microscopy and image plane holography systems and their PSFs.

Even though both image plane holography and transmission confocal microscopy belong to coherent systems, the light source requirement is opposite in the two systems. While transmission confocal microscopy requires a spatially coherent source, image plane holography requires an incoherent source. The size of the broad source in image plane holography determines the degree of the confocal effect, i.e., the larger the source size, the stronger the degree of the confocal effect. Unlike image plane holography, the confocal effect in confocal microscopy is limited by the increase in

size of the detector pinhole, i.e., the smaller the pinhole size, the stronger the degree of the confocal effect. The summary of the differences in transmission confocal microscopy and image plane holography is shown in Table 2.1.

	Confocal Microscopy (Transmission)	Image Plane Holography
Optical sectioning property	No	Yes
Object-plane scanning	Yes	No
Imaging type	Only amplitude	Both amplitude and phase
Light source requirement	Point source (coherent)	Broad source (incoherent)
Confocal controller	Pinhole size	Source size

Table 2.1: Comparison of the differences between conventional confocal microscopy and image plane holography

As with confocal microscopy, resolution and noise problems still appear in image plane holography due to the limitation of the optical system. Here again image recovery techniques offer an attractive solution.

2.2.6 Existing Reconstruction Techniques

Similar to confocal microscopy, practical image plane holography suffers from limited spatial resolution due to the out-of-focus contributions from other planes which are limited by the size of the light source, and from optical noise in the photodetector. Therefore, image recovery offers a convenient approach to overcome these problems. Because image plane holography is a new technique, not many proposed recovery techniques have been explored. A simple approach to image recovery would be to perform any typical image restoration technique on a reconstructed holographic image. However, a reconstructed holographic image acquired through existing numerical reconstruction may contain corrupted information. With this approach, good restoration based on bad data might not be achieved. A better approach is to recover the image directly from the complete data of the hologram. In this approach, a

complex object is reconstructed from the real-valued hologram intensity data. Since image reconstruction for image plane holography resembles that of digital holography, we review some common existing numerical reconstruction techniques used in digital holography instead.

Filtering Method

Conventional reconstruction is performed by using a digital filter applied in the frequency domain to extract only the primary or conjugate image. Assuming the reference beam is a plane wave at normal incident, the Fourier transform of the hologram intensity in (2.4) is

$$\mathcal{I}(f) = \mathcal{I}_o(f) + \mathbf{U}_{\text{ref}}^2 \delta(f) + \mathbf{U}_{\text{ref}} \mathcal{U}_o(f - \alpha) + u_r \mathcal{U}_o^*(-f - \alpha) \quad (2.7)$$

where f denotes spatial frequencies, \mathcal{I} , \mathcal{I}_o , and \mathcal{U}_o denote the Fourier transform of $|u|^2$, $|u_o|^2$, and u_o , respectively. Since the intensity of the reference beam, $\mathbf{U}_{\text{ref}}^2$, is uniform (ideally), its Fourier transform is a Dirac function located at the origin. The first two terms in (2.7) form the zero-order spectra located at the center of the Fourier plane. The last two terms form the first-order spectra located at spatial frequencies $f = \pm\alpha$ away from the origin. Figure 2.10 shows an example of a hologram and the magnitude of its Fourier transform. If α is large enough to separate the two first-order spectra from the zero-order spectra, then a mask (a bandpass filter) can be used to extract desired frequency components that yield the holographic image corresponding to the primary or conjugate image for the case of image formation. For Fresnel holography, one more step of Fresnel transform is needed to obtain the reconstructed holographic image. Although, this approach is very simple and not time-consuming, the resulting holographic image is degraded due to the effect of the filter.

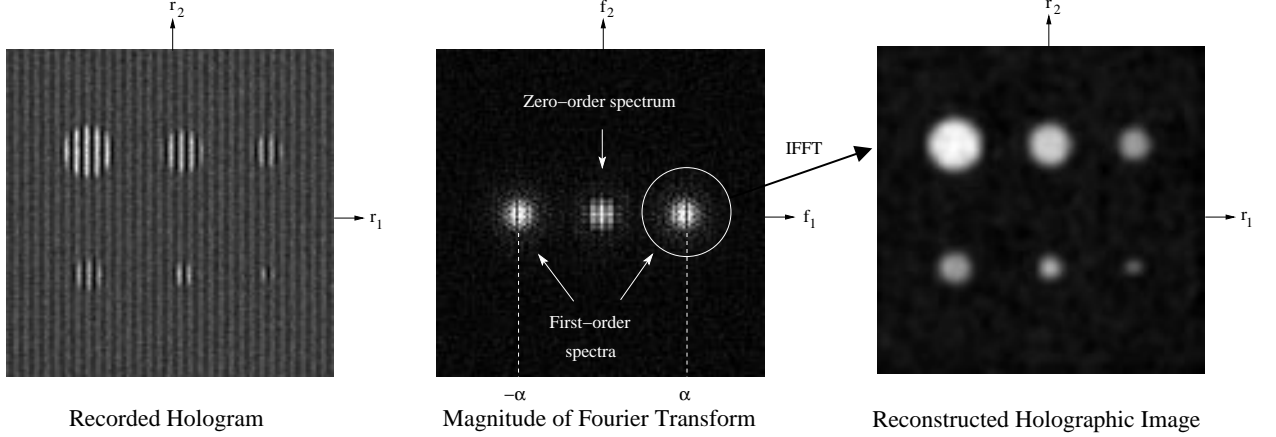


Figure 2.10: Holographic reconstruction using a filtering method.

Phase-Shifting Method

Phase-shifting or phase-modulation method [35, 117, 131] was proposed to suppress the zero-order image and one of twin images in off-axis holography through the use of several recording holograms. In this approach, many holograms are generated from different incident angles of the reference beam and used for removing undesired images. For example, one of the phase-shifting methods proposed by Takaki *et al.* can extract the third term in (2.4) through the means of the following calculation:

$$I_{\theta_1} e^{i\theta_1} - I_{\theta_2} e^{-i\theta_2} + I[e^{i\theta_1} + e^{-i\theta_2}] = \left[\frac{e^{i\theta_1} - 1}{e^{-i\theta_1} - 1} - \frac{e^{i\theta_2} - 1}{e^{-i\theta_2} - 1} \right] u_o u_{\text{ref}}^*$$

where θ_1 and θ_2 are angles of the reference beams, and the following three holograms are captured

$$\begin{aligned} I &= I_o + I_r + u_o u_{\text{ref}}^* + u_o^* u_{\text{ref}} \\ I_{\theta_1} &= I_o + I_r + u_o u_{\text{ref}}^* e^{i\theta_1} + u_o^* u_{\text{ref}} e^{-i\theta_1} \\ I_{\theta_2} &= I_o + I_r + u_o u_{\text{ref}}^* e^{i\theta_2} + u_o^* u_{\text{ref}} e^{-i\theta_2}. \end{aligned}$$

Although this technique requires fewer holograms than other phase-shifting methods proposed by De Nicola *et al.* [35] and by Yamaguchi and Zhang [131], using three

holograms is still inconvenient for reconstructing just one holographic image.

Statistical Method

A primary drawback of the above methods is the lack of random noise in the model. Unlike filtering and phase-shifting methods, a statistical method includes characteristics of noise into its model to reconstruct the image. Statistical reconstruction for holography introduced by Çetin *et al.* [20] is based on additive Gaussian noise model and uses least-squares approach to solve the problem. This technique was applied to Fourier holography. In Chapter VII of the dissertation, we propose a statistical reconstruction technique based on Poisson statistics, which is a major source of noise, to reconstruct the complex-valued object from the real-valued hologram intensity data [112]. Our statistical reconstruction technique can be applied to many types of digital holography including Fresnel and Fourier holography.

With knowledge of the background and limitations in the optical systems, we can use statistical image recovery techniques. Before proposing new, fast, converging algorithms and a new statistical reconstruction technique, we will review the concept of statistical techniques used in this dissertation and construct statistical models in the next chapter.

CHAPTER III

Statistical Techniques for Image Recovery

As mentioned in the previous chapters, deterministic techniques for image recovery, though simple to implement and computationally fast, are not based on any particular noise model of the optical system. Therefore, they cannot efficiently improve the resolution of degraded images, and thus do not provide good image recovery. Unlike deterministic techniques, statistical techniques, such as maximum likelihood (ML) [65, 67], maximum *a posteriori* (MAP) [62], and penalized likelihood (PL) [49, 125] estimation, are based on a specific noise model that characterizes the physical model of the optical system. In this way, better image recovery can be achieved. However, most statistical techniques are complex to implement and require large amounts of computation time. Thus, the main goal for this dissertation is to construct statistical techniques that simplify the image recovery problem and require less computation time, while still providing a good quality image. In this chapter, we first analyze the physical and measurement models for confocal microscopy (including incoherent imagery) and image plane holography (including digital holography), and develop statistical models for these systems. After that, we review the concepts behind relevant statistical techniques, and examine some existing iterative algorithms for solving the problems associated with statistical image recovery.

3.1 Models for Confocal Microscopy and Other Incoherent Imagery

For ML/PL estimation, one needs to specify a statistical model of an optical system. A statistical image model that matches physical and measurement models of a system well tends to produce a good quality image. In this section, we describe the physical and measurement models for confocal microscopy, which can also be generalized to other incoherent imagery, and design its statistical model based on the noise characteristics and measurement model.

3.1.1 Physical and Measurement Models

Confocal fluorescence microscopy and other similar incoherent imagery acquire images of photon intensity through a photodetector, such as a PMT or a CCD camera. These images usually deviate from the true object intensity due to the imaging process as illustrated in Figure 3.1.

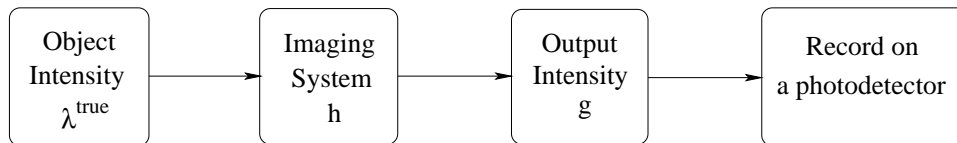


Figure 3.1: Diagram of incoherent imagery

From Figure 3.1, the (fluorescent) intensity of the object in the continuous space is denoted by $\lambda^{\text{true}}(\vec{r}, \mathbf{z})$ and the corresponding output intensity $g(\vec{r}, \mathbf{z})$ is determined by using a superposition integral of the object intensity and the PSF of the system as follows:

$$g(\vec{r}, \mathbf{z}) = \iint h(\vec{r}, \mathbf{z}; \vec{r}', \mathbf{z}') \lambda^{\text{true}}(\vec{r}', \mathbf{z}') d\vec{r}' d\mathbf{z}' \quad (3.1)$$

where \vec{r} represents 2-D spatial coordinates, \mathbf{z} represents the scanning plane of interest, and $h(\vec{r}, \mathbf{z}; \vec{r}', \mathbf{z}')$ represents the 3-D intensity PSF of the system. To discretize the

object space, we approximate the true object intensity in terms of basis functions

$$\lambda^{\text{true}}(\vec{r}, \mathbf{z}) \approx \lambda(\vec{r}, \mathbf{z}) = \sum_{j=1}^P x_j \chi_j(\vec{r}, \mathbf{z}) \quad (3.2)$$

where $\lambda(\vec{r}, \mathbf{z})$ is an approximation of the true object intensity in the continuous space, x_j is the unknown coefficient of the j th basis function, P is the total number of unknown parameters to be estimated, and $\chi_j(\vec{r}, \mathbf{z})$ is the j th continuous-spaced basis function, such as an indicator function (a rect function). Because the output $g(\vec{r}, \mathbf{z})$ is recorded on a photodetector, the discrete version of $g(\vec{r}, \mathbf{z})$ in the detector space can be written in the following form:

$$\begin{aligned} g(\vec{r}, \mathbf{z}) \Big|_{(\vec{r}, \mathbf{z})=(\vec{r}_i, \mathbf{z}_i)} &= \iint h(\vec{r}_i, \mathbf{z}_i; \vec{r}', \mathbf{z}') \sum_{j=1}^P x_j \chi_j(\vec{r}', \mathbf{z}') d\vec{r}' d\mathbf{z}' \\ &= \sum_{j=1}^P a_{ij} x_j = [Ax]_i, \quad i = 1, \dots, N \end{aligned} \quad (3.3)$$

where \vec{r}_i is the center location of the i th element of the photodetector, z_i is the i th focal plane, N is the total number of measured pixels for all planes, and a_{ij} is the ij th component of the system matrix A , which can be expressed in terms of basis functions

$$a_{ij} = \iint h(\vec{r}_i, \mathbf{z}_i; \vec{r}', \mathbf{z}') \chi_j(\vec{r}', \mathbf{z}') d\vec{r}' d\mathbf{z}'. \quad (3.4)$$

For simplicity, we assume that the response of the photodetector itself is a Dirac function located at the center of each detector element so that the PSF of the photodetector hardly affects the overall PSF of the system. Since the measurement data usually contains noise, we can regard them as random variables having the mean according to (3.3):

$$\mathbb{E}[Y_i] = [Ax]_i + b_i, \quad i = 1, \dots, N \quad (3.5)$$

where Y_i denotes the i th pixel of the measurement data, and b_i denotes an offset due to effects, such as dark current and background noise. The goal is to estimate the unknown image x from the measurement data Y . Owing to existence of noise in the measurement data, we consider the characteristics of noise in the statistical model for solving this inverse problem.

3.1.2 Statistical Models

Due to noise in the measurement, one can use the statistical characteristics of the measurement to construct its noise model. In this section, we first consider the complete statistical model of the confocal microscope system by combining all possible sources of noise. Since there exists a variety of statistical distributions, statistical image restoration for confocal microscopy becomes a complicated optimization problem. Therefore, an approximation of these complex distributions becomes another alternative model to simplify the optimization problem. These statistical models play an important role for achieving a good quality image.

Complete Model

For confocal microscopy as well as other incoherent imagery, the photodetector behind the detector pinhole collects light. Images acquired through the detector may be contaminated by a variety of noise sources, and many of these noise sources follow different statistical distributions.

- Photon noise is due to photon emissions and detections, and is a Poisson process. This is a major source of noise.
- Thermal noise or dark current is due to the finite temperature of the elements of the detector system, which occurs even when no light is present. Dark current

is a Poisson process.

- Readout noise in the amplifier is an additive Gaussian noise, and independent of the signal [104, 105].
- Black level is a deterministic constant offset for adjusting the lowest pixel value to lie above zero.
- Analog-to-digital (A/D) quantization noise is caused by conversion from an analog signal to a digital number. This noise is not considered in most image recovery methods, including the work presented here, because uniform distribution of quantization noise is difficult to integrate with Poisson and Gaussian distributions, and its importance on the quality of estimates is unclear [104, 105].

Therefore, the complete model of the measurement data at each pixel, Y'_i , is:

$$Y'_i \sim \alpha_1 \left\{ \text{Poisson} \{ f_i [A(h)x]_i + b'_i \} + b''_i \right\} + \mathcal{N}(m, \sigma^2), \quad i = 1, \dots, N \quad (3.6)$$

where:

- Y' denotes the degraded image (noisy measurement), which is ordered lexicographically by stacking a 3-D image into a vector.
- x denotes the true object corresponding to a number of fluorescent photons per second, and is ordered lexicographically by stacking a 3-D image into a vector.
- $A(h)$ denotes the 3-D system matrix which is a function of a 3-D PSF (h) of a microscope. $[A(h)x]_i$ is a shorthand notation for the i th entry of the vector $A(h)x$ or $[A(h)x]_i = \sum_{j=1}^P a_{ij}x_j$. This notation is generalized to both shift-variant and shift-invariant systems.

- α_1 denotes the scaling factor which adjusts the output image into a 0-255 range (for 8 bits).
- f_i denotes the scan time factor proportional to an amount of scanning time and quantum efficiency of the photodetector. With the same quantum efficiency, the longer we scan, the better the SNR of the image.
- b'_i denotes the mean of the dark current.
- b''_i denotes the black level.
- $\mathcal{N}(m, \sigma^2)$ denotes the Gaussian readout noise with mean m and variance σ^2 .

Approximate Model

Since the Poisson-Gaussian mixture model provides a very complicated optimization problem and the major source of noise has a Poisson distribution, we reform the noise model of the measurement, combine different terms, and then ignore the Gaussian noise. To simplify the Poisson-Gaussian model, we define the i th measurement, Y_i , in terms of Y'_i as follows:

$$Y_i \triangleq \frac{Y'_i - \alpha_1 b''_i - m}{\alpha_1} + \frac{\sigma^2}{\alpha_1}, \quad i = 1, \dots, N. \quad (3.7)$$

Thus the model of the measurement becomes

$$Y_i \sim \text{Poisson}\{f_i[A(h)x]_i + b'_i\} + \mathcal{N}\left(\frac{\sigma^2}{\alpha_1}, \frac{\sigma^2}{\alpha_1}\right), \quad i = 1, \dots, N. \quad (3.8)$$

Combining the readout noise variance into the background noise and dark current term and ignoring the Gaussian noise [104], we end up with the simpler model of the measurement at each pixel:

$$Y_i \sim \text{Poisson}\{f_i[A(h)x]_i + b_i\}, \quad i = 1, \dots, N \quad (3.9)$$

where $b_i = b'_i + \frac{\sigma^2}{\alpha_1}$ denotes the mean of the dark current and background noise. Since this model has been shown to provide good restoration [25, 28, 104], we mostly use this model for confocal microscopy throughout this dissertation.

System Matrix and PSF

The PSF of the system plays a very important role in the recovery process. Using an accurate PSF in the recovery techniques leads to a high quality image. The PSF is either known or unknown. If the PSF is unknown, then it must be estimated somehow in the restoration technique and this technique is regarded as blind restoration [29, 61, 66, 77, 90, 121, 133]. Blind restoration is more difficult because only the degraded image is used to simultaneously estimate both the image and the PSF. Practically, the PSF of the system is usually unknown; however, one can either derive the theoretical PSF [60, 75, 76] from the optical system or measure the experimental PSF [100] from a point-like object (small fluorescence beads) or a very thin line object. Although the theoretical PSF has a closed form, it does not account for defects in the system, such as aberration of lenses. Thus, ignoring noise, the measured PSF tends to yield a closer approximation to the true PSF of the system. Since estimating the image using partial information about the PSF tends to yield better restoration than using no information about the PSF at all, we mainly focus on non-blind restoration in this dissertation. The methods can be extended to the case of blind restoration.

Regardless of whether the PSF is known or unknown, imaging systems can be divided into two categories. If the PSFs are similar at any location of the image, then the system is called space-invariant. In contrast, if the PSFs vary with locations, then the system is called space-variant. Strictly speaking, optical systems are space-

variant due to the nature of finite-sized lenses. However, it makes the problem more complicated. If the PSFs do not vary too much, then an approximated model using the space-invariant system can simplify the problem and still provide good restoration.

According to the statistical model discussed above, if a linear space-invariant system is assumed, then $A(h)$ is a Toeplitz (or block-Toeplitz) matrix simply representing the linear convolution operator. Therefore, we can represent $A(h)x$ as $h * x$, where $*$ is the convolution operator. For example, for a 1-D linear space-invariant system, A becomes a Toeplitz matrix and we obtain the following equality:

$$Ax = \begin{bmatrix} h(0) & h(-1) & 0 & 0 \\ h(1) & h(0) & h(-1) & 0 \\ 0 & h(1) & h(0) & h(-1) \\ 0 & 0 & h(1) & h(0) \end{bmatrix} \begin{bmatrix} x(0) \\ x(1) \\ x(2) \\ x(3) \end{bmatrix} = \begin{bmatrix} (h * x)(0) \\ (h * x)(1) \\ (h * x)(2) \\ (h * x)(3) \end{bmatrix}$$

However, for 2-D and 3-D, matrix A is more complicated. To illustrate, consider the following 3×3 PSF for a 2-D case:

$$\begin{bmatrix} h(-1, -1) & h(-1, 0) & h(-1, 1) \\ h(0, -1) & h(0, 0) & h(0, 1) \\ h(1, -1) & h(1, 0) & h(1, 1) \end{bmatrix}.$$

If x is assumed to be an $m \times n$ matrix, then the corresponding system matrix becomes an $(mn) \times (mn)$ block-Toeplitz matrix as follows:

$$A(h) = \begin{bmatrix} H(0) & H(-1) & 0 & \cdots & 0 \\ H(1) & H(0) & H(-1) & \ddots & \vdots \\ 0 & \ddots & \ddots & \ddots & 0 \\ \vdots & \ddots & \ddots & \ddots & H(-1) \\ 0 & \cdots & 0 & H(1) & H(0) \end{bmatrix}$$

where each $m \times m$ sub-matrix $H(i)$ is itself a Toeplitz matrix,

$$H(i) = \begin{bmatrix} h(0, i) & h(-1, i) & 0 & \cdots & 0 \\ h(1, i) & h(0, i) & h(-1, i) & \ddots & \vdots \\ 0 & \ddots & \ddots & \ddots & 0 \\ \vdots & \ddots & \ddots & \ddots & h(-1, i) \\ 0 & \cdots & 0 & h(1, i) & h(0, i) \end{bmatrix}.$$

3.2 Models for Image Plane Holography and Other Digital Holography

As discussed previously, the raw data recorded as the hologram intensity is more complete than the data obtained from a reconstructed holographic image; therefore, we use the raw hologram data directly to reconstruct a high quality holographic image. In this section, we describe the physical and measurement models for digital holography, in general, including image plane holography, and develop its statistical model based on the measurement model and characteristics of noise in the system. Because a digital detector is used for recording data, the statistical model for digital holography closely follows the same noise sources as in confocal microscopy.

3.2.1 Physical and Measurement Models

The diagram of the recording process in digital holography is illustrated in Figure 3.2. After recording a hologram on a digital detector, numerical reconstruction from the digitally recorded hologram is performed on the computer to reconstruct the estimate of the object.

The relation between the object beam u_o at the hologram plane and the object field f at the object plane can be described through the system PSF as image formation for the case of image plane holography, the Fourier transform for the case of

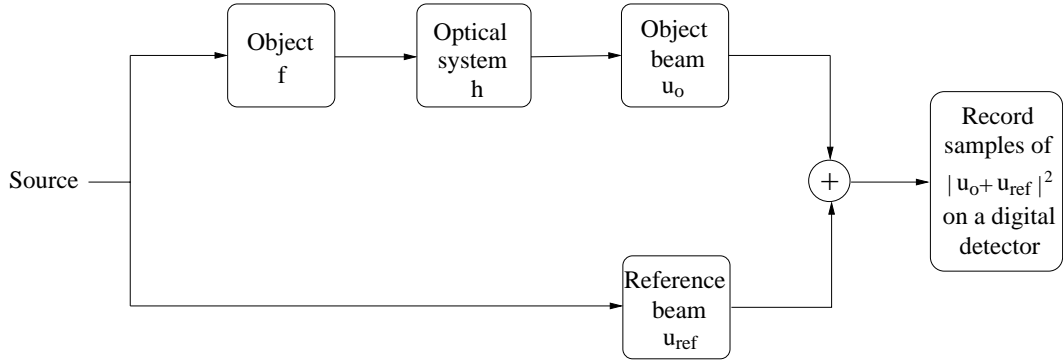


Figure 3.2: Diagram of digital holography

Fourier or Fraunhofer holography, or the Fresnel transform for the case of Fresnel holography. Thus, the holographic image of the object to be reconstructed is embedded in the object beam u_o . In general, one can express the object beam u_o in Figure 3.2 in terms of the object using a superposition integral of the following form:

$$u_o(\vec{r}, \mathbf{z}) = \iint h(\vec{r}, \mathbf{z}; \vec{r}', \mathbf{z}') f^{\text{true}}(\vec{r}', \mathbf{z}') d\vec{r}' d\mathbf{z}', \quad (3.10)$$

where $h(\vec{r}, \mathbf{z}; \vec{r}', \mathbf{z}')$ denotes the amplitude PSF of the system, and $f^{\text{true}}(\vec{r}', \mathbf{z}')$ denotes the true object field. This expression is generalized to both 2-D and 3-D objects. In practice, the recording medium has finite thickness, but we ignore this effect here for simplicity.

For conventional holography, the interference between the object and reference beams at the recording plane has the following continuous-space intensity:

$$\begin{aligned} I(\vec{r}, \mathbf{z}) &= |u_o(\vec{r}, \mathbf{z}) + u_{\text{ref}}(\vec{r})|^2 \\ &= |u_o(\vec{r}, \mathbf{z})|^2 + |u_{\text{ref}}(\vec{r})|^2 + u_o(\vec{r}, \mathbf{z})u_{\text{ref}}^*(\vec{r}) + u_o^*(\vec{r}, \mathbf{z})u_{\text{ref}}(\vec{r}) \end{aligned} \quad (3.11)$$

where u_{ref} denotes the (known) field of the reference beam. The first two terms in (3.11) relate to the zero-order image. The third term, which is proportional to u_o , relates to the primary image. The fourth term, which is proportional to u_o^* , relates to the conjugate image. For off-axis holography, the reference beam is oriented at

some angle resulting in a known spatial carrier frequency denoted by $\vec{\alpha}$. An example of such a reference beam is a plane wave that is tilted by an angle θ with respect to the optical axis, i.e., $u_{\text{ref}}(\vec{r}) = \mathbf{U}_{\text{ref}} e^{-i2\pi\vec{r}\cdot\vec{\alpha}}$ and $\vec{\alpha} = \frac{\sin\theta}{\lambda}$ where \mathbf{U}_{ref} is the amplitude of the reference wave and λ is the wavelength.

Let $Y = [Y_1, \dots, Y_N]$ denote the hologram measurement data recorded on a digital detector, where N is the total number of measurement elements for all planes. Similar to confocal microscopy, because the measurement data are usually noisy, we consider the measurement reported by the i th element of the digital detector to be a random variable whose mean is modeled as follows:

$$\mathbb{E}[Y_i] = |u_o(\vec{r}, \mathbf{z}) + u_{\text{ref}}(\vec{r})|^2 + b_i \Big|_{(\vec{r}, \mathbf{z}) = (\vec{r}_i, \mathbf{z}_i)}, \quad i = 1, \dots, N. \quad (3.12)$$

For simplicity, we treat the digital detector response as a Dirac impulse at the center of each element. Since conventional holography is in the continuous space, one needs to convert the continuous space of (3.11) into a discrete space. The true object, $f^{\text{true}}(\vec{r}, \mathbf{z})$, in (3.10) can be approximately represented in terms of basis functions:

$$f^{\text{true}}(\vec{r}, \mathbf{z}) \approx f(\vec{r}, \mathbf{z}) = \sum_{j=1}^P x_j \chi_j(\vec{r}, \mathbf{z}) \quad (3.13)$$

where $f(\vec{r}, \mathbf{z})$ is an approximation of the true object in the continuous space, x_j is the unknown complex coefficient of the j th basis function, P is the total number of parameters to be estimated, and $\chi_j(\vec{r}, \mathbf{z})$ is a basis function, such as a rect function. Combining (3.10) and (3.13), we can write $u_o(\vec{r}_i, \mathbf{z}_i)$ in the following discrete form:

$$u_o(\vec{r}_i, \mathbf{z}_i) = \iint h(\vec{r}_i, \mathbf{z}_i; \vec{r}', \mathbf{z}') \sum_{j=1}^P x_j \chi_j(\vec{r}', \mathbf{z}') d\vec{r}' d\mathbf{z}' = \sum_{j=1}^P a_{ij} x_j = [Ax]_i \quad (3.14)$$

where a_{ij} is the ij th component of the system matrix A , which is the response of the object beam $u_o(\vec{r}_i, \mathbf{z}_i)$ to the input x_j , and can be expressed in terms of the system

PSF and the basis functions as

$$a_{ij} = \iint h(\vec{r}_i, \mathbf{z}_i; \vec{r}', \mathbf{z}') \chi_j(\vec{r}', \mathbf{z}') d\vec{r}' d\mathbf{z}'. \quad (3.15)$$

Combining these expressions with the definition $u_i \triangleq u_{\text{ref}}(\vec{r}_i, \mathbf{z}_i)$ leads to the following model for the measurement means which we use in the statistical model for statistical holographic reconstruction:

$$\mathbb{E}[Y_i] = |[Ax]_i + u_i|^2 + b_i, \quad i = 1, \dots, N. \quad (3.16)$$

The goal is to estimate the complex unknown x from the real measured Y_i , since x parameterizes the unknown object f of interest.

3.2.2 Statistical Model

Similar to confocal microscopy, the hologram data acquired from the digital detector are degraded by blur and noise; therefore, we can follow similar noise sources when constructing the complete and approximate statistical measurement models for image plane holography and other digital holography.

Complete Model

According to the complete model for confocal microscopy in (3.6) and the measurement means of photon noise for digital holography in (3.16), we derive the similar complete model of the measurement data, Y_i , for digital holography as follows:

$$Y_i \sim \alpha_1 \{\text{Poisson}\{f_i|[Ax]_i + u_i|^2 + b_i\}\} + \mathcal{N}(m, \sigma^2), \quad i = 1, \dots, N \quad (3.17)$$

where f_i represents the quantum efficiency of the digital detector only because xy scanning is not needed here. Unlike confocal microscopy, this model involves the magnitude squared of the field due to the coherent system, and thus the unknown parameter to be estimated is the field of the object, i.e., both magnitude and phase of the object are available, instead of the object intensity.

Approximate Model

To simplify the Poisson-Gaussian mixture optimization problem, we approximate the measurement model by using the same technique as discussed in confocal microscopy. Thus we model the noisy measurement data for digital holography as

$$Y_i \sim \text{Poisson}\{|[Ax]_i + u_i|^2 + b_i\}, \quad i = 1, \dots, N. \quad (3.18)$$

In fact, the quantum efficiency factor can be ignored in the reconstruction process because it is merely a constant parameter. We will use this model for digital holography throughout this thesis. To our knowledge, this Poisson model for digital holography has not been explored yet. Moreover, it can be generalized to many applications of digital holography, such as image plane holography, Fresnel holography and Fourier holography, and to phase retrieval problems by changing the system matrix or the PSF accordingly.

3.3 Maximum Likelihood Estimates

Based on the noise models of the measurements designed above, one can apply statistical image recovery techniques to recover an approximation of the original image. In ML estimation, the parameter that we wish to estimate is obtained by maximizing the log-likelihood function:

$$\hat{x} = \arg \max_x \Phi(x). \quad (3.19)$$

In this case, the objective function is the concave log-likelihood function, which is the data-fit term. The objective function can be either maximized or minimized depending on the shape of the objective function. If the objective function has a minimum, then the ML problem becomes the minimization of the objective function

instead. An example of the objective function for ML estimation based on the model (3.9) of confocal microscopy is

$$L(x) = \sum_{i=1}^N (y_i \log \bar{y}_i(x) - \bar{y}_i(x) - \log y_i!) \quad (3.20)$$

where $\bar{y}_i = f_i[A(h)x]_i + b_i$. This function is concave but not necessarily strictly concave so there may be multiple values of x that all maximize L . When the likelihood function corresponds to a Gaussian distribution, the ML estimation becomes the least-squares method. If the true object is known *priori* to always be nonnegative, such as in confocal microscopy, then a nonnegativity constraint can be imposed on the estimation in (3.19) which can sometimes lead to faster convergence. Directly maximizing the likelihood function with respect to x is cumbersome due to the nested sums with logarithms. Since closed-form solution for the maximizer \hat{x} is not available, iterative algorithms are needed to compute \hat{x} . The most common approach to maximizing the likelihood function is the expectation-maximization (EM) algorithm [39].

3.3.1 Expectation-Maximization Algorithm

The basic idea of an EM algorithm is as follows. The measurement, or observed data, is a random vector Y that has the probability density function $g(Y; x)$, where x is a true parameter to be estimated. Since it is difficult to maximize $g(Y; x)$ with respect to x , the sample space of Y is embedded in a larger sample space where optimization problems are easier to solve. Thus, the EM algorithm postulates a complete (unobservable) data, a random vector Z , such that Y is a function of Z , and Z has a probability function $f(Z; x)$. Each iteration of an EM algorithm consists of two steps: the expectation step (E-step) and maximization step (M-step). The E-step comes first and forms the Q function which is the following conditional

expectation of the log-likelihood function:

$$Q_Z(x; x^n) = E[\log f(Z; x) | Y = y; x^n] \quad (3.21)$$

where x^n is a current parameter estimate. The M-step comes second and maximizes the Q function with respect to x to obtain a new estimate

$$x^{n+1} = \arg \max_x Q_Z(x; x^n).$$

One can show that with this approach the log-likelihood function is guaranteed to increase at each iteration [39]. Furthermore, the following equality is satisfied at each iteration:

$$\left. \frac{\partial}{\partial x_j} Q_Z(x; x^n) \right|_{x=x^n} = \frac{\partial}{\partial x_j} \log f(Y; x^n). \quad (3.22)$$

One can also find sufficient conditions for convergence [129]. The next section will show a derivation example of the EM algorithm to the application of confocal microscopy.

E-Step

In the classical EM algorithm (ML-EM) for image restoration, the PSF of the system is assumed to be known. In the E-step, the Q function is derived by taking the conditional expectation of the log-likelihood function of Z^1 with respect to Y , where Z^1 is the set of complete or unobservable data given by:

$$Z^1 = \left\{ \{Z_{ij}\}_{j=1}^P, \{B_i\}_{i=1}^N \right\} \quad (3.23)$$

where $Z_{ij} \sim \text{Poisson}\{f_i a_{ij}(h) x_j\}$ and $B_i \sim \text{Poisson}\{b_i\}$. Thus, from (3.21), the Q function is

$$Q_{Z^1}(x; x^n) = \sum_{i=1}^N \sum_{j=1}^P \{-f_i a_{ij}(h) x_j + N_{ij}^n \log(f_i a_{ij}(h) x_j)\} + \text{constant} \quad (3.24)$$

where

$$N_{ij}^n = E \left[Z_{ij} \mid Y = y; x^n \right] = f_i a_{ij}(h) x_j^n \frac{y_i}{\bar{y}_i^n} \quad (3.25)$$

and

$$\bar{y}_i^n = f_i \sum_{l=1}^P a_{il}(h) x_l^n + b_i. \quad (3.26)$$

M-Step

In the M-step, the Q function is maximized with respect to x_j by taking its derivative and then setting it to zero. Therefore, the pixel update at the next iteration, x_j^{n+1} , is:

$$x_j^{n+1} = \arg \max_{x_j} Q_{Z^1}(x; x^n) = \frac{x_j^n}{\sum_{i=1}^N f_i a_{ij}(h)} \sum_{i=1}^N f_i a_{ij}(h) \frac{y_i}{\bar{y}_i^n}.$$

Even though this EM algorithm converges globally if initiated with a positive image [123], it converges very slowly. Therefore, faster algorithms have been investigated.

After performing many iterations of the ML-EM, the resolution of the image is improved, but noise is also amplified. This is because image recovery is an ill-posed problem where the existence, uniqueness, and stability of the solution are not guaranteed. The ill-posedness of the continuous problem results in an ill-conditioned system matrix. Small changes in the data may result in a significant change in the solution [8,9]. As a result, a regularization technique for the ML problem is necessary. Examples of regularization approaches include stopping the iteration before convergence [64, 124], post-smoothing the image [107], and adding a roughness penalty function to the log-likelihood function [49, 81, 106]. The last method is called penalized likelihood (PL) estimation. The PL estimation can be viewed as maximum *a posteriori* (MAP) estimation with a Gibbs (Gauss-Markov) prior [62, 63], where

the log prior corresponds to the penalty function. The next section will discuss PL estimation.

3.4 Penalized-Likelihood Estimates

Regularizing the ML problem by including a penalty function in the likelihood function can help iterative algorithms to converge faster. A variety of penalty functions are available, and one can choose as desired. This approach is stable and predictable, and furthermore, it allows us to control the resolution of the recovered image as well. Therefore, we focus on PL estimation in this thesis.

As with ML estimation, PL estimation is based on optimizing an objective function. The PL method, however, involves an additional term to the objective function we saw earlier. Thus, for the concave likelihood function, the objective function using PL estimation becomes

$$\Phi(x) = L(x) - \beta R(x) \tag{3.27}$$

where $R(x)$ is the roughness penalty function, which is convex, and β denotes a parameter that controls the tradeoff between resolution and noise in the recovered image. In this case, the goal is to estimate x by finding the maximizer of the objective function as follows:

$$\hat{x} \triangleq \arg \max_x \Phi(x). \tag{3.28}$$

Similarly, for the convex likelihood function, the objective function is:

$$\Phi(x) = L(x) + \beta R(x), \tag{3.29}$$

and the goal is to estimate x by minimizing the objective function:

$$\hat{x} \triangleq \arg \min_x \Phi(x). \tag{3.30}$$

Unlike in the ML case, by choosing R properly, the objective function Φ can be made *strictly* concave, so \hat{x} is unique. The design of the penalty function is discussed next.

3.4.1 Penalty Functions

In general, penalty functions are used to remove the effects of noise caused by the ill-posed nature of the problem. A simple penalty approach is to penalize the differences between neighboring pixels that might cause noise. In this thesis, we consider only convex penalty functions because they lead to a unique maximum and are easier to optimize than nonconvex penalty functions. Our roughness penalty function can be represented in the following general form:

$$R(x) = \sum_i \psi([Cx]_i), \quad (3.31)$$

where the potential function ψ characterizes the behavior of the penalty function and the penalty matrix C defines the adjacent neighboring pairs of pixels. For a 2-D image, a penalty involving pixels that consist of horizontal and vertical adjacent neighbors of pixels is known as the first-order neighborhood. If the diagonal adjacent neighbors are included beside the horizontal and vertical neighbors, then it is called the second-order neighborhood. Figure 3.3 shows the neighborhood system of the first and second orders for a 2-D image.

The weighting elements in matrix C is determined from the inverse of the pixel distance, i.e., the further the distance, the smaller weight. For the first-order neighborhood in a 2-D image, matrix C consists of horizontal and vertical adjacent neighbors with the weighting of 1. For example, with a 2×2 image, the matrix C can be

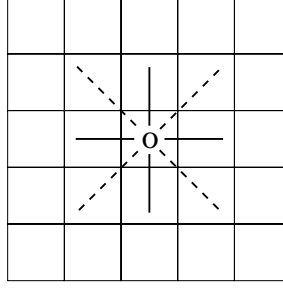


Figure 3.3: Illustration of the first-order and second-order neighborhood on one pixel of a 2-D image. The solid lines represents the pairs of penalized pixels in the first-order neighborhood. The solid plus dash lines illustrate the second-order neighborhood.

written as follows:

$$Cx = \begin{bmatrix} -1 & 1 & 0 & 0 \\ 0 & 0 & -1 & 1 \\ -1 & 0 & 1 & 0 \\ 0 & -1 & 0 & 1 \end{bmatrix} \begin{bmatrix} x_1 \\ x_2 \\ x_3 \\ x_4 \end{bmatrix} = \begin{bmatrix} x_2 - x_1 \\ x_4 - x_3 \\ x_3 - x_1 \\ x_4 - x_2 \end{bmatrix}.$$

For the second-order neighborhood, matrix C consists of horizontal, vertical, and diagonal cliques, where the element entries of the diagonal neighbors in matrix C are $\pm 1/\sqrt{2}$.

The potential function $\psi(t)$ is designed according to the degree of smoothness on the smooth region and edges. We assume that each potential penalty function $\psi(t)$ satisfies the following conditions [40, 43, 68]:

- $\psi(t)$ is symmetric.
- $\psi(t)$ is everywhere differentiable (and therefore continuous).
- $\dot{\psi}(t) = \frac{d}{dt}\psi(t)$ is non-decreasing (and hence $\psi(t)$ is convex).
- $\omega(t) = \frac{\dot{\psi}(t)}{t}$ is non-increasing for $t \geq 0$.
- $\omega(0) = \lim_{t \rightarrow 0} \frac{\dot{\psi}(t)}{t}$ is finite and nonzero.

Mathematically, there are two types of convex penalty functions: quadratic and nonquadratic. These two differ only on how the potential functions has an effect on the edges. Each of these is discussed in detail below.

Quadratic Penalty Function

The quadratic penalty function is simple to optimize. It merely applies a quadratic term to the difference of pixel neighbors. Thus, the quadratic potential function is

$$\psi(t) = \frac{1}{2}t^2.$$

Although easy to apply, this penalty function globally smooths the image because large pixel differences including the edges are penalized in the same manner as small pixel differences. Therefore, the quadratic penalty oversmooths the edges resulting in unsharp edges.

Nonquadratic Penalty Function

For cases in which sharper edges are desired, nonquadratic penalty functions become more attractive because of their edge-preserving properties. In this technique, large differences between neighboring pixels are penalized less than in the quadratic penalty function, while small differences remain penalized the same as in the quadratic penalty. Therefore, sharp edges are still preserved in the resulting images. However, the nonquadratic penalty function provides a more complicated optimization than the quadratic penalty function, and it can cause an unusual noise effect [45]. One example of an edge-preserving nonquadratic potential function introduced by Lange [81] is

$$\psi(t) = \delta^2 \left[\left| \frac{t}{\delta} \right| - \log \left(1 + \left| \frac{t}{\delta} \right| \right) \right] \quad (3.32)$$

where δ is a user-specified parameter that controls the degree of edge preservation. The smaller δ , the stronger the degree of edge preservation and the more unusual noise effects. If δ is very large, then this penalty will approach the quadratic penalty. This nonquadratic penalty behaves like the absolute penalty when $|t| \gg \delta$, but like the quadratic penalty when $|t| \ll \delta$. We choose δ such that the neighbor differences at the edges are less penalized than the differences in the smooth regions. In this dissertation, we use this potential function for the nonquadratic penalty function.

The second example of a nonquadratic penalty function is the Huber function [68], which has the following form:

$$\psi(t) = \begin{cases} t^2/2, & |t| \leq \delta \\ \delta|t| - \delta^2/2, & |t| > \delta. \end{cases} \quad (3.33)$$

This potential function is quadratic for $|t| \leq \delta$, and behaves like the absolute penalty for $|t| > \delta$. Although the Huber function has a continuous first derivative, it is not everywhere twice differentiable. Therefore, it is not applicable for an algorithm that requires the second derivative such as the Newton-Raphson method.

Another interesting choice of a nonquadratic potential function is the generalized Gaussian Markov random field (GGMRF) function which is developed by Bouman and Sauer [13]. The GGMRF function is defined as

$$\psi(t) = |t|^p, \quad 1 \leq p \leq 2. \quad (3.34)$$

This function becomes the absolute penalty when $p = 1$ and the quadratic penalty when $p = 2$. Unlike the Huber and Lange penalties above where a very wide range of the edge-preserving parameter δ needs to be determined, the GGMRF function offers a smaller range of p to provide edge-preservation. However, this potential function has the undefined second derivative at $t = 0$ when $p < 2$.

Figure 3.4 shows the plots of different potential functions: quadratic, Lange, Huber, and GGMRF. Other choices of nonquadratic penalty functions include the log-cosh function developed by Green [58], and many potential functions developed by Lange [81].

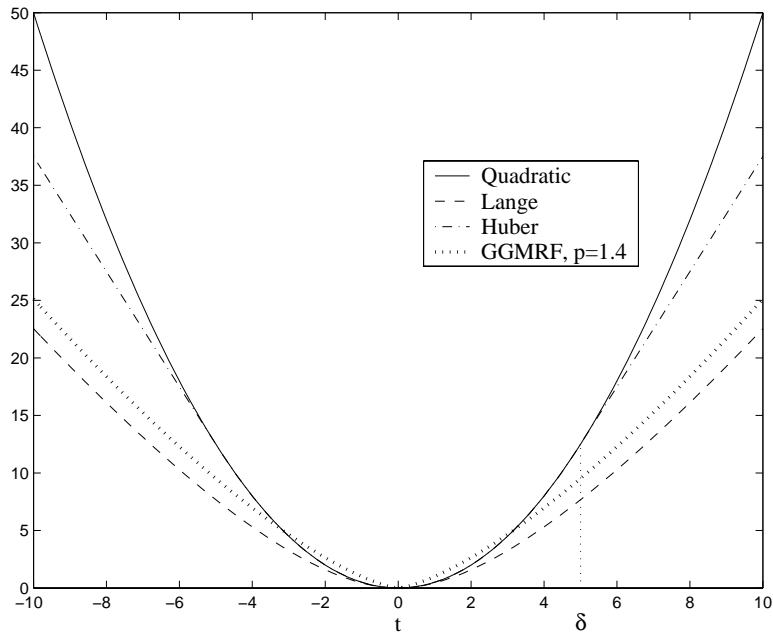


Figure 3.4: Illustration of different potential functions. For the Huber and Lange nonquadratic functions, $\delta = 5$.

After specifying the objective function, one needs to find the maximizer or minimizer of the objective function in (3.27) or (3.29), respectively. As in the ML problem, directly optimizing the objective function in the PL problem is difficult; therefore, an iterative algorithm is necessary to obtain the optimizer. The next section will discuss the use of iterative algorithms to solve these optimization problems.

3.5 Iterative Algorithms for Optimization Problems

Iterative algorithms are needed in PL estimation because a closed-form solution for the maximizer/minimizer of the objective function is not available. If we use

convergent iterative algorithms, then the same objective function will lead to the same estimate \hat{x} regardless of which particular iteration is used, so the image quality depends on the objective function but not on the algorithm. Thus, one desires iterative algorithms to have the following properties: the guarantee of convergence, rapid convergence rate, efficient computation, parallelizability, stability, robustness, simplicity and flexibility. Because existing algorithms do not have all of these properties, many new algorithms have been proposed to satisfy as many properties as possible. All iterative algorithms considered in this thesis are gradient-based. The gradient-based algorithms use the first derivative of the objective function at each iteration as a “search direction” to find the maximum/minimum point. Throughout this section, we assume that the objective function is concave.

3.5.1 Conditions for Convergence

A necessary condition for a gradient-based algorithm in an unconstrained case to converge to the maximum point (local or global) is:

$$\nabla\Phi(x) = 0$$

when $x = x^*$, where x^* is the optimal point. For the case of nonnegativity-constrained maximization, the condition for convergence becomes:

$$\left. \frac{\partial}{\partial x_j} \Phi(x) \right|_{x=x^*} \begin{cases} = 0, & x_j^* > 0 \\ \leq 0, & x_j^* = 0. \end{cases}$$

This is called Karush-Kuhn-Tucker conditions. These conditions only guarantee that the algorithm converges to a local maximum when the objective function has multiple maxima. Therefore, a global maximum is not guaranteed.

Another condition that can help ensure convergence of $\{x^n\}$ but is not a necessary

condition is monotonicity. An algorithm is said to be monotonic if

$$\Phi(x^{n+1}) \geq \Phi(x^n), \quad \forall x^n.$$

For a strictly concave objective function, algorithms that monotonically increase the objective function at each iteration can usually be shown to be guaranteed to converge to the optimal point. Therefore, monotonicity is one of desirable properties of an iterative algorithm.

3.5.2 Examples of Gradient-Based Algorithms

In this section, we review some basic gradient-based algorithms, such as the gradient-ascent, steepest-ascent, Newton-Raphson, and coordinate-ascent algorithms.

Gradient-Ascent Algorithm

For the gradient-ascent algorithm, the estimate of x at the next iteration, x^{n+1} , is

$$x^{n+1} \triangleq x^n + \alpha \nabla \Phi(x^n)$$

where α is the step-size. The the gradient of the objective function is defined as $\nabla \Phi = [\frac{\partial}{\partial x_1} \Phi, \dots, \frac{\partial}{\partial x_P} \Phi]^T$, where the superscript T stands for the transpose. In this algorithm, one does not need to evaluate the step-size at every iteration, thus reducing the computation time. However, the use of the constant step-size for the entire algorithm can either slow down the convergence if the step-size is too small, or skip the optimal solution if the step-size is too large.

Steepest-Ascent Algorithm

The steepest-ascent algorithm is similar to the gradient-ascent algorithm except that it requires the step size to be updated at every iteration: $\alpha^n \triangleq \arg \max_{\alpha} \Phi(x^n + \alpha \nabla \Phi(x^n))$.

This slows down the execution. Moreover, the steepest-ascent algorithm does not easily accommodate the nonnegativity constraint.

Newton-Raphson Algorithm

The Newton-Raphson method is based on the quadratic approximation of the objective function at the current estimate, x^n , as follows:

$$\Phi(x) \approx \phi(x; x^n) \triangleq \Phi(x^n) + \nabla\Phi(x)(x - x^n) + \frac{1}{2}(x - x^n)^T \nabla^2\Phi(x^n)(x - x^n)$$

where $\nabla^2\Phi(x)$ is called the Hessian matrix. The ij th entry of the Hessian matrix is $\frac{\partial^2}{\partial x_i \partial x_j} \Phi(x)$. The update x^{n+1} is the maximizer of the quadratic approximation where the derivative of ϕ is equal to zero. This yields:

$$\begin{aligned} x^{n+1} &\triangleq \arg \max_x \phi(x; x^n) \\ &= x^n - [\nabla^2\Phi(x^n)]^{-1} \nabla\Phi(x^n). \end{aligned}$$

This algorithm usually converges faster than the gradient ascent algorithm and has a super-linear convergence rate if convergent. However, the Newton-Raphson algorithm requires a twice differentiable objective function. Moreover, this algorithm is not guaranteed to converge and does not enforce the nonnegativity constraint. Due to matrix inversion of the Hessian matrix, this algorithm is not practical for a large-scale optimization problem of image recovery.

Coordinate-Ascent Algorithm

The coordinate-ascent algorithm [aka Gauss-Siedal, successive over-relaxation (SOR), iterated conditional modes (ICM) algorithm] updates one pixel at a time and holds others fixed to their most recent values as follows:

$$x_j^{new} = \arg \max_{x_j} \Phi(x_1^{new}, \dots, x_{j-1}^{new}, x_j, x_{j+1}^{old}, \dots, x_P^{old}), j = 1, \dots, P$$

This algorithm converges quickly if starting from a good initial image. It is intrinsically monotonic and has a global convergence; however, the maximizing step can require large computation time for nonquadratic problems. To reduce the computation time, one can replace the maximizing step with a 1-D Newton-Raphson step. Unfortunately, this approach loses the guarantee of monotonicity for the nonquadratic objective function and requires large computation time for calculating the second partial derivatives of the nonquadratic objective function as well.

3.5.3 Classification of Gradient-Based Algorithms

One can classify algorithms according to their properties and behaviors. Based on an updating method or a parallelizability property, we can divide gradient-based algorithms into four categories: simultaneous-update, sequential-update, grouped-update, and ordered-subset algorithms. These categories are discussed below:

Simultaneous-Update Algorithms

Simultaneous update algorithms update all pixels simultaneously using all data. Algorithms in this class are fully parallelizable because each pixel update is decoupled from all other pixel updates. When using an optimization transfer principle to construct surrogate functions (which will be discussed later), one can further divide simultaneous-update algorithms into two subgroups according to the separability of the surrogate functions used in the algorithms. Simultaneous-update algorithms using separable surrogate functions, such as the gradient-ascent, EM [39], separable-paraboloidal-surrogate (SPS) [40,109], and De Pierro’s MAP-EM [36] algorithms, accommodate the nonnegativity constraint easily, while simultaneous-update algorithms using nonseparable surrogate functions, such as the conjugate-gradient (CG) [44,47,96] and steepest ascent algorithms, do not.

Sequential-Update (Column Action) Algorithms

Sequential update algorithms update one pixel at time, while using all data and the most recent estimates of other pixels. One iteration consists of a cycle through all pixels. In this way, the optimization problem reduces to a 1-D problem for each pixel. These algorithms often have fast convergence. Moreover, the nonnegativity constraint can be enforced easily to each pixel update. Due to sequential updates, this class of algorithms is poorly suited to parallel processing. Examples of sequential update algorithms include coordinate ascent (CA) [14], paraboloidal surrogate coordinate ascent (PSCA) [40], and space-alternating generalized EM (SAGE) [48,49] algorithms.

Grouped-Update (Multiple-Column-Action) Algorithms

Grouped update algorithms update a group of pixels at a time while using all data. These algorithms are intermediate between the simultaneous and sequential update algorithms, and they are partially parallelizable. These grouped update algorithms were proposed by Sauer *et al.* [99] and Fessler (who called them grouped coordinate ascent) [42, 43] to solve the parallelizability problem of the CA algorithm, which converges rapidly.

Row Action or Ordered-Subset Algorithms

Ordered-subset (OS) algorithms update all pixels simultaneously using only a subset of the data. Conventional OS algorithms are not guaranteed to converge to the optimal solution in the inconsistent problems, but they converge very fast at the early iterations, and their image quality is often acceptable. Examples of the algorithms in this category include ordered-subset EM (OSEM) [69], rescaled block-iterative EM (RBI-EM) [18,19], and row-action maximum likelihood algorithm

(RAMLA) [17]. More recently, the relaxed OS-SPS algorithm [4] was proposed to fix the convergence problem of conventional OS algorithms.

New Algorithms to Be Developed

In the next chapters, we will introduce new fast converging algorithms for pixel-based image recovery called the partitioned-separable paraboloidal surrogate coordinate ascent (PPCA) and relaxed ordered-subset separable paraboloidal surrogate (OS-SPS) algorithms. In Chapter IV, we introduce the PPCA algorithm to overcome the tradeoff between the convergence rate and parallelizability. This algorithm belongs to the class of grouped-update algorithms but converges faster than those existing algorithms. In Chapter V, we adapt the relaxed OS-SPS algorithm, which is used widely in image reconstruction for tomography, to the problems of pixel-based image recovery because of its initial fast convergence. Both PPCA and relaxed OS-SPS are guaranteed to converge to the optimal solution.

CHAPTER IV

Partitioned-Separable Paraboloidal Surrogate Coordinate Ascent Algorithm

4.1 Introduction

Statistical methods such as ML, PL, and MAP estimation have been widely applied to recover an approximation of the original image. Because closed-form solutions are usually unavailable, iterative maximization algorithms are needed. This chapter¹ presents a new fast monotonic algorithm for image recovery that is well suited to parallel computing.

Many algorithms for statistical image recovery have been constructed; however, no existing algorithm has all the properties of an “ideal” algorithm, such as a fast convergence rate, quick computation time, stability, simplicity, and parallelizability. EM algorithms [36, 39] are widely used to compute ML estimates. Although EM algorithms are simple to implement and guaranteed to converge, they converge slowly since they simultaneously update all parameters. Fast converging algorithms are particularly desirable for large 3D images and real-time analysis in medical imaging and biological applications. Several algorithms have been proposed to improve the convergence rate of the EM algorithms. For example, the space-alternating general-

¹This chapter is based on [109].

ized EM (SAGE) algorithm developed by Fessler and Hero [48, 49] converges quickly but is typically nonparallelizable and difficult to implement. Similarly, the classical coordinate ascent algorithm, which updates parameters sequentially each iteration, is nonparallelizable, and furthermore does not have an explicit form for the update. To obtain a closed form for the update, one can use a coordinate ascent algorithm with Newton-Raphson updates (CA-NR) developed by Bouman and Sauer [14]. However, the CA-NR algorithm is not guaranteed to converge if the objective function is non-quadratic. Erdoğan and Fessler [40] proposed the paraboloidal surrogate coordinate ascent (PSCA) algorithm to solve the convergence problem of the CA-NR algorithm by maximizing paraboloidal surrogate functions instead of directly maximizing the original objective function. However, the PSCA algorithm is still not parallelizable. In summary, existing algorithms are either fast converging, as in the CA-NR or PSCA algorithms, or fully parallelizable, as in the EM algorithms, but not both.

The grouped coordinate ascent (GCA) algorithm introduced by Sauer *et al.* [99] and Fessler [42, 43] represents an alternative approach to parallelization. The GCA algorithm simultaneously updates pixels within a group of spatially separated pixels and sequentially updates each group of pixels. This approach does not fully capture the fast convergence properties of CA, and thus the GCA algorithm converges slower than the proposed PPCA algorithm².

In addition to the family of the CA algorithms above, the parallel successive overrelaxation (PSOR) method [130] using domain decomposition techniques was proposed for solving the five-point and nine-point stencil approximation of Poisson's equations, but it is inapplicable to the more general optimization problem of interest in imaging. Therefore, it will not be considered in this particular study.

²Matlab m-files for comparison are available at <http://www.eecs.umich.edu/~fessler>.

To respond to the convergence rate and parallelizable tradeoff that existing algorithms have, we developed a new, fast converging, parallelizable algorithm called partitioned-separable paraboloidal surrogate coordinate ascent (PPCA). This new approach overcomes the convergence rate and parallelizability tradeoff of existing algorithms [108]. To provide parallelizability, we partition the set of pixels into subsets that are updated in parallel, usually by a different processor for each subset to reduce execution time. To provide fast convergence, each processor *sequentially* updates the pixels *within* each subset. This approach captures most of the rapid convergence of the CA algorithm, but remains parallelizable. A simplistic implementation of this idea would not ensure convergence; therefore, we derive the algorithm by applying optimization transfer principles. This approach guarantees that the proposed algorithm will monotonically increase the objective function. It also intrinsically accommodates the nonnegativity constraints. The PSCA algorithm of [40] is the special case of the PPCA algorithm when only one subset (and hence only one processor) is used.

Since our long-term interest is space-varying systems, we implemented the proposed algorithm using direct convolution rather than FFT algorithms, so that it easily extends to problems where the space-invariant property is inapplicable or invalid, such as in positron emission tomography (PET) and single photon emission computed tomography (SPECT) systems. In microscopy, many papers such as [28, 91] have assumed space-invariance of the microscope, and thus EM algorithms using FFT techniques have been applied to reduce the computation time. However, to accommodate the space-varying systems in the future as well, we derived the proposed algorithm in image space rather than frequency space.

This chapter is organized as follows. Section 4.2 describes the image recovery

Acronym	Algorithm Name	Parallelizability	Speed	Guaranteed to Converge
EM	Expectation-maximization algorithm [36, 39]	Yes	Slow	Yes
SAGE	Space-alternating generalized expectation-maximization [48, 49]	No	Medium	Yes
SPS	Separable paraboloidal surrogates [36]	Yes	Slow	Yes
PSCA	Paraboloidal surrogate coordinate ascent [40]	No	Fast	Yes
CA-PS	Coordinate ascent with parabola surrogates	No	Slow	Yes
GCA	Grouped coordinate ascent [42, 43, 99]	Partially	Medium	Yes
PPCA	Partitioned-separable paraboloidal surrogate coordinate ascent [108]	Almost fully	Fast	Yes
CA-NR	Coordinate ascent with Newton-Raphson updates [14]	No	Fast	No
CA,P	Coordinate ascent with precomputed curvature	No	Fast	No
PSCA,P	PSCA with precomputed curvature [40]	No	Fast	No
PPCA,P	PPCA with precomputed curvature	Almost fully	Fastest	No

Table 4.1: Acronyms and description of different algorithms. “Speed” refers qualitatively to the combination of number of iterations and execution time per iteration.

problem. Section 4.4 reviews some existing algorithms. Section 4.5 presents the proposed algorithm in a general form suitable for many applications. Section 4.6 discusses convergence of this algorithm. Section 4.7 compares the convergence rate of the proposed algorithm with other algorithms. In Section 4.8, the proposed algorithm is specifically applied to image restoration for confocal microscopy. Since a 3-D image from a confocal microscope has poor resolution, especially in the axial direction, due to out-of-focus contributions from other planes, image restoration techniques have been applied to remove the out-of-focus contributions and reduce elongation in the axial direction. Simulation results are presented in Section 4.9 and conclusions are given in Section 4.10. Since several algorithms are mentioned in this chapter, for convenience, we summarize their acronyms and description in Table 4.1.

4.2 The Problem

In image recovery problems, the measurements are usually degraded by blur and noise. To recover the original image, one can use the statistical characteristics of the measurement system to specify an objective function that is maximized. In this

chapter, we consider a very broad class of objective functions having the following form:

$$\Phi(x) = \sum_{i=1}^M \psi_i([Bx]_i) \quad (4.1)$$

where $x \in \Re^P$ represents the true image ordered lexicographically in the vector form and B is an $M \times P$ matrix that typically includes both an $N \times P$ system matrix and an $r \times P$ coefficient matrix of a roughness penalty function where $M = N+r$, N is the number of measurements, and r is roughly the number of neighbors of pixels. For $i = 1, \dots, N$, each ψ_i function characterizes the agreement between a noisy measurement and a linear function of the unknown image, namely $[Bx]_i = \sum_{j=1}^P b_{ij}x_j$. For $i = N+1, \dots, M$, each ψ_i function corresponds to the roughness penalty function due to the ill-posed nature of the problem. Section 4.8 shows a concrete example where some of the ψ_i functions correspond to a Poisson log-likelihood function, which describes fluorescent photons detected at a photodetector in a confocal microscope system, and the remaining ψ_i functions represent a nonquadratic penalty function. We assume that the objective function has a unique global maximum. Thus our goal is to estimate x by finding the maximizer of the objective function as follows:

$$\hat{x} \triangleq \arg \max_{x \geq 0} \Phi(x). \quad (4.2)$$

The ML, PL, and MAP estimators are all special cases of this maximization problem. We focus on the nonnegativity constrained problem, but of course all the algorithms are also applicable to the unconstrained case.

4.3 Optimization Transfer Functions

Directly maximizing the objective function in (4.2) is difficult when ψ_i 's are non-quadratic, such as for the log-likelihood function of Poisson noise. To simplify the

optimization problem and to assure monotonic increases in the objective function at each iteration, one can apply an optimization transfer approach by finding a “surrogate” function ϕ (Figure 4.1) that lies below the objective function.

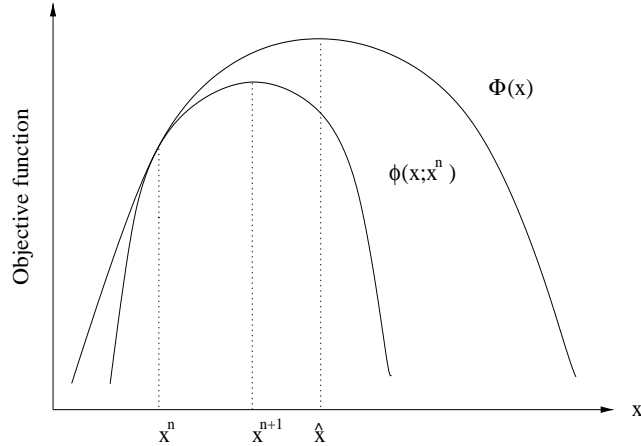


Figure 4.1: Illustration of a surrogate function

As illustrated in Figure 4.1, we obtain the next estimate by maximizing the surrogate function³:

$$x^{n+1} \triangleq \arg \max_{x \geq 0} \phi(x; x^n) \quad (4.3)$$

where x^n denotes the estimate at the n th iteration. Choosing a surrogate function ϕ that satisfies the following monotonicity condition ensures that the iterates x^n will monotonically increase the objective function Φ [40, 42, 43]:

$$\Phi(x) - \Phi(x^n) \geq \phi(x; x^n) - \phi(x^n; x^n), \quad \forall x \geq 0. \quad (4.4)$$

Rather than using (4.4), we choose surrogate functions $\phi(x; x^n)$ that satisfy the following sufficient conditions:

1. $\phi(x^n; x^n) = \Phi(x^n)$

³In practice, it usually suffices for the next iteration to simply increase the surrogate function rather than requiring a strict maximization of ϕ .

2. $\phi(x; x^n) \leq \Phi(x)$ for $x \geq 0$
3. $\frac{\partial}{\partial x_j} \phi(x; x^n)|_{x=x^n} = \frac{\partial}{\partial x_j} \Phi(x)|_{x=x^n}, \quad \forall j.$

The third condition follows from the other conditions for differentiable surrogate and objective functions.

4.4 Existing Algorithms

Many existing algorithms have been applied to obtain a maximizer of $\Phi(x)$ in (4.2). Generally there is a tradeoff between convergence rate and parallelizability. Although EM algorithms are guaranteed to converge to at least a local maximum, they converge very slowly. However, EM algorithms are usually fully parallelizable. At the other extreme, the CA algorithm, which updates the unknown parameters sequentially, converges much faster than the EM algorithms. However, the CA algorithm is not parallelizable. The following subsections summarize some existing algorithms illustrating the convergence rate and parallelizability tradeoff.

4.4.1 Separable Paraboloidal Surrogates (SPS) Algorithm

To obtain a fully parallelizable algorithm, the surrogate function ϕ should be separable so that we can simultaneously update the unknown parameters. Like the EM algorithms, the SPS algorithm is fully parallelizable. It is derived by using the concavity technique developed by De Pierro [36].

To derive the SPS algorithm, we begin by considering the following quadratic surrogate function:

$$\Phi(x) \geq Q(x; x^n) \triangleq \sum_{i=1}^M q_i([Bx]_i; [Bx^n]_i). \quad (4.5)$$

The separable paraboloidal surrogate function Q lies below the objective function and is constructed from the parabola q_i having the following form:

$$q_i(t; t_i^n) \triangleq \psi_i(t_i^n) + \dot{\psi}_i(t_i^n)(t - t_i^n) - \frac{1}{2}c_i(t_i^n)(t - t_i^n)^2 \quad (4.6)$$

where $t_i^n \triangleq [Bx^n]_i = \sum_{j=1}^P b_{ij}x_j^n$, $\dot{\psi}_i$ denotes the first derivative of ψ_i , and $c_i(t_i^n)$ represents the curvature of the parabola $q_i(t; t_i^n)$. We choose the parabola in (4.6) to satisfy the following conditions:

1. $q_i(t_i^n; t_i^n) = \psi_i(t_i^n)$
2. $\psi_i(t) \geq q_i(t; t_i^n), \quad \forall t \in \{[Bx]_i : x \geq 0\}$
3. $\dot{q}_i(t_i^n; t_i^n) = \dot{\psi}_i(t_i^n)$.

The choice of $c_i(t_i^n)$ in (4.6) controls the parabola curvature which affects the algorithm convergence rate [40]. To obtain the fastest convergence rate while still guaranteeing monotonicity, we choose the optimal curvature [40] as follows:

$$c_i^{\text{opt}}(t_i^n) = \min\{c \geq 0 : \psi_i(t) \geq \psi_i(t_i^n) + \dot{\psi}_i(t_i^n)(t - t_i^n) - \frac{c}{2}(t - t_i^n)^2\}. \quad (4.7)$$

For ψ_i corresponding to the Poisson log-likelihood, there is a closed form solution for the optimal curvature as described in (4.45).

To construct a separable surrogate function, we apply the additive concavity technique developed by De Pierro [36] to the quadratic surrogate functions. First, we rewrite the argument $[Bx]_i$ in (4.1) as follows:

$$[Bx]_i = \sum_{j=1}^P \pi_{ij} \left(\frac{b_{ij}}{\pi_{ij}}(x_j - x_j^n) + [Bx^n]_i \right) \quad (4.8)$$

where the π_{ij} 's are any nonnegative⁴ constants for which $\sum_{j=1}^P \pi_{ij} = 1, \forall i$. A simple

⁴ $\pi_{ij} = 0$ only if $b_{ij} = 0$.

choice is

$$\pi_{ij} = \frac{|b_{ij}|}{\sum_{j=1}^P |b_{ij}|}. \quad (4.9)$$

Since each q_i is concave,

$$q_i([Bx]_i; t_i^n) \geq \sum_{j=1}^P \pi_{ij} q_i \left(\frac{b_{ij}}{\pi_{ij}} (x_j - x_j^n) + t_i^n; t_i^n \right). \quad (4.10)$$

Thus from (4.5), the separable paraboloidal surrogate function ϕ is obtained as follows:

$$Q(x; x^n) \geq \phi(x; x^n) \triangleq \sum_{j=1}^P Q_j(x_j; x^n)$$

where

$$Q_j(x_j; x^n) = \sum_{i=1}^M \pi_{ij} q_i \left(\frac{b_{ij}}{\pi_{ij}} (x_j - x_j^n) + t_i^n; t_i^n \right).$$

Since Q_j is quadratic, we implement the maximization (4.3) by using Newton's method:

$$\begin{aligned} x_j^{n+1} &\triangleq \arg \max_{x_j \geq 0} Q_j(x_j; x^n) \\ &= \left[x_j^n + \frac{\frac{d}{dx_j} Q_j(x_j; x^n) \Big|_{x_j=x_j^n}}{-\frac{d^2}{dx_j^2} Q_j(x_j; x^n)} \right]_+ \end{aligned} \quad (4.11)$$

where

$$\frac{d}{dx_j} Q_j(x_j; x^n) \Big|_{x_j=x_j^n} = \sum_{i=1}^M b_{ij} \dot{q}_i(t_i^n; t_i^n) = \frac{\partial}{\partial x_j} \Phi(x) \Big|_{x=x^n} \quad (4.12)$$

$$-\frac{d^2}{dx_j^2} Q_j(x_j; x^n) = \sum_{i=1}^M b_{ij}^2 \frac{c_i^n}{\pi_{ij}} \quad (4.13)$$

where $c_i^n \triangleq c_i^{\text{opt}}(t_i^n)$. The symbol $[x]_+$ represents x if $x \geq 0$ and 0 if $x \leq 0$. The explicit form for the SPS algorithm for the choice (4.9) is thus as follows:

$$x_j^{n+1} = \left[x_j^n + \frac{\sum_{i=1}^M b_{ij} \dot{\psi}_i(t_i^n)}{\sum_{i=1}^M b_{ij} (\sum_l |b_{il}|) c_i^n} \right]_+, \quad j = 1, \dots, P. \quad (4.14)$$

As shown in Section 4.6, for suitable ψ_i 's, this SPS algorithm is guaranteed to converge. However, since it simultaneously updates all the parameters, the convergence rate of this algorithm is usually very slow, much like the closely related EM algorithms.

The SPS algorithm is closely related to the “half-quadratic” optimization methods [21, 38, 53, 54]. However, the quadratic surrogate (4.6) applies to a broader family of ψ_i 's than the half-quadratic approach, and the derivation of the paraboloidal surrogate Q is somewhat simpler than the corresponding derivation of half-quadratic algorithms.

4.4.2 Coordinate Ascent Algorithm with 1D Newton-Raphson Step (CA-NR)

The CA algorithm updates one pixel at a time using the most recent values of all other pixels as follows:

$$x_j^{n+1} \triangleq \arg \max_{x_j \geq 0} \Phi(x_1^{n+1}, \dots, x_{j-1}^{n+1}, x_j, x_{j+1}^n, \dots, x_P^n).$$

In practice, it is usually impractical to perform an exact maximization. Using the one-dimensional Newton-Raphson algorithm, we obtain a closed-form approximate solution as follows:

$$x_j^{n+1} = \left[x_j^n + \frac{\frac{\partial}{\partial x_j} \Phi(x)|_{x=\tilde{x}}}{-\frac{\partial^2}{\partial x_j^2} \Phi(x)|_{x=\tilde{x}}} \right]_+ \quad (4.15)$$

where \tilde{x} denotes the current estimate, i.e., \tilde{x} is a shorthand for $[x_1^{n+1}, \dots, x_{j-1}^{n+1}, x_j^n, x_{j+1}^n, \dots, x_P^n]$,

and

$$\frac{\partial}{\partial x_j} \Phi(x) \Big|_{x=\tilde{x}} = \sum_{i=1}^M b_{ij} \dot{\psi}_i([B\tilde{x}]_i) \quad (4.16)$$

$$\frac{\partial^2}{\partial x_j^2} \Phi(x) \Big|_{x=\tilde{x}} = \sum_{i=1}^M b_{ij}^2 \ddot{\psi}_i([B\tilde{x}]_i). \quad (4.17)$$

Being sequential, the CA-NR algorithm [14] converges rapidly if it converges. However, the curvature of the objective function in (4.17) does not ensure monotonic increases in the objective function, thus divergence is possible. The CA-NR algorithm is also poorly suited to parallel processing.

4.4.3 Coordinate Ascent Algorithm with Parabola Surrogates (CA-PS)

We can overcome the lack of monotonicity of the CA-NR algorithm by applying the optimization transfer principle using parabola surrogates. We call the resulting algorithm CA-PS. The CA-NR algorithm in (4.15) uses the curvature of the objective function $\Phi(x)$. This is equivalent to making a parabolic *approximation* to $\Phi(x)$, which will not satisfy the monotonicity condition in (4.4) in general. To guarantee monotonicity, we replace $\frac{\partial^2}{\partial x_j^2}\Phi(x)$ with the curvature of a parabola surrogate that satisfies the conditions discussed above. This approach leads to the following CA-PS iterative algorithm:

$$x_j^{n+1} = \left[x_j^n + \frac{\frac{\partial}{\partial x_j}\Phi(x)|_{x=\tilde{x}}}{-\frac{\partial^2}{\partial x_j^2}Q(x; \tilde{x})} \right]_+ \quad (4.18)$$

where $Q(x; \tilde{x})$ is a parabola that lies below the objective function $\Phi(x)$ as in (4.5), defined here by

$$Q(x; \tilde{x}) = \sum_{i=1}^M q_i([Bx]_i; [B\tilde{x}]_i)$$

where q_i is similar to (4.6) but with the curvature $c_i([B\tilde{x}]_i)$. Thus the curvature of the surrogate function becomes:

$$-\frac{\partial^2}{\partial x_j^2}Q(x; \tilde{x}) = \sum_{i=1}^M b_{ij}^2 c_i([B\tilde{x}]_i). \quad (4.19)$$

The CA-PS algorithm is guaranteed to monotonically increase Φ . Furthermore, CA-PS is applicable to ψ_i 's like the Huber function [68], which is only once differentiable,

whereas CA-NR requires twice differentiable ψ_i 's. However, CA-PS is still not parallelizable, and it is computationally expensive since the curvature $c_i([B\tilde{x}]_i)$ must be recomputed after *every* pixel update.

4.4.4 Paraboloidal Surrogates Coordinate Ascent (PSCA) Algorithm

In contrast to the CA-PS algorithm, the PSCA algorithm [40] is derived by first finding a paraboloidal surrogate function at each iteration and then using the CA algorithm to maximize that surrogate iteratively. Thus the next estimate is obtained as follows:

$$x_j^{n+1} = \left[x_j^n + \frac{\frac{\partial}{\partial x_j} Q(x; x^n)|_{x=\tilde{x}}}{-\frac{\partial^2}{\partial x_j^2} Q(x; x^n)} \right]_+ \quad (4.20)$$

where $Q(x; x^n)$ is the same as in (4.5) and (4.6). The derivatives of $Q(x; x^n)$ are as follows:

$$\frac{\partial}{\partial x_j} Q(x; x^n) \Big|_{x=\tilde{x}} = \sum_{i=1}^M b_{ij} \dot{q}_i([B\tilde{x}]_i; t_i^n) \quad (4.21)$$

$$-\frac{\partial^2}{\partial x_j^2} Q(x; x^n) = \sum_{i=1}^M b_{ij}^2 c_i^n \quad (4.22)$$

where c_i^n was defined below (4.13). Like the CA-PS algorithm, this algorithm will monotonically increase the objective function and is guaranteed to converge if Φ is strictly concave (Section 4.6). Furthermore, the PSCA algorithm requires much less computation per iteration than the CA-PS algorithm, since we can precompute the curvature in (4.22) prior to cycling through the pixels, unlike the curvature in (4.19) which changes with every pixel update. However, the PSCA algorithm remains ill-suited to parallel processing since it sequentially updates each pixel.

4.4.5 “Naive” Parallel Coordinate Ascent Algorithm

The naive approach to parallelizing the CA algorithm would be to directly separate pixels into subsets and then assign one parallel processor to each subset to perform the CA algorithm (Figure 4.2). However, this technique is not guaranteed to increase the objective function at each iteration, and thus can diverge. To ensure convergence, we must somehow account for the “coupling” between pixels at the boundaries between subsets. The next section shows that the optimization transfer approach provides a suitable framework for deriving a monotonic parallelizable algorithm.

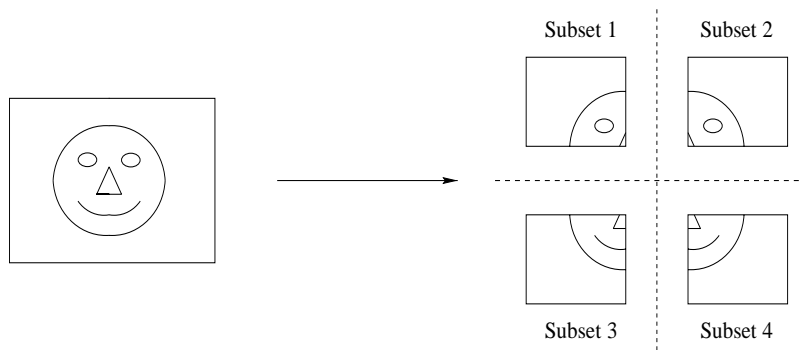


Figure 4.2: A “naive” parallel coordinate ascent algorithm. Each parallel processor performs the CA algorithm on each subset of pixels separately.

4.5 PPCA Algorithm

This section describes a new algorithm that not only converges quickly, but is also well-suited to coarse-grain parallel processing. The PPCA algorithm is based on a concavity technique developed by De Pierro [36] and uses tangent parabolas. The idea is to sequentially update pixels within each subset while simultaneously updating all subsets.

4.5.1 Overview

To derive the PPCA algorithm, we first find a paraboloidal surrogate function for the original objective function, and then partition pixels into K subsets. Since the parabola is concave, we can derive a partitioned-separable surrogate function using a concavity technique. Finally, the CA algorithm is applied in parallel to each set of pixels. Here is an overview of the surrogates derived in this section:

$$\Phi(x) \geq Q(x; x^n) \geq \phi(x; x^n) \triangleq \sum_{k=1}^K Q_k(x_{J_k}; x^n) \quad (4.23)$$

where Q denotes the paraboloidal surrogate function, ϕ denotes the subset-separated paraboloidal surrogate function, and Q_k denotes the surrogate function for the k th subset. We let J_k denote the k th subset of pixels, and x_{J_k} denote the vector of length $|J_k|$ consisting of the elements of x indexed by J_k . The condition (4.23) ensures monotonicity in the objective function: $\Phi(x^{n+1}) \geq \Phi(x^n)$. To implement the update (4.3), we must obtain the next estimate x in each set by maximizing $Q_k(x_{J_k}; x^n)$ as follows:

$$x_{J_k}^{n+1} \triangleq \arg \max_{x_{J_k} \geq 0} Q_k(x_{J_k}; x^n), \quad k = 1, \dots, K. \quad (4.24)$$

For the example illustrated in Figure 4.3, after obtaining the partitioned-separable paraboloidal surrogates, we divide the image into 4 subsets and then assign 4 parallel processors to perform the PPCA algorithm.

4.5.2 Derivation

First, we construct a paraboloidal surrogate function Q for the original objective function as in (4.5)-(4.7). After obtaining the paraboloidal surrogate function, we apply a form of the concavity technique to separate pixels into partitioned sets.

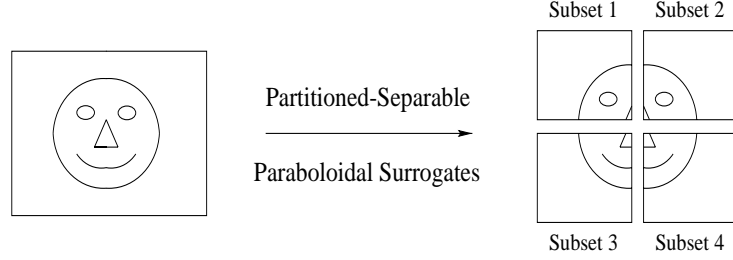


Figure 4.3: Schematic of the PPCA algorithm

Similarly to (4.8), we can rewrite $[Bx]_i$ as follows:

$$[Bx]_i = \sum_{k=1}^K \rho_{ik} \left(\frac{s_{ik}^n(x_{J_k})}{\rho_{ik}} + t_i^n \right)$$

where

$$s_{ik}^n(x_{J_k}) \triangleq [B_{J_k}(x_{J_k} - x_{J_k}^n)]_i = \sum_{j \in J_k} b_{ij}(x_j - x_j^n)$$

and the matrix B_{J_k} is formed by selecting the columns of B that are indexed by elements of J_k . To satisfy the constraint that $\sum_{k=1}^K \rho_{ik} = 1$ and $\rho_{ik} \geq 0$, which guarantees monotonicity of the algorithm, we choose

$$\rho_{ik} \triangleq \frac{\sum_{j \in J_k} |b_{ij}|}{\sum_{j=1}^P |b_{ij}|}.$$

Similar to (4.10), since q_i is concave, the following inequality is satisfied:

$$q_i([Bx]_i; t_i^n) \geq \sum_{k=1}^K \rho_{ik} q_i \left(\frac{s_{ik}^n(x_{J_k})}{\rho_{ik}} + t_i^n; t_i^n \right) \quad (4.25)$$

where from (4.6),

$$q_i(t + t_i^n; t_i^n) = \psi_i(t_i^n) + \dot{\psi}_i(t_i^n)t - \frac{1}{2}c_i^n t^2. \quad (4.26)$$

For simplicity, we define the following notation:

$$q_{ik}^n(s) \triangleq \rho_{ik} q_i \left(\frac{s}{\rho_{ik}} + t_i^n; t_i^n \right). \quad (4.27)$$

Thus from (4.25), we obtain the following partitioned-separable paraboloidal surrogate function:

$$\phi(x; x^n) = \sum_{i=1}^M \sum_{k=1}^K q_{ik}^n(s_{ik}^n(x_{J_k})) \quad (4.28)$$

where from (4.23), the k th subset surrogate function is

$$Q_k(x_{J_k}; x^n) \triangleq \sum_{i=1}^M q_{ik}^n(s_{ik}^n(x_{J_k})). \quad (4.29)$$

Now we update all the subsets simultaneously, while the pixels in each set are sequentially updated for fast convergence. One approach to implement the maximization in (4.24) is to apply the CA algorithm over each pixel of x_j by using the most recent values of other pixels of x_j in that set. Letting \tilde{x} denote the current estimates, we define the 1D quadratic function for each pixel as follows:

$$Q_{kj}(x_j) \triangleq Q_k([\dots, \tilde{x}_{j-1}, x_j, \tilde{x}_{j+1}, \dots, j \in J_K]; x^n) \quad (4.30)$$

$$= Q_{kj}(\tilde{x}_j) + \dot{Q}_{kj}(\tilde{x}_j)(x_j - \tilde{x}_j) - \frac{1}{2}d_{kj}^n(x_j - \tilde{x}_j)^2 \quad (4.31)$$

where the first derivative of $Q_{kj}(x_j)$ evaluated at $x_j = \tilde{x}_j$ is

$$\dot{Q}_{kj}(\tilde{x}_j) \triangleq \frac{d}{dx_j} Q_{kj}(x_j) \Big|_{x_j=\tilde{x}_j} = \sum_{i=1}^M b_{ij} \dot{q}_{ik}^n(s_{ik}^n(\tilde{x}_{J_k})) \quad (4.32)$$

and the curvature of the parabola $Q_{kj}(x_j)$ is given by:

$$d_{kj}^n \triangleq -\frac{d^2}{dx_j^2} Q_{kj}(x_j) = \sum_{i=1}^M w_{ik}^n b_{ij}^2, \quad (4.33)$$

where $w_{ik}^n \triangleq c_i^n / \rho_{ik}$. Thus we obtain the update x_j in each partitioned set by applying one or more CA cycles to maximize the surrogate function Q_k in (4.29). Sequentially, for each $j \in J_k$, we perform the following update:

$$\begin{aligned} x_j^{\text{new}} &= \arg \max_{x_j \geq 0} Q_{kj}(x_j) \\ &= \left[\tilde{x}_j + \frac{\dot{Q}_{kj}(\tilde{x}_j)}{d_{kj}^n} \right]_+. \end{aligned} \quad (4.34)$$

To minimize computation, we first differentiate q_{ik}^n in (4.27) with respect to s and evaluate at $s = \tilde{t}_{ik} - t_{ik}^n$ as follows:

$$\dot{q}_{ik}^n(\tilde{t}_{ik} - t_{ik}^n) = \dot{\psi}_i(t_i^n) - w_{ik}^n(\tilde{t}_{ik} - t_{ik}^n) \quad (4.35)$$

where $\tilde{t}_{ik} \triangleq [B_{J_k} \tilde{x}_{J_k}]_i = \sum_{j \in J_k} b_{ij} \tilde{x}_j$. Then rearranging (4.35) yields

$$\tilde{t}_{ik} = t_{ik}^n + \frac{\dot{\psi}_i - \dot{q}_{ik}^n}{w_{ik}^n}, \quad \forall i \text{ s.t. } b_{ij} \neq 0, \forall j \in J_k,$$

This is a faster way to update \tilde{t}_{ik} . Table 4.2 shows the PPCA algorithm outline.

This algorithm generalizes the SPS and PSCA algorithms described in Section 4.4. When $K = P$ and $J_k = \{k\}$, the PPCA algorithm is equivalent to the SPS algorithm. When $K = 1$ and $J_k = \{1, \dots, P\}$, the PPCA algorithm is equivalent to the PSCA algorithm. The most useful cases are when $2 \leq K \ll P$, corresponding to a small number of processors such as might be found in a workstation cluster.

An alternate approach to deriving a parallelizable algorithm is to first separate pixels into subsets using De Pierro's concavity technique and then to fit the paraboloidal surrogates inside the resulting surrogates. However, this approach only applies to concave objective functions, unlike the approach in (4.23). The surrogate functions of this approach are given as follows:

$$\Phi(x) \geq \tilde{\phi}(x; x^n) = \sum_{k=1}^K \tilde{\phi}_k(x_{J_k}; x^n) \geq \sum_{k=1}^K \tilde{Q}_k(x_{J_k}; x^n)$$

where $\tilde{\phi}_k(x_{J_k}; x^n)$ denotes the partitioned-separable surrogate function and $\tilde{Q}_k(x_{J_k}; x^n)$ denotes the paraboloidal partitioned-separable surrogate function. In case of a concave objective function, these two approaches yield the same results. Without sub-iterations, this second approach yields the same results as the previous approach for concave objective functions. However, with sub-iterations, this approach becomes more complicated and requires more computation since computing the curvature of

the parabola, which is an expensive part, is needed for every sub-iteration, unlike the first approach.

\tilde{x} = initial image
 $\tilde{t}_{ik} = \sum_{j \in J_k} b_{ij} \tilde{x}_j, \quad k = 1, \dots, K$
 $\rho_{ik} = \frac{\sum_{j \in J_k} |b_{ij}|}{\sum_{j=1}^P |b_{ij}|}, \quad k = 1, \dots, K$
 for $n = 1, \dots, \text{Niters}$
 $\tilde{t}_i = \sum_k \tilde{t}_{ik}$ (inter-processor communication)
 compute c_i^n from \tilde{t}_i using (4.7)
 compute ψ_i at \tilde{t}_i
 for each processor k
 $w_{ik}^n = c_i^n / \rho_{ik}, \quad \forall i \text{ s.t. } b_{ij} \neq 0, \forall j \in J_k$
 $\dot{q}_{ik} = \psi_i, \quad \forall i \text{ s.t. } b_{ij} \neq 0, \forall j \in J_k$
 $d_{kj}^n = \sum_{i=1}^M b_{ij}^2 w_{ik}^n, \quad j \in J_k$
 for $j \in J_k$
 $x_j^{\text{old}} = \tilde{x}_j$
 $\dot{Q}_{kj} = \sum_{i=1}^M b_{ij} \dot{q}_{ik}$
 $\tilde{x}_j = \left[\tilde{x}_j + \frac{\dot{Q}_{kj}}{d_{kj}^n} \right]_+$
 $\dot{q}_{ik} = \dot{q}_{ik} - w_{ik}^n b_{ij} (\tilde{x}_j - x_j^{\text{old}}), \quad \forall i \text{ s.t. } b_{ij} \neq 0$
 end
 $\tilde{t}_{ik} = \tilde{t}_{ik} + \frac{\psi_i - \dot{q}_{ik}}{w_{ik}^n}, \quad \forall i \text{ s.t. } b_{ij} \neq 0, \forall j \in J_k$
 end
 combine \tilde{x} from all processors
 end

Table 4.2: The PPCA Algorithm Outline.

4.6 Convergence Analysis

Based on the general sufficient conditions for convergence stated in [49], we prove convergence of the algorithm (4.24) by first stating some sufficient conditions for convergence and then verifying that the algorithm satisfies all the required conditions for convergence. We assume that the objective function, $\Phi(x)$, is strictly concave, continuous, and differentiable for $x \geq 0$. Moreover, the set $\{x \geq 0 : \Phi(x) \geq \Phi(x')\}$ is assumed to be bounded for any x' . We assume that each iteration is associ-

ated with disjoint index sets $\{J_1, \dots, J_K\}$ s.t. $\bigcup_{k=1}^K J_k = \{1, \dots, p\}$, and functionals $Q_k(x_{J_k}, x^n), k = 1, \dots, K$. The following conditions pertain to the functionals Q_k in (4.29).

Condition 1: For $k = 1, \dots, K$, the functionals Q_k satisfy

$$\Phi(x_{J_k}, x_{\bar{J}_k}^n) - \Phi(x^n) \geq Q_k(x_{J_k}; x^n) - Q_k(x_{J_k}^n; x^n)$$

$\forall x_{J_k} \geq 0, \forall x_{\bar{J}_k}^n \geq 0, \forall x^n \geq 0$, and $\forall x_{\bar{J}_k}^n \geq 0$, where $x_{\bar{J}_k}^n$ is the elements of x^n that are not in set J_k .

Condition 2: Each functional $Q_k(x_{J_k}; x^n)$ is strictly concave and twice differentiable on $x_{J_k} \geq 0, x^n \geq 0$, and each $Q_k(x_{J_k}; x^n)$ is jointly continuous on $x_{J_k} \geq 0, x^n \geq 0$.

Condition 3: The following derivatives match $\forall n$:

$$\frac{\partial}{\partial x_j} \Phi(x^n) = \frac{\partial}{\partial x_j} Q_k(x_{J_k}^n; x^n)$$

for any $x^n \geq 0, x_{J_k}^n \geq 0$, and $j \in J_k$.

Condition 4: For $x_{J_k}^{n+1} \geq 0$ and $x^n \geq 0$, the iterates satisfy the Karush-Kuhn-Tucker conditions, $\forall j \in J_k$:

$$\frac{\partial}{\partial x_j} Q_k(x_{J_k}^{n+1}; x^n) \begin{cases} = 0, & x_j^{n+1} > 0 \\ \leq 0, & x_j^{n+1} = 0. \end{cases}$$

Condition⁵5:* For any bounded set S , there exists a constant $C_S > 0$ such that $\forall v \neq 0, x_{J_k} \geq 0$, and $\forall x^n \in S$;

$$v'G(x_{J_k}; x^n)v \geq C_S \|v\|^2$$

where $G(x_{J_k}; x^n)$ is the $|J_k| \times |J_k|$ matrix with the (i, j) th element representing $-\frac{\partial^2}{\partial x_i \partial x_j} Q_k(x_{J_k}; x^n), \forall (i, j) \in J_k$.

⁵A sufficient condition for Condition 5 in [49].

Theorem: If the curvatures $c_i(\cdot)$ of the surrogates are continuous and have a positive lower bound, then any sequence $\{x^n\}$ generated by the algorithm (4.24) for penalized-maximum likelihood image recovery converges globally to the unique maximizer of a strictly concave objective function $\Phi(x)$ satisfying the assumptions given in the first paragraph above.

Proof:

- Condition 1 follows the second property of the surrogate function given in Section 4.4.1 or (4.23).
- Condition 2 is satisfied since $Q_k(x_{J_k}; x^n)$ is a concave quadratic function and thus differentiable and jointly continuous.
- Condition 3 follows the third property of the surrogate function in Section 4.4.1.
- Condition 4 is inherent to the update (4.24).
- Condition 5* is satisfied due to the following proof.

Let $w_{ik}^n \geq \varepsilon, \forall i, k, n$, where ε is the positive lower bound of the curvature, then

$$\begin{aligned} v'G(x_{J_k}; x^n)v &= v'B'_{J_k}D(w_{ik}^n)B_{J_k}v \\ &\geq v'B'_{J_k}(\varepsilon I)B_{J_k}v \\ &\geq \varepsilon\lambda_{\min}\{B'_{J_k}B_{J_k}\}\|v\|^2 \end{aligned}$$

where $D(w_{ik}^n)$ is the diagonal matrix with diagonal elements belonging to w_{ik}^n , and $\lambda_{\min}\{B'_{J_k}B_{J_k}\}$ is the minimum eigenvalue of the matrix $B'_{J_k}B_{J_k}$. Thus $v'G(x_{J_k}; x^n)v \geq C_S\|v\|^2$ is satisfied, where $C_S = \varepsilon\lambda_{\min}\{B'_{J_k}B_{J_k}\}$.

Thus, all the conditions needed for the convergence proof in [49] are satisfied. □

Theorem 1 shows that (4.24) converges to the global maximizer of a strictly concave objective function. In practice, we use one or more cycles of the CA update (4.34) rather than the exact maximization (4.24). However, we believe the proof in [49] can be generalized even to include the case (4.34).

4.7 Convergence Rate

The curvature of the surrogate function strongly influences the convergence rate. Smaller curvatures generally yield faster convergence. The surrogate function curvatures for each of the algorithms described above are given as follows:

$$\begin{aligned}
d_j^{\text{SPS}} &= \sum_{i=1}^M b_{ij} c_i^n \cdot \left(\sum_{l=1}^p b_{il} \right) \\
d_j^{\text{GCA}} &= \sum_{i=1}^M b_{ij} c_i^n \cdot \left(\sum_{k \in S^n} b_{ik} \right), \quad j \in S^n \\
d_j^{\text{PPCA}} &= \sum_{i=1}^M b_{ij} c_i^n \cdot \left(b_{ij} \frac{\sum_{l=1}^p b_{il}}{\sum_{l' \in J_k} b_{il'}} \right), \quad j \in J_k \\
d_j^{\text{PSCA}} &= \sum_{i=1}^M b_{ij} c_i^n \cdot (b_{ij}) \\
d_j^{\text{CA-NR}} &= \sum_{i=1}^M b_{ij} \ddot{\psi}_i([B\tilde{x}]_i) \cdot (b_{ij}).
\end{aligned}$$

The grouped coordinate ascent (GCA) algorithms [42, 43, 99], which are related to the PPCA algorithm, are discussed in Appendix C. By comparing the arguments within parentheses of the above equations for the curvatures, we obtain the following inequalities:

$$d_j^{\text{SPS}} \geq d_j^{\text{PPCA}} \geq d_j^{\text{PSCA}} \geq d_j^{\text{CA-NR}} \geq 0$$

assuming that $\ddot{\psi}_i([B\tilde{x}]_i) < c_i^n$. The GCA algorithms are not included because they are not directly comparable with the PPCA algorithms. Different number of groups

in the GCA algorithms yields different results. When the number of group in GCA algorithms is the same as the number of sets in the PPCA algorithm, the PPCA algorithm yields a faster convergence rate than the GCA algorithms. As expected, the SPS algorithm has the largest curvature, hence generally smallest step sizes and slowest convergence. On the other hand, the CA-NR algorithm has the smallest curvature, thus it has the biggest step sizes which yield the fastest convergence rate (when it converges).

4.8 Application to Image Restoration for Confocal Microscopy

Confocal fluorescence microscopy is widely used in cell biology to image thick biological tissues in three dimensions. Unfortunately, most obtainable images contain out-of-focus signals from other planes and have poor resolution due to a resolution/signal-to-noise ratio tradeoff as the detector pinhole size is increased. Therefore, image restoration techniques have been applied to improve the resolution and SNR of the images. In confocal microscopy, the noisy measurement Y can be modeled as follows:

$$Y_i \sim \alpha_1 \text{Poisson}\{f_i[Ax]_i + b_i\}, \quad i = 1, \dots, N$$

where the $N \times P$ system matrix A is assumed to be known⁶, x denotes the mean number of fluorescent photons per second, α_1 denotes a known measurement scaling factor, f_i denotes the product of the scan time and the detector efficiency, and b_i denotes the background noise and the dark current [104]. The corresponding log-likelihood function is given by:

$$L(x) = \sum_{i=1}^N \frac{y_i}{\alpha_1} \log(f_i[Ax]_i + b_i) - (f_i[Ax]_i + b_i) \quad (4.36)$$

⁶In practice, the point spread function (PSF) of a confocal microscope is not exactly known; however, one can measure the PSF by using very small microsphere beads.

(ignoring irrelevant constants independent of x), which is concave. Due to the ill-posed nature of image restoration problems, we modify the likelihood function by including a penalty function $R(x)$ to form the following penalized-likelihood objective function:

$$\Phi(x) = L(x) - \beta R(x) \quad (4.37)$$

where β controls the degree of smoothness in the restored image. Our goal is to estimate x by maximizing the objective function $\Phi(x)$:

$$\hat{x} \triangleq \arg \max_{x \geq 0} \Phi(x) = \arg \max_{x \geq 0} L(x) - \beta R(x). \quad (4.38)$$

For the penalty function $R(x)$ of interest here, the objective function Φ in (4.37) is a special case of the general form (4.1); therefore, the algorithms of sections 4.4 and 4.5 are applicable. For clarification, we separately derive the surrogate functions for the likelihood part and the penalty part.

4.8.1 The Likelihood Part

Similarly to (4.23), the surrogates for the likelihood part can be obtained as follows:

$$L(x) \geq Q^L(x; x^n) \geq \phi^L(x; x^n) \triangleq \sum_{k=1}^K Q_k^L(x_{J_k}; x^n) \quad (4.39)$$

The likelihood function in (4.36) can be expressed in the following form:

$$L(x) = \sum_{i=1}^N \psi_i^L([Bx]_i) \quad (4.40)$$

with $b_{ij} = f_i a_{ij}$, which is the (ij) th element of the matrix B , and

$$\psi_i^L(l) = \frac{y_i}{\alpha_1} \log(l + b_i) - (l + b_i). \quad (4.41)$$

The first and second derivatives of ψ_i^L are given by

$$\psi_i^L(l) = \frac{y_i}{l + b_i} - 1 \quad (4.42)$$

$$\ddot{\psi}_i^L(l) = -\frac{y_i}{(l + b_i)^2}. \quad (4.43)$$

Due to concavity of the objective function, ψ_i^L is strictly concave, its first derivative is strictly convex and monotonically decreasing, and its second derivative is monotonically increasing.

As in (4.5), the paraboloidal surrogate function for the likelihood function is given by:

$$Q^L(x; x^n) \triangleq \sum_{i=1}^N q_i^L(f_i[Ax]_i; l_i^n)$$

where $l_i^n \triangleq f_i[Ax^n]_i = f_i \sum_{j=1}^P a_{ij} x_j^n$. The surrogate function $q_i^L(l; l_i^n)$ has the following quadratic form which satisfies the conditions of the paraboloidal surrogate given in Section 4.4.1.

$$q_i^L(l; l_i^n) \triangleq \psi_i^L(l_i^n) + \dot{\psi}_i^L(l_i^n)(l - l_i^n) - \frac{1}{2}c_i^n(l - l_i^n)^2 \quad (4.44)$$

where $\dot{\psi}_i^L$ denotes the first derivative of ψ_i^L and c_i^n denotes the curvature of the parabola $q_i^L(l; l_i^n)$. Since the convergence rate depends on the curvature of the surrogates and $b_i > 0$, we can choose c_i^n to be the optimal curvature as derived in (4.7) [40, 46]:

$$c_i^{\text{opt}}(l) = \begin{cases} \left[\frac{2y_i}{\alpha_1 l^2} \left\{ \log\left(\frac{l+b_i}{b_i}\right) - \frac{l}{l+b_i} \right\} \right]_+, & l > 0 \\ \frac{y_i}{\alpha_1 b_i^2}, & l = 0. \end{cases} \quad (4.45)$$

With an additive concavity technique, we obtain the partitioned separable paraboloidal surrogate function as follows:

$$Q_k^L(x_{J_k}; x^n) = \sum_{i=1}^N \pi_{ik} q_i^L \left(\frac{f_i}{\pi_{ik}} [A_{J_k}(x_{J_k} - x_{J_k}^n)]_i + l_i^n; l_i^n \right)$$

where $\pi_{ik} \triangleq \frac{\sum_{j \in J_k} |a_{ij}|}{\sum_{j=1}^P |a_{ij}|}$. Then we apply a coordinate ascent algorithm to maximize $Q_k^L(x_{J_k}; x^n)$. The first derivative of $Q_{kj}^L(\tilde{x}_j)$ as defined in (4.30) and (4.31) is given by

$$\dot{Q}_{kj}^L(\tilde{x}_j) = \sum_{i=1}^N f_i a_{ij} \dot{q}_i^L \left(\frac{f_i}{\pi_{ik}} [A_{J_k}(\tilde{x}_{J_k} - x_{J_k}^n)]_i + l_i^n; l_i^n \right)$$

Again, as in 4.35, we obtain

$$\dot{q}_i^L = \dot{\psi}_i^L(l_i^n) - w_{ik}^{L,n} (\tilde{l}_{ik} - l_{ik}^n) \quad (4.46)$$

where $w_{ik}^{L,n} = c_i^n / \pi_{ik}$, $\tilde{l}_{ik} \triangleq f_i A_{J_k} \tilde{x}_{J_k} = f_i \sum_{j \in J_k} a_{ij} \tilde{x}_j$, and $l_{ik}^n = f_i A_{J_k} x_{J_k}^n$. Rearranging (4.46), we obtain

$$\tilde{l}_{ik} = l_{ik}^n + \frac{\dot{\psi}_i^L - \dot{q}_i^L}{w_{ik}^{L,n}} \quad (4.47)$$

which is useful in algorithm implementation. The curvature of the parabola $Q_{kj}^L(\tilde{x}_j)$ for the likelihood part is:

$$d_{kj}^L = \sum_{i=1}^N w_{ik}^{L,n} f_i^2 a_{ij}^2. \quad (4.48)$$

4.8.2 The Penalty Part

As in the likelihood function, we can use similar techniques to obtain the partitioned separable surrogates for the penalty function. Since the penalty function is convex, the following surrogate functions are derived:

$$R(x) \leq Q^R(x; x^n) \leq \phi^R(x; x^n) \triangleq \sum_{k=1}^K Q_k^R(x_{J_k}; x^n) \quad (4.49)$$

The general form of the penalty function which is described in Chapter III is given by:

$$R(x) = \sum_{i=1}^r \psi_i^R([Cx]_i) \quad (4.50)$$

where ψ_i^R is the potential function, C is the weighting matrix, and r is the number of pairs of neighboring pixels.

In this section, we derive only the nonquadratic penalty function. The quadratic penalty function is straightforward since the separable technique can be directly applied to the penalty function. The paraboloidal surrogate function which lies above the convex penalty function is given by:

$$Q^R(x; x^n) = \sum_{i=1}^r q_i^R([Cx]_i; v_i^n)$$

where $v_i^n \triangleq [Cx^n]_i$. The parabola $q_i^R(v_i; v_i^n)$ is tangent to the potential function at the current points v_i^n and $-v_i^n$ and has the curvature $\omega_i(v_i^n)$ [68].

$$q_i^R(v_i; v_i^n) = \psi_i^R(v_i^n) + \dot{\psi}_i^R(v_i^n)(v_i - v_i^n) + \frac{1}{2}c_i(v_i^n)(v_i - v_i^n)^2$$

According to [68], the optimal curvature for such a symmetric nonquadratic penalty function is given by:

$$c_i^{\text{opt}}(v_i^n) \triangleq \frac{\dot{\psi}_i^R(v_i^n)}{v_i^n} = \omega_i^R(v_i^n) \quad (4.51)$$

where $\dot{\psi}_i^R$ is the first derivative of the potential penalty function at the i th element.

After applying the convexity technique, we can obtain the partitioned separable paraboloidal surrogate function $Q_k^R(x_{J_k}; x^n)$ as follows:

$$Q_k^R(x_{J_k}; x^n) = \sum_{i=1}^r \gamma_{rk} q_i^R \left(\frac{1}{\gamma_{rk}} [C_{J_k}(x_{J_k} - x_{J_k}^n)]_i + v_i^n; v_i^n \right)$$

where $\sum_{k=1}^K \gamma_{rk} = 1$ and similarly, we choose $\gamma_{rk} \triangleq \frac{\sum_{j \in J_k} |c_{rj}|}{\sum_{j=1}^P |c_{rj}|}$.

Similar to the likelihood part, we need to find the quadratic function for each pixel within a set in order to apply the CA algorithm in each set. The first derivative and the curvature of $Q_{kj}^R(x_j)$ evaluated at $x_j = \tilde{x}_j$ are

$$\dot{Q}_{kj}^R(\tilde{x}_j) = \sum_{i=1}^r \left[c_{rj} \dot{\psi}_i^R(v_i^n) + \frac{c_{rj}}{\gamma_{rk}} c_i(v_i^n) [C_{J_k}(\tilde{x}_{J_k} - x_{J_k}^n)]_i \right]$$

$$d_{kj}^R = - \sum_{i=1}^r \frac{c_{rj}^2}{\gamma_{rk}} c_i(v_i^n). \quad (4.52)$$

Combining all the likelihood and penalty surrogate functions, we obtain the following update for each $j \in J_k$ by maximizing these surrogate functions as in (4.34):

$$\begin{aligned} x_j^{n+1} &= \arg \max_{x_j \geq 0} Q_{kj}^L(x_j) - \beta Q_{kj}^R(x_j) \\ &= \left[x_j^n + \frac{\dot{Q}_{kj}^L(\tilde{x}_j) - \beta \dot{Q}_{kj}^R(\tilde{x}_j)}{d_{kj}^L + \beta d_{kj}^R} \right]_+ \end{aligned} \quad (4.53)$$

An algorithm outline for the PPCA algorithm is shown in Table 4.3. The parameter π_{ik} is precomputed for each set before the iteration loop. To compute c_i^n , \tilde{l}_i is computed at the beginning of every iteration by combining \tilde{l}_{ik} from each partitioned set together. Instead of using the convolution to compute \tilde{l}_{ik} , \tilde{l}_{ik} can be updated by using (4.47) to reduce the computation time. \dot{Q}_{kj}^R is separated into two terms so that the term \dot{Q}_{kj1}^R that depends on the n th update of x can be computed only once per iteration. Likewise, the curvature of the surrogate penalty function, d_{kj}^R , is calculated only once per iteration. To have (4.47) work properly, $w_{ik}^{L,n} > 0$ is required, and thus we constrain $w_{ik}^{L,n}$ to some value > 0 .

4.9 Results

4.9.1 2-D Simulation Results

A 512×512 pepper image was degraded by a 15×15 Gaussian point spread function (PSF) with FWHM of 11.7 pixels (standard deviation = 5.0) and Poisson noise with $\text{PSNR}_{\text{data}}^7$ of 25 dB as shown in Figure 4.4(b). Since our long-term

⁷The peak signal-to-noise ratio for the data is defined as follows:

$$\text{PSNR}_{\text{data}} = 10 \log_{10} \left(\frac{\max_i (y_i - \alpha_1 b_i)^2}{\frac{1}{N} \sum_{i=1}^N (y_i - \mathbb{E}[y_i])^2} \right),$$

where N is the total number of pixel size.

\tilde{x} = initial image
 $b_{ij} = f_i a_{ij}$
 $y_i = \frac{y_i}{\alpha_1}, \quad \forall i = 1, \dots, N$
 $\tilde{l}_{ik} = \sum_{j \in J_k} b_{ij} \tilde{x}_j, \quad k = 1, \dots, K$
 $\rho_{ik} = \frac{\sum_{j \in J_k} |b_{ij}|}{\sum_{j=1}^P |b_{ij}|}, \quad k = 1, \dots, K$
 for $n = 1, \dots, \text{Niters}$
 $x^n = \tilde{x}$
 $\tilde{l}_i = \sum_k \tilde{l}_{ik}$
 $c_i = \begin{cases} \frac{2y_i}{(\tilde{l}_i)^2} \left[\log \left(1 + \frac{\tilde{l}_i}{b_i} - \frac{\tilde{l}_i}{\tilde{l}_i + b_i} \right) \psi_i^L(\tilde{l}_i) \right], & \tilde{l}_i > 0 \\ -\psi_i^L(0), & \tilde{l}_i = 0 \end{cases}, \quad \forall i = 1, \dots, N$
 $\dot{Q}_{kj1}^R = \sum_{i=1}^r c_{ij} \psi_i^R([Cx^n]_i)$
 $d_{kj}^R = \sum_{i=1}^r \frac{c_{ij}^2}{\gamma_{ik}} \omega_i([Cx^n]_i)$
 for each processor k
 $w_i^L = c_i / \rho_{ik}, \quad \forall i = 1, \dots, N \text{ s.t. } b_{ij} \neq 0, \forall j \in J_k$
 $\dot{q}_i^L = \psi_i^L, \quad \forall i = 1, \dots, N \text{ s.t. } b_{ij} \neq 0, \forall j \in J_k$
 $d_{kj}^L = \sum_{i=1}^N b_{ij}^2 w_i^L$
 for $j \in J_k$
 $x_j^{\text{old}} = \tilde{x}_j$
 $\dot{Q}_{kj}^L = \sum_{i=1}^N b_{ij} \dot{q}_i^L$
 $\dot{Q}_{kj2}^R = \sum_{i=1}^r \frac{c_{ij}}{\gamma_{ik}} \omega_i([Cx^n]_i) [C_{J_k}(\tilde{x}_{J_k} - x_{J_k}^n)]_i$
 $\dot{Q}_{kj}^R = \dot{Q}_{kj1}^R + \dot{Q}_{kj2}^R$
 $\tilde{x}_j = \left[\tilde{x}_j + \frac{\dot{Q}_{kj}^L - \beta \dot{Q}_{kj}^R}{d_{kj}^L + \beta d_{kj}^R} \right]_+$
 $\dot{q}_i^L = \dot{q}_i^L - w_i^L b_{ij} (\tilde{x}_j - x_j^{\text{old}}), \quad \forall i = 1, \dots, N \text{ s.t. } b_{ij} \neq 0$
 end
 $\tilde{l}_{ik} = \tilde{l}_{ik} + \frac{\psi_i^L - \dot{q}_i^L}{w_i^L}, \quad \forall i = 1, \dots, N \text{ s.t. } b_{ij} \neq 0, \forall j \in J_k$
 end
 end

Table 4.3: Algorithm Outline of the PPCA Algorithm for Confocal Microscopy.

interest is space-varying PSFs, we used convolution rather than FFT techniques for these algorithms. We used the following nonquadratic penalty function [81]:

$$\psi_i^R(t) = \delta^2 \left[\left| \frac{t}{\delta} \right| - \log \left(1 + \left| \frac{t}{\delta} \right| \right) \right] \quad (4.54)$$

where δ controls the degree of edge preservation. Figure 4.4(d) shows the restoration (PSNR⁸ of 26.68 dB) using the 4-PPCA algorithm (with four parallel processors). For comparison, the PSNR of the noise-free image in Figure 4.4(c), which is a blurred version of Figure 4.4(b) without Poisson noise, is 22.71 dB.



(a) Original Image



(b) Degraded Image



(c) Noise-free Image



(d) Restored Image

Figure 4.4: 2-D simulation and restoration using a 4-PPCA algorithm with $\beta = 0.01$ and $\delta = 1.5$.

⁸The peak signal-to-noise ratio is defined as follows:

$$\text{PSNR} = 10 \log_{10} \left(\frac{\max_j x_j^2}{\frac{1}{N} \sum_{j=1}^P (x_j - \hat{x}_j)^2} \right)$$

where \hat{x}_j is the restored image.

Tables 4.4-4.5 compares wall times of monotonic algorithms (PSCA and PPCA), and nonmonotonic algorithms (CA-NR, CA,P, PSCA,P, PPCA,P), respectively. The letter “P” in nonmonotonic algorithms represents the precomputed curvature [40], where we replace $c_i^{\text{opt}}(\cdot)$ with ${}^9c_i^{\text{pre}}(\cdot) = -\ddot{\psi}_i^L(l_i^{\text{max}})$, and $l_i^{\text{max}} = \frac{y_i}{\alpha_1} - b_i$. The algorithms above were performed on the IBM SP2 parallel processors. Convergence in these tables is defined as the smallest n such that $\Phi(x^n) - \Phi(x^0) > 0.999(\Phi(x^*) - \Phi(x^0))$, where $\Phi(x^0)$ is the objective value of the initial image, and $\Phi(x^*)$ is the largest objective value among all methods obtained in 50 iterations. Figure 4.5 shows the subset partitions. Figure 4.6 shows the performance in elapsed time of the PPCA algorithm with different number of processors applying to the 2-D data. Since the PSF is fairly small, interprocessor communication time becomes significant as the number of processors increases; therefore, the speedup factor is less than the ideal relationship, as predicted by Amdahl’s law [6]. Nevertheless, these results confirm that the PPCA algorithm is well suited for parallel processing.

Convergence	Monotonic Algorithms			
	PSCA	2-PPCA	4-PPCA	8-PPCA
#iters	38	39	39	41
Wall time (s)	318.20	213.85	156.20	132.34
Wall time/iter (s)	8.37	5.48	4.01	3.23
Speedup factor	1	1.52	2.09	2.59

Table 4.4: Comparison of wall times and number of iterations to converge using monotonic for a 512×512 pepper image.

Figure 4.7 shows that the PPCA algorithms increase the objective function essentially as much per iteration as the PSCA algorithm. This effect implies that subset-separation technique barely slows the convergence rate of the PPCA algorithm compared with the PSCA algorithm, which is a one subset version of the PPCA al-

⁹This ad hoc modification loses the guarantee of monotonicity, but reduces computation and *usually* seems to converge.

Convergence	Nonmonotonic algorithms					
	CA-NR	CA,P	PSCA,P	2-PPCA,P	4-PPCA,P	8-PPCA,P
#iters	28	29	27	28	28	28
Wall time (s)	612.5	517.91	195.89	123.48	89.33	80.55
Wall time/iter (s)	21.87	17.86	7.26	4.41	3.19	2.88
Speedup factor	0.33	0.41	1	1.64	2.28	2.52

Table 4.5: Comparison of wall times and number of iterations to converge using nonmonotonic algorithms for a 512×512 pepper image.

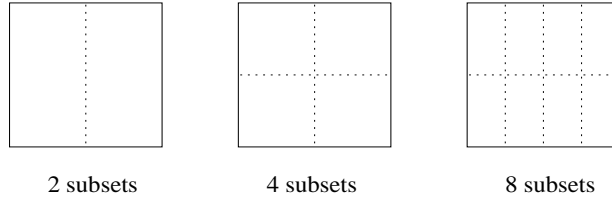


Figure 4.5: Partitioned set patterns of a 2-D image.

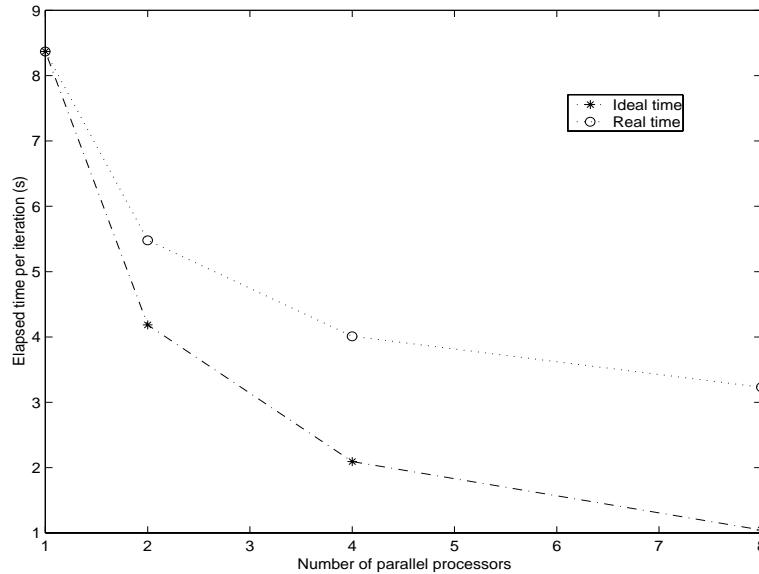


Figure 4.6: Performance on parallel processors in elapsed time for the PPCA algorithms using a 512×512 image and a 15×15 PSF.

algorithm. Figure 4.8 shows that the PPCA algorithms converge in less elapsed time than the PSCA algorithm. Using the precomputed curvatures, Figure 4.9 illustrates that the CA-NR, CA,P, PSCA,P, and PPCA,P algorithms increase the objective function nearly at the same rate; however, Figure 4.10 confirms that the PPCA,P algorithm converges in less time than other nonmonotonic algorithms.

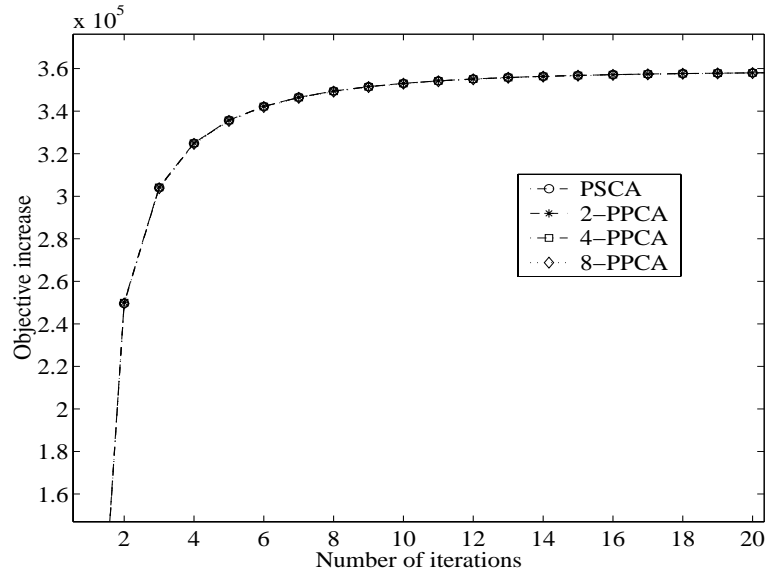


Figure 4.7: Comparison of objective function increase versus number of iterations using monotonic algorithms on a 2-D image.

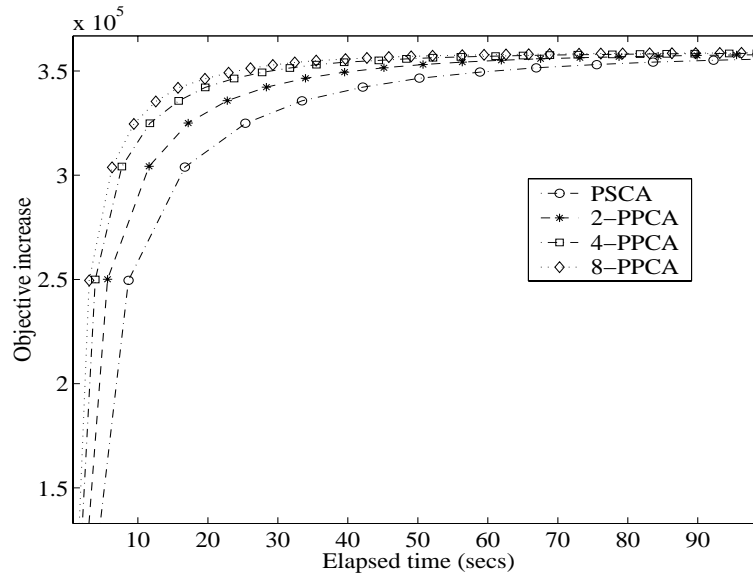


Figure 4.8: Comparison of objective function increase versus elapsed time using monotonic algorithms on a 2-D image.

4.9.2 3-D Simulation Results for Confocal Microscopy

Following [91], a spherical shell test specimen was generated on a $256 \times 256 \times 64$ pixel grid and was degraded by a $15 \times 15 \times 15$ PSF created from the XCOSM package [1] having pixel sizes $\Delta x = \Delta y = \Delta z = 0.15 \mu\text{m}$, $40\times /1.0$ NA oil-immersion ob-

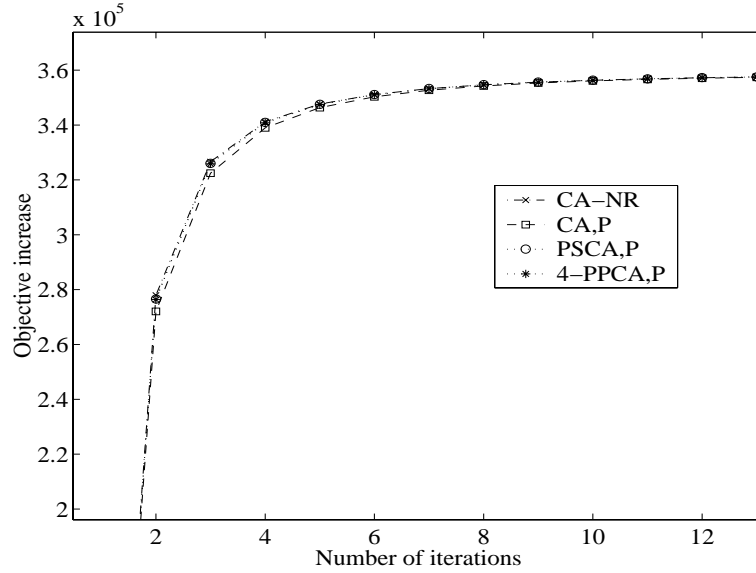


Figure 4.9: Comparison of objective function increase versus number of iterations using nonmonotonic algorithms on a 2-D image.

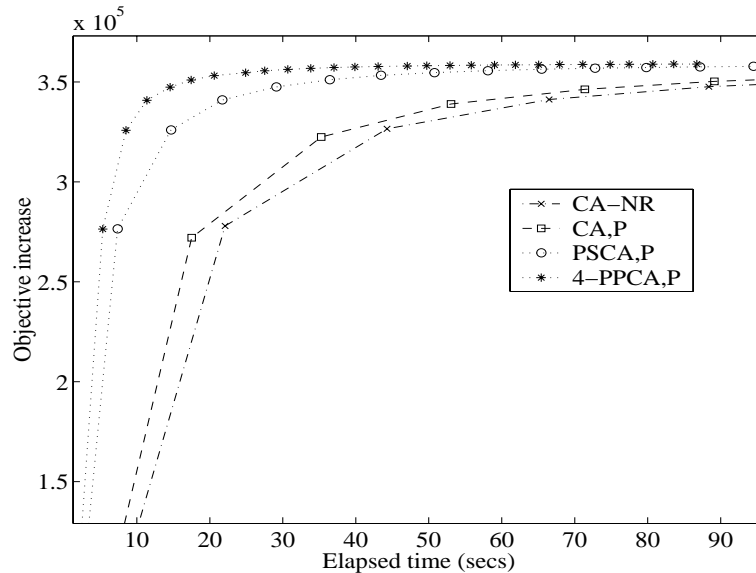


Figure 4.10: Comparison of objective function increase versus elapsed time using nonmonotonic algorithms on a 2-D image.

jective, and a fluorescent wavelength of $0.63 \mu\text{m}$, and the Poisson noise with $\text{PSNR}_{\text{data}}$ of 40 dB. This PSF is circularly symmetric in the xy plane but it has elongation in the z direction which causes a very poor resolution in the axial direction. Figure 4.11 shows the lateral and axial medial sections through the original, degraded, noise-free,

and restored images performed for 20 iterations. The restored image has the PSNR of 28.57 dB. For comparison, the noise-free image in Figure 4.11(c) has the PSNR of 20.66 dB. The images on the xz plane have been scaled up to the same scale as those in the xy plane for display purpose. As seen from the center slice of the xz plane of the restored image (Figure 4.11(d)), the elongation in the z direction of the restored image have been dramatically reduced.

Figure 4.12 shows that the total wall times for 3D results are nearly inversely proportional to the number of processors. This is because a larger amount of work in 3D data has been assigned to each processor which means less communication time relative to the total computation time.

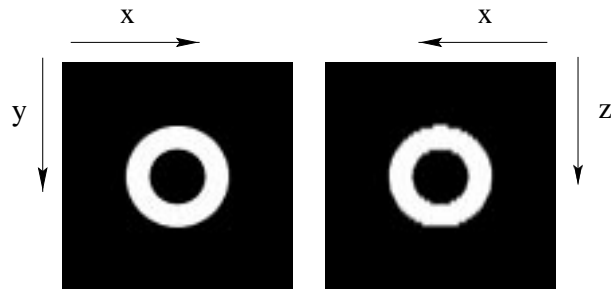
Table 4.6 shows the performance of the wall times of the PSCA, and PPCA algorithms for 20 iterations. Since we used convolution rather than the FFT algorithms, the total time requirement is quite large. Similarly to 2-D simulation results, Figures 4.13-4.14 verify that the PPCA algorithm increases the objective function almost at the same rate as the PSCA algorithm but it requires much less total wall time for computation.

20 iterations	PSCA	2-PPCA	4-PPCA	8-PPCA
Wall time (hrs)	11.54	5.93	3.06	1.64
Wall time/iter (mins)	34.62	17.79	9.18	4.92
Speedup factor	1	1.95	3.77	7.04

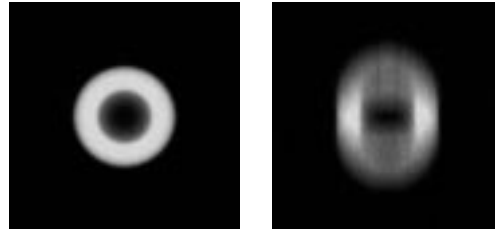
Table 4.6: Comparison of wall times of PSCA, and PPCA algorithms for a 3D image.

4.10 Conclusions for the PPCA Algorithm

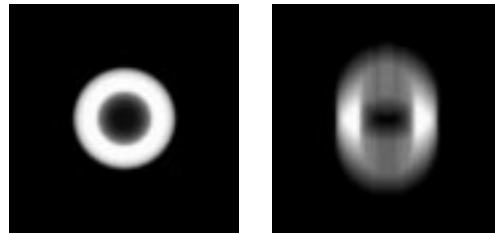
We have developed a new fast converging parallelizable algorithm called the partitioned-separable paraboloidal surrogate coordinate ascent algorithm. This approach overcomes the drawback of the ordinary coordinate ascent algorithm which



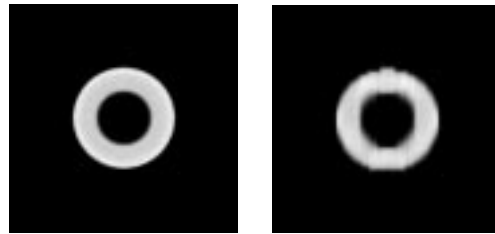
(a) Original Image



(b) Degraded Image



(c) Noise-free Image



(d) Restored Image

Figure 4.11: Results for a 3D simulated spherical shell using a 4-PPCA algorithm for 20 iterations with $\beta = 0.1$ and $\delta = 10$. Lateral and axial medial sections through the image are in the left and right, respectively. For display purpose, the axial sections were scaled in z to obtain a 1:1 aspect ratio.

is a nonparallelizable algorithm. Compared to completely simultaneous updates like EM and SPS algorithms, this algorithm has a faster convergence rate due to larger

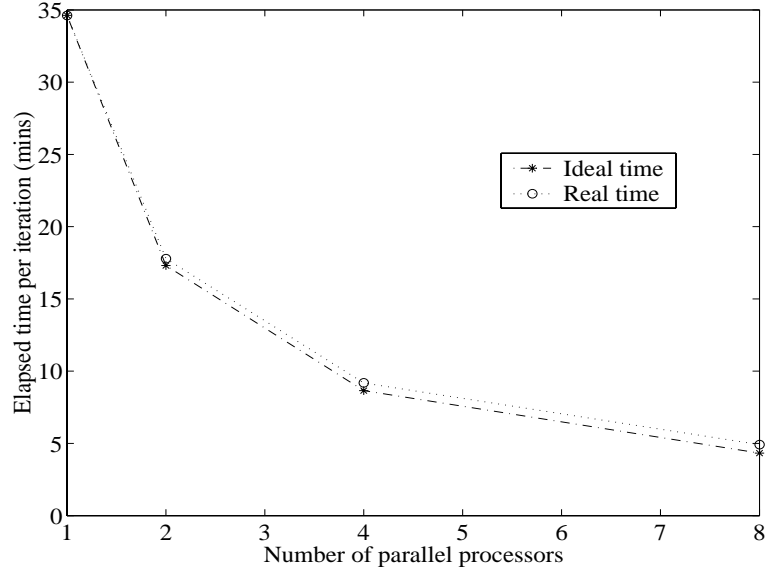


Figure 4.12: Performance on parallel processors in elapsed time for the PPCA algorithms using a $256 \times 256 \times 64$ image and a $15 \times 15 \times 15$ PSF.

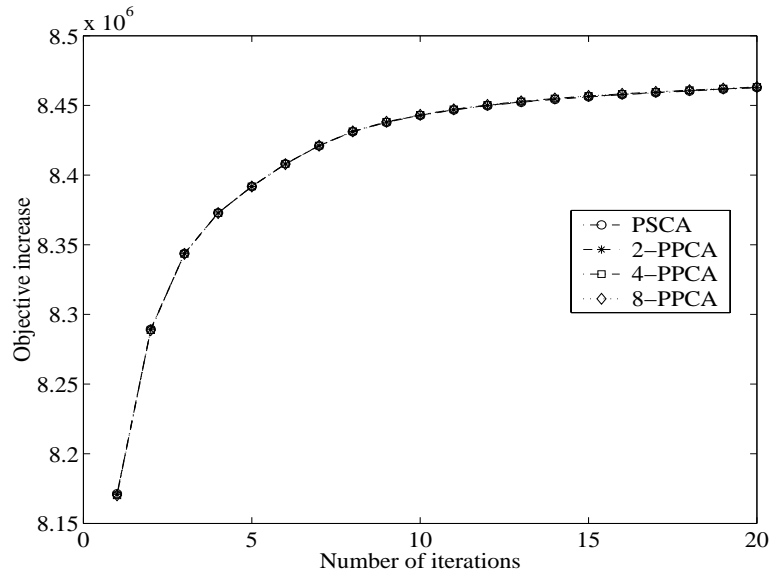


Figure 4.13: Comparison of objective function increase versus number of iterations using PSCA and PPCA algorithms on a 3D image.

updating step sizes. Unlike the PSCA [40] algorithm, the surrogate functions in the PPCA algorithm are separable between subsets to allow simultaneous update across pixel subsets. Thus parallel processors can be assigned to the subsets to reduce total time requirement. Since the PPCA algorithm increases the objective function

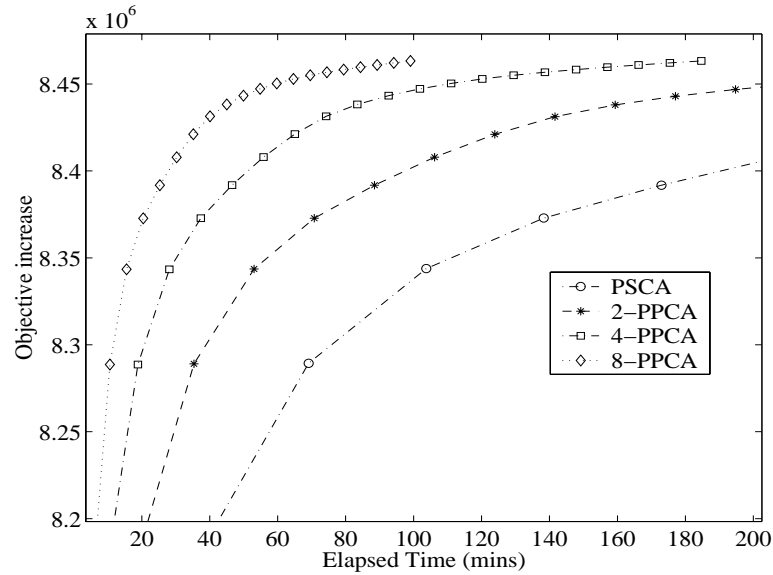


Figure 4.14: Comparison of objective function increase versus elapsed time of PSCA and PPCA algorithms on a 3D image.

nearly at the same rate as the PSCA algorithm, parallelizability in the PPCA algorithm only slightly reduces the convergence rate. The PPCA algorithm using the precomputed curvature, which is a nonmonotonic algorithm, converges much faster than the CA-NR and CA,P algorithms. Thus the PPCA algorithm yields the fastest convergence among the monotonic and nonmonotonic algorithms tested.

CHAPTER V

Relaxed Ordered-Subset Algorithm For Image Restoration

5.1 Introduction

The PPCA algorithm introduced in Chapter IV is more suitable for the space-variant systems where FFTs are not applicable. Because many image restoration techniques for confocal microscopy are usually assumed the space-invariant system of the microscope for simplicity [3, 28, 67, 91], we desire to have a fast converging algorithm that can be performed with FFTs for further acceleration. Therefore, in this chapter¹, we consider a fast converging algorithm belonging to the group of ordered-subset algorithms for image restoration since it can be combined with FFTs and has initial fast convergence.

EM algorithms [36, 39] and their ordered-subset (OS) versions [18, 19, 69] are among the most commonly used algorithms; however, they have limitations of either speed or convergence. Although EM algorithms are guaranteed to converge, they converge very slowly. The OS-EM algorithm [69] has become very attractive for image reconstruction in tomography due to its fast convergence rate compared with the EM algorithms. It “converges” approximately M times faster than the

¹This chapter is based on [111].

EM algorithms, where M is the number of subsets. However, the OS-EM algorithm is not guaranteed to converge. After many iterations, the OS-EM algorithm appears to oscillate between solutions rather than converge to an ML solution. Several approaches have been proposed to solve the convergence problem of the OS-EM algorithm, such as the rescaled block-iterative EMML (RBI-EMML) algorithm [18, 19], the row-action maximum likelihood algorithm (RAMLA) [17], and its regularized version, the block sequential regularized EM (BSREM) algorithm [37]. However, the RBI-EMML algorithm only converges to a solution in the consistent case. The RBI-EMML with a “feedback” approach [18] seems to be impractical for real applications and it does not include the smoothness penalty function. The convergence proofs for the RAMLA and BSREM algorithms invoked a strong “*a posteriori*” assumption that the objective sequence is convergent.

An alternative to the EM algorithms for image restoration and reconstruction is the separable paraboloidal surrogate (SPS) algorithm [40, 46]. An OS version of the SPS algorithm [41] was first introduced for transmission tomography. Although the OS-SPS algorithm improves the objective function more rapidly than the SPS algorithm in the early iterations, convergence is not necessarily achieved. To overcome the convergence problem of the OS-SPS algorithm, the relaxed OS-SPS algorithm [4, 5] was proposed recently by introducing the relaxation parameter into the algorithm. This algorithm not only retains the fast convergence rate of the OS-SPS algorithm, but also is guaranteed to converge globally. In contrast, the relaxed version of the OS-EM algorithm is not guaranteed to converge to the optimal point [4, 5, 17]. Therefore, in this chapter, we focus entirely on the relaxed OS-SPS algorithm for image restoration [110].

Due to the ill-posed nature of image restoration, our algorithm is based on PL

estimation. Most existing OS methods have been applied to image reconstruction in tomography only rather than to image restoration. Effective use of OS methods in image restoration requires one to choose subsets appropriately to provide fast convergence rates. The global convergence property of relaxed OS-SPS holds for all choices of subsets. However, the convergence *rates* of most OS algorithms depend on the choice of subsets and scaling functions (the scaling functions are the diagonal entries of the scaling matrix D in (5.12) below). Since the scaling functions in the ordinary OS-SPS algorithm provide reasonably fast convergence, we focus here on finding subsets that can deliver fast initial convergence rates.

In tomography, the data are organized by projection angles, so the subsets used in tomography are unsuitable for pixel-based image restoration. Bertero and Boccacci applied the OS-EM method to the restoration of the large binocular telescope (LBT) images [10]. However, the structure of the LBT imaging is similar to that of computed tomography: multiple views of the same object are observed at different angles. Thus, this technique cannot be applied to typical image restoration problems. In this chapter, we focus on the more traditional image restoration problem of recovering a scene from a single blurred, noisy measured image under the simplifying assumption that the point spread function (PSF) is known. Instead of choosing subsets by downsampling projection angles as in tomography, for restoration, we choose subsets by downsampling pixels, rather than dividing pixels into subblocks. We show quantitatively that the downsampling approach satisfies the “subset-gradient-balance” conditions [11], which are less restrictive than the subset-balance conditions defined in Ref. [69]. These gradient balance conditions are important for fast convergence.

This chapter is organized as follows. Section 5.2 describes the measurement model and the objective function based on PL estimation. The derivation of the

relaxed OS-SPS algorithm for image restoration starting from the basic idea of OS methods and the OS-SPS algorithm is presented in Section 5.3. Subset design for restoration problems is discussed in Section 5.4. In Section 5.5, we develop some efficient implementation strategies, and quantify the computational complexity for the relaxed OS-SPS algorithm. The performance of subset designs and restoration results using 2-D simulation data and 3-D real data are presented in Section 5.6. Conclusions are given in Section 5.7.

5.2 Measurement Model

Because the measurements in image restoration problems are usually degraded by blur and noise, one can use the statistical characteristics of the measurement system to recover an approximation of the original image by specifying an objective function that is to be maximized. Due to an ill-posed problem of image restoration, we consider PL estimation using an objective function of the following form:

$$\Phi(x) = L(x) - \beta R(x) \quad (5.1)$$

where x denotes the image parameter vector to be estimated, L denotes the log-likelihood function of the measurement, R denotes a roughness penalty function, and β denotes a parameter that controls the tradeoff between resolution and noise in the restored image.

For photon-limited imaging (such as confocal microscopy), the noisy measurement $Y = [Y_1, \dots, Y_N]$ can be modeled (approximately [104, 105]) as follows:

$$Y_i \sim \text{Poisson}\{[Ax]_i + b_i\}, \quad i = 1, \dots, N \quad (5.2)$$

where x is ordered lexicographically in the vector form, A is the system matrix which is assumed to be known, b_i represents the mean number of the background noise and

dark current, and N is the number of measurement pixels. The corresponding log-likelihood function is given by:

$$L(x) = \sum_{i=1}^N \psi_i(l_i(x)) \quad (5.3)$$

where $\psi_i(l) = y_i \log(l + b_i) - (l + b_i)$, ignoring irrelevant constants independent of x , $l_i(x) = [Ax]_i = \sum_{j=1}^P a_{ij}x_j$, P is the number of pixels to be estimated, and the measured values y_i 's are samples of independent Poisson random variables Y_i 's.

To reduce noise, we penalize the differences between neighboring pixels using a roughness penalty function of the form

$$R(x) = \sum_{i=1}^r \psi^R([Cx]_i) \quad (5.4)$$

where ψ^R is the potential function, C is the penalty matrix, and r is the number of pairs of neighboring pixels. We assume that each potential penalty function $\psi^R(t)$ satisfies all the conditions given in Chapter III.

With proper regularization, the objective function in this problem has a unique global maximum. Thus, our goal is to estimate x by finding the maximizer of the objective function:

$$\hat{x} \triangleq \arg \max_{x \geq 0} \Phi(x).$$

Because closed-form solutions are unavailable for the maximizer, iterative algorithms are needed. Due to fast initial convergence of OS algorithms, we focus on this class of algorithms in this chapter.

5.3 The Algorithms

This section summarizes the general principles of ordered subsets (also called block iterative) methods and reviews the OS-SPS algorithm.

5.3.1 Ordered-Subset Technique

One can decompose the objective function in (5.1) into sub-objective functions f_m 's as follows:

$$\Phi(x) = \sum_{m=1}^M f_m(x) \quad (5.5)$$

where M is the total number of subsets, chosen by the algorithm designer. Let $\{S_m\}_{m=1}^M$ be a disjoint partition of $\{1, \dots, N\}$ such that $\bigcup_{m=1}^M S_m = \{1, \dots, N\}$. Then f_m 's are obtained by replacing a sum over all pixel indices in the likelihood function of (5.3) with a sum over a subset of data S_m and scaling the penalty term by M as follows:

$$f_m(x) \triangleq \sum_{i \in S_m} \psi_i(l_i(x)) - \frac{\beta}{M} R(x). \quad (5.6)$$

Instead of the restrictive subset-balance conditions originally defined in [69], we define the following less restrictive conditions called the “subset-gradient-balance” conditions which use an “approximate gradient” computed from only a part of data:

$$\nabla f_1(x) \cong \nabla f_2(x) \cong \dots \cong \nabla f_M(x) \quad (5.7)$$

where $\nabla f_m(x)$ is the gradient of the sub-objective function at the m th subset. When these conditions hold, the gradient of the objective function $\Phi(x)$ can be approximated as follows:

$$\nabla \Phi(x) \cong M \nabla f_m(x), \quad m = 1, \dots, M. \quad (5.8)$$

Using approximate (5.8), one can replace $\nabla \Phi(x)$ with $M \nabla f_m(x)$ in any gradient-based algorithm to construct an OS version of that algorithm. If proper subsets satisfying the above conditions are combined with suitable scaling functions [e.g., see (5.12) below], then the OS algorithms often exhibit acceleration by a factor of M

in the early iterations. These conditions influence the rate of convergence of OS-SPS, but are not required for global convergence of relaxed OS-SPS.

Figure 5.1 illustrates how ordinary OS algorithms work. For this figure, we assumed that $\nabla\Phi(x) = \nabla f_1(x) + \nabla f_2(x)$. For x far from the solution, the condition $\nabla f_1(x) \cong \nabla f_2(x)$ holds and accelerated convergence speed is achieved. However, in the later iterations when x is close to the optimal solution, the “subset-gradient-balance” conditions are no longer valid and a limit cycle behavior around the optimal solution appears. Because ordinary OS algorithms use the same step-size at each iteration, the limit cycle does not vanish. One way to suppress this limit cycle is to use a diminishing step-size at each iteration (relaxation).

Illustration of OS Algorithms

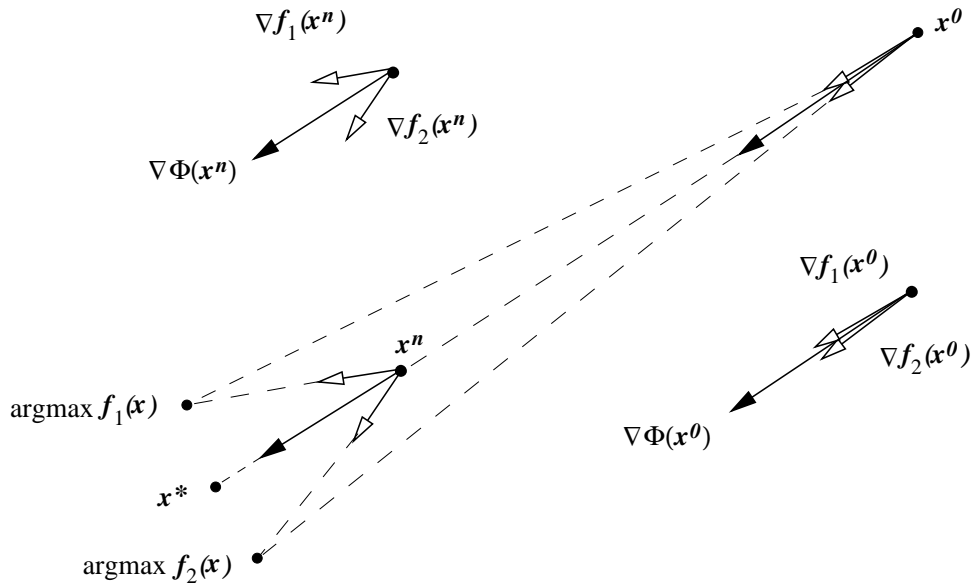


Figure 5.1: Illustration of how the OS algorithms work. Assume that $\nabla\Phi(x) = \nabla f_1(x) + \nabla f_2(x)$. When x is far from the solution, the “subset-gradient-balance” conditions hold and an order-of-magnitude acceleration can be achieved in the early iterations. However, for later iterations or when x is near the optimal solution, those conditions are no longer valid and a limit-cycle behavior is observed.

As previously discussed, OS-EM is not guaranteed to converge even in the relaxed version [4, 5, 17]. Therefore, we focus on the convergent relaxed OS-SPS algorithm hereafter.

5.3.2 Ordered-Subset, Separable Paraboloidal Surrogate Algorithm

The SPS algorithm is based on paraboloidal surrogate functions [40, 46, 109] and the concavity technique developed by De Pierro [36]. The pixel update for the SPS algorithm can be summarized as follows:

$$x_j^{n+1} = \left[x_j^n + \frac{\nabla_j \Phi(x^n)}{\sum_{i=1}^N a_{ij} \gamma_i c_i^n + \beta p_j^n} \right]_+ \quad (5.9)$$

where the symbol $[x]_+$ represents x if $x > 0$ and 0 if $x \leq 0$. The gradient of the objective function at the j th pixel in the SPS algorithm is as follows:

$$\nabla_j \Phi(x) = \frac{\partial}{\partial x_j} \Phi(x) = \sum_{i=1}^N a_{ij} \dot{\psi}_i(l_i(x)) - \beta \sum_{i=1}^r c_{ij} \dot{\psi}^R([Cx]_i) \quad (5.10)$$

where c_{ij} is the ij th element of the matrix C . In (5.9), $\gamma_i = \sum_{j=1}^P a_{ij}$, and c_i^n is the following optimal curvature that guarantees convergence of SPS [40, 109]:

$$c_i^n = \begin{cases} \left[\frac{2}{(l_i^n)^2} \left(\psi_i(l_i^n) - \psi_i(0) - l_i^n \dot{\psi}_i(l_i^n) \right) \right]_+, & l_i^n > 0 \\ \left[-\ddot{\psi}_i(0) \right]_+, & l_i^n = 0 \end{cases}$$

where $l_i^n = \sum_{j=1}^P a_{ij} x_j^n$. For the penalty function terms, the curvature p_j^n in (5.9) is given by:

$$p_j^n = \sum_{i=1}^r c_{ij} \nu_i \omega([Cx^n]_i)$$

where $\nu_i = \sum_{j=1}^P c_{ij}$, and $\omega(t) = \frac{\dot{\psi}^R(t)}{t}$.

Erdoğlan and Fessler [41] introduced the OS version of the SPS algorithm for transmission tomography. With the use of approximation (5.8), the gradient of the

objective function in (5.9) is replaced by the sub-objective function multiplied by the number of subsets. We define $x_j^n \triangleq x_j^{(n,0)}$ and $x_j^{(n+1)} \triangleq x_j^{(n,M)}$. The first superscript refers to iterations and the second superscript refers to subsets. Then the pixel update x_j for the OS-SPS algorithm becomes

$$x_j^{(n,m)} = \left[x_j^{(n,m-1)} + M \frac{\nabla_j f_m(x^{(n,m-1)})}{d_j + \beta p_j} \right]_+, \quad m = 1, \dots, M \quad (5.11)$$

where

$$\nabla_j f_m(x) = \sum_{i \in S_m} a_{ij} \dot{\psi}_i(l_i(x)) - \frac{\beta}{M} \sum_{i=1}^r c_{ij} \dot{\psi}^R([Cx]_i).$$

Since the global convergence is not affected by the curvatures as long as they are positive, we precompute the curvatures d_j and p_j to save computation [5]. The curvature of the likelihood d_j in (5.11) is precomputed as follows:

$$d_j = \sum_{i=1}^N a_{ij} \gamma_i c_i$$

where $c_i = -\ddot{\psi}_i(y_i - b_i)$. Likewise, the curvature of the penalty function p_j is precomputed as follows:

$$p_j = \sum_{i=1}^r c_{ij} \nu_i \omega(0).$$

Although the OS-SPS algorithm yields an order-of-magnitude acceleration over the SPS algorithm in the early iterations, it is not guaranteed to converge to the optimal solution.

5.3.3 Relaxed Ordered-Subset Separable Paraboloidal Surrogate Algorithm

To guarantee the convergence of the OS-SPS algorithm, Ahn and Fessler [4, 5] modified the OS-SPS algorithm to include relaxation. Without relaxation, the

OS-SPS algorithm has a constant step-size, thus exhibiting a limit cycle behavior. Modifying (5.11), the pixel update of the relaxed OS-SPS algorithm becomes

$$x_j^{(n,m)} = \left[x_j^{(n,m-1)} + \alpha_n M \frac{\nabla_j f_m(x^{(n,m-1)})}{d_j + \beta p_j} \right]_+, \quad m = 1, \dots, M.$$

Equivalently, in the matrix-vector form,

$$x^{(n,m)} = [x^{(n,m-1)} + \alpha_n D \nabla f_m(x^{(n,m-1)})]_+ \quad (5.12)$$

where $D = \text{diag}\{\frac{M}{d_j + \beta p_j}\}$ is the diagonal scaling matrix. We use the same scaling functions as in the ordinary OS-SPS algorithm because they were shown to provide fairly fast initial convergence in the ordinary OS-SPS algorithm [41]. Finding optimal scaling functions for convergence speed is still an open question. A positive relaxation parameter α_n is chosen such that $\sum_n \alpha_n = \infty$ and $\sum_n \alpha_n^2 < \infty$. We use $\alpha_n = \frac{\xi}{(\xi-1)+n}$, where ξ is a positive constant, a ‘‘tuning parameter’’ that affects the rate of convergence and is chosen empirically. The optimal choice of the relaxation parameter still remains an open question. With the diminishing step-size, the relaxed OS-SPS algorithm is globally convergent [4, 5]. The outline for the relaxed OS-SPS algorithm is shown in Table 5.1.

5.3.4 Blind Restoration

Many blind restoration techniques have been applied to simultaneously restore the image and estimate the PSF [66, 79, 91, 119]. The relaxed OS-SPS algorithm is applicable to blind restoration as well. For a blind restoration technique, the image can be updated with the relaxed OS-SPS algorithm, whereas the PSF can be updated with the ordinary SPS or EM algorithms because of the small number of parameters in the PSF.

Precompute:

$$d_j = -\sum_{i=1}^N a_{ij} \gamma_i \ddot{\psi}_i(y_i - b_i)$$

$$p_j = \sum_{i=1}^r c_{ij} \nu_i \omega(0)$$

for $n = 1, \dots, \text{Niters}$

$$\alpha_n = \frac{\xi}{(\xi-1)+n}$$

for $m = 1, \dots, M$

$$\hat{l}_i = \sum_{j=1}^P a_{ij} x_j^{(n,m-1)}, \quad \forall i \in S_m \quad (5.13)$$

$$\dot{\psi}_i = \frac{y_i}{\hat{l}_i + b_i} - 1, \quad \forall i \in S_m$$

for $j = 1, \dots, P$

$$\dot{L}_j = \sum_{i \in S_m} a_{ij} \dot{\psi}_i \quad (5.14)$$

$$\dot{R}_j = \sum_{i=1}^r c_{ij} \dot{\psi}^R([Cx^{(n,m-1)}]_i)$$

$$x_j^{(n,m)} = \left[x_j^{(n,m-1)} + \alpha_n M \frac{\dot{L}_j - \frac{\beta}{M} \dot{R}_j}{d_j + \beta p_j} \right]_+$$

end

end

end

Table 5.1: The Relaxed OS-SPS Algorithm Outline.

5.4 Subset Design

Since most OS algorithms have been used for image reconstruction to date, a different strategy for choosing subsets in image restoration needs to be considered because of differences in data acquisition. A good choice of subsets should satisfy the “subset-gradient-balance” conditions stated in (5.7) and (5.8) to provide rapid convergence. In tomography, the subsets are chosen from downsampling projection angles. Since data in image restoration are based on pixel locations, instead of projection angles as in tomography, one possible approach for choosing the subsets in the restoration problem is to downsample pixels in the image. Figure 5.2 shows possible choices of four subsets for a 2D image. We define “4×1” OS-SPS

for a downsampling approach with 4 subsets in each column and 1 subset in each row as shown in Figure 5.2(a). The downsampling approaches seem to satisfy the “subset-gradient-balance” conditions. To verify this, we compared the gradients of the original objective function and the sub-objective functions using four subsets with a “2×2” configuration (Figure 5.3). Specifically, we computed the gradients of the sub-objective functions belonging to subsets 1 and 4, and then compared them to the gradient of the original objective function as shown in the second and third columns of Figure 5.3. These differences are very small: the normalized root mean squared (RMS) error between the actual gradient $\nabla\phi$ and the subgradient $4\nabla f_m$ is less than 0.5%.

Possible Choices for Four Subsets by a Downsampling Approach

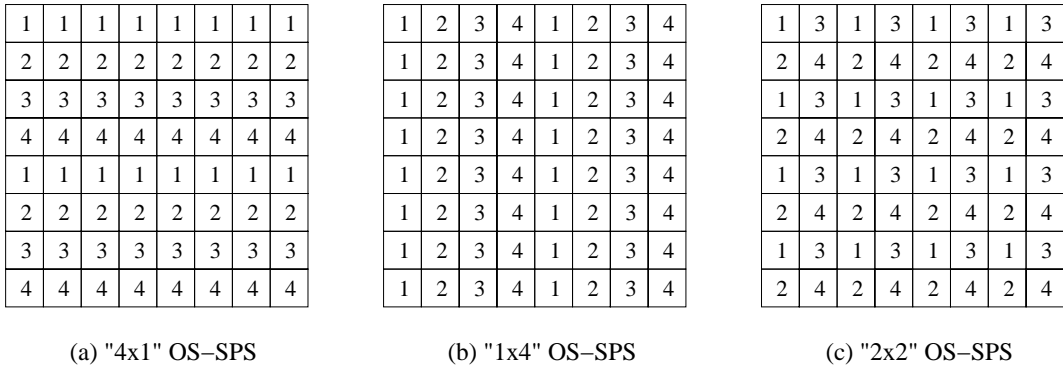


Figure 5.2: These subsets tend to satisfy the “subset-gradient-balance” conditions. The first number in quotation marks is the number of subsets in each column, and the second number is the number of subsets in each row. The total number of subsets is the product of these two numbers. The pixel label m belongs to the respective set S_m .

Another choice for choosing subsets is to divide the image into large contiguous blocks, called the subblock approach (Figure 5.4). We define “4×1B” OS-SPS for the subblock approach with 4 subblocks in each column and 1 subblock in each row as shown in Figure 5.4(a). This approach tends to be a poor choice of subsets because it fails to satisfy the “subset-gradient-balance” conditions as illustrated in the last

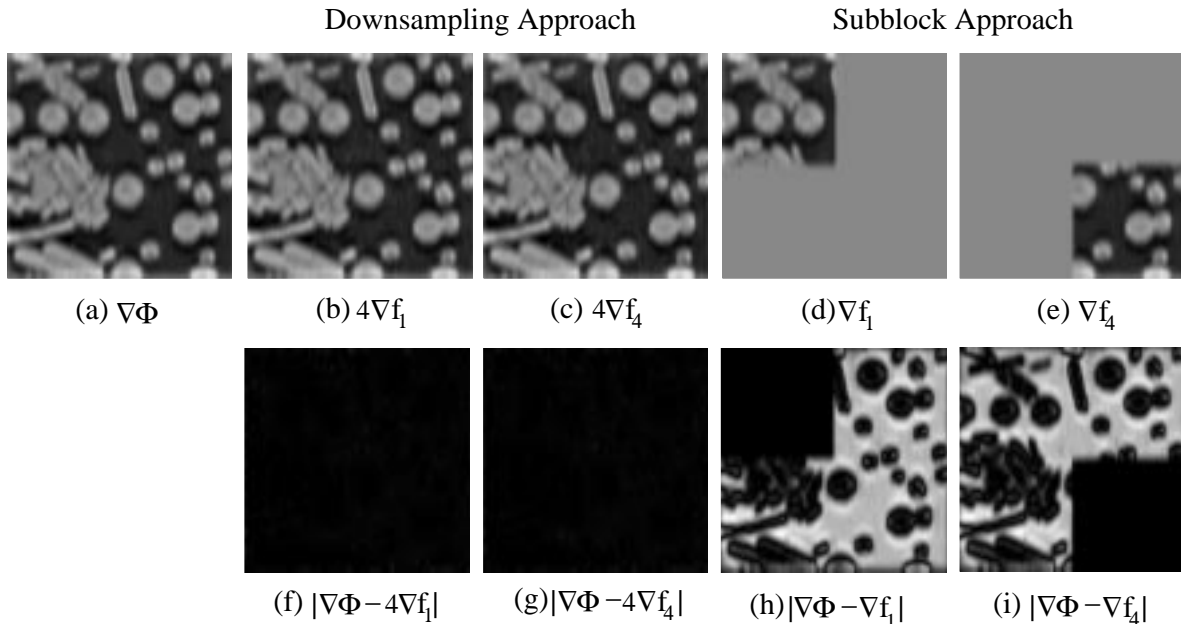


Figure 5.3: Investigation of the “subset-gradient-balance” conditions in the OS-SPS algorithm. Four subsets with a “ 2×2 configuration” were used. The second and third columns show the gradients of the sub-objective functions from the downsampling approach with use of subset 1 and subset 4, respectively, and their differences compared with the gradient of the objective function. Similarly, the last two columns are from the subblock approach. The gradients of the sub-objective functions in the downsampling approach were multiplied by 4 to compensate for the downsampled data. However, this scaling factor is not needed in the subblock approach, because a block of contiguous pixels is used.

two columns of Figure 5.3. The differences between the gradients of the various sub-objective functions using different subsets are large: the normalized RMS is more than 65%. Section 5.6 reports empirical comparisons of how these possible choices of subsets affect the convergence speed.

5.5 Implementation Techniques and Complexity

Most of the computation time in the OS-SPS algorithm takes place in (5.13) and (5.14). In this section, we discuss how to efficiently implement these two expressions for both space-variant and space-invariant systems.

Possible Choices for Four Subsets by a Subblock Approach

1	1	1	1	1	1	1	1
1	1	1	1	1	1	1	1
2	2	2	2	2	2	2	2
2	2	2	2	2	2	2	2
3	3	3	3	3	3	3	3
3	3	3	3	3	3	3	3
4	4	4	4	4	4	4	4
4	4	4	4	4	4	4	4

(a) "4x1B" OS-SPS

1	1	2	2	3	3	4	4
1	1	2	2	3	3	4	4
1	1	2	2	3	3	4	4
1	1	2	2	3	3	4	4
1	1	2	2	3	3	4	4
1	1	2	2	3	3	4	4
1	1	2	2	3	3	4	4
1	1	2	2	3	3	4	4

(b) "1x4B" OS-SPS

1	1	1	1	3	3	3	3
1	1	1	1	3	3	3	3
1	1	1	1	3	3	3	3
1	1	1	1	3	3	3	3
2	2	2	2	4	4	4	4
2	2	2	2	4	4	4	4
2	2	2	2	4	4	4	4
2	2	2	2	4	4	4	4

(c) "2x2B" OS-SPS

Figure 5.4: These subsets tend to violate the “subset-gradient-balance” conditions. The first number in quotation marks is the number of subblocks in each column, and the second number is the number of subblocks in each row.

5.5.1 Space-Variant Systems

A literal implementation of (5.13) and (5.14) in the algorithm outline would be appropriate for a shift-variant imaging system whose collection of PSFs is tabulated as a sparse set of a_{ij} values. With this technique, the computational complexity of the OS-SPS algorithm is essentially the same as in the nonordered-subsets (non-OS) algorithm, except that the penalty-function gradient must be evaluated m times per iteration. However, usually the likelihood-gradient computation dominates.

5.5.2 Space-Invariant Systems with Convolution

For shift-invariant systems, however, one would typically implement (5.13) and (5.14) using convolution or fast Fourier transform(FFT)-based convolution in the conventional single-subset type of the gradient-based iteration. Since these operations dominate the algorithm, it is essential to formulate efficient implementations of these two expressions. Computing all values of \hat{l} by using ordinary convolution would be inefficient when only some values of \hat{l} will be used in a given subiteration. Therefore, in this section, we introduced the following technique for computing (5.13)

and (5.14) efficiently with convolution.

For a space-invariant system, we rewrite (5.13) in the convolution form as follows:

$$\hat{l}_i = \sum_{j=1}^P h_{i-j} x_j, \quad \forall i \in S_m \quad (5.15)$$

where h is the PSF. For illustration, we describe 1-D convolution. Extension to 2-D and 3-D is straightforward. To compute some values of \hat{l} efficiently, we rewrite (5.15) using two summations:

$$\hat{l}_i = \sum_{m=1}^M \sum_{j \in S_m} h_{i-j} x_j, \quad \forall i \in S_m. \quad (5.16)$$

Using this expression, we can compute \hat{l}_i for $i \in S_m$ by convolving the downsampled image and the PSF belonging to subset S_m , and then summing all the subsets (Figure 5.5).

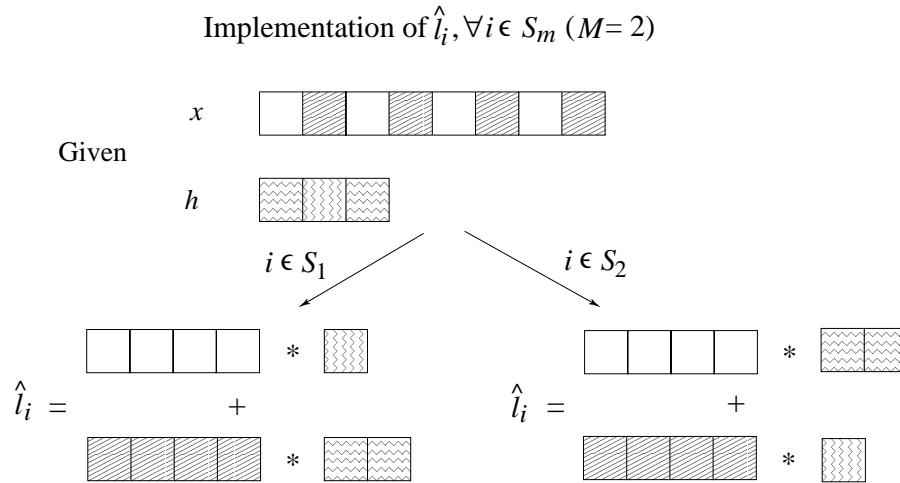


Figure 5.5: Illustration for computing $\hat{l}_i, \forall i \in S_m (M=2)$, using all the information of x and h . The asterisk represents convolution. The white blocks denote elements of x belonging to subset $m=1$, and the striped blocks denote elements of x belonging to subset $m=2$.

Similarly, to compute (5.14) efficiently by convolution, we can rewrite that expression as follows:

$$\dot{L}_j = \sum_{i \in S_m} h_{i-j} \dot{\psi}_i. \quad (5.17)$$

For each j , \dot{L}_j can be computed by using $\dot{\psi}_i$ and a downsampled PSF. Different j 's require a different downsampling of the PSF, but use the same $\dot{\psi}_i$'s (Figure 5.6). In this figure, the PSF is assumed to be symmetric. Otherwise, the indices of the PSF must be inverted before convolving.

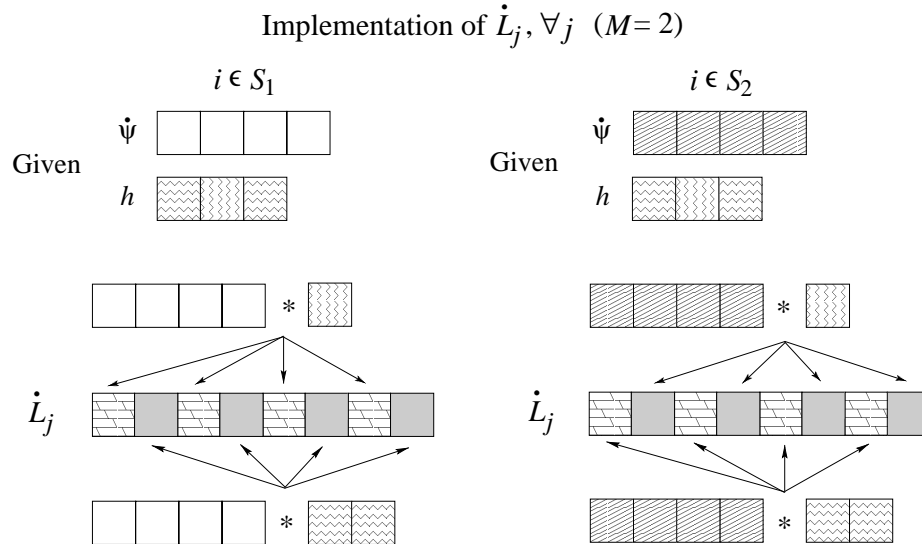


Figure 5.6: Illustration of computing $\dot{L}_j, \forall j$ ($M=2$), using some information of $\dot{\psi}_i$ but all the information of h .

If implemented carefully, computational complexity for this convolution technique does not increase as the number of subsets increases.

5.5.3 Space-Invariant Systems with Use of Fast Fourier Transforms

For simultaneous update methods, such as the EM algorithms for image restoration, one can use FFTs to reduce computation, especially for large 3D problems. Similarly, a strategy for using FFTs in the OS-SPS algorithm would be desirable to compute \dot{L}_j and \hat{l}_i efficiently. One possible solution is to implement the partial FFT algorithm [34], where only a small number of frequencies are evaluated. Since there is a specific pattern for computing \hat{l}_i and \dot{L}_j in each subset, rather than adapting and implementing this partial FFT technique into our algorithm, we develop the

following technique based on the ordinary FFT algorithm, which should yield the same complexity but avoids implementing new FFT code.

To describe our technique, we consider 1-D data and 2 subsets ($M = 2$). Let spatial indices be replaced by η to avoid confusion, $H(k)$ be an N -point FFT of h , and $X(k)$ be an N -point FFT of x . We assume that $P = N$ in this case. To compute \hat{l} for 2 subsets using FFTs, we reformulate (5.15) into the following expression:

$$\hat{l}(\eta) = \frac{1}{N} \sum_{k=0}^{N-1} H(k)X(k) \exp\left(i\frac{2\pi\eta k}{N}\right), \quad \forall \eta \in S_m.$$

Let $\eta = 0, \dots, N/2 - 1$. Then the even indices of \hat{l} belonging to subset 1 and the odd indices belonging to subset 2 are computed as follows:

$$\begin{aligned} m = 1; \quad \hat{l}(2\eta) &= \frac{1}{N} \sum_{k=0}^{N/2-1} [H(k)X(k) + H(k + N/2)X(k + N/2)] \exp\left(i\frac{2\pi\eta k}{N/2}\right) \\ m = 2; \quad \hat{l}(2\eta + 1) &= \frac{1}{N} \sum_{k=0}^{N/2-1} [H(k)X(k) - H(k + N/2)X(k + N/2)] \exp\left(i\frac{2\pi k}{N}\right) \\ &\quad \exp\left(i\frac{2\pi\eta k}{N/2}\right). \end{aligned}$$

In this technique, a full N -point FFT is performed for h and x , but an N/M -point inverse FFT (IFFT) is performed on \hat{l} for each subset. Given that the FFT of H is precomputed, the total number of complex multiplications required for computing \hat{l}_i in one iteration of the OS-SPS algorithm with M subsets with the use of FFT is given as follows:

$$\frac{MN}{2} \log_2 N + MN + \frac{N(M-1)}{M} + \frac{N}{2} \log_2 \left(\frac{N}{M}\right). \quad (5.18)$$

The first term is for computing the FFT of x . The second term is for multiplying X and H . The third term is for multiplication by $\exp(i\frac{2\pi k}{N})$. The fourth term is for the IFFT that yields $\hat{l}_i, i \in S_m$. For comparison, the number of complex multiplications for computing \hat{l}_i in the non-OS algorithm is $N \log_2(2N)$. Table 5.2

compares the complexity of computing \hat{l}_i in one iteration for the OS algorithm relative to the non-OS algorithm when FFTs are used. Although the number of complex multiplications increases as the number of subsets increases, it increases less rapidly than the number of subsets. Since the convergence rate increases roughly by a factor of number of subsets [4, 5, 69, 110], there is still an advantage in using FFTs in the OS-SPS algorithm, especially when N is large.

Number of data points	Number of subsets	Complexity ratio of OS and non-OS algorithms
64	2	1.57
	4	2.68
	8	4.91
512	2	1.55
	4	2.62
	8	4.79

Table 5.2: Multiplication complexity ratio for computing \hat{l}_i (with the use of FFTs) of OS-SPS and non-OS algorithms with different numbers of subsets

Similar to the case of \hat{l} , to compute \dot{L}_j efficiently using FFT, we rewrite (5.17) in the following FFT form (assuming h is symmetric):

$$\dot{L}(\eta) = \frac{1}{N} \sum_{k=0}^{N-1} H(k) \Psi(k) \exp\left(\imath \frac{2\pi\eta k}{N}\right), \quad \forall \eta.$$

\dot{L} is obtained by performing an N -point IFFT of the product of $H(k)$ and $\Psi(k)$; however, $H(k)$ and $\Psi(k)$ are computed from the reduced data given in each subset, i.e., even and odd sets of data for a 2-subset case. Thus, for $k = 0, \dots, N/2 - 1$, we

compute N -point $H(k)$ and N -point $\Psi(k)$ for both subsets as follows:

$$\begin{aligned}
m = 1; \quad H(k) &= \sum_{\eta=0}^{N/2-1} h(2\eta) \exp\left(-i\frac{2\pi\eta k}{N/2}\right) = H(k + N/2) \\
\Psi(k) &= \sum_{\eta=0}^{N/2-1} \psi(2\eta) \exp\left(-i\frac{2\pi\eta k}{N/2}\right) = \Psi(k + N/2) \\
m = 2; \quad H(k) &= \exp\left(-i\frac{2\pi k}{N}\right) \sum_{\eta=0}^{N/2-1} h(2\eta + 1) \exp\left(-i\frac{2\pi\eta k}{N/2}\right) = -H(k + N/2) \\
\Psi(k) &= \exp\left(-i\frac{2\pi k}{N}\right) \sum_{\eta=0}^{N/2-1} \psi(2\eta + 1) \exp\left(-i\frac{2\pi\eta k}{N/2}\right) = -\Psi(k + N/2).
\end{aligned}$$

Thus $N/2$ -point FFTs are performed to obtain the first halves of $H(k)$ and $\Psi(k)$. In this case, the multiplication complexity for computing \hat{L} is the same as the complexity for computing \hat{l} .

In the FFT technique described above, we illustrate the techniques only for radix-2 FFT. If the data sizes are not powers of 2, then zero padding should be applied to avoid large prime factors [95]. Our technique can yield either circular or linear convolution depending on the amount of zero padding. However, we usually perform zero padding to obtain a linear convolution.

5.6 Simulation and Real Results

In this section, we illustrate the proposed algorithm with 2-D simulated data and 3-D real data in comparison with existing algorithms. We also report the characteristics of various subset choices as discussed in Section 5.4.

5.6.1 2-D Simulation Results

A 256×256 cell image in Figure 5.8(a) was degraded by a 15×15 PSF (Figure 5.7), created from the XCOSM package [1], and Poisson noise with peak signal-to-noise ratio (PSNR) of 40 dB, as shown in Figure 5.8(b). The PSNR for the data is defined

as follows:

$$\text{PSNR} = 10 \log_{10} \left(\frac{\max_i (y_i - b_i)^2}{\frac{1}{N} \sum_{i=1}^N (y_i - \mathbb{E}[y_i])^2} \right).$$

The following parameters were used to create the confocal PSF from the XCOSM package [1]: pixel sizes of $0.15 \mu\text{m}$ (in all directions), $40\times /1.0 \text{ NA}$ oil-immersion objective, and a fluorescent wavelength of $0.63 \mu\text{m}$. However, we used only the central xz plane for the 2-D simulation to clearly illustrate how elongation in the z direction has been reduced after restoration.

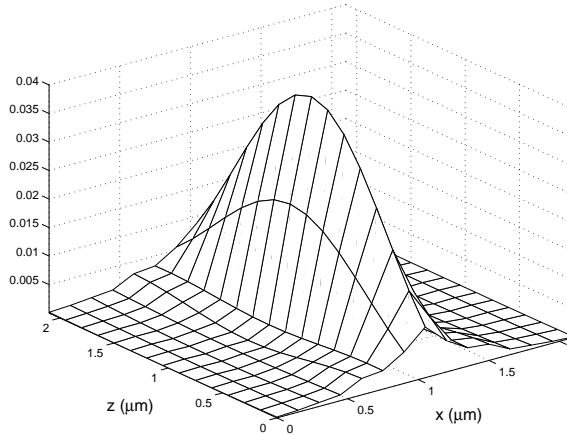


Figure 5.7: 2-D theoretical confocal PSF in the xz plane.

Figure 5.8(c) and (d) show the restored images using the constrained least squares (CLS) method and the relaxed OS-SPS algorithm, respectively. The CLS method does not produce the image as good as the relaxed OS-SPS algorithm. For the relaxed OS-SPS algorithm, we used the relaxation parameter $\alpha_n = 11/(10 + n)$ and, for edge preservation, we used the nonquadratic roughness penalty function [81] $\psi^R(t) = \delta^2 \left[\left| \frac{t}{\delta} \right| - \log \left(1 + \left| \frac{t}{\delta} \right| \right) \right]$, where δ controls the degree of edge preservation. The relaxed OS-SPS algorithm was run for 50 iterations using 8 subsets. To clearly see the improvement, the zoom-in versions of images in the boxes in Figure 5.8 are shown in Figure 5.9. The elongation in the z direction, very apparent in the degraded image,

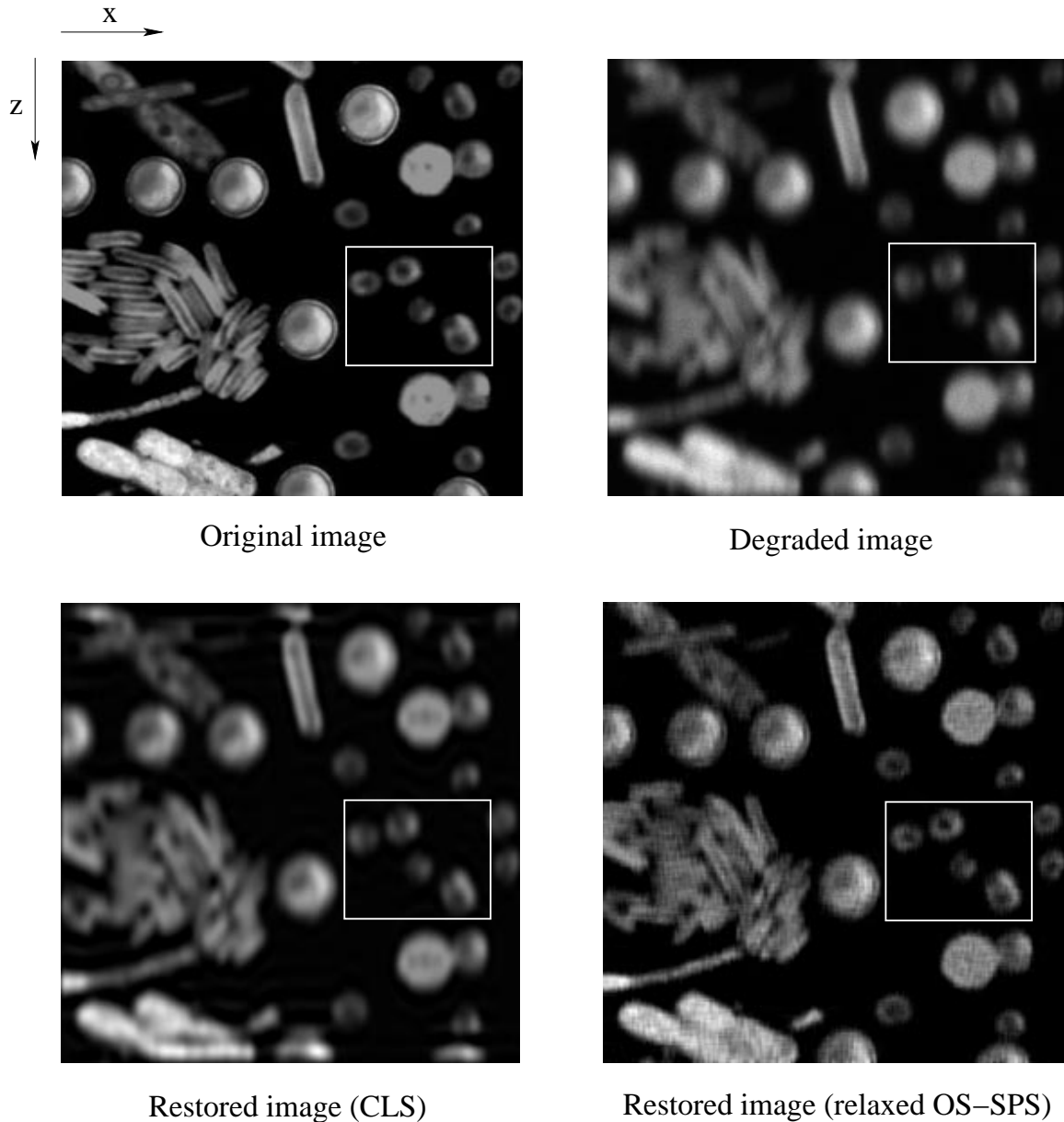


Figure 5.8: Simulated images and restoration using the relaxed OS-SPS algorithm with $\beta = 10^{-6}$ and $\delta = 100$. The PSF in the noisy blurry image was simulated from the 2D PSF of the confocal microscope only in the xz direction, where x is along the horizontal axis and z is along the vertical axis, to show elongation in the z direction. This elongation is reduced in the restored image with CLS but mostly disappears in the restored image with relaxed OS-SPS.

is greatly reduced in the restored image with relaxed OS-SPS, thus improving the (axial) resolution. To quantify restoration improvement, we find standard deviations

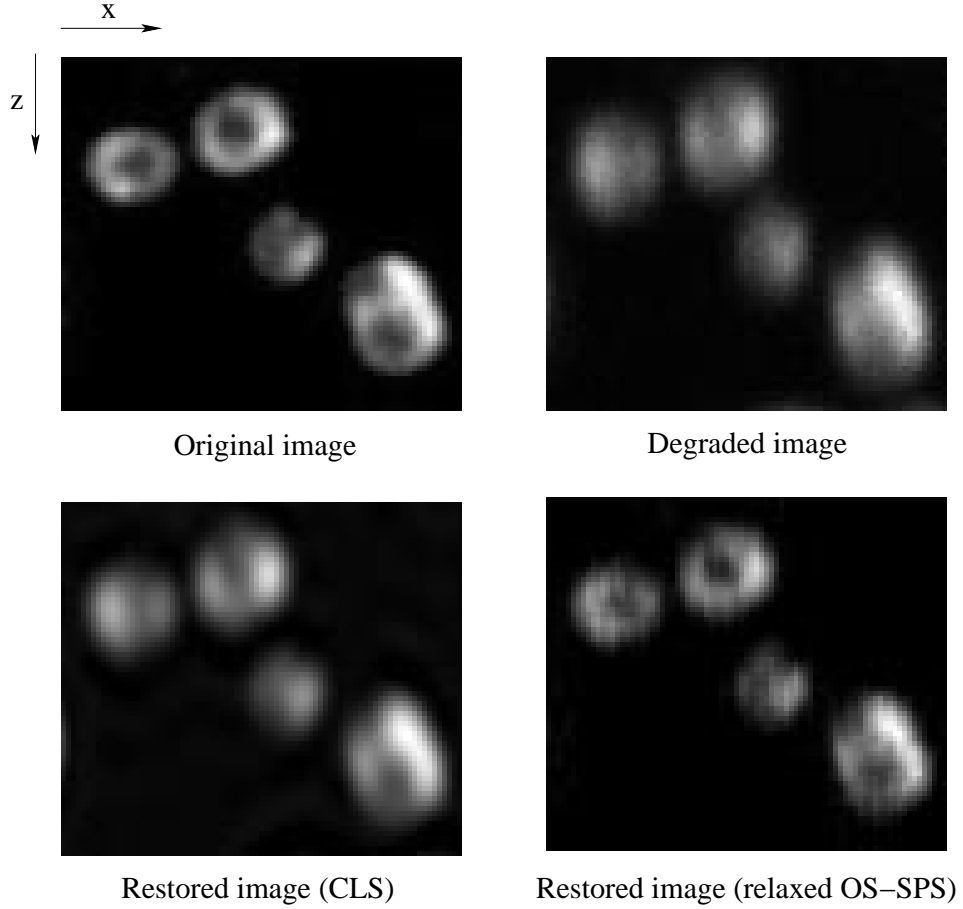


Figure 5.9: Zoom-in versions

of the Gaussian function that minimize the following term:

$$\min_{\sigma_x, \sigma_z} \|x^{\text{true}} * g_{\sigma_x, \sigma_z} - \hat{x}\|$$

where \hat{x} is the estimated image and g_{σ_x, σ_z} is the Gaussian function with standard deviations σ_x and σ_z in the x and z directions. The standard deviation corresponds to the half width of the peak at about 60% of the full height; therefore, it is related to the full width at half maximum (FWHM) as follows:

$$\text{FWHM} = 2\sigma\sqrt{2\ln 2} = 2.35\sigma.$$

We summarized the improvement in terms of FWHMs of restored images in Table 5.3.

Table 5.4 compares the elapsed time per iteration of different algorithms: De

Image	FWHM (μm)		% Improvement	
	in x	in z	in x	in z
Degraded image with no noise	0.12	0.52	-	-
Restored image with CLS	0.10	0.24	15 %	54 %
Restored image with relaxed OS-SPS for 50 iters	0.05	0.13	60 %	75 %
Restored image with relaxed OS-SPS for 5 iters	0.05	0.17	60 %	67 %

Table 5.3: Restoration improvement using FWHM

Algorithm	Time/iter (s)	Time Comparison	Number of FLOPs	FLOPs Comparison
DPEM	1.03	0.92	84,937,142	0.92
SPS	1.12	1	92,406,026	1
OS-SPS-2	1.23	1.10	92,522,010	1.00
OS-SPS-4	1.86	1.66	95,944,812	1.04
OS-SPS-8	3.65	3.26	102,919,258	1.11
OS-SPS-16	6.83	6.10	116,976,572	1.27

Table 5.4: Comparison of elapsed times per iteration and number of FLOPs for DPEM, SPS, and OS-SPS algorithms

Pierro’s modified EM (DPEM) [36], SPS (with optimal curvature), and relaxed OS-SPS (with precomputed curvature) algorithms. Theoretically, different subsets of the relaxed OS-SPS algorithm (with use of the convolution technique described in Subsection 5.5.2) should yield approximately the same computation time per iteration as the non-OS version. We were unable to achieve that invariance due to MATLAB overhead, but nevertheless the computation time per iteration increases less rapidly than the number of subsets. Another way to compare the complexity of the OS-SPS algorithm with the nonOS version is by calculating the number of floating-point operations (FLOPs). Table 5.4 shows that the number of FLOPs required in the OS-SPS algorithms differs only slightly from the number of FLOPs required in the SPS algorithm. This agrees with our discussion given in Subsection 5.5.2.

Figure 5.10 shows the objective increase, $\Phi(x^n) - \Phi(x^0)$, at each iteration of DPEM, SPS, ordinary OS-SPS (8 subsets), and relaxed OS-SPS (8 subsets) algo-

rithms. In this figure, both ordinary OS-SPS and relaxed OS-SPS algorithms increase the objective function faster than the DPEM algorithm by roughly the number of subsets. However, the relaxed OS-SPS algorithm is guaranteed to eventually converge to the optimal point, unlike the ordinary OS-SPS algorithm. Figure 5.11 compares the convergence rates for different numbers of subsets. The relaxed OS-SPS-16 yields the fastest convergence rate as expected. From Figure 5.10, the OS algorithms converge very rapidly compared with DPEM and SPS; therefore, we could stop the algorithms at the early iteration. Figure 5.12 shows the restored image at 5 iterations of relaxed OS-SPS.

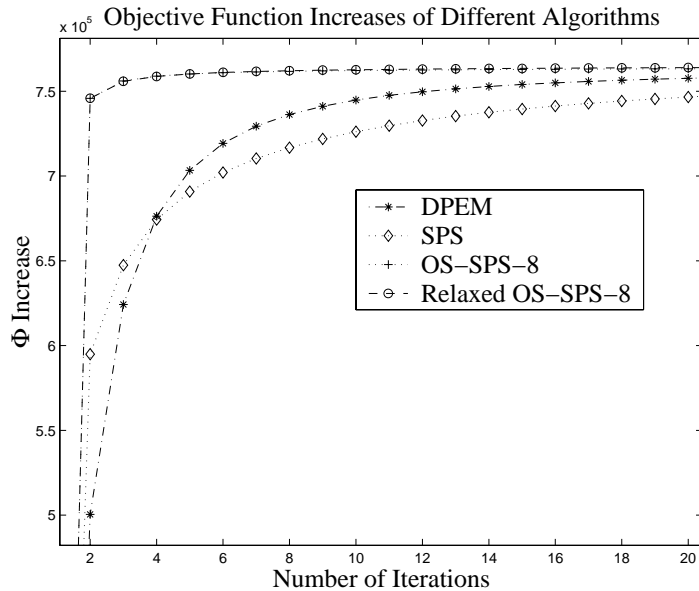


Figure 5.10: Comparison of objective function increases of DPEM, SPS, OS-SPS, and relaxed OS-SPS algorithms. OS-SPS-8 stands for the OS-SPS algorithm with 8 subsets. Both nonrelaxed and relaxed OS-SPS algorithms have order-of-magnitude acceleration over the DPEM and SPS algorithms.

5.6.2 Subset Design Analysis

Because one's choice of subsets can affect the convergence rate of the algorithm, we investigated the choices of subsets discussed in Section 5.4. Figure 5.13 shows

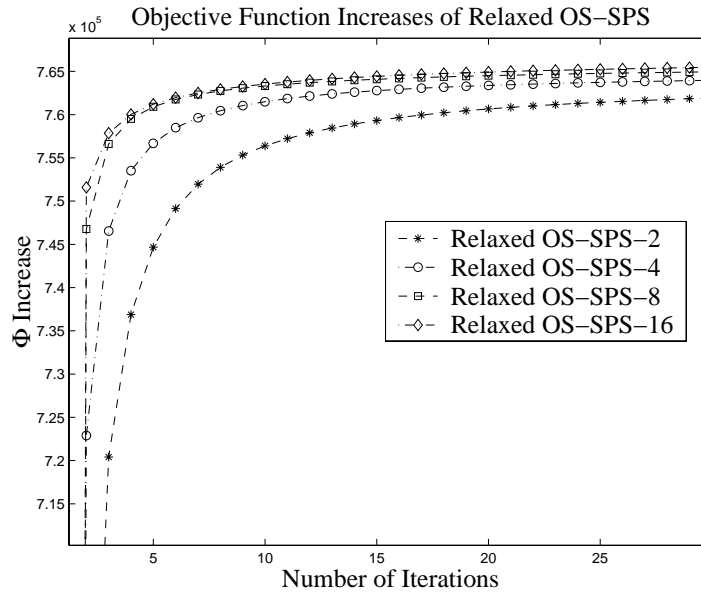


Figure 5.11: Comparison of objective function increase versus elapsed time of relaxed OS-SPS with different numbers of subsets. The 16-subset relaxed OS-SPS algorithm yielded the fastest convergence rate.

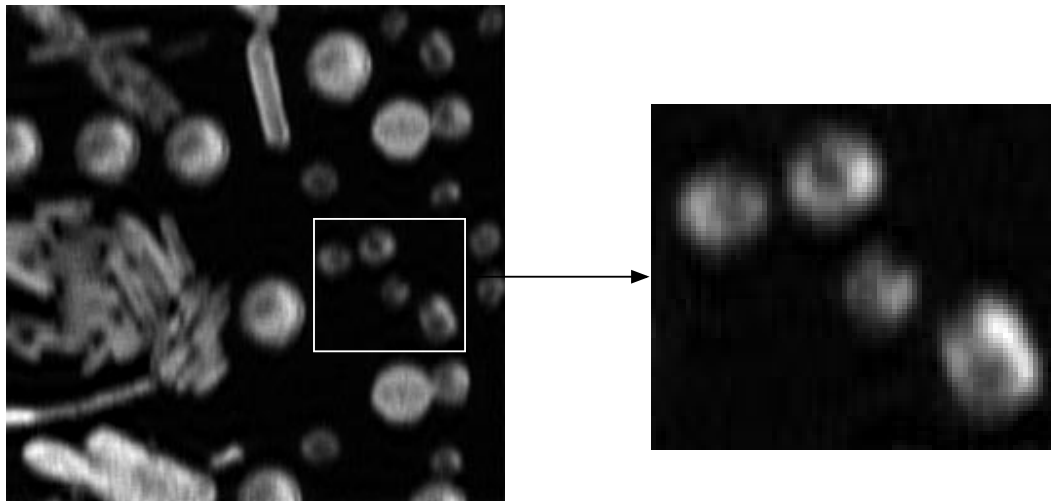


Figure 5.12: Restored image using 5 iterations of relaxed OS-SPS-8.

the objective increase versus iteration for different choices of subsets (Figures 5.2 and 5.4) with use of relaxed OS-SPS. The subsets with the subblock approach show a poor unpredictable behavior in the early iterations; however, due to relaxation, the relaxed OS-SPS algorithm with use of these subsets will eventually converge to the optimal point. However, the subblock approach does not yield an order-of-

magnitude acceleration in the early iterations. This unpredictable behavior is due to the violation of the “subset-gradient-balance” conditions.

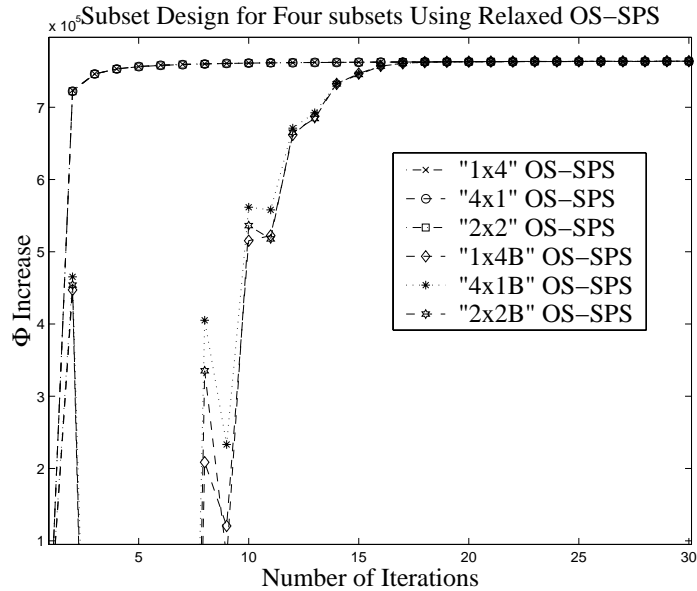


Figure 5.13: Comparison of different choices of subsets with use of the relaxed OS-SPS algorithm. The subset unbalance of relaxed OS-SPS with the subblock approach causes an unpredictable behavior of the objective function increase at the beginning of iterations but the algorithm eventually converges as a result of relaxation. The relaxed OS-SPS algorithms with the downsampling approach converge at almost the same rate for different choices of subsets.

Unlike the subblock approach, the downsampling approach provides an order-of-magnitude acceleration in the early iterations. Therefore, the downsampling approach is preferable. With the downsampling approach, different designs of subsets provided almost the same convergence rate and a similar number of FLOPs. Thus, the subset configuration does not affect the convergence rate much as long as the downsampling approach is used.

5.6.3 Limitation on the Number of Subsets

There exists a limit on the number of subsets that can yield the speedup factor by the number of subsets at early iterations. Figure 5.14 compares the order-of-

magnitude acceleration for different number of subsets when starting from different initial images. Figure 5.14(a) clearly shows the order-of-magnitude acceleration by a factor of the number of subsets at early iterations even with the 16-subset configuration. This is because the “subset-gradient-balance” conditions are still valid when the estimate is far from the solution. On the other hand, when the estimate is approaching the solution, using many subsets may no longer improve the acceleration at early iterations. Figure 5.14(b) illustrates that the order-of-magnitude acceleration starts to decrease at the 4-subset configuration.

5.6.4 Real Confocal Data

To restore an approximation of the original image from real data, we need to determine the PSF of the system and the mean of the dark current and background noise. Thus, we first discuss how to obtain these parameters and then apply image restoration. Since the experimental PSF tends to provide a more accurate estimation of the true system PSF than the theoretical PSF, we measure the experimental PSF by imaging small fluorescent microsphere beads with the same setting as the cell image. The Argon gas laser was used to produce the 488 nm wavelength (blue light) to excite the fluorescent agent (FITC) that emits the green light (around 520 nm in wavelength). We used the microsphere beads with the size of $0.175\ \mu\text{m}$ in diameter, the objective lens with the magnification of 63x and the NA of 1.2, and the detector pinhole size of $112\ \mu\text{m}$. The in-plane spacing and the z step size were set to $0.14\ \mu\text{m}$. A slice of the bead image is shown in Figure 5.15. Since the bead image contains noise, the PSFs at different locations may not be exactly the same. Due to small differences in FWHM of these PSFs, we assumed that the space-invariance of the system and averaged the beads that are similar in the intensity to yield a single

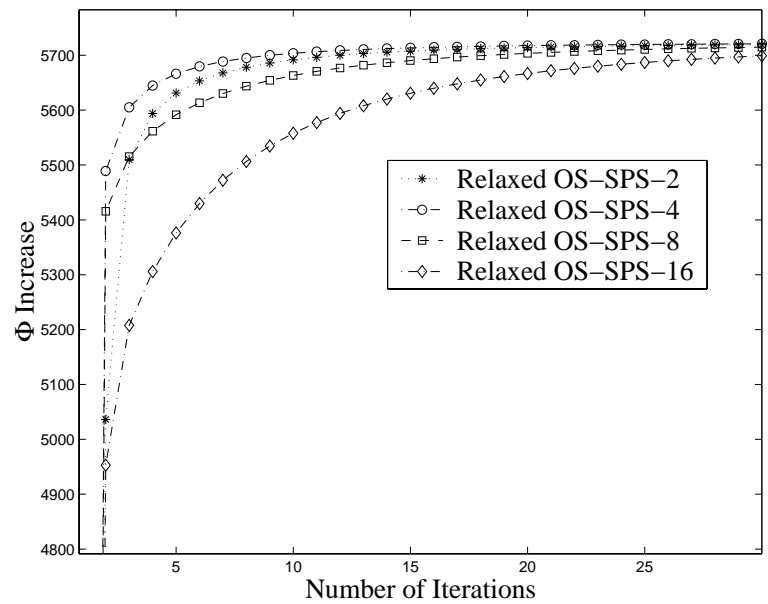
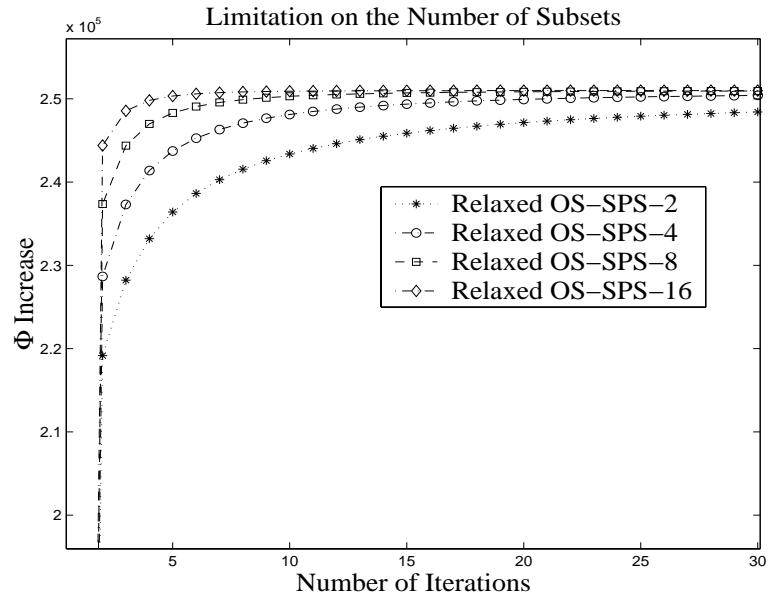


Figure 5.14: Illustration of limitation on the number of subsets when using different initial images. (a) When the initial image is far from the solution, the 16-subset case provides the fastest convergence. (b) When the initial image is close to the solution, the 4-subset case converges faster than the 8-subset and 16-subset ones.

system PSF for use in restoration. The 3-D measured PSF is shown in Figures 5.16-5.17. The FWHMs of the central lobe are approximately $0.31\ \mu\text{m}$, $0.33\ \mu\text{m}$, and $0.90\ \mu\text{m}$ in the x , y , and z directions, respectively. As expected, elongation appears along the z direction and the size of the first lobe at each slice increases as it moves away from the central slice.



Figure 5.15: Bead image

The dark current can be measured through the image of the blank scan when no light is present. We approximated the mean of the dark current and background noise, b_i , from the mean of the blank scan. Having calculated all parameters needed, we applied image restoration techniques on the $256 \times 256 \times 64$ confocal image of a breast cancer cell showing actin filaments in Figure 5.18(a). Figure 5.18(b) shows the restored images of one xy plane and one yz plane using the CLS method with the regularization parameter $\alpha = 1$. Figure 5.18(c) shows the iterative algorithms from the restoration software called Volocity for 5 iterations. For this image, running this software for more than 5 iterations produced a noisier image. This iterative algorithm is based on the maximum entropy technique. Note that the very bright

spots appear because only 8-bit exporting option is available. Figure 5.18(d) shows 2-D restoration with the 2-D PSF obtained from the central slice of the 3-D PSF. In this case, the relaxed OS-SPS algorithm was performed at each slice of the cell image for 15 iterations. This approach barely improves the axial resolution. Figure 5.18(e) shows 3-D restoration using the relaxed OS-SPS algorithm for 15 iterations. The 3-D relaxed OS-SPS algorithm provides the highest quality image compared with other techniques: actin filaments become more distinct and show more detail than other restored images. Moreover, the resolution is improved in the z direction. This can be shown in Figures 5.19 and 5.20 by plotting the z profiles from xz images in Figure 5.18. Since the true object is unknown, a similar technique used for measuring FWHM improvement as in the simulation data is unavailable.

5.7 Conclusions for the Relaxed OS-SPS Algorithm

In this chapter, we demonstrated that the relaxed OS-SPS algorithm, conventionally used for tomography, can be adapted for use in image restoration by choosing appropriate subsets of (measured) pixels. As long as the subsets are chosen by downsampling the pixels, different choices of subsets hardly affect the convergence rate of the algorithm. Similar to tomography, our method is able to achieve an order-of-magnitude acceleration over the non-OS algorithm by combining subsets that approximately satisfy our “subset-gradient-balance” conditions with appropriate scaling functions in the iterative update as shown in (5.12). The computational complexity of the OS-SPS algorithm with the convolution approach described in Subsection 5.5.2 is theoretically the same for any number of subsets. Although the FFT approach described in Subsection 5.5.3 increases the computational complexity of the algorithm when the number of subsets increases, the overall convergence rate is still

faster than that of the non-OS algorithm. In addition to the fast initial convergence and computational advantages of relaxed OS-SPS, the restoration results show the improvement in the resolution and the reduction of elongation in the z direction of confocal images.

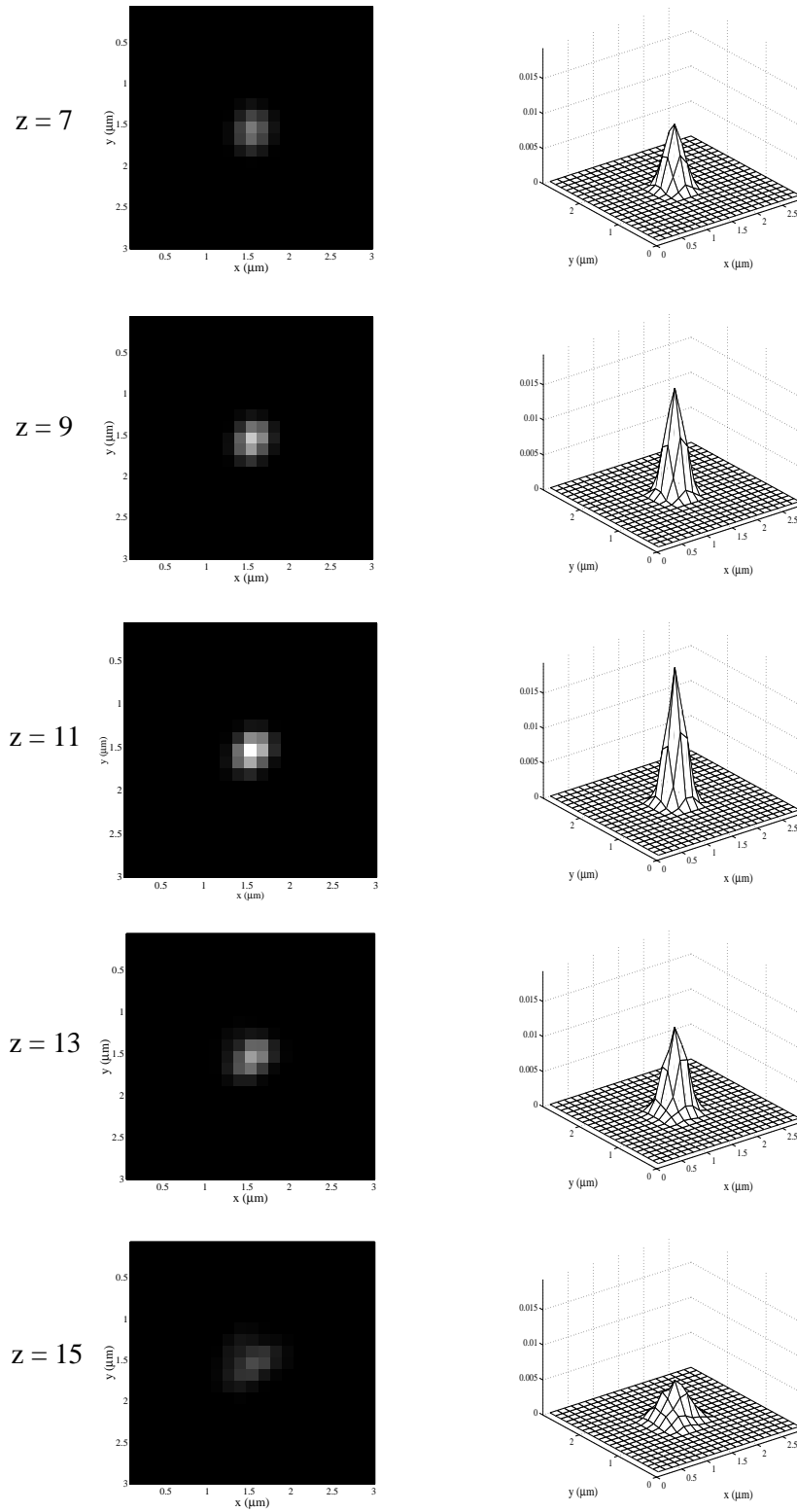


Figure 5.16: The $21 \times 21 \times 21$ measured PSF at different slices. The central slice is at slice 11.

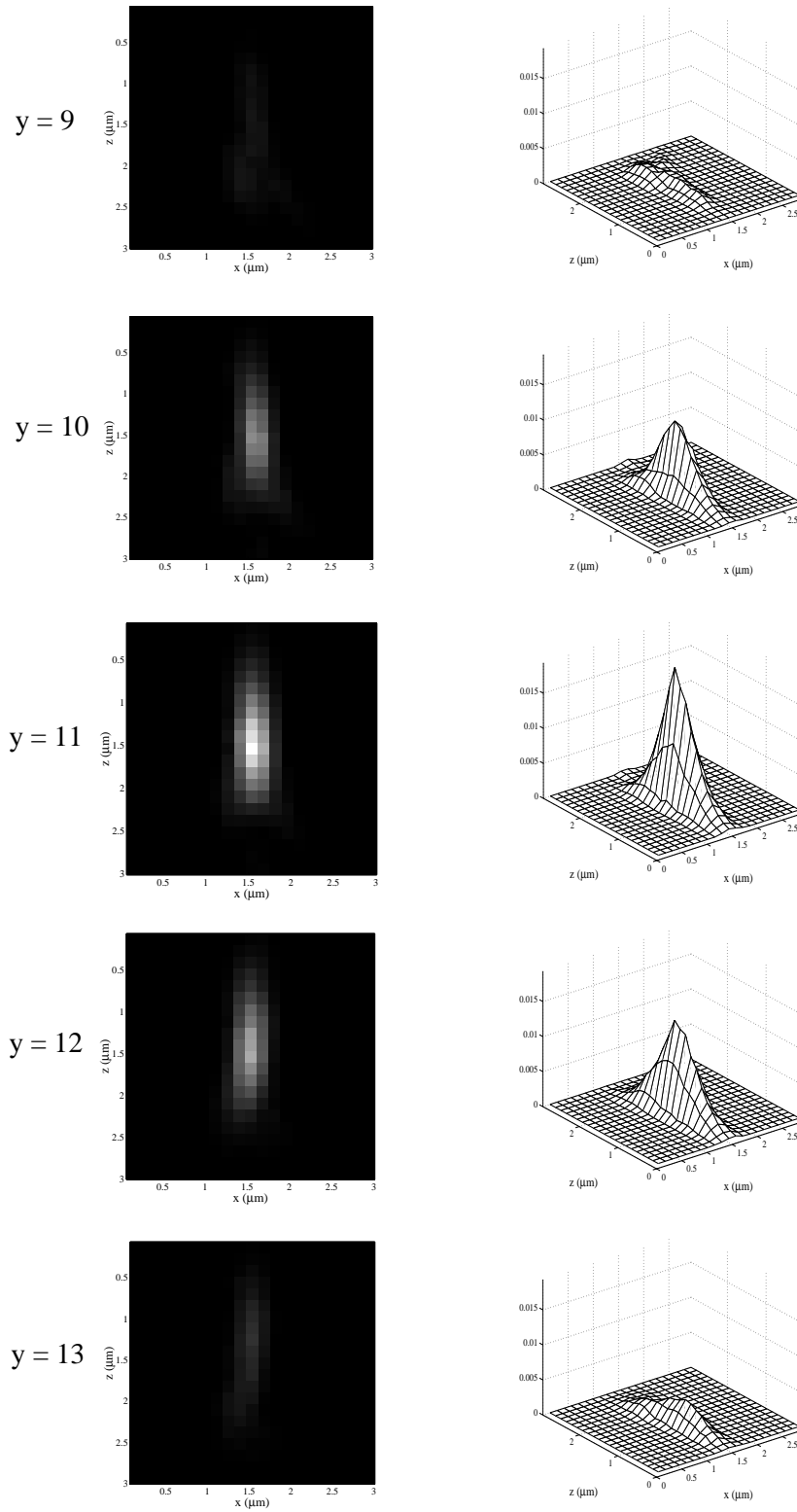


Figure 5.17: The $21 \times 21 \times 21$ Measured PSF at different y locations. The central slice is at slice 11.

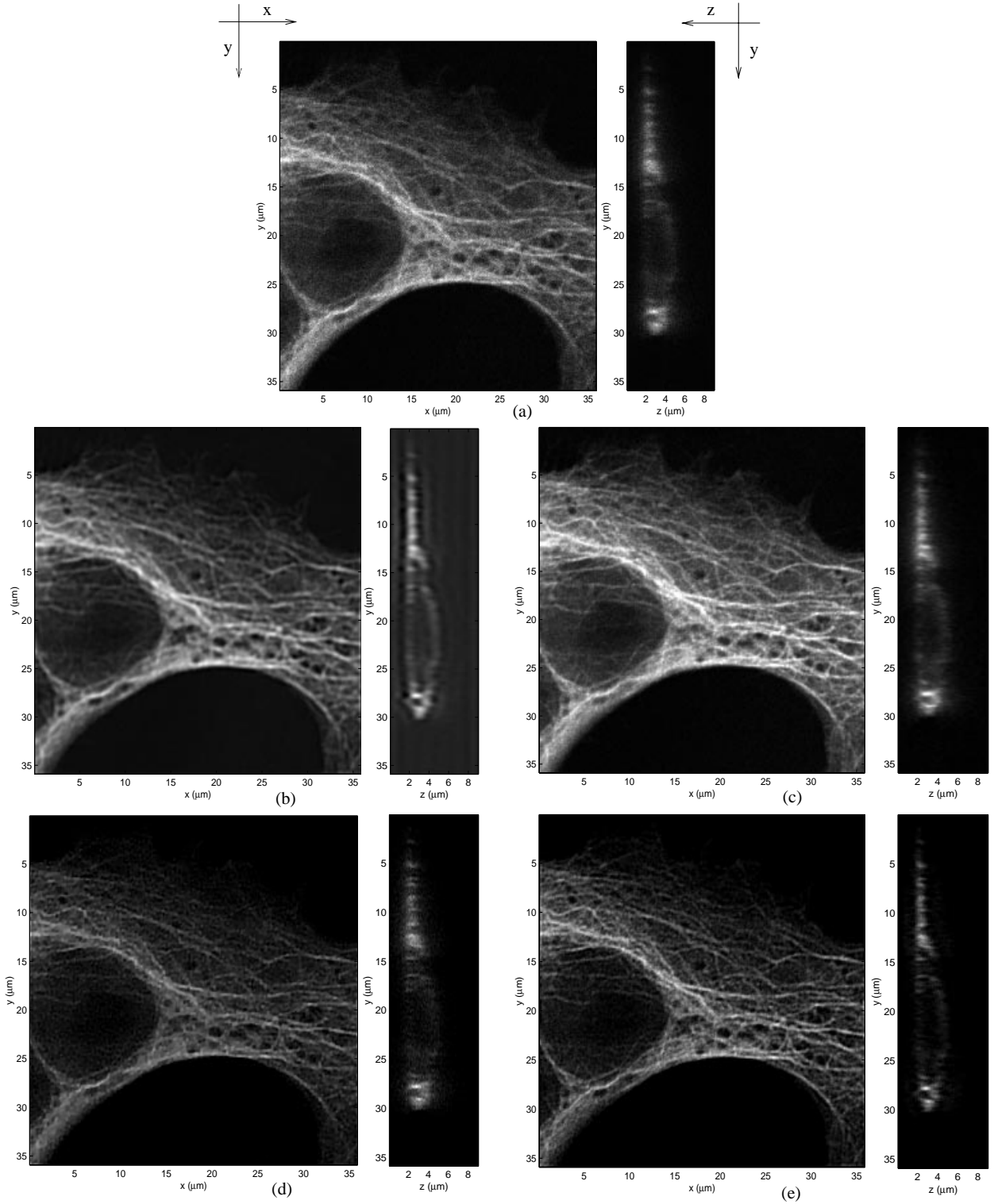


Figure 5.18: Noisy and restored images at $z = 2.38\mu\text{m}$ for xy images and at $x = 7\mu\text{m}$ for yz images. (a) Noisy cell images. Restored images using (b) CLS, (c) the iterative algorithm from Volocity software, (d) 2-D relaxed OS-SPS, and (e) 3-D relaxed OS-SPS.

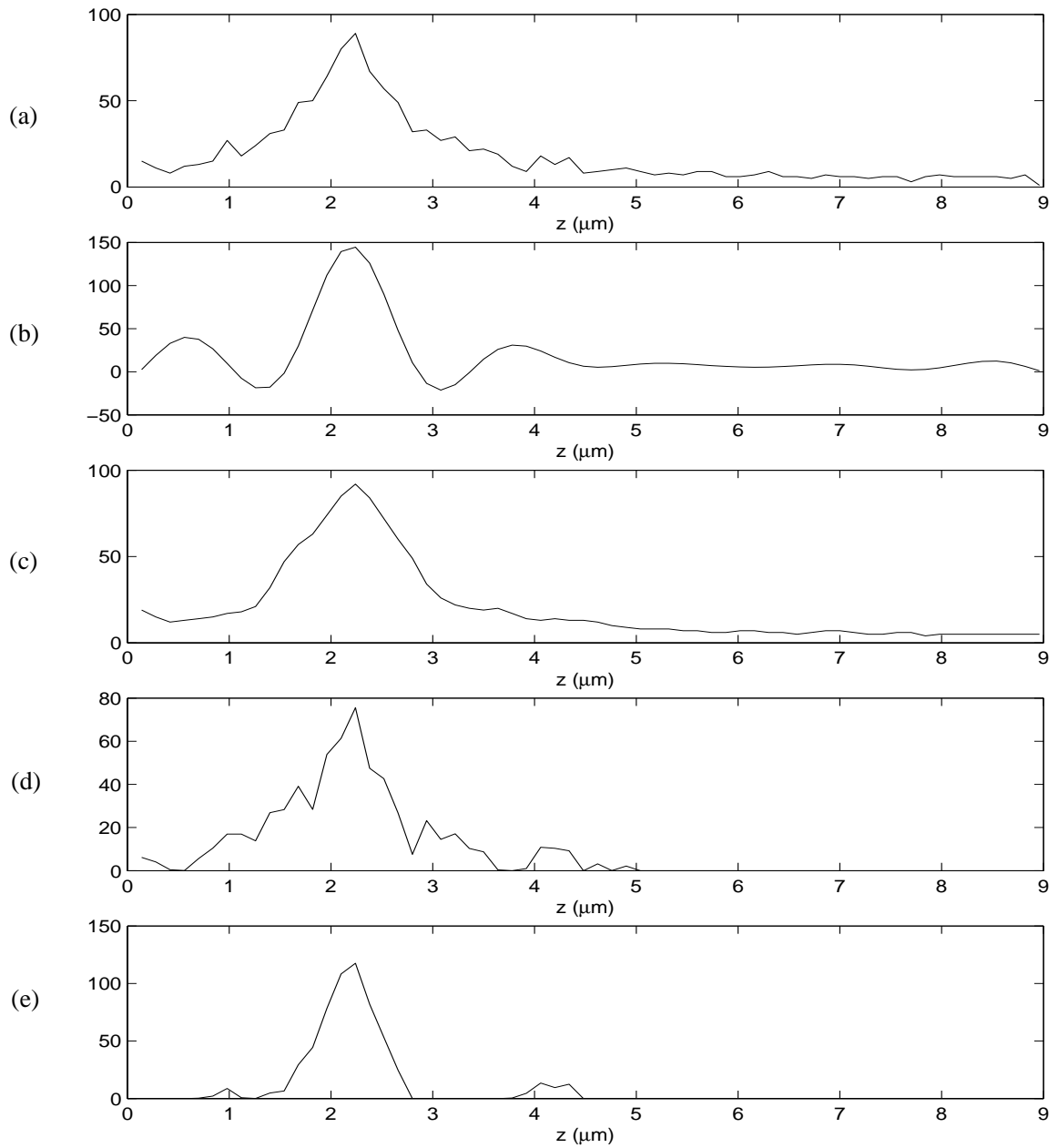


Figure 5.19: Profiles of noisy and restored images in the z direction at $x = 7\mu\text{m}$ and $y = 7\mu\text{m}$. (a) Noisy cell images. Restored images using (b) CLS, (c) the iterative algorithm from Volocity software, (d) 2-D relaxed OS-SPS, and (e) 3-D relaxed OS-SPS.

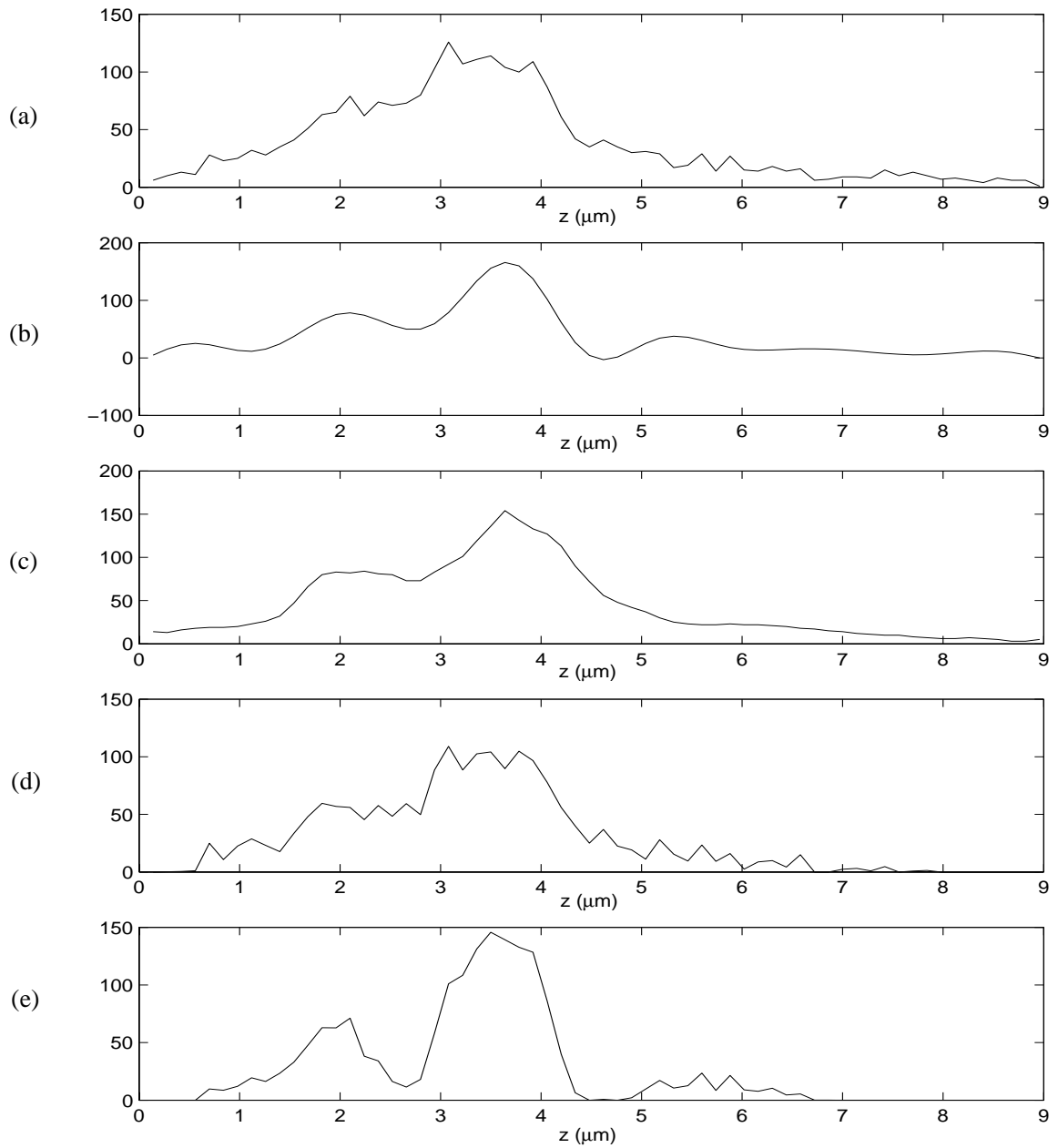


Figure 5.20: Profiles of noisy and restored images in the z direction at $x = 7\mu m$ and $y = 28.14\mu m$. (a) Noisy cell images. Restored images using (b) CLS, (c) the iterative algorithm from Volocity software, (d) 2-D relaxed OS-SPS, and (e) 3-D relaxed OS-SPS.

CHAPTER VI

Computational Comparison of Iterative Algorithms

In this dissertation, we have proposed two new, fast, iterative algorithms for image recovery. One might ask how these two algorithms compare with each other and with other existing iterative algorithms. In this chapter, we quantitatively compare the computational performance of different iterative converging algorithms, including EM, SPS, PSCA, PPCA, and relaxed OS-SPS for both space-variant and space-invariant systems. For fairness, we measure the computational complexity by calculating the total number of numerical operations required per iteration for each algorithm. Thus, the overall computational complexity is the product of the computational requirement per iteration and the number of iterations to converge.

6.1 Comparison of Algorithm Complexity

In this section, we compare the complexity requirement of iterative algorithms including EM, SPS, PSCA, PPCA, and relaxed OS-SPS algorithms in three different situations: space-variant, convolution-based space-invariant, and FFT-based space-invariant systems. All the complexity formulas calculated in this section are based on all the number of complex additions, subtractions, multiplications, and divisions

necessary for computing one iteration in an iterative algorithm.

To begin such a complexity calculation, we must first specify several parameters, including those representing the size of the image and those associated with specific algorithms. Let N be the total number of pixels in the object and data, N_f be the total number of FFT elements including the amount of zero padding, N_h be the total number of pixels for the PSF, K be the number of parallel processors, and M be the number of subsets. For space-variant systems, matrix multiplication is used for computing an expression like $l_i = \sum_{j=1}^N a_{ij}x_j, \forall i = 1, \dots, N$, which requires $2N^2 - N$ complex additions and multiplications. For space-invariant systems, the above expression can be computed with convolution or FFTs, and the total number of complex additions and multiplications required becomes $2N_hN - N$ for convolution and $N_f \log_2(2N_f^3)$ for FFTs (precomputing the FFT of the PSF). As discussed in previous chapters, although the PPCA and PSCA algorithms are not quite suitable for FFTs because of their sequential configurations, a partial FFT can be performed on the PPCA algorithm when computing the curvature of the likelihood function at each iteration. However, because FFTs cannot be used in other places in the algorithm, the PPCA algorithm with the partial FFT may not be as efficient as other algorithms, such as EM, SPS, and relaxed OS-SPS.

Tables 6.1-6.3 summarize the number of complex operations required for computing one iteration of the iterative algorithms discussed above, using matrix multiplication, convolution, and FFTs, respectively. Tables 6.4 and 6.5 show examples of complexity requirement for 2-D and 3-D cases. In both cases, we used 8 subsets ($M = 8$) in the relaxed OS-SPS algorithm, 4 processors ($K = 4$) in the PPCA algorithm, and no zero padding ($N_f = N$) in the FFT case. For the 2-D case, the image size was assigned to be 256×256 ($N = 256^2$), and the PSF size was assigned to be

15×15 ($N_h = 15^2$). For the 3-D case, the image size was assigned to be $256 \times 256 \times 256$ ($N = 256^3$), and the PSF size was assigned to be $15 \times 15 \times 15$ ($N_h = 15^3$). As shown in Tables 6.4 and 6.5, the PPCA algorithm requires the fewest number of complex operations for the space-variant and convolution-based space-invariant cases, while EM and SPS using precomputed curvatures require the fewest number of operations for the FFT-based space-invariant case. However, to determine the overall computation time, we need to consider the number of iterations needed to converge, or the convergence rate. Although the relaxed OS-SPS algorithm requires a higher degree of complexity than others, it provides fast initial convergence by a factor approximately equal to the number of subsets, and is suitable for parallel computing. Thus, relaxed OS-SPS might be comparable to PPCA for the space-variant and convolution-based space-invariant systems, and to EM and SPS with precomputed curvatures for the FFT-based space-invariant system.

Algorithm	Number of Operations
EM	$4N^2 + 2N$
SPS	$6N^2 + 10N$
SPS,P	$4N^2 + 3N$
PSCA	$7N^2 + 14N$
PSCA,P	$5N^2 + 8N$
PPCA	$7\frac{N^2}{K} + 4\frac{N}{K} + 11N$
PPCA,P	$5\frac{N^2}{K} + 4\frac{N}{K} + 4N$
Relaxed OS-SPS	$4N^2 + MN + 2N$

Table 6.1: Per-iteration complexity comparison of EM, SPS, PSCA, PPCA and relaxed OS-SPS algorithms for the space-variant case. The letter ‘‘P’’ after the name of the algorithm means that the precomputed curvature was used in the algorithm.

Algorithm	Number of Operations
EM	$4N_h N + 2N$
SPS	$6N_h N + 10N$
SPS,P	$4N_h N + 3N$
PSCA	$7N_h N + 14N$
PSCA,P	$5N_h N + 8N$
PPCA	$7N_h \frac{N}{K} + 4\frac{N}{K} + 11N$
PPCA,P	$5N_h \frac{N}{K} + 4\frac{N}{K} + 4N$
Relaxed OS-SPS	$4N_h N + MN + 2N$

Table 6.2: Per-iteration complexity comparison of EM, SPS, PSCA, PPCA and relaxed OS-SPS algorithms for the convolution-based space-invariant system. The letter ‘‘P’’ after the name of the algorithm means that the precomputed curvature was used in the algorithm.

Algorithm	Number of Operations
EM	$6N_f \log_2 N_f + 2N_f + 4N$
SPS	$9N_f \log_2 N_f + 3N_f + 13N$
SPS,P	$6N_f \log_2 N_f + 2N_f + 5N$
PPCA	$3\frac{N}{K} \log_2 \left(\frac{N}{K}\right) + 5N_h \frac{N}{K} + 6\frac{N}{K} + 11N$
PPCA,P	$5N_h \frac{N}{K} + 4\frac{N}{K} + 4N$
Relaxed OS-SPS	$MN_f \log_2(2N_f^3) + N_f \log_2 \left(\frac{N_f^3}{2M^3}\right) + 2MN_f + \frac{2N_f(M-1)}{M} + 3N + 2MN$

Table 6.3: Per-iteration complexity comparison of EM, SPS, PSCA, PPCA and relaxed OS-SPS algorithms for the FFT-based space-invariant system. The letter ‘‘P’’ after the name of the algorithm means that the precomputed curvature was used in the algorithm.

Algorithm	Number of Operations		
	Matrix Multiplication ($\times 10^{10}$)	Convolution ($\times 10^8$)	FFT ($\times 10^7$)
EM	1.72	0.59	0.67
SPS	2.58	0.89	1.05
SPS,P	1.72	0.59	0.68
PSCA	3.01	1.04	-
PSCA,P	2.15	0.74	-
PPCA	0.75	0.27	2.00
PPCA,P	0.54	0.19	1.88
Relaxed OS-SPS	1.72	0.60	3.06

Table 6.4: Quantitative comparison of the complexity per iteration of different algorithms in a 2-D case where $N = N_f = 256^2$, $N_h = 15^2$, $K = 4$, and $M = 8$.

Algorithm	Number of Operations		
	Matrix Multiplication ($\times 10^{10}$)	Convolution ($\times 10^8$)	FFT ($\times 10^7$)
EM	1.13	2.27	0.25
SPS	1.69	3.40	0.39
SPS,P	1.13	2.27	0.25
PSCA	3.01	1.04	-
PSCA,P	1.41	2.83	-
PPCA	0.49	0.99	7.13
PPCA,P	0.35	0.71	7.08
Relaxed OS-SPS	1.13	2.27	1.15

Table 6.5: Quantitative comparison of the complexity per iteration of different algorithms in a 3-D case where $N = N_f = 256^3$, $N_h = 15^3$, $K = 4$, and $M = 8$.

6.2 Comparison of Convergence Rates and Overall Computational Complexity

In this section, we compute the convergence rate of iterative algorithms, including EM, SPS, PSCA, PPCA, and relaxed OS-SPS, and then compare their overall computation time using convergence rates and complexity derived in Section 6.1.

To compare convergence rates and the overall computational complexity of different algorithms, we consider two different stages of convergence in this study. Because the relaxed OS-SPS algorithm has the fastest initial convergence of the algorithms shown in Figure 6.1, we could stop the algorithm after a few iterations or let it run until convergence to the optimal solution. Therefore, it would be interesting to study the behavior of other algorithms in meeting the same object value achieved by relaxed OS-SPS after only a few iterations, as well as after many iterations. In this study, we consider a 2-D simulation in which a 256×256 image was degraded by a 15×15 PSF and Poisson noise. The offset, b_i , was set to 5. The degraded image was used as an initial image. The regularization parameter, β , was set to 0.0001 and the edge-preserving parameter, δ , was set to 1. Figure 6.1 shows the plot of objective

function increase of EM, SPS, PSCA, PPCA, and relaxed OS-SPS for 50 iterations. Since the SPS algorithm using the optimal curvature converges very slowly due to a small offset value, we used the precomputed curvature for the SPS algorithm instead. However, for the PSCA and PPCA algorithms, we used the optimal curvature because it provides reasonable convergence rates. The relaxed OS-SPS algorithm with 8 subsets and the PPCA algorithm with 4 parallel processors were considered here.

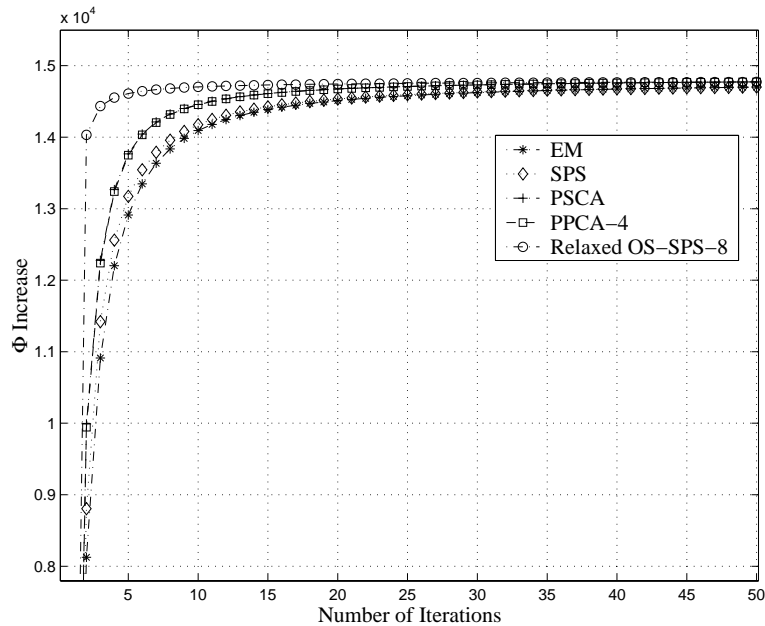


Figure 6.1: Comparison of objective function increase versus number of iterations using EM, SPS, PSCA, PPCA, and relaxed OS-SPS for 50 iterations. Note that the relaxed OS-SPS algorithm with 8 subsets achieves the fastest initial convergence.

In the first case, we compare the computational efficiency of relaxed OS-SPS after a few iterations with other iterative algorithms. Thus, we stop the OS-SPS algorithm after 5 iterations, and run the other algorithms until they reach the value of the objective increase at the 5th iteration of relaxed OS-SPS. Table 6.6 shows the convergence rate and overall computational complexity that is computed from the multiplication of the number of iterations and the total number of required operations

per iteration derived in Section 6.1. For this case, the relaxed OS-SPS algorithm requires the least overall computations for both convolution-based and FFT-based space-invariant systems, thus providing the fastest convergence. Although the PPCA algorithm in the convolution case requires more computations than the relaxed OS-SPS algorithm, we can increase the number of parallel processors to reduce the computational requirement, while maintaining a similar convergence rate. Figures 6.2 and 6.3 show the objective increase versus the normalized complexity based on the largest amount of overall computational requirements for the convolution-based and FFT-based space-invariant systems, respectively. These figures show that the relaxed OS-SPS algorithm converges faster than other algorithms in both cases, and the PPCA algorithm is not suitable for FFTs.

Algorithm	Number of Iterations to Converge	Overall Computational Complexity	
		Convolution ($\times 10^9$)	FFTs ($\times 10^8$)
EM	33	1.95	2.21
SPS	32	1.89	2.18
PSCA	17	1.77	-
PPCA	17	0.46	3.40
Relaxed OS-SPS	5	0.30	1.53

Table 6.6: Comparison of convergence rates and overall computational complexity of EM, SPS, PSCA, PPCA, and relaxed OS-SPS algorithms to achieve the same objective function increase obtained from relaxed OS-SPS-8 after only 5 iterations. The overall computational complexity was measured by the total number of numerical operations to converge.

In the second case, we compare the later stage of convergence in which convergence is defined as the smallest number of iteration, n , such that $\Phi(x^n) - \Phi(x^0) > 0.999(\Phi(x^*) - \Phi(x^0))$, where $\Phi(x^0)$ is the objective value of the initial image, and $\Phi(x^*)$ is the largest objective value among all iterative algorithms obtained in 50 iterations. For this case, the PPCA and PSCA algorithms have a slightly higher objective value at the 50th iteration than that of the relaxed OS-SPS algorithm.

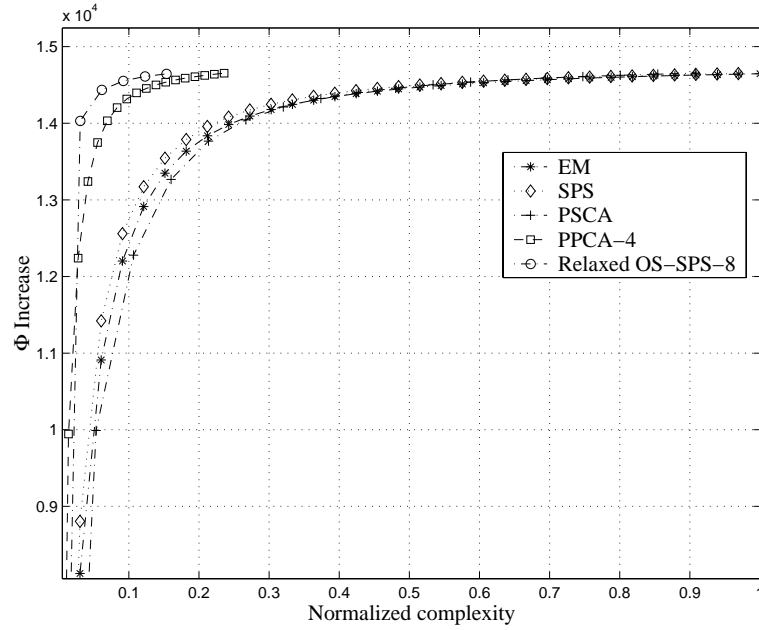


Figure 6.2: Comparison of objective function increase versus normalized complexity using EM, SPS, PSCA, PPCA and relaxed OS-SPS with convolution to achieve the same objective function increase obtained from relaxed OS-SPS-8 after only 5 iterations.

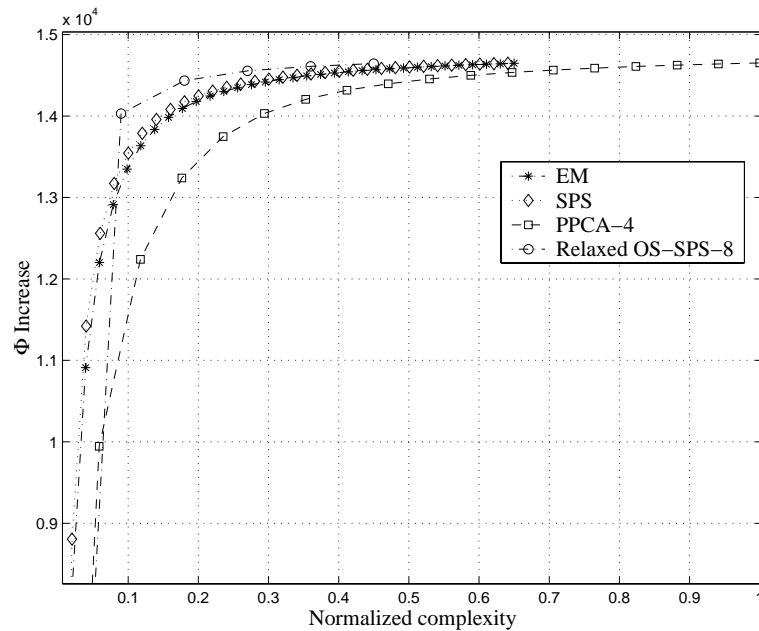


Figure 6.3: Comparison of objective function increase versus normalized complexity using EM, SPS, PSCA, PPCA and relaxed OS-SPS with FFT to achieve the same objective function increase obtained from relaxed OS-SPS-8 after only 5 iterations.

Table 6.7 shows the convergence rate and the overall computational complexity for convolution-based and FFT-based space-invariant systems. Although the relaxed OS-SPS algorithm still remains the fastest algorithm to converge, its overall computational complexity is no longer the smallest. The PPCA algorithm requires the fewest computations for the convolution-based space-invariant system, while the SPS and EM algorithms requires fewer computations than do the PPCA and relaxed OS-SPS algorithms. Figures 6.4 and 6.5 compare the overall computation of different algorithms in terms of normalized complexity. The relaxed OS-SPS algorithm becomes less efficient when running many iterations because the relaxation parameter reduces the algorithm step-size as it is getting close to the solution so that convergence is guaranteed. Owing to this reason, the PPCA algorithm eventually becomes the fastest as it approaches the optimal solution.

Algorithm	Number of Iterations to Converge	Overall Computational Complexity	
		Convolution ($\times 10^9$)	FFTs ($\times 10^8$)
EM	112	6.61	7.50
SPS	110	6.49	7.48
PSCA	40	4.16	-
PPCA	40	1.08	8.00
Relaxed OS-SPS	29	1.74	8.87

Table 6.7: Comparison of convergence rates and overall computational complexity of EM, SPS, PSCA, PPCA and relaxed OS-SPS algorithms to achieve the same objective function increase that approaches the optimal solution. The overall computational complexity was measured by the total number of numerical operations to converge.

To determine whether stopping the algorithm at the early stage of convergence is a good choice, we have to investigate the quality of the restored image. Figures 6.6(c) and 6.6(d) compare image quality at the 5th and 29th iterations of relaxed OS-SPS with 8 subsets. Both images dramatically improve the resolution and reduce most of the elongation that occurs in the vertical direction compared with the degraded

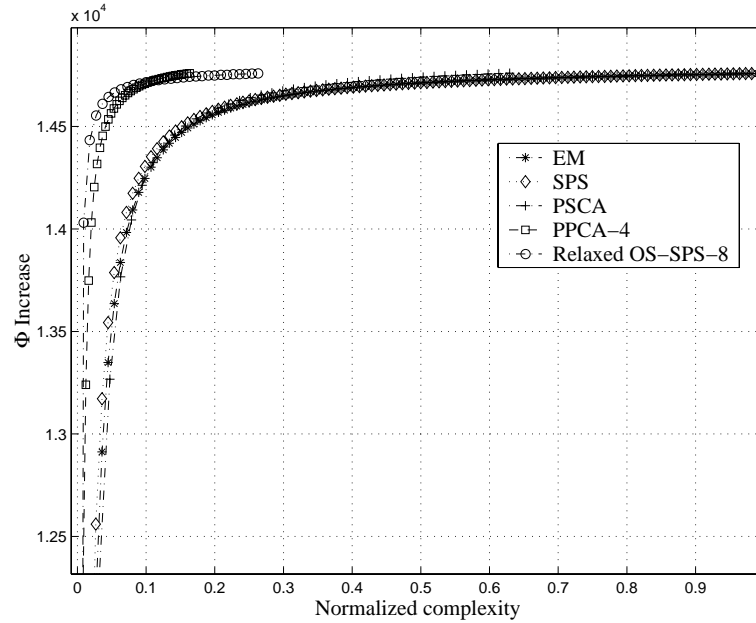


Figure 6.4: Comparison of objective function increase versus normalized complexity using EM, SPS, PSCA, PPCA, and relaxed OS-SPS with convolution to achieve the same objective function increase that approaches the optimal solution.

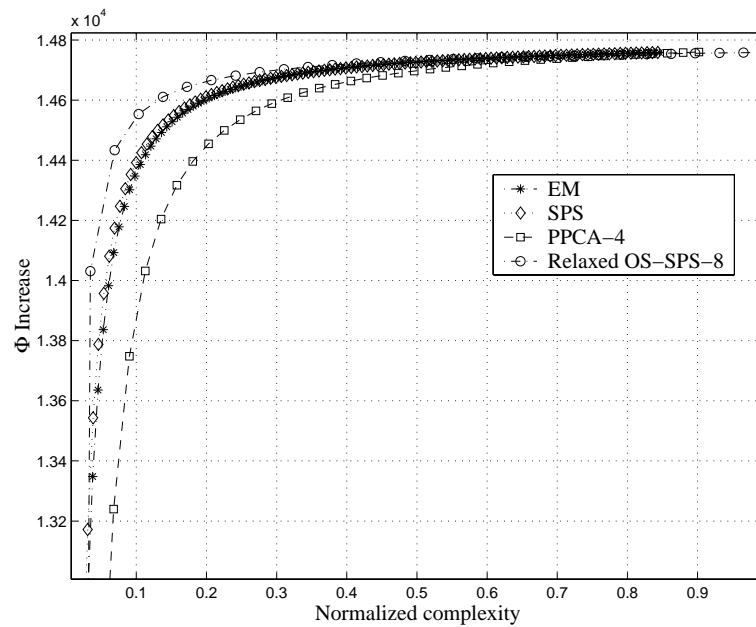
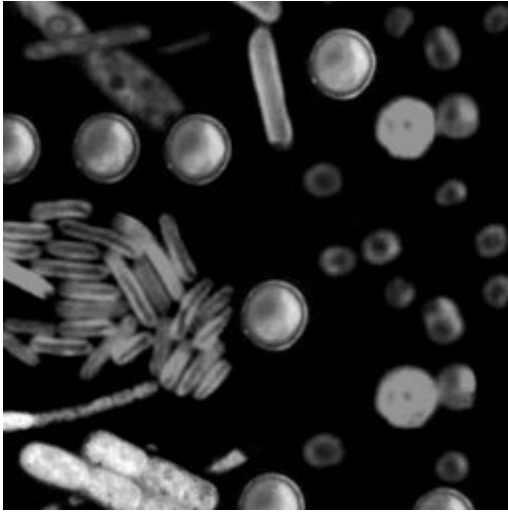
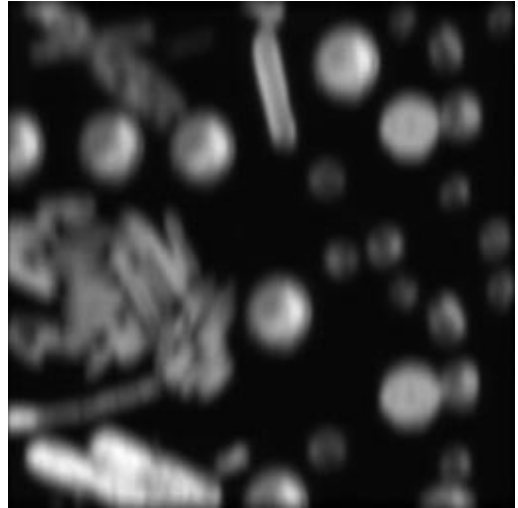


Figure 6.5: Comparison of objective function increase versus normalized complexity using EM, SPS, PSCA, PPCA, and relaxed OS-SPS with FFTs to achieve the same objective function increase that approaches the optimal solution.

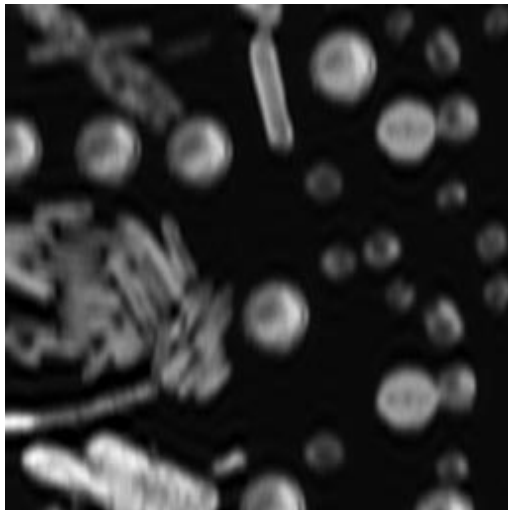
image (Figure 6.6(b)). Although the quality of the image at the 5th iteration of relaxed OS-SPS is not as good as that at the 29th iteration, using 5 iterations of relaxed OS-SPS provides a reasonably good image with much less computation than is needed for using 29 iterations of relaxed OS-SPS.



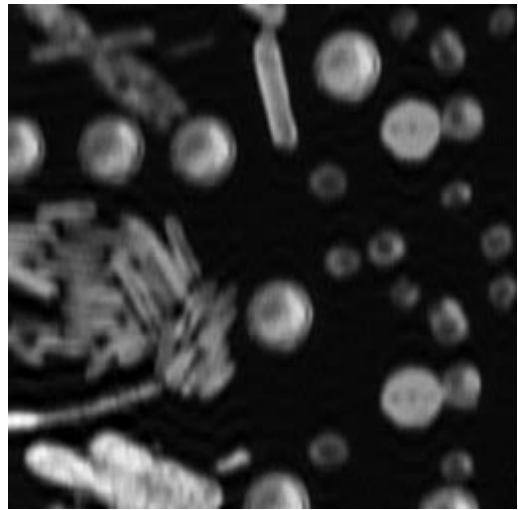
(a)



(b)



(c)



(d)

Figure 6.6: Restoration comparison at early and later iterations. (a) Original image. (b) Degraded image. (c) Restored image using relaxed OS-SPS-8 for 5 iterations. (d) Restored image using relaxed OS-SPS-8 for 29 iterations.

The overall computational complexity computed in this section considers only specific parameters of each iterative algorithm to illustrate its performance. The number of subsets in the relaxed OS-SPS algorithm and the number of parallel processors in the PPCA algorithm can be varied to increase the convergence rate or to reduce the number of computations. In addition to the PPCA algorithm, other parallelizable algorithms, including EM, SPS, and relaxed OS-SPS, can be implemented on parallel processors to reduce the required number of computations. Furthermore, the complexity requirement we computed focuses on the likelihood component part of the objective function and ignores the penalty part. Use of a penalty function in the relaxed OS-SPS algorithm can slow computation if the number of subsets is large, because it requires computing penalty terms many times in one iteration, which increases the computational complexity.

6.3 Conclusions for Computational Comparison

In this chapter, we have demonstrated the performance of the PPCA and relaxed OS-SPS algorithms compared with other iterative, converging algorithms. For space-variant and convolution-based space-invariant systems, the PPCA and relaxed OS-SPS algorithms are among the fastest algorithms available, depending on the convergence criteria. When the algorithms are compared for initial convergence only, the relaxed OS-SPS algorithm provides the fastest convergence rate and requires the least amount of computation time. Furthermore, this initial convergence of relaxed OS-SPS was shown to produce much improved restored images compared to the original degraded images. However, when the algorithms are iterated until convergence near the optimal solution, the PPCA algorithm may converge faster than the relaxed OS-SPS algorithm, due to the effect of relaxation on the relaxed OS-SPS algorithm,

and requires less computation time.

For the FFT-based space-invariant system, the relaxed OS-SPS, EM, and SPS algorithms are very comparable. The PPCA algorithm, however, has been shown to be unsuitable for FFT computing. Because of its fast initial convergence, the relaxed OS-SPS algorithm has a computational advantage over the EM and SPS algorithms in the first few iterations. Again, we demonstrated the improvement of the restored image after a few iterations of relaxed OS-SPS. However, running many iterations of relaxed OS-SPS using FFTs may result in an increase in computational expense relative to EM and SPS. To overcome this disadvantage of relaxed OS-SPS when performing many iterations, one should begin with the relaxed OS-SPS algorithm for a few iterations and then migrate to another algorithm, such as EM and SPS, for the remaining iterations.

CHAPTER VII

Statistical Image Reconstruction for Digital Holography

7.1 Introduction

In addition to the development of two new, fast, converging algorithms for PL image recovery problems in the previous chapters, in the last part¹ of this dissertation, we develop a novel statistical image reconstruction technique based on Poisson models for use in digital holography, including image plane holography. Instead of applying image restoration techniques on corrupted reconstructed holographic images as in confocal microscopy, we directly reconstruct holographic images with less degradation by using raw hologram data.

Holography is a technique for recording and reconstructing both the amplitude and phase of a wavefield. Conventional holography consists of two optical processes: recording and reconstructing. The recording process records the interference between the object and reference beams, which is regarded as a hologram, using a photographic material. The optical reconstruction process reconstructs the complex wavefield of the object by illuminating the recording medium with a wave that is similar to the original reference beam. This process generates the zero-order im-

¹This chapter is based on [112].

age and the twin images called the primary (virtual) and conjugate (real) images. In in-line holography invented by Gabor [50], the reconstructed holographic image suffers from an overlap of these three images, thus reducing the resolution and contrast of the image. To separate the primary image from other terms, Leith and Upatnieks [85] invented off-axis holography by introducing the reference beam at an angle with respect to the object beam. With this technique, the zero-order, primary and conjugate images appear at different locations, so each image can be observed separately.

Because the processes of optical recording on photographic film and optical reconstruction preparation in conventional holography are time consuming, digital recording of a hologram on a CCD camera and a numerical reconstruction of a complex object field on a computer become attractive alternatives and have been very useful in many applications [22,32,82,117,118,126]. In digital off-axis holography, the most common approach for extracting only the primary image in numerical reconstruction is to perform a digital “spatial filter” that selects only desirable spatial frequencies in the Fourier domain of a hologram [33]. The main drawbacks of this approach are the loss of high frequency components in the reconstructed holographic image and interference from other terms in the hologram, which can degrade the image quality. Phase-shifting or phase modulation [35,117,131] methods were proposed to suppress the zero-order and conjugate images, but they require at least three holograms to reconstruct one holographic image. The approach proposed in [87] retrieves the complex object beam by solving the system equation; however, no noise model was considered.

To overcome the drawbacks of existing approaches, in this chapter we propose a new numerical holographic reconstruction approach using a statistical technique.

This approach is attractive because the statistical model is based on the physical model of the optical system and statistical techniques have been shown to provide a good reconstruction in many applications [14, 25, 40, 65]. Statistical image reconstruction for digital holography can be formulated as an inverse problem in which we try to obtain a complex reconstructed holographic image from hologram intensity data that are real. Çetin *et al.* [20] proposed a statistical technique for Fourier holography and other coherent imaging applications. Their method was based on a Gaussian noise model and used a least-squares approach.

According to the digitally recording process of a hologram, our statistical model follows a Poisson distribution having the mean associated with a squared magnitude of the interference between the object and reference beams. Due to the ill-posed nature of image reconstruction, our statistical technique uses penalized-likelihood (PL) estimation. This optimization problem is very challenging because its negative log-likelihood function contains multiple global minimizers. Therefore, regularization is necessary to improve the problem conditioning and to reduce non-uniqueness. Moreover, we show that using two measured holograms can improve the results when reconstructing a complex holographic image with the same number of pixels as the recording device. (The use of two data sets to help estimate complex quantities has been applied in other optical problems [74, 92].)

In PL estimation, the unknown parameter vector, which represents the complex object field, is estimated by minimizing a cost function. Since closed-form solutions are unavailable, we need an iterative algorithm to solve the problem. However, for a gradient-based iterative algorithm, directly minimizing the cost function in the Poisson model is difficult. Therefore, to simplify the optimization problem, our proposed statistical image reconstruction approach is based on the use of optimization

transfer and convexity techniques by finding a surrogate function that lies inside the original cost function. Instead of minimizing the cost function, we minimize the surrogate function using an iterative algorithm, such as the separable-paraboloidal-surrogate [40, 109] or conjugate gradient algorithm. These methods monotonically decrease the cost function, thus ensuring convergence to a local minimizer.

In this study, we demonstrate our statistical holographic reconstruction for digital holography through image plane holography. However, the proposed technique can also be applied to phase retrieval problems and Fourier holography when the system matrix represents the Fourier transform, and to Fresnel holography when the system matrix represents the Fresnel transform.

This chapter is organized as follows. Section 7.2 describes the measurement model of a digitally recorded hologram. Section 7.3 reviews conventional numerical reconstruction using a spatial filtering technique applied in the frequency domain. Section 7.4 proposes a statistical model for digital holography and introduces a new statistical holographic reconstruction technique based on PL estimation. Section 7.5 derives the surrogate functions and the iterative algorithms for holographic image reconstruction. Section 7.6 compares different holographic reconstructed images using our statistical approach with the conventional reconstruction approach. Finally, conclusions are given in Section 7.7.

7.2 Measurement Model of Digital Holography

A detailed measurement model of digital holography is discussed previously in Chapter III; therefore, we review only the general idea here. For conventional holography, the interference between the object and reference beams at the recording plane

has the following continuous-space intensity:

$$\begin{aligned} I(\vec{r}) &= |u_o(\vec{r}) + u_{\text{ref}}(\vec{r})|^2 \\ &= |u_o(\vec{r})|^2 + |u_{\text{ref}}(\vec{r})|^2 + u_o(\vec{r})u_{\text{ref}}^*(\vec{r}) + u_o^*(\vec{r})u_{\text{ref}}(\vec{r}) \end{aligned} \quad (7.1)$$

where u_o denotes the (unknown) object beam, u_{ref} denotes the (known) reference beam, \vec{r} denotes 2-D spatial coordinates, and $*$ stands for the complex conjugate. For off-axis holography, the reference beam is oriented at some angle resulting in a known spatial carrier frequency denoted by $\vec{\alpha}$. An example of such a reference beam is a plane wave that is tilted by an angle θ with respect to the optical axis, i.e., $u_{\text{ref}}(\vec{r}) = \mathbf{U}_{\text{ref}} \exp\{-i2\pi\vec{r} \cdot \vec{\alpha}\}$ and $\vec{\alpha} = \frac{\sin\theta}{\lambda}$ where \mathbf{U}_{ref} is the amplitude of the reference wave and λ is the wavelength.

With digital holography, a discretized version of the recording intensity needs to be considered. Let $Y = [Y_1, \dots, Y_N]$ denote the hologram measurement data recorded on a CCD camera, where N is the number of measurement elements. Because the measurement data are usually noisy, we consider the measurement reported by the i th element of the CCD camera to be a random variable whose mean is modeled as follows:

$$\begin{aligned} \mathbb{E}[Y_i] &= |u_o(\vec{r}) + u_{\text{ref}}(\vec{r})|^2 + b_i \Big|_{\vec{r}=\vec{r}_i} \\ &= |[Ax]_i + u_i|^2 + b_i, \quad i = 1, \dots, N \end{aligned} \quad (7.2)$$

where x_j is the j th unknown complex parameter to be estimated, A is the system matrix which is the response of the object beam $u_o(\vec{r}_i)$ to the input x_j , u_i is the discretized reference beam, b_i is an offset due to effects such as dark current, and \vec{r}_i is the center location of the i th CCD element. For simplicity, we treat the CCD camera response as a Dirac impulse at the center of each element. The goal is to

estimate x from the measured Y_i 's, since x parameterizes the unknown object of interest.

7.3 Numerical Holographic Reconstruction Methods

This section reviews the conventional numerical reconstruction using a filtering method and introduces iterative reconstruction techniques.

7.3.1 Conventional Filtering Approach

The conventional numerical reconstruction approach for digital holography described here mainly focuses on image plane holography where the reconstructed image is produced directly from the data without further deconvolution. For digital Fresnel or Fourier holography, one more step of the Fresnel or Fourier transform is needed to yield the reconstructed image. The conventional numerical reconstruction approach involves the Fourier filtering method to extract either the primary or conjugate image corresponding to the last two terms of (7.1). This conventional approach to digital holography assumes that the reference beam is planar: $u_{\text{ref}}(\vec{r}) = \mathbf{U}_{\text{ref}} \exp\{-i2\pi\vec{r} \cdot \vec{\alpha}\}$. Substituting the plane wave of the reference beam into (7.1) and taking the Fourier transform, the spatial-frequency spectrum of the recorded interference pattern is converted into an angular spectrum of diffracted waves

$$\mathcal{I}(f) = \mathcal{I}_o(f) + \mathbf{U}_{\text{ref}}^2 \delta(f) + \mathbf{U}_{\text{ref}} \mathcal{U}_o(f - \vec{\alpha}) + \mathbf{U}_{\text{ref}} \mathcal{U}_o^*(-f - \vec{\alpha}) \quad (7.3)$$

where f denotes 2-D spatial frequencies, \mathcal{I}_o denotes the Fourier transform of the intensity of the object beam, and \mathcal{U}_o denotes the Fourier transform of the field of the object beam. The zero-order spectrum consists of the first two terms of (7.3) in which one desires to eliminate to improve the image quality. The two first-order spectra in the last two terms of (7.3) lead to the primary and conjugate images. Figure 7.1

shows an example of the magnitude of the Fourier transform of a hologram. In this figure, the spatial carrier frequency is in the x direction.

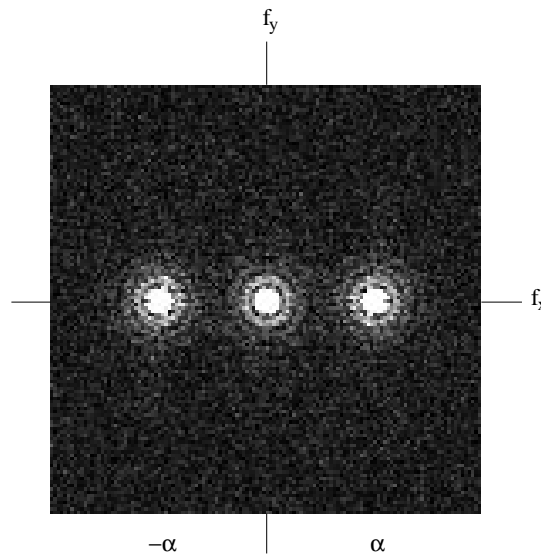


Figure 7.1: The magnitude of the Fourier transform of a hologram.

From Figure 7.1, a simple way to extract either the primary or conjugate image from other terms is by using a mask to select only one of the first-order spectra in the frequency domain of the hologram, and then taking the inverse Fourier transform. Because (7.3) consists of four terms and only one term is extracted, one might raise a question about the size of the image to be reconstructed or the amount of zero padding to be added. A common choice is to reconstruct the holographic image having the same size as the CCD array. Regardless of the size of the reconstructed image, the conventional numerical reconstruction approach can reduce the resolution of the reconstructed image due to the loss of high frequency components and the interference from the residual frequency components of other undesirable terms.

7.3.2 Iterative Reconstruction

Based on (7.2), iterative techniques can be used to estimate the complex object field from the measurement data. Unlike the filtering method, iterative techniques

use all the information in the model in (7.1), rather than discarding all but one of those terms. Furthermore, they do not require the plane wave assumption of the reference beam; therefore, they could work for both in-line and off-axis holography. As in the filtering method, reconstructing a complex holographic image whose size is more than half of the size of the CCD array may result in an under-determined problem. To avoid this problem, one should use the data whose size is twice the number of unknown parameters, i.e., $N = 2P$. Because measurement data usually contain noise, solving this inverse problem based on noisy data results in an ill-posed condition. One often employs regularization to remedy the condition of the problem. Due to noise in the system, a statistical noise model can be constructed to yield a more accurate model of the system, and an iterative algorithm used for estimating the object field depends on the corresponding noise model. Therefore, we will construct the statistical noise model for digital holography in the next section, and then develop an iterative algorithm for this holographic problem in the later section.

7.4 Statistical Model

In statistical techniques for inverse problems, one uses the statistical characteristics of the measurement system to design the noise model. The two major noise sources are light quanta statistics characterized by a Poisson distribution, and electronic readout noise characterized by a Gaussian distribution. Since Poisson distributed photon noise is the dominant source of noise in a CCD camera, for simplicity, we ignore the Gaussian noise and assume a Poisson distribution of background noise [104]. (Readout noise variance can be included in the b_i term if needed [104].) Thus we model the noisy measurement of the hologram recorded on a CCD camera

as a Poisson distribution with the mean described in (7.2):

$$Y_i \sim \text{Poisson}\{|[Ax]_i + u_i|^2 + b_i\}, \quad i = 1, \dots, N. \quad (7.4)$$

We assume that the system matrix (or the PSF), the reference beam and the background are known. Because the unknown image vector x is complex, the size of the data vector Y should be at least twice the number of elements of x , i.e., $N \geq 2P$, otherwise the problem will be under-determined. The system matrix A can represent an imaging system matrix as well as Fresnel and Fourier transforms. Thus for Fresnel and Fourier holography, the reconstructed image can be obtained in a single step and is free of the zero-order image and one of the twin images.

To reconstruct a holographic image, we specify a cost function to be minimized. Since image reconstruction is an ill-posed problem, we focus on PL estimation having the cost function in the following form:

$$\Phi(x) = L(x) + V(x) \quad (7.5)$$

where L denotes the negative log-likelihood function of the measurement, and V denotes the roughness penalty function.

The negative log-likelihood function corresponding to the model (7.4) is given by:

$$L(x) = \sum_{i=1}^N h_i([Ax]_i) \quad (7.6)$$

where the argument $l = l^R + \imath l^I$ for $h_i(l)$ is complex, and

$$h_i(l) = h_i(l^R, l^I) = -y_i \log(|l + u_i|^2 + b_i) + (|l + u_i|^2 + b_i) \quad (7.7)$$

ignoring irrelevant constants independent of x . The superscripts R and I indicate the real and imaginary parts, respectively. The measured values y_i 's that are real-valued are samples of independent Poisson random variables Y_i 's.

We consider penalty functions that penalize the differences between neighboring object pixels using the following form [109]:

$$V(x) = \beta \sum_{i=1}^r \psi([Cx]_i)$$

where ψ is a potential function, C is a penalty matrix, β is a regularization parameter that controls the degree of smoothness in the reconstructed image, and r is the number of pairs of neighboring object pixels. For the first-order neighborhood, the matrix C consists of horizontal and vertical neighbors.

Our goal is to estimate x by finding the minimizer of the cost function:

$$\hat{x} \triangleq \arg \min_x \Phi(x).$$

Since closed-form solutions for the minimizer are unavailable, one needs to apply an iterative algorithm.

7.5 The Algorithm

In this section, we approach the minimization problem by using optimization transfer and convexity techniques. These lead to an iterative algorithm that monotonically decreases the cost function and ensures convergence to a local minimum.

7.5.1 Optimization Transfer

Directly minimizing the cost function in (7.5) is difficult when h_i 's are non-quadratic. To simplify the optimization problem and to assure monotonic decreases in the cost function at each iteration, one can apply an optimization transfer approach by finding a “surrogate” function ϕ that lies above the cost function [40, 42, 43, 109]. Therefore, we obtain the next estimate by minimizing the surrogate function instead:

$$x^{n+1} \triangleq \arg \min_x \phi(x; x^n) \tag{7.8}$$

where x^n denotes the estimate at the n th iteration.

Choosing a surrogate function ϕ that satisfies the following monotonicity condition ensures that the iterates x^n will monotonically decrease the cost function Φ [40, 42, 43]:

$$\Phi(x^n) - \Phi(x) \geq \phi(x^n; x^n) - \phi(x; x^n), \quad \forall x \geq 0. \quad (7.9)$$

Instead of using the condition above, we choose a surrogate function $\phi(x; x^n)$ that satisfies the following sufficient conditions:

1. $\phi(x^n; x^n) = \Phi(x^n)$
 2. $\phi(x; x^n) \geq \Phi(x), \quad \forall x \in \mathbb{C}^P$
 3. $\left. \frac{\partial}{\partial x_j} \phi(x; x^n) \right|_{x=x^n} = \left. \frac{\partial}{\partial x_j} \Phi(x) \right|_{x=x^n}, \quad \forall j.$
- (7.10)

The next section presents the surrogate functions for the cost function given in (7.5).

7.5.2 Paraboloidal-Surrogate Functions

We first focus on the likelihood part. Since quadratic choices for the surrogate ϕ are particularly easy to minimize, our goal now is to find a parabola that lies above the negative log-likelihood function. Figure 7.2 illustrates the one-dimensional plot of the marginal cost function $h_i(l^R, 0)$. In this plot the marginal cost function has two optimal minima. However, a 2-D plot of $h_i(l^R, l^I)$ has multiple minimizers like a circle. Therefore, it is a challenging problem to find the correct optimal solution.

Since l and u_i are complex, we can rewrite $h_i(l)$ in (7.7) as follows:

$$\begin{aligned} h_i(l^R, l^I) &= -y_i \log \left(\alpha_i^{R,n} \left[\frac{(l^R + u_i^R)^2 + b_i/2}{\alpha_i^{R,n}} \right] + \alpha_i^{I,n} \left[\frac{(l^I + u_i^I)^2 + b_i/2}{\alpha_i^{I,n}} \right] \right) \\ &\quad + [(l^R + u_i^R)^2 + b_i/2] + [(l^I + u_i^I)^2 + b_i/2]. \end{aligned} \quad (7.11)$$

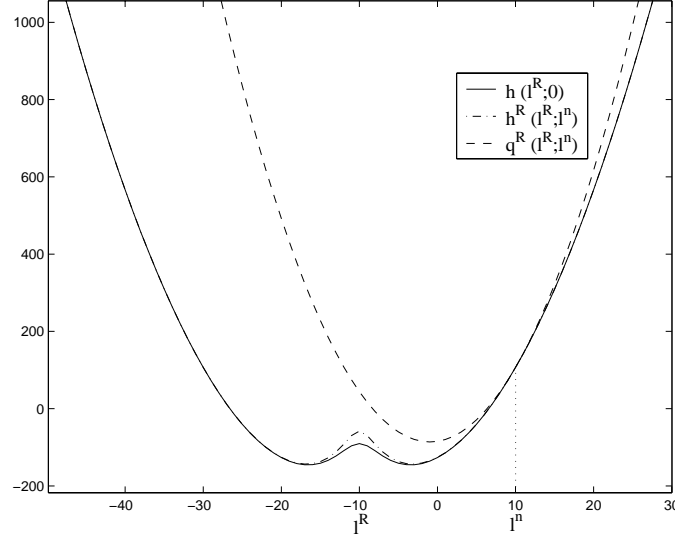


Figure 7.2: Illustration of the marginal cost, $h_i(l^R, 0)$, and surrogate functions as a function of l^R . The solid line is the original marginal cost function. The other two lines lying above the cost function are the surrogate functions. The function with the dashed line is called the paraboloidal surrogate function which has the same first derivative and the same point as the original cost function at $l = l^n$.

Because the negative log function is convex, we can apply De Pierro's multiplicative trick [36] to separate the real and imaginary parts by choosing $\alpha_i^{R,n} = \frac{(l^{R,n} + u_i^R)^2 + b_i/2}{k_i^n}$ and $\alpha_i^{I,n} = \frac{(l^{I,n} + u_i^I)^2 + b_i/2}{k_i^n}$, where $k_i^n = |l^n + u_i|^2 + b_i$ and $l^n = [Ax^n]_i$. Combining the fact that $\alpha_i^{R,n} + \alpha_i^{I,n} = 1$ with the convexity of h_i in (7.11) leads to our first surrogate function:

$$h_i(l) \leq h_i^R(l^R; l^n) + h_i^I(l^I; l^n)$$

where

$$h_i^R(l^R; l^n) \triangleq -y_i \alpha_i^{R,n} \log \left(\frac{(l^R + u_i^R)^2 + b_i/2}{\alpha_i^{R,n}} \right) + (l^R + u_i^R)^2 + b_i/2 \quad (7.12)$$

and

$$h_i^I(l^I; l^n) \triangleq -y_i \alpha_i^{I,n} \log \left(\frac{(l^I + u_i^I)^2 + b_i/2}{\alpha_i^{I,n}} \right) + (l^I + u_i^I)^2 + b_i/2. \quad (7.13)$$

The surrogates h_i^R and h_i^I each have two minima (see Figure 7.2) and are symmetric about the line $l = -u_i$. To facilitate the minimization in (7.8), we want to find parabolic surrogates that lie above these curves. A parabolic surrogate function for the real part has the following form:

$$q_i^R(l^R; l^n) = h_i^R(l^{R,n}; l^n) + \dot{h}_i^R(l^{R,n}; l^n)(l^R - l^{R,n}) + \frac{1}{2}c_i^R(l^R - l^{R,n})^2 \quad (7.14)$$

where \dot{h}_i^R is the first derivative of h_i^R and c_i^R is the curvature of the parabola q_i^R . This parabola has the same value as h_i^R at the current estimate $l^R = l^{R,n}$ and the same first derivatives at that point. A parabolic surrogate function for the imaginary part is denoted by $q_i^I(l^I, l^n)$ and has an analogous form.

According to the sufficient conditions in (7.10), we must choose the parabolas q_i^R and q_i^I to satisfy the following conditions:

1. $q_i^R(l^{R,n}; l^n) + q_i^I(l^{I,n}; l^n) = h_i^R(l^{R,n}; l^n) + h_i^I(l^{I,n}; l^n) = h_i(l^n)$
2. $q_i^R(l^R; l^n) + q_i^I(l^I; l^n) \geq h_i^R(l^R; l^n) + h_i^I(l^I; l^n), \quad \forall l^R, l^I$
3. $\dot{q}_i^R(l^{R,n}; l^n) + \dot{q}_i^I(l^{I,n}; l^n) = \dot{h}_i^R(l^{R,n}; l^n) + \dot{h}_i^I(l^{I,n}; l^n)$.

The first and third conditions are satisfied by the construction of q_i^R and q_i^I . The only remaining problem is to find curvatures c_i^R and c_i^I that satisfy the second conditions. For the fastest convergence rate [40], ideally we would choose the *smallest* curvature for which the second condition is satisfied. However, a closed-form solution for this optimal choice has proven elusive. Instead, we have chosen the curvatures using the following general expression:

$$c_i^o = \max_{l \in \mathbb{R}} \left\{ \frac{\dot{h}_i^o(l; l^n) - \dot{h}_i^o(l^{o,n}; l^n)}{l - l^{o,n}} \right\}, \quad (7.15)$$

where o represents the real and imaginary parts, R and I . Although this curvature is not optimal, it is proven in Appendix D that this choice leads to a parabolic

surrogate that is guaranteed to lie above the cost function. For the specific model given in (7.4), the curvatures in (7.15) have the following closed-form solution:

$$c_i^o = \frac{2y_i \sqrt{b_i^2 + 4(l^{o,n} + u_i^o)^2} (l^{o,n} + u_i^o)^2}{k_i^n \left\{ (l^{o,n} + u_i^o)^2 (b_i + 2) + b_i \left[b_i + \sqrt{b_i^2 + 4(l^{o,n} + u_i^o)^2} \right] \right\}} + 2. \quad (7.16)$$

A detailed derivation of the above expression is given in Appendix E.

Computing the curvature in (7.16) at every iteration may slow down the computation time. To avoid this issue, one can use a precomputed curvature. One simple option of the precomputed curvature is

$$c_i^{o,\text{pre}} = \max_{l^{o,n} \in \mathbb{R}} \max_{l \in \mathbb{R}} \left\{ \frac{\dot{h}_i^o(l; l^n) - \dot{h}_i^o(l^{o,n}; l^n)}{l - l^{o,n}} \right\}. \quad (7.17)$$

This basically becomes a 1-D problem because we have derived the closed-form solution for the inner maximum expression in (7.16). According to the proof in Appendix D, this precomputed curvature still provides a parabolic surrogate that always lies above the cost function. To compare this precomputed curvature with the iteratively calculated curvature in (7.16), we plot c_i^R in (7.16) as a function of l^R in Figure 7.3.

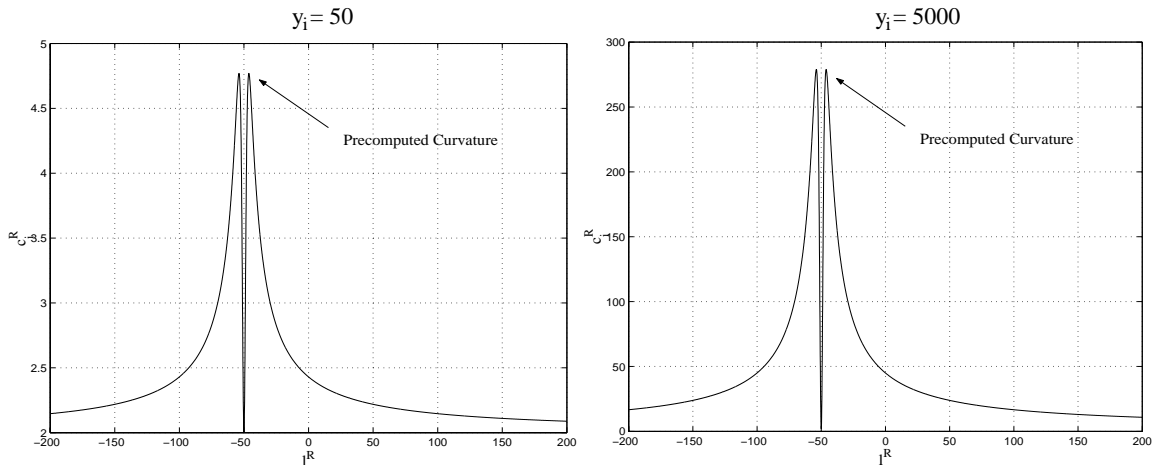


Figure 7.3: A plot of curvature c_i^R as a function of l^R at two different values of y_i .

The precomputed curvature evaluated at the maximum value of the curvature

in Figure 7.3 depends on the value of y_i . When y_i is small, then the precomputed curvature is not too different from other curvatures at different values of l^R . However, when y_i is large, then the precomputed curvature becomes too big for most values of l^R . Although, this may require many iterations to converge, the computation time per iteration is largely reduced. However, other choices of precomputed curvature can be considered to reduce the computation time and the number of iterations to converge.

The following inequalities summarizes the construction of the surrogate functions:

$$\begin{aligned}
L(x) &= \sum_{i=1}^N h_i([Ax]_i) \\
&\leq \sum_{i=1}^N h_i^R([Ax]_i^R; [Ax^n]_i) + h_i^I([Ax]_i^I; [Ax^n]_i) \\
&\leq \sum_{i=1}^N q_i^R([Ax]_i^R; [Ax^n]_i) + q_i^I([Ax]_i^I; [Ax^n]_i) \\
&\triangleq Q(x; x^n). \tag{7.18}
\end{aligned}$$

Since the likelihood surrogate function Q is quadratic, many algorithms could be applied to obtain the minimizer. This is simpler than directly minimizing the original cost function. In this chapter, we implement the separable-paraboloidal-surrogate (SPS) [40, 109] and conjugate gradient (CG) algorithms for this problem. The CG method can be applied easily because nonnegativity constraint is not enforced in this problem.

7.5.3 The Separable-Paraboloidal-Surrogate Algorithm

In this section, we derive the SPS algorithm for this specific model. To apply the SPS approach, we separate pixels by using the additive convexity technique developed by De Pierro [36] so that simultaneous updating can be performed. Thus,

we perform the additive convexity trick on q_i^R as follows:

$$\begin{aligned} q_i^R([Ax]_i^R; [Ax^n]_i) &= q_i^R \left(\sum_{j=1}^P \pi_{ij} \left[\frac{[a_{ij}(x_j - x_j^n)]^R}{\pi_{ij}} + [Ax^n]_i^R; [Ax^n]_i \right] \right) \\ &\leq \sum_{j=1}^P \pi_{ij} q_i^R \left(\frac{a_{ij}^R(x_j - x_j^n)^R - a_{ij}^I(x_j - x_j^n)^I}{\pi_{ij}} + [Ax^n]_i^R; [Ax^n]_i \right) \end{aligned}$$

where $\pi_{ij} \geq 0$ and $\sum_{j=1}^P \pi_{ij} = 1$. As in previous work [109], we chose $\pi_{ij} = \frac{|a_{ij}|}{\sum_{j=1}^P |a_{ij}|}$.

An analogous technique is applied to the parabola q_i^I for the imaginary part. Combining the real and imaginary parts, we finally obtain the following surrogate function:

$$Q(x, x^n) \leq \sum_{j=1}^P Q_j(x_j, x^n) = \sum_{j=1}^P Q_j^R(x_j^R, x_j^I; x^n) + Q_j^I(x_j^R, x_j^I; x^n)$$

where the separable-paraboloidal-surrogate function for the real part is

$$Q_j^R(x_j^R, x_j^I; x^n) = \sum_{i=1}^N \pi_{ij} q_i^R \left(\frac{a_{ij}^R(x_j - x_j^n)^R - a_{ij}^I(x_j - x_j^n)^I}{\pi_{ij}} + [Ax^n]_i^R; [Ax^n]_i \right)$$

and the separable-paraboloidal-surrogate function belonging to the imaginary part is

$$Q_j^I(x_j^R, x_j^I; x^n) = \sum_{i=1}^N \pi_{ij} q_i^I \left(\frac{a_{ij}^R(x_j - x_j^n)^I + a_{ij}^I(x_j - x_j^n)^R}{\pi_{ij}} + [Ax^n]_i^I; [Ax^n]_i \right).$$

To obtain the update at each iteration, these two functions are minimized instead of the original negative log-likelihood function. When no penalty is involved, we obtain the maximum-likelihood estimate which is derived in the next section.

7.5.4 Maximum-Likelihood Estimation

Since Q_j is a quadratic function of two variables: x_j^R and x_j^I , minimizing Q_j using Newton's method includes a 2×2 matrix-vector multiplication for each pixel as follows:

$$\begin{aligned} x_j^{n+1} &\triangleq \arg \min_{x_j} Q_j(x_j^R, x_j^I; x^n) \\ &= x_j^n - H_j^{-1} \nabla Q_j(x_j^n; x^n), \quad j = 1, \dots, P \end{aligned} \quad (7.19)$$

where the gradient of Q_j is

$$\begin{aligned}
\nabla Q_j(x_j^n; x^n) &= \left(\begin{array}{c} \frac{\partial Q_j^R}{\partial x_j^R} + \frac{\partial Q_j^I}{\partial x_j^R} \\ \frac{\partial Q_j^R}{\partial x_j^I} + \frac{\partial Q_j^I}{\partial x_j^I} \end{array} \right)_{x_j=x_j^n} \\
&= \left(\begin{array}{c} \sum_{i=1}^N a_{ij}^R \dot{h}_i^R([Ax^n]_i^R; [Ax^n]_i) + a_{ij}^I \dot{h}_i^I([Ax^n]_i^I; [Ax^n]_i) \\ \sum_{i=1}^N -a_{ij}^I \dot{h}_i^R([Ax^n]_i^R; [Ax^n]_i) + a_{ij}^R \dot{h}_i^I([Ax^n]_i^I; [Ax^n]_i) \end{array} \right) \\
&= \left(\begin{array}{c} \frac{\partial L(x)}{\partial x_j^R} \\ \frac{\partial L(x)}{\partial x_j^I} \end{array} \right)_{x=x^n} \triangleq \left(\begin{array}{c} \dot{L}_j^R \\ \dot{L}_j^I \end{array} \right)
\end{aligned}$$

and the j th 2×2 Hessian matrix, H_j , is

$$\begin{aligned}
H_j &\triangleq \begin{bmatrix} d_j^{RR} & d_j^{RI} \\ d_j^{IR} & d_j^{II} \end{bmatrix} = \begin{bmatrix} \frac{\partial^2 Q_j^R}{\partial (x_j^R)^2} + \frac{\partial^2 Q_j^I}{\partial (x_j^R)^2} & \frac{\partial^2 Q_j^R}{\partial x_j^R \partial x_j^I} + \frac{\partial^2 Q_j^I}{\partial x_j^R \partial x_j^I} \\ \frac{\partial^2 Q_j^R}{\partial x_j^I \partial x_j^R} + \frac{\partial^2 Q_j^I}{\partial x_j^I \partial x_j^R} & \frac{\partial^2 Q_j^R}{\partial (x_j^I)^2} + \frac{\partial^2 Q_j^I}{\partial (x_j^I)^2} \end{bmatrix}_{x_j=x_j^n} \\
&= \begin{bmatrix} \sum_{i=1}^N \frac{1}{\pi_{ij}} [(a_{ij}^R)^2 c_i^R + (a_{ij}^I)^2 c_i^I] & \sum_{i=1}^N \frac{a_{ij}^R a_{ij}^I}{\pi_{ij}} [-c_i^R + c_i^I] \\ \sum_{i=1}^N \frac{a_{ij}^R a_{ij}^I}{\pi_{ij}} [-c_i^R + c_i^I] & \sum_{i=1}^N \frac{1}{\pi_{ij}} [(a_{ij}^I)^2 c_i^R + (a_{ij}^R)^2 c_i^I] \end{bmatrix}.
\end{aligned}$$

After matrix multiplication, the explicit form for the update of the SPS algorithm simply becomes:

$$\begin{pmatrix} x_j^{R,n+1} \\ x_j^{I,n+1} \end{pmatrix} = \begin{pmatrix} x_j^{R,n} - \frac{1}{\det(H_j)} (d_j^{II} \dot{L}_j^R - d_j^{RI} \dot{L}_j^I) \\ x_j^{I,n} - \frac{1}{\det(H_j)} (-d_j^{RI} \dot{L}_j^R + d_j^{RR} \dot{L}_j^I) \end{pmatrix} \quad (7.20)$$

where the determinant of the Hessian matrix, H_j , is

$$\det(H_j) = d_j^{RR} d_j^{II} - (d_j^{RI})^2.$$

The surrogate functions derived in this section do not include the penalty function. Without regularization, a noisy image might be obtained after several iterations. Therefore, in the next section we derive the surrogate function for the penalty term in PL estimation. The derivation is an extension of our previous work [40, 109] to the case of complex images.

7.5.5 Penalty Surrogate Function and Penalized-Likelihood Estimation

Lacking any prior information that would relate the real and imaginary parts of the unknown image x , we employ separate penalty functions for the two parts. Since we separately penalize the real and imaginary parts, using different regularization parameters for the real and imaginary parts would provide more flexibility than having only one regularization parameter for both. Thus, the penalty function can be expressed in the following form:

$$V(x) = \beta^R \sum_{i=1}^r \psi([C^R x^R]_i) + \beta^I \sum_{i=1}^r \psi([C^I x^I]_i), \quad (7.21)$$

where C^R and C^I are the penalty matrices for the real and imaginary parts of the estimates, and β^R and β^I are the regularization parameters for the real and imaginary parts. To preserve edges, we use a nonquadratic potential function ψ of the following form [81]:

$$\psi(t) = \delta^2 \left[\left| \frac{t}{\delta} \right| - \log \left(1 + \left| \frac{t}{\delta} \right| \right) \right] \quad (7.22)$$

where δ is a user-specified parameter that controls the degree of edge preservation. The smaller δ , the stronger the degree of edge preservation.

Similar to the nonquadratic likelihood function, we derive the following surrogate functions:

$$V(x) \leq V'(x; x^n) \leq \sum_{j=1}^P S_j(x_j; x^n) \quad (7.23)$$

where V' is called the paraboloidal-surrogate function for the penalty function and S_j is called the separable-paraboloidal surrogate function for the penalty function. The first inequality is derived by forming a parabola that lies above the original penalty function and the second inequality is derived by using the convexity of ψ . If

a quadratic potential function is used instead, then the parabola step can be skipped.

The paraboloidal-surrogate function $V'(x; x^n)$ has the following form:

$$V'(x; x^n) = \beta^R \sum_{i=1}^r \varphi([C^R x^R]_i; [C^R x^{R,n}]_i) + \beta^I \sum_{i=1}^r \varphi([C^I x^I]_i; [C^I x^{I,n}]_i) \quad (7.24)$$

where the parabola φ is

$$\varphi(t; t^n) = \psi(t^n) + \dot{\psi}(t^n)(t - t^n) + \frac{1}{2}\omega(t^n)(t - t^n)^2 \quad (7.25)$$

and the curvature ω of the parabola [68] is

$$\omega(t) = \frac{\dot{\psi}(t)}{t}.$$

Since the paraboloidal-surrogate function V' is convex, we can apply the additive convexity technique developed by De Pierro [36] to obtain the separable-paraboloidal-surrogate function that lies above V' as follows:

$$\begin{aligned} S_j(x_j; x^n) &= S_j^R(x_j^R; x^n) + S_j^I(x_j^I; x^n) \\ &= \beta^R \sum_{i=1}^r \gamma_{ij}^R \varphi \left(\frac{c_{ij}^R (x_j - x_j^n)^R}{\gamma_{ij}^R} + [C^R x^{R,n}]_i; [C^R x^{R,n}]_i \right) \\ &\quad + \beta^I \sum_{i=1}^r \gamma_{ij}^I \varphi \left(\frac{c_{ij}^I (x_j - x_j^n)^I}{\gamma_{ij}^I} + [C^I x^{I,n}]_i; [C^I x^{I,n}]_i \right) \end{aligned} \quad (7.26)$$

and $\gamma_{ij}^o = \frac{|c_{ij}^o|}{\sum_{j=1}^P |c_{ij}^o|}$ where o represents R or I . From (7.25), the first derivative of φ evaluated at $t = t^n$ is $\dot{\psi}(t^n)$, thus the gradient of S_j is

$$\begin{aligned} \nabla S_j(x_j^n; x^n) &= \begin{pmatrix} \frac{\partial S_j^R}{\partial x_j^R} \\ \frac{\partial S_j^I}{\partial x_j^I} \end{pmatrix}_{x_j=x_j^n} = \begin{pmatrix} \beta^R \sum_{i=1}^r c_{ij}^R \dot{\psi}([C^R x^{R,n}]_i) \\ \beta^I \sum_{i=1}^r c_{ij}^I \dot{\psi}([C^I x^{I,n}]_i) \end{pmatrix} \\ &= \begin{pmatrix} \frac{\partial V(x)}{\partial x_j^R} \\ \frac{\partial V(x)}{\partial x_j^I} \end{pmatrix}_{x=x^n} \triangleq \begin{pmatrix} \dot{V}_j^R \\ \dot{V}_j^I \end{pmatrix}. \end{aligned}$$

Because there is no coupling between x_j^R and x_j^I in the penalty surrogate function, the Hessian matrix for S_j is diagonal:

$$\nabla^2 S_j(x_j^n; x^n) = \begin{bmatrix} p_j^{R,n} & 0 \\ 0 & p_j^{I,n} \end{bmatrix}$$

where

$$p_j^{o,n} = \frac{\partial^2 S_j^o}{\partial (x_j^o)^2} \Big|_{x_j=x_j^n} = \beta^o \sum_{i=1}^r \frac{(c_{ij}^o)^2 \dot{\psi}([C^o x^{o,n}]_i)}{\gamma_{ij}^o [C^o x^{o,n}]_i}.$$

To obtain the update of the SPS algorithm in PL estimation, we combine the surrogates for the likelihood and penalty. Thus, the surrogate function to be minimized becomes

$$\phi_j(x_j; x^n) = Q_j^R(x_j; x^n) + Q_j^I(x_j; x^n) + S_j^R(x_j^R; x^n) + S_j^I(x_j^I; x^n).$$

So the update x_j is obtained by:

$$x_j^{n+1} = \arg \min_{x_j} \phi_j(x_j; x^n).$$

Similar to (7.20), the update of the SPS algorithm with regularization becomes

$$\begin{pmatrix} x_j^{R,n+1} \\ x_j^{I,n+1} \end{pmatrix} = \begin{pmatrix} x_j^{R,n} \\ x_j^{I,n} \end{pmatrix} - \frac{1}{\det \tilde{H}_j} \begin{pmatrix} (d_j^{II} + p_j^R)(\dot{L}_j^R + \dot{V}_j^R) - d_j^{RI}(\dot{L}_j^I + \dot{V}_j^I) \\ -d_j^{RI}(\dot{L}_j^R + \dot{V}_j^R) + (d_j^{RR} + p_j^R)(\dot{L}_j^I + \dot{V}_j^I) \end{pmatrix} \quad (7.27)$$

where the new Hessian matrix \tilde{H}_j is

$$\tilde{H}_j = H_j + \begin{bmatrix} p_j^R & 0 \\ 0 & p_j^I \end{bmatrix}$$

and its determinant is

$$\det \tilde{H}_j = (d_j^{RR} + p_j^R)(d_j^{II} + p_j^I) - (d_j^{RI})^2.$$

The SPS algorithm outline for holographic image reconstruction is shown in Table 7.1.

\hat{x} = initial image
 $a_i = \sum_{j=1}^P |a_{ij}|, \quad \forall i = 1, \dots, N$
 for $n = 1, \dots, \text{Niters}$
 $\hat{l} = \sum_{j=1}^P a_{ij} \hat{x}_j, \quad \forall i = 1, \dots, N$
 $k_i^n = |\hat{l} + u_i|^2 + b_i, \quad \forall i = 1, \dots, N$
 $\hat{h}_i = \frac{-2y_i(\hat{l} + u_i)}{k_i^n} + 2(\hat{l} + u_i), \quad \forall i = 1, \dots, N$
 $c_i^R = 2 + \frac{2y_i \sqrt{b_i^2 + 4(\hat{l}^R + u_i^R)^2} (\hat{l}^R + u_i^R)^2}{k_i^n \{(\hat{l}^R + u_i^R)^2 (b_i + 2) + b_i [b_i + \sqrt{b_i^2 + 4(\hat{l}^R + u_i^R)^2}]\}}, \quad \forall i = 1, \dots, N$
 $c_i^I = 2 + \frac{2y_i \sqrt{b_i^2 + 4(\hat{l}^I + u_i^I)^2} (\hat{l}^I + u_i^I)^2}{k_i^n \{(\hat{l}^I + u_i^I)^2 (b_i + 2) + b_i [b_i + \sqrt{b_i^2 + 4(\hat{l}^I + u_i^I)^2}]\}}, \quad \forall i = 1, \dots, N$
 for $j = 1, \dots, P$
 $\dot{L}_j = \sum_{i=1}^N a_{ij}^* \dot{h}_i$
 $d_j^{RR} = \sum_{i=1}^N \frac{a_i}{|a_{ij}|} [(a_{ij}^R)^2 c_i^R + (a_{ij}^I)^2 c_i^I]$
 $d_j^{II} = \sum_{i=1}^N \frac{a_i}{|a_{ij}|} [(a_{ij}^I)^2 c_i^R + (a_{ij}^R)^2 c_i^I]$
 $d_j^{RI} = d_j^{IR} = \sum_{i=1}^N \frac{a_i a_{ij}^R a_{ij}^I}{|a_{ij}|} [-c_i^R + c_i^I]$
 $\dot{V}_j^R = \beta^R \sum_{i=1}^r c_{ij}^R \dot{\psi}([C^R \hat{x}^R]_i)$
 $\dot{V}_j^I = \beta^I \sum_{i=1}^r c_{ij}^I \dot{\psi}([C^I \hat{x}^I]_i)$
 $p_j^R = \beta^R \sum_{i=1}^r \frac{(c_{ij}^R)^2}{\gamma_{ij}^R} \dot{\psi}([C^R \hat{x}^R]_i)$
 $p_j^I = \beta^I \sum_{i=1}^r \frac{(c_{ij}^I)^2}{\gamma_{ij}^I} \dot{\psi}([C^I \hat{x}^I]_i)$
 $\det(H_j) = (d_j^{RR} + p_j^R)(d_j^{II} + p_j^I) - (d_j^{RI})^2$
 $\hat{x}_j^R = \hat{x}_j^R - \frac{1}{\det(H_j)} [(d_j^{II} + p_j^R)(\dot{L}_j^R + \dot{V}_j^R) - d_j^{RI}(\dot{L}_j^I + \dot{V}_j^I)]$
 $\hat{x}_j^I = \hat{x}_j^I - \frac{1}{\det(H_j)} [-d_j^{RI}(\dot{L}_j^R + \dot{V}_j^R) + (d_j^{II} + p_j^R)(\dot{L}_j^I + \dot{V}_j^I)]$
 end
 end

Table 7.1: The SPS algorithm outline for holographic reconstruction

7.5.6 The Conjugate Gradient Method

Without the nonnegativity constraint, the CG method can be applied easily to this problem; therefore, we derive the CG method in this section. For simplicity, we focus only on the likelihood part. The penalty part can follow the same concept as the SPS algorithm and is included in the algorithm outline. Starting from (7.18), we use CG to minimize the quadratic surrogate function Q .

The update x^{n+1} using CG can be obtained as follows:

$$\begin{pmatrix} x^{R,n+1} \\ x^{I,n+1} \end{pmatrix} = \begin{pmatrix} x^{R,n} \\ x^{I,n} \end{pmatrix} - \mu^n d^n \quad (7.28)$$

where μ^n is the step size at the n th iteration given by

$$\mu^n = \frac{-\dot{Q}^T d^n}{(d^n)^T \ddot{Q} d^n}, \quad (7.29)$$

T stands for complex transpose, d^n is the search direction at the n th iteration, and the gradient and Hessian matrices of Q are given by

$$\begin{aligned} \dot{Q} &\triangleq \begin{bmatrix} \frac{\partial Q}{\partial x^R} \\ \frac{\partial Q}{\partial x^I} \end{bmatrix}_{x=x^n} = \begin{bmatrix} (A^R)^T \dot{h}^R + (A^I)^T \dot{h}^I \\ -(A^I)^T \dot{h}^R + (A^R)^T \dot{h}^I \end{bmatrix} = \begin{bmatrix} \frac{\partial L}{\partial x^R} \\ \frac{\partial L}{\partial x^I} \end{bmatrix}_{x=x^n} = \dot{L} \\ \ddot{Q} &\triangleq \begin{bmatrix} \frac{\partial^2 Q}{\partial (x^R)^2} & \frac{\partial^2 Q}{\partial x^R \partial x^I} \\ \frac{\partial^2 Q}{\partial x^I \partial x^R} & \frac{\partial^2 Q}{\partial (x^I)^2} \end{bmatrix}_{x=x^n} \\ &= \begin{bmatrix} (A^R)^T D^R A^R + (A^I)^T D^I A^I & -(A^R)^T D^R A^I + (A^I)^T D^I A^R \\ -(A^I)^T D^R A^R + (A^R)^T D^I A^I & (A^I)^T D^R A^I + (A^R)^T D^I A^R \end{bmatrix}. \end{aligned}$$

Each entry along the diagonal of the diagonal matrix D^o consists of the curvature c_i^o in (7.15). The search direction d is initialized by $-\dot{Q}$ and iterated as follows:

$$\begin{aligned} d^{n+1} &= e^{n+1} + \xi^{n+1} d^n \\ \xi^{n+1} &= \max \left\{ 0, \frac{(e^{n+1})^T (e^{n+1} - e^n)}{(e^n)^T e^n} \right\} \end{aligned} \quad (7.30)$$

where the residual e is always set to the negation of the gradient: $e^n = -\dot{Q}^n$. Instead of computing the large Hessian matrix \ddot{Q} at every iteration in order to compute μ^n , we can simplify the evaluation of $(d^n)^T \ddot{Q} d^n$ as follows:

$$\begin{aligned} (d^n)^T \ddot{Q} d^n &= [(d_1^n)^T (A^R)^T - (d_2^n)^T (A^I)^T] D^R [A^R(d_1^n) - A^I(d_2^n)] + \\ &\quad [(d_1^n)^T (A^I)^T + (d_2^n)^T (A^R)^T] D^I [A^I(d_1^n) + A^R(d_2^n)] \end{aligned}$$

where d_1^n and d_2^n are the first and second halves of d^n . Although these derivation is only for the likelihood part, the penalty part can be derived in the similar manner as the SPS algorithm discussed above. The algorithm outline for penalized-likelihood holographic reconstruction using the CG method are summarized in Table 7.2.

\hat{x} = initial image	
$d = -[\dot{L}^R + \dot{V}^R; \dot{L}^I + \dot{V}^I]$	
$e = d$	
for $n = 1, \dots, \text{Niters}$	
$\hat{l} = \sum_{j=1}^P a_{ij} \hat{x}_j, \quad \forall i = 1, \dots, N$	
$k_i^n = \hat{l} + u_i ^2 + b_i, \quad \forall i = 1, \dots, N$	
$\hat{h}_i = \frac{-2y_i(\hat{l}+u_i)}{k_i^n} + 2(\hat{l} + u_i), \quad \forall i = 1, \dots, N$	
$c_i^R = 2 + \frac{2y_i \sqrt{b_i^2+4(\hat{l}^R+u_i^R)^2}(\hat{l}^R+u_i^R)^2}{k_i^n \{(\hat{l}^R+u_i^R)^2(b_i+2)+b_i[b_i+\sqrt{b_i^2+4(\hat{l}^R+u_i^R)^2}]\}}, \quad \forall i = 1, \dots, N$	
$c_i^I = 2 + \frac{2y_i \sqrt{b_i^2+4(\hat{l}^I+u_i^I)^2}(\hat{l}^I+u_i^I)^2}{k_i^n \{(\hat{l}^I+u_i^I)^2(b_i+2)+b_i[b_i+\sqrt{b_i^2+4(\hat{l}^I+u_i^I)^2}]\}}, \quad \forall i = 1, \dots, N$	
$\dot{L}_j = \sum_{i=1}^N a_{ij}^* \hat{h}_i, \quad \forall j = 1, \dots, P$	
$\dot{V}_j^R = \beta^R \sum_{i=1}^r c_{ij}^R \dot{\psi}([C^R \hat{x}^R]_i), \quad \forall j = 1, \dots, P$	
$\dot{V}_j^I = \beta^I \sum_{i=1}^r c_{ij}^I \dot{\psi}([C^I \hat{x}^I]_i), \quad \forall j = 1, \dots, P$	
$p_j^R = \beta^R \sum_{i=1}^r \frac{(c_{ij}^R)^2}{\gamma_{ij}^R} \dot{\psi}([C^R \hat{x}^R]_i), \quad \forall j = 1, \dots, P$	
$p_j^I = \beta^I \sum_{i=1}^r \frac{(c_{ij}^I)^2}{\gamma_{ij}^I} \dot{\psi}([C^I \hat{x}^I]_i), \quad \forall j = 1, \dots, P$	
$\dot{Q} = -[\dot{L}^R + \dot{V}^R; \dot{L}^I + \dot{V}^I]$	
$\mu = \frac{-\dot{Q}^T d}{[c^R; c^I]^T [A^R d_1 - A^I d_2; A^I d_1 + A^R d_2]^2 + [p^R; p^I]^T d^2}$	
$[\hat{x}^R; \hat{x}^I] = [\hat{x}^R; \hat{x}^I] + \mu d$	
$e^{\text{old}} = e$	
$e = -\dot{Q}$	
$\xi = \max\{0, \frac{e^T(e-e^{\text{old}})}{(e^{\text{old}})^T e^{\text{old}}}\}$	
$d = e + \xi d$	
end	

Table 7.2: The CG outline for holographic reconstruction

7.5.7 Number of Data Sets Used

In principle, our statistical technique can be applied to data with any number of measurement elements N and to a model with any number of image pixels P .

Whereas N is fixed by the choice of the measurement device (e.g., CCD camera pixels), the value of P can be selected by the algorithm designer. A natural choice for P would be the number of the CCD elements, which is the size of a single hologram. Theoretically, to estimate P complex unknown parameters, the given number of data should be at least $2P$ ($N \geq 2P$) such that the problem is not under-determined. Another alternative is to estimate only half the number of the CCD elements ($P/2$) using only one set of data ($N = P$). However, this alternative option involves interpolation and downsampling processes, which might introduce some artifacts in the reconstructed image. To study the effect of the sizes of the reconstructed image and data, in simulation, we consider the following three different cases for statistical reconstruction:

Case 1: Use one hologram to reconstruct a holographic image whose size is half the number of CCD elements (half-size reconstruction), i.e., $P = N/2$

Case 2: Use one hologram to reconstruct a holographic image whose size is the same as the number of CCD elements (full-size reconstruction), i.e., $P = N$

Case 3: Use two holograms to reconstruct a holographic image whose size is the same as the number of CCD elements (full-size reconstruction), i.e., $N = 2P$

7.6 Simulation Results

In this section, we compare the conventional numerical reconstruction technique with our statistical reconstruction based on three different cases discussed previously. Moreover, we consider a real object constraint in which the imaginary part of the estimate is forced to zero at every iteration when the object is known *priori* to be real.

7.6.1 Effect of Numbers of Data Sets

A 128×128 original image (Figure 7.4(a)) that is complex was degraded by the PSF, interference pattern, and Poisson noise (Figure 7.4(b)) as in (7.4). We assumed a shift-invariant optical system for which the system matrix is Toeplitz, so Ax can be implemented by convolution with the system PSF. To imitate the real imaging system in holography, we used a 7×7 jinc function, $\frac{J_1(2\pi r)}{\pi r}$ where J_1 is a Bessel function of the first kind and r is a polar-coordinate parameter, with full width at half maximum (FWHM) of 3.5 pixels as the PSF of the system. We used the following reference beams:

$$\begin{aligned} u_{r1}(n_1, n_2) &= 200 \exp\left(-i\frac{2\pi}{3}n_1\right), & n_1, n_2 &= 0, \dots, 127 \\ u_{r2}(n_1, n_2) &= 150 \exp\left(-i\frac{2\pi}{4}n_1\right), & n_1, n_2 &= 0, \dots, 127. \end{aligned}$$

For experiments with only one data set, we used the first reference beam. The offset b_i is assigned to be 5 and 10 for the first and second data, respectively. The Poisson noise has the peak signal-to-noise ratio (PSNR) of 29 dB and 24 dB in the first and second hologram data (Figure 7.4(b)), respectively. The PSNR in the data is defined as follows:

$$\text{PSNR} \triangleq 10 \log_{10} \left[\frac{\max_i (y_i - b_i)^2}{\frac{1}{N} \sum_{i=1}^N (y_i - \mathbf{E}[y_i])^2} \right].$$

Each simulated real-valued hologram data has the same size (128×128 pixels) as the original complex-valued image.

Figure 7.4(c) shows the conventional reconstruction using an apodizing Gaussian mask. The 41×41 Gaussian mask with FWHM of 27.2 pixels is performed on the selected region in the frequency domain of the hologram. The magnitude and phase of the reconstructed image appear to be blurry while noise still remains. Owing to

the effect of the filtering method, noise cannot be removed completely without over-smoothing edges. Figures 7.4(d)-(f) show our statistical holographic reconstruction from three different cases. Because of the ill condition of the problem, the reconstructed image can be quite sensitive to the initial image. We used the image from the conventional approach as the initial image and included the nonquadratic penalty function with the regularization parameters $\beta^R = \beta^I = 10$ and the edge-preserving parameters $\delta^R = \delta^I = 1$. The SPS algorithm was run for 200 iterations. Unlike the conventional technique, the statistical technique with the nonquadratic penalty can greatly reduce noise while still preserving edges. We expect that the number of data should be at least twice the number of unknown parameters for a complex image to avoid an under-determined problem. Figure 7.4(d) shows half-size reconstruction using one data set (Case 1). The resulting reconstructed image is linearly interpolated in the vertical direction to have the same size as the original image for the purpose of display. Figures 7.4(e)-(f) show full-size reconstruction using one and two data sets, respectively (Cases 2 and 3). From these figures, half-size reconstruction produces less noise but a little more artifacts than full-size reconstruction using one data set. This might be because the quality of the image using half-size reconstruction is reduced as a result of interpolation and downsampling processes. Moreover, the penalty function can improve the ill conditioning of the problem and reduce some ambiguity solutions. The profiles of the magnitude and phase of the reconstructed images are shown in Figures 7.5 and 7.6. As expected, full-size reconstruction with two data sets yields the best reconstructed image with the smallest normalized root mean-squared error (NRMSE). The NRMSE in percentage is defined as follows:

$$\text{NRMSE} = \frac{\|\hat{x} - x_{\text{true}}\|}{\|x_{\text{true}}\|} \times 100\%$$

where \hat{x} is the reconstructed image, x_{true} is the true image, and $\|\cdot\|$ represents the Euclidean norm.

Figure 7.7 shows the contours of the marginal objective functions at a particular pixel using one and two data sets. For illustration, we examined the noiseless and blurless case without regularization to clearly demonstrate how the statistical technique using two sets of data can help reducing non-uniqueness of the problem. As shown in Figure 7.7(a), since there are multiple minimizers, the algorithm converges to an estimate that depends strongly on the initial guess. When two data sets are used, the solutions become more distinct, and thus the algorithm often converges to the desired solution as in Figure 7.7(b). However, we sometimes experience convergence to a different solution even with two data sets. This situation is possible because the problem does not have a unique global solution.

All cases of our statistical technique have a monotonic decreasing cost function; therefore, our technique is guaranteed to converge to one of the local minimum solutions. The unique global solution is not guaranteed in this problem because the original negative log-likelihood function does not have a unique minimizer. Nevertheless, the penalty function can greatly reduce this non-uniqueness.

7.6.2 Real Object Constraint

If the object is known *a priori* to be real, then we constrain the imaginary part of the estimates to be zero. In this case, we may not need to have $N \geq 2P$. Thus we expect similar results for three cases in the statistical approach but some artifacts caused by interpolation and downsampling might exist in the case of half-size reconstruction. A 128×128 real image (Figure 7.8(a)) was degraded using the same parameters as in the previous section. The conventional numerical reconstruction in Figure 7.8(d)

is blurry as a result of the Gaussian filter. Figures 7.8(e)-(g) show the statistical reconstruction performed with the nonquadratic penalty function ($\beta^R = \beta^I = 5, \delta^R = \delta^I = 5$) for 200 iterations. Although the NRMSEs for all three cases are slightly different, they all provide similar reconstructed holographic images with less blur than the resulting image from the conventional approach. Because of the real object constraint, using one data set is adequate to provide a good holographic reconstructed image.

7.7 Conclusions for Holographic Image Reconstruction

We have demonstrated the potential for reconstructing a digital holographic image using the proposed statistical technique. Because the method uses all the information in the recorded hologram rather than just one term, this approach can improve the quality of the image relative to the conventional numerical reconstruction technique that uses a spatial filter applied in the spatial frequency domain. Moreover, unlike the conventional approach, our statistical technique is not limited by the plane wave assumption of the reference beam. Because of the ill conditioning and non-uniqueness of the problem, our statistical holographic reconstruction is based on PL estimation. We constructed a statistical model for this system and developed a monotonic algorithm which guarantees convergence to at least a local minimum. Although the unique global minimum is not guaranteed due to the non-uniqueness nature of the negative log-likelihood function in this problem, we mostly overcome the problem of multiple minima through the help of the penalty function and the increase in the number of the measurement data. For a real object, the realness constraint can be enforced at each iteration so that the algorithm can converge faster and only one data set should be sufficient to yield a good reconstructed image.

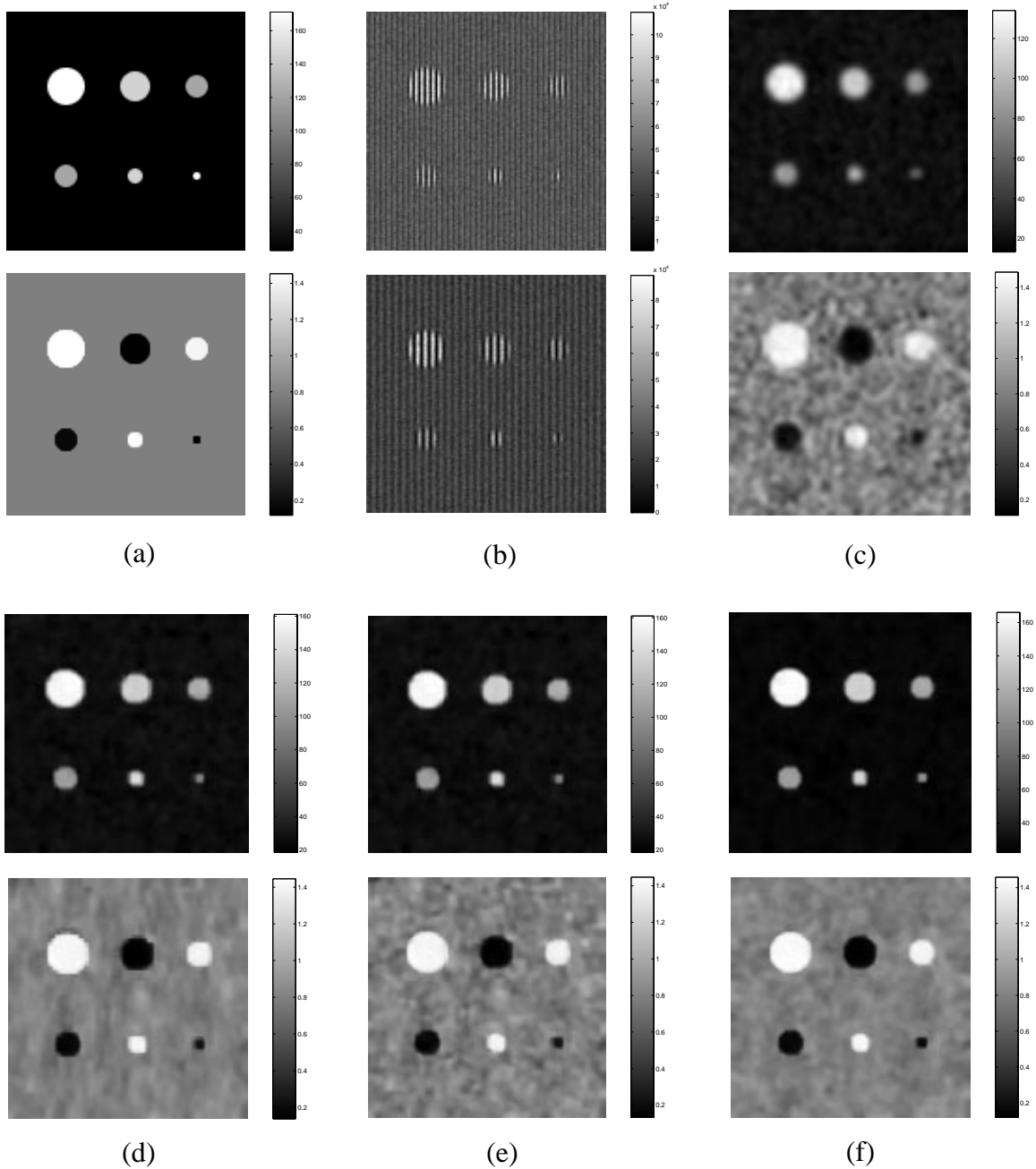


Figure 7.4: Holographic reconstruction of a complex object. The top image of each pair represents the magnitude of the image and the bottom image represents the phase of the image, except for the hologram data. (a) Original image. (b) Two different hologram data. (c) Conventional reconstruction using an apodizing Gaussian filter (NRMSE=40.0%). (d) Half-size statistical reconstruction using one data set (NRMSE=17.5%). Linear interpolation in the vertical direction to the same size as the original image is performed for display. (e) Full-size statistical reconstruction using one data set (NRMSE=17.3%). (f) Full-size statistical reconstruction using two data sets (NRMSE=14.1%).

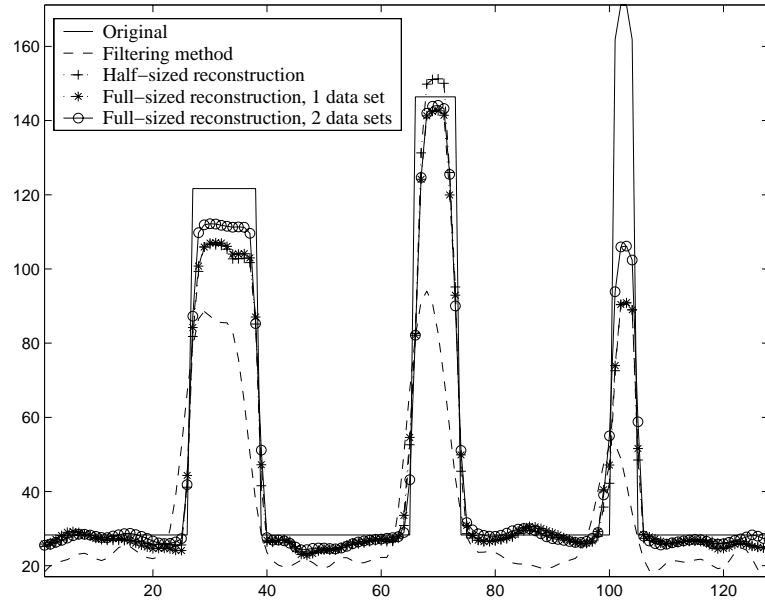


Figure 7.5: Profiles of the magnitude of the numerical reconstructed images across the second row of circles.

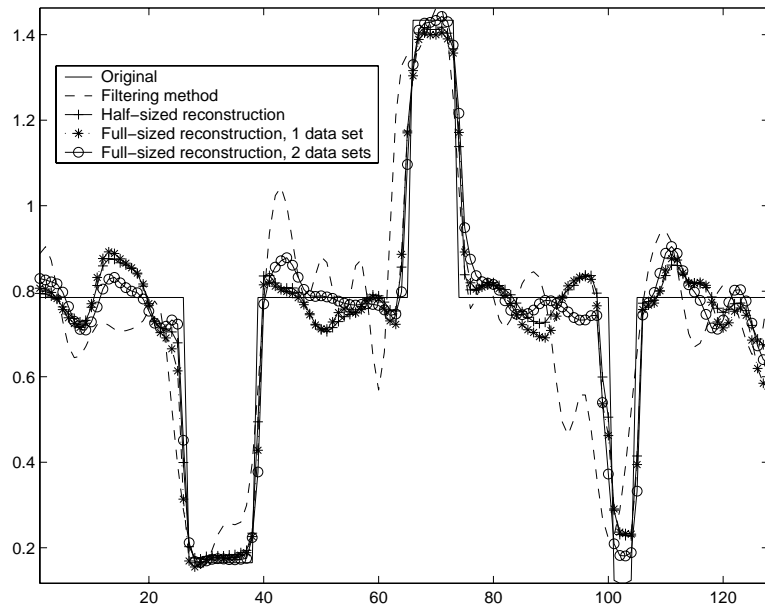
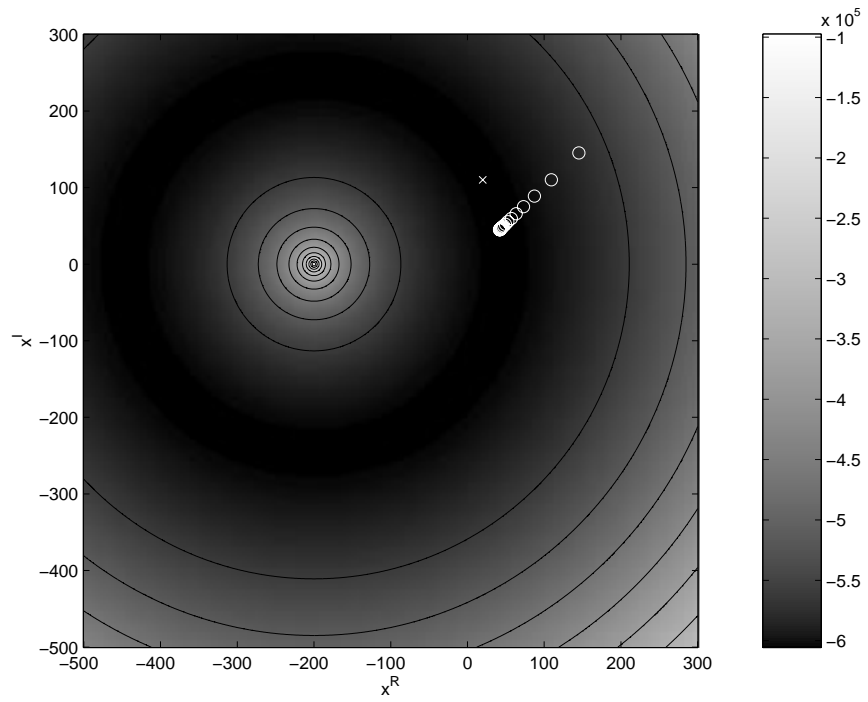
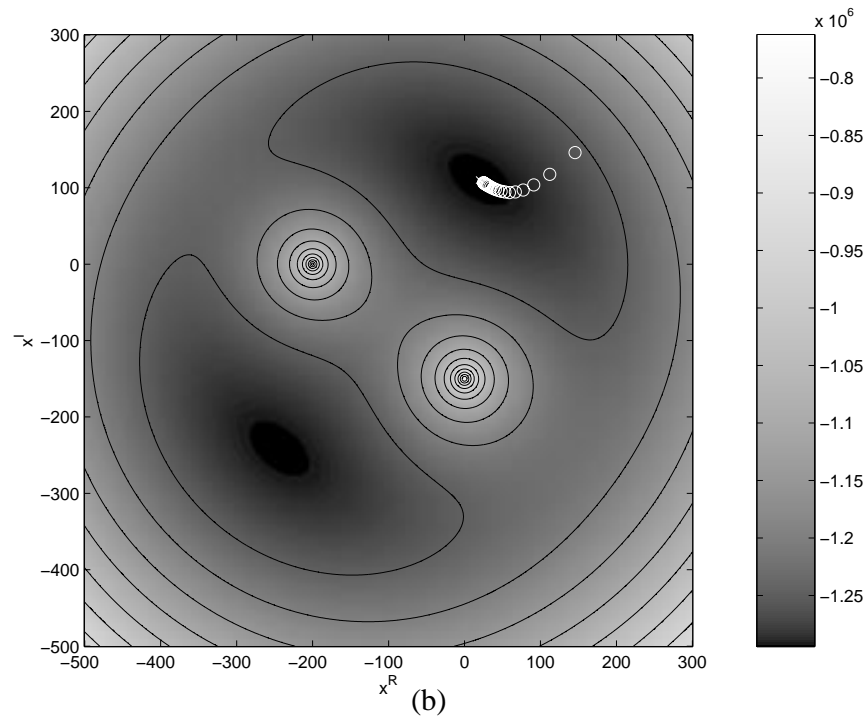


Figure 7.6: Profiles of the phase of the numerical reconstructed images across the second row of circles.



(a)



(b)

Figure 7.7: Contours of the marginal objective functions at one pixel when (a) using one data set and (b) using two data sets for full-size reconstruction. The “x” mark is the optimal solution at $20 + i110$ and the “o” marks indicate the updates of the estimates starting at $150 + i150$.

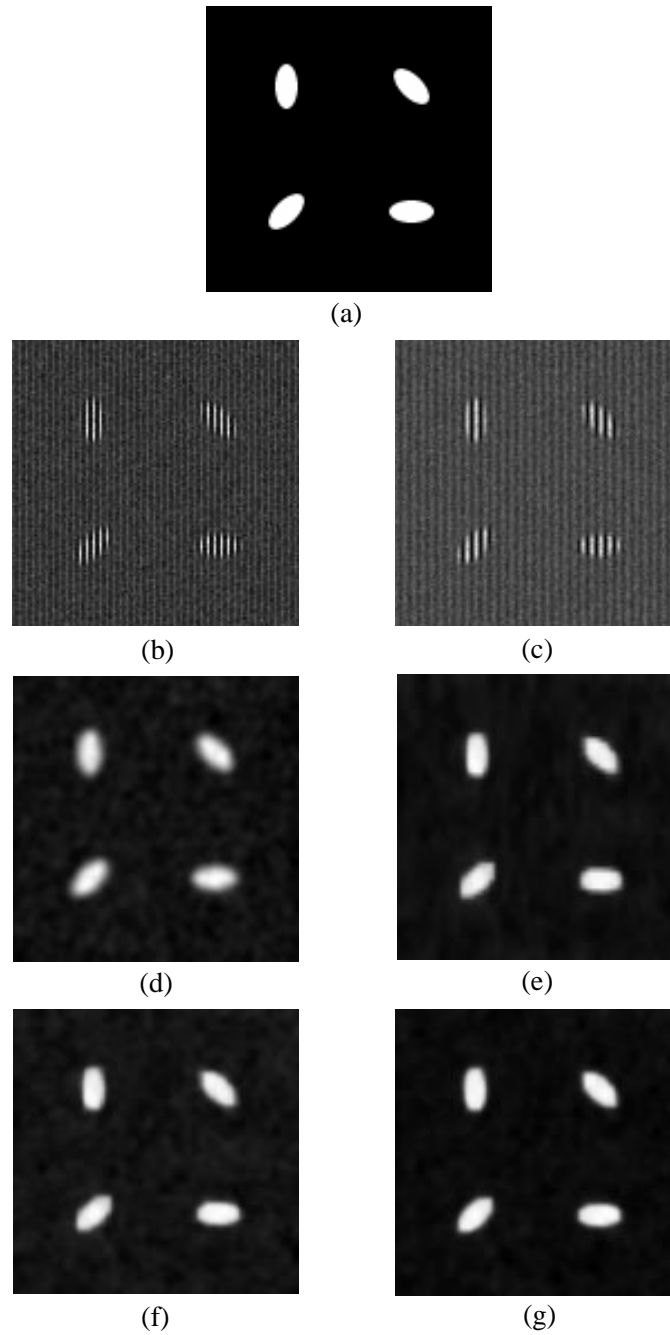


Figure 7.8: Statistical reconstruction of a real object using the real object constraint. (a) Original image. (b) and (c) Hologram data. (d) Conventional reconstruction using an apodizing Gaussian filter (NRMSE=43.8%). (e) Half-size statistical reconstruction using one data set (NRMSE=22.8%). (f) Full-size statistical reconstruction using one data set (NRMSE=21.1%). (g) Full-size statistical reconstruction using two data sets (NRMSE=17.2%).

CHAPTER VIII

Conclusions and Future Work

8.1 Conclusions

In this dissertation, we introduced two new, fast-converging, iterative algorithms for penalized-likelihood image restoration. These algorithms can be generalized for use with a very broad class of imaging systems. We demonstrated use of these algorithms through confocal microscopy problems. First, we introduced the PPCA algorithm, which is based on the optimization transfer principle and convexity technique. This algorithm not only guarantees the monotonicity of objective function increases and intrinsically accommodates nonnegativity constraints, but also converges very rapidly and is parallelizable. We implemented the PPCA algorithm to run on parallel processors by using a message-passing interface and its portable version. For a large 3-D data set as in confocal microscopy, the PPCA algorithm yields a speedup factor approaching the number of parallel processors used. Although it converges quickly, the PPCA algorithm is more suitable for space-variant systems in which FFTs cannot be employed for further acceleration. Since a confocal microscopy system is usually assumed to be space invariant, an algorithm that is compatible with FFTs is preferred.

To meet this preference, we developed the second algorithm, the relaxed OS-

SPS algorithm. Ordered-subset algorithms are widespread in image reconstruction for tomography because of their order-of-magnitude acceleration improvement over single-subset versions. Therefore, we adapted the relaxed OS-SPS algorithm for image restoration. Because data acquisition is different in image restoration than in tomography, we employed a different strategy for choosing subsets in image restoration. Thus, we used pixel location, rather than projection angles. The subsets chosen by downsampling pixels satisfy the subset-gradient-balance conditions; therefore, the relaxed OS-SPS algorithm can provide an order-of-magnitude acceleration improvement for image restoration similar to what it provides for tomography. Furthermore, we derived implementation techniques to perform the relaxed OS-SPS efficiently with convolution and FFTs. Although FFTs can be used in this algorithm, the resulting computational complexity per iteration is somewhat higher than the non-ordered-subset version, unlike the convolution approach. Nevertheless, the overall convergence rate is still faster than that of the non-ordered-subset algorithm, especially when using large data sets. Thus, the relaxed OS-SPS algorithm provides the speed and guaranteed convergence necessary for efficient image restoration.

Our results verify that PL estimation using these proposed algorithms not only yields fast convergence, but also is capable of reducing noise and improving the resolution, especially in the axial direction, of confocal images. To determine which algorithm should be used, we need to consider whether the system is assumed to be space-variant or space-invariant, and what the convergence criteria are. If the algorithms will be run for only a few iterations, then relaxed OS-SPS is most desirable due to its fast initial convergence. On the other hand, if the algorithms will be run for many iterations—until convergence near the optimal solution—then PPCA is most preferred for the space-variant and convolution-based space-invariant systems, and

EM (or De Pierro's modified EM [36] for PL), as well as SPS, are preferred for the FFT-based space-invariant system. This is because the relaxation parameter in relaxed OS-SPS slows down convergence when approaching the optimal solution.

For confocal microscopy, we applied image restoration directly to the raw measured images. Similarly, for digital holography we reconstructed holographic images directly from the raw data of the hologram, instead of applying image restoration on corrupted holographic images obtained from conventional numerical reconstruction. In particular, we developed a new statistical image reconstruction technique for digital holography based on penalized-likelihood estimation. This approach reconstructs the complex field of the object from the real-valued hologram intensity data. In this technique, we developed a Poisson statistical model for holographic problems and derived optimization transfer algorithms that monotonically decrease the cost function at each iteration and ensure convergence to a local minimum. Moreover, we derived new curvatures for obtaining parabolic-surrogate functions that always lie above the original cost function, thus guaranteeing convergence to the local minimum. The results demonstrated that our statistical reconstruction technique improves the quality of holographic images relative to the conventional reconstruction technique based on a filtering method. Because the plane-wave assumption of the reference beam is not restricted in the statistical approach, this approach could be applied to both digital in-line and off-axis holography. Although achieving the unique global minimum is not guaranteed in this problem, because of the non-uniqueness of the cost function, the problem of multiple minima is often mitigated by increasing the number of data sets and using a penalty function.

8.2 Future Work

In this dissertation, we have accomplished much work on iterative algorithms for penalized-likelihood image restoration, but there are always improvements and extensions that can be made to this work. Moreover, since statistical image reconstruction for digital holography is a new field, many improvements and analyses can be made for holographic problems. Some possible recommendations for future work are summarized below.

- In this dissertation, we considered only the approximate model based on Poisson noise and ignored some effects, such as the response of the photodetector, CCD thickness, photobleaching in fluorescent objects, and multiple scatters of the objects. A complete model that includes a Gaussian distribution of the readout noise from the amplifier and those existing effects may further improve the image quality. Moreover, a shift-variant model due to the nature of lenses in optical systems is, in fact, a more accurate model than using a shift-invariant model, and this also can be considered next.
- For penalized-likelihood estimates, the regularization parameter, as well as the edge-preserving parameter for the nonquadratic penalty, needs to be assigned. Instead of obtaining them by trial and error, a better way for determining these parameters would help users to obtain good images quickly. One possible choice for choosing the regularization parameter is based on a shift-varying penalty that yields uniform resolution properties [113].
- The relaxation parameter in relaxed OS-SPS controls convergence of the algorithm. If it is not designed properly, then relaxed OS-SPS may converge slower than OS-SPS without relaxation for a converging case. Thus, a careful

design for the relaxation parameter can preserve the rapid convergence rate while ensuring convergence.

- Statistical holographic image reconstruction developed in this dissertation uses the SPS algorithm, which converges slowly. We can apply the PPCA and relaxed OS-SPS algorithms to this problem for faster convergence. Moreover, since the curvatures used for constructing parabolic surrogate functions at each iteration are not optimal, and the precomputed curvatures seem to be too large, an optimal curvature and a better precomputed curvature can improve the convergence rate and the computation time. Instead of using parabolic surrogate functions, other surrogate functions that are simple to optimize can also be considered, such as quartic functions.
- Our statistical model for digital holography ignores aberration, CCD thickness, and other noise sources such as Gaussian readout noise. As discussed in the future work for confocal microscopy problems, we could also consider the space-variant model in digital holography to account for the accurate characteristics of lenses used, CCD thickness, as well as other sources of noise.
- In this dissertation, the statistical holographic reconstruction technique we developed was tested only with simulated data for image plane holography. It would be interesting, however, to apply our reconstruction technique to real holographic data. Moreover, since our technique can be generalized more broadly, applying it to other digital holography, including Fresnel, Fourier, non-planar off-axis, and on-line holography, as well as to phase retrieval problems, would be interesting for future work.
- When using real data to reconstruct a holographic image, other parameters,

such as the PSF, the reference beam, and the offset, must be determined. The PSF can be obtained from either the theoretical PSF or the experimental PSF. The offset can be estimated from the blank scan when no light is present on both object and reference beams. The amplitude of the reference beam can be simply obtained by imaging only the reference beam; however, acquiring the phase of the reference beam may be challenging. If the reference beam is a tilted plane wave, then its spatial carrier frequency relating to the phase can be estimated from the Fourier transform of the hologram. One simple option to obtain 2 different hologram data sets is to use 0° and 90° reference beams. Another common use for a reference beam is a spherical wave. In general, the parameters relating to its phase can be experimentally obtained. However, these parameters might be difficult to determine in the setup for image plane holography. In addition to plane and spherical waves, obtaining phase information from other non-plane waves seems to be a challenging problem.

- The current experimental setup for image plane holography is designed for a transparent object. If a fluorescent object is placed in the object beam, then it might act as incoherent sources, thus destroying the coherence property of holography. This might decrease the degree of confocal effect and the resolution of the image. Since most biological specimens are usually labeled with fluorescent materials, it would be very useful if this holography setup could be adopted to work with fluorescent objects as well.

APPENDICES

APPENDIX A

Theoretical PSF Derivation for Confocal Microscopy

A.1 Single Lens System

The 3-D amplitude PSF of a single lens at a defocus plane z can be expressed as follows [60, 114, 127]:

$$h_l(\mathbf{r}, \mathbf{z}) = K \int_0^1 P(\rho) \exp(i\mathbf{u}\rho^2/2) J_0(\mathbf{v}\rho) \rho d\rho \quad (\text{A.1})$$

where K is a constant, \mathbf{r} is the radial coordinate [$\mathbf{r} = (\mathbf{x}^2 + \mathbf{y}^2)^{1/2}$], \mathbf{z} is the spatial coordinate along the axial direction, P is the pupil function of the lens, and J_0 is the Bessel function of the zeroth order of the first kind. The transverse and axial optical coordinates (\mathbf{v} and \mathbf{u} , respectively) are defined as follows:

$$\mathbf{v} = \frac{2\pi}{\lambda} \mathbf{r} n \sin \alpha, \quad \mathbf{u} = \frac{2\pi}{\lambda} \mathbf{z} n \sin^2 \alpha$$

where λ is the incident wavelength, n is the index of refraction in the lens, and $n \sin \alpha$ is the numerical aperture (NA) of the lens. For a circular symmetric lens, the amplitude PSF at the in-focus plane becomes

$$h_l(\mathbf{r}, 0) = \frac{2J_1(\mathbf{v})}{\mathbf{v}}$$

where J_1 is the Bessel function of the first order and the first kind. This Hankel transform of the circular pupil function is called the “jinc” function. Its intensity distribution or the image of a point object is

$$I(\mathbf{r}) = |h_l(\mathbf{r}, 0)|^2 = \left[\frac{2J(\mathbf{v})}{\mathbf{v}} \right]^2$$

which is known as the Airy pattern [30, 57, 60, 127]. This is, in fact, the intensity PSF for the conventional nonconfocal microscope. The amplitude PSF along the axial direction ($\mathbf{v} = 0$) can be approximated as follows [12, 30, 60, 127]:

$$h_l(0, \mathbf{z}) \approx \frac{\sin(\mathbf{u}/4)}{\mathbf{u}/4}.$$

The CTF of the system is defined as the Fourier transform of the amplitude PSF. Likewise, the OTF of the system is defined as the Fourier transform of the intensity PSF.

A.2 Reflection and Transmission Confocal Microscopes

For confocal microscopy, we assume the objective lens is used twice. In the case of a point detector, the intensity PSFs of reflection and transmission confocal microscopes [15, 30, 127, 128] are given by:

$$I(\mathbf{r}, \mathbf{z}) = |h_l(\mathbf{r}, \mathbf{z})|^4.$$

This power to the fourth in the intensity distribution of a point object provides the resolution improvement of confocal microscopy over the convention nonconfocal microscope.

The behaviors of the 3-D CTFs in the reflection and transmission modes are different. The latter exhibits a missing Fourier components in the missing cone region

around the origin, while the former does not. Thus, there is no optical sectioning effect in the transmission confocal microscope [60].

The 3-D CTF for a reflection confocal microscope is the auto-convolution of the 3-D CTF for conventional nonconfocal microscope [60]:

$$H(s, t, w) = \mathcal{F}\{h_l(\mathbf{r}, \mathbf{z})\} *** \mathcal{F}\{h_l(\mathbf{r}, \mathbf{z})\}$$

where \mathcal{F} represents the Fourier transformation and the symbol $[***]$ represents the 3-D convolution. The role of auto-convolution implies that the bandwidths of the CTF in the reflection confocal microscope are twice as wide as those in the single lens system. The wider bandwidth implies sharper image resolution. The 3-D CTF of the confocal microscope in the transmission mode turns out to be the same as the OTF of the conventional microscope [30, 60, 75, 76], which can be expressed in the following form:

$$H(s, t, w) = \mathcal{F}\{|h_l(\mathbf{r}, \mathbf{z})|^2\} = \begin{cases} \frac{1}{\rho} \left[1 - \left(\frac{|w|}{\rho} + \frac{\rho}{2} \right)^2 \right]^{1/2} \text{rect} \left(\frac{w}{2(\rho - \rho^2/2)} \right), & \rho < 2 \\ 0, & \text{else} \end{cases}$$

where $\rho = (s^2 + t^2)^{1/2}$ and $\text{rect}(a) = 1, |a| \leq 1/2$ and 0 elsewhere. The term in the rect function corresponds to the region of support as shown in Figure 2.4. This is because in the transmission mode the beam traverses the object, and thus the defocus distance for the collector (second lens) has a sign opposite to that for the objective (first lens) [60]. The normalized spatial frequencies s, t , and w , are defined as follows:

$$s = \frac{\lambda}{n \sin \alpha} f_x, \quad t = \frac{\lambda}{n \sin \alpha} f_y, \quad w = \frac{\lambda}{n \sin^2 \alpha} f_z$$

where f_x, f_y , and f_z are spatial frequencies in the \mathbf{x}, \mathbf{y} , and \mathbf{z} directions.

A.3 Confocal Fluorescence Microscope

Similarly, the intensity PSF in the fluorescence mode [15, 30, 127, 128] is

$$h_I(\mathbf{r}, \mathbf{z}) = |h_l(\mathbf{r}, \mathbf{z})|^4. \quad (\text{A.2})$$

The intensity PSF of the in-focus plane with the circular objective lens is

$$h_I(\mathbf{r}) = \left[\frac{2J_1(\mathbf{v})}{\mathbf{v}} \right]^4$$

and the intensity PSF along the axial direction can be approximately as follows [30, 60, 127, 128]:

$$h_I(\mathbf{z}) \approx \left[\frac{\sin(\mathbf{u}/2)}{\mathbf{u}/2} \right]^2.$$

The 3-D OTF of the fluorescence confocal microscope is the Fourier transform of the intensity PSF in (A.2) which is the same as the auto-convolution of the 3-D OTF of a conventional nonconfocal microscope [26, 75]. This OTF does not exhibit a missing cone region around the origin; therefore, there exists an optical sectioning property in the confocal fluorescence microscope. Its 3-D OTF can expressed as

$$\mathcal{H}(s, t, w) = \mathcal{F}\{|h_l(\mathbf{r}, \mathbf{z})|^2\} *** \mathcal{F}\{|h_l(\mathbf{r}, \mathbf{z})|^2\}.$$

The bandwidth of this OTF is twice as wide as that of the nonconfocal microscope. Moreover, because the confocal fluorescence microscope is an incoherent system while the reflection and transmission confocal microscopes are coherent systems, under an ideal situation, the bandwidth of the OTF for the fluorescence mode is twice as large in the transverse direction as the CTF in the reflection and transmission modes [75].

With a finite-sized circular detector, the intensity PSF of the confocal microscope (in all modes) [60] becomes

$$h_I(\mathbf{r}, \mathbf{z}) = |h_l(\mathbf{v}, \mathbf{u})|^2 [|h_l(\mathbf{v}, \mathbf{u})|^2 ** D(\mathbf{v})]$$

where $D(\mathbf{v})$ is the intensity sensitivity of the detector, which can be expressed as follows:

$$D(\mathbf{v}) = \begin{cases} 1, & \mathbf{v} < \mathbf{v}_d \\ 0, & \text{otherwise} \end{cases}$$

where $\mathbf{v}_d = \frac{2\pi}{\lambda} \mathbf{r}_d n \sin \alpha$ is the normalized radius of the detector and \mathbf{r}_d is the radius of the pinhole. Its corresponding OTF [60, 76] is the following Fourier transform of the above intensity PSF:

$$\mathcal{H}(s, t, w) = \mathcal{F}\{|h_l(\mathbf{v}, \mathbf{u})|^2\} *** [\mathcal{F}\{|h_l(\mathbf{v}, \mathbf{u})|^2\} \mathcal{F}\{D(\mathbf{v})\delta(\mathbf{u})\}].$$

This finite-sized detector pinhole results in the appearance of the missing cone region as the pinhole size increases.

APPENDIX B

Theoretical PSF Derivation for Image Plane Holography

To derive the 3-D PSF for image plane holography, first we start with the object beam. Let the object be a transparency with some suitable thickness.

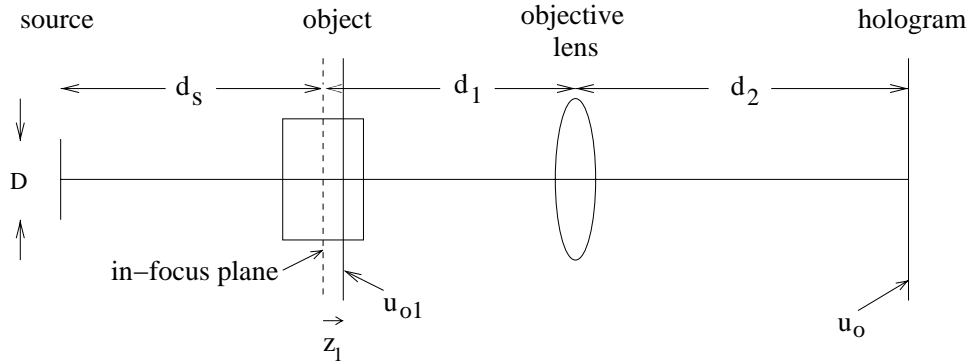


Figure B.1: Light propagation through the object path

We can assume that points on the source are statistically independent from each other. Thus we compute the field at the hologram recording plane for each source element and then integrate the irradiance over the source distribution. By using the Fresnel approximation, the field induced by a point at coordinates $(\mathbf{x}_s, \mathbf{y}_s)$ on the source propagating to the plane at distance \mathbf{z}_1 away from the object plane that we want to generate is given by:

$$u_{o1}(\mathbf{x}_1, \mathbf{y}_1, \mathbf{z}_1; \mathbf{x}_s, \mathbf{y}_s) = \frac{\exp\{i\frac{2\pi}{\lambda}(d_s + \mathbf{z}_1)\}}{i\lambda(d_s + \mathbf{z}_1)} \exp\left\{i\frac{\pi}{\lambda(d_s + \mathbf{z}_1)}[(\mathbf{x}_1 - \mathbf{x}_s)^2 + (\mathbf{y}_1 - \mathbf{y}_s)^2]\right\}$$

where $(\mathbf{x}_1, \mathbf{y}_1, \mathbf{z}_1)$ are coordinates in the object plane and d_s is the distance between the source and the in-focus plane of the object. Following [57], the field distribution u_o at distance d_2 behind the objective lens can be expressed as the superposition integral

$$\begin{aligned} u_o(\mathbf{x}, \mathbf{y}, \mathbf{z}_1; \mathbf{x}_s, \mathbf{y}_s) &= \iint t(\mathbf{x}_1, \mathbf{y}_1, \mathbf{z}_1) u_{o1}(\mathbf{x}_1, \mathbf{y}_1, \mathbf{z}_1; \mathbf{x}_s, \mathbf{y}_s) h'_o(\mathbf{x}, \mathbf{y}; \mathbf{x}_1, \mathbf{y}_1, \mathbf{z}_1) d\mathbf{x}_1 d\mathbf{y}_1 \\ &= \iint t(\mathbf{x}_1, \mathbf{y}_1, \mathbf{z}_1) \exp \left\{ i \frac{\pi}{\lambda(d_s + \mathbf{z}_1)} [(\mathbf{x}_1 - \mathbf{x}_s)^2 + (\mathbf{y}_1 - \mathbf{y}_s)^2] \right\} \\ &\quad \frac{\exp \left\{ i \frac{2\pi}{\lambda} (d_s + \mathbf{z}_1) \right\}}{i\lambda(d_s + \mathbf{z}_1)} h'_o(\mathbf{x}, \mathbf{y}; \mathbf{x}_1, \mathbf{y}_1, \mathbf{z}_1) d\mathbf{x}_1 d\mathbf{y}_1 \end{aligned}$$

where t is the amplitude transmittance of the object and h'_o is the PSF of the objective lens which can be expressed as

$$\begin{aligned} h'_o(\mathbf{x}, \mathbf{y}; \mathbf{x}_1, \mathbf{y}_1, \mathbf{z}_1) &= \frac{1}{\lambda^2 d_1 d_2} \exp \left\{ i \frac{\pi}{\lambda d_2} (\mathbf{x}^2 + \mathbf{y}^2) \right\} \exp \left\{ i \frac{\pi}{\lambda(d_s - \mathbf{z}_1)} (\mathbf{x}_1^2 + \mathbf{y}_1^2) \right\} \\ &\quad \iint P(\xi_x, \xi_y) \exp \left\{ i \frac{\pi}{\lambda} \left(\frac{1}{d_1 - \mathbf{z}_1} + \frac{1}{d_2} - \frac{1}{F} \right) (\xi_x^2 + \xi_y^2) \right\} \\ &\quad \exp \left\{ -i \frac{2\pi}{\lambda} \left[\left(\frac{\mathbf{x}_1}{d_1 - \mathbf{z}_1} + \frac{\mathbf{x}}{d_2} \right) \xi_x + \left(\frac{\mathbf{y}_1}{d_1 - \mathbf{z}_1} + \frac{\mathbf{y}}{d_2} \right) \xi_y \right] \right\} d\xi_x d\xi_y. \end{aligned}$$

Thus we define the PSF in the object beam h_o as

$$\begin{aligned} h_o(\mathbf{x}, \mathbf{y}; \mathbf{x}_1, \mathbf{y}_1, \mathbf{z}_1) &= \frac{\exp \left\{ i \frac{2\pi}{\lambda} (d_s + \mathbf{z}_1) \right\}}{i\lambda(d_s + \mathbf{z}_1)} h'_o(\mathbf{x}, \mathbf{y}; \mathbf{x}_1, \mathbf{y}_1, \mathbf{z}_1) \\ &= \frac{\exp \left\{ i \frac{2\pi}{\lambda} (d_s + \mathbf{z}_1) \right\}}{i\lambda^3 d_1 d_2 (d_s + \mathbf{z}_1)} \exp \left\{ i \frac{\pi}{\lambda d_2} (\mathbf{x}^2 + \mathbf{y}^2) \right\} \\ &\quad \exp \left\{ i \frac{\pi}{\lambda(d_s - \mathbf{z}_1)} (\mathbf{x}_1^2 + \mathbf{y}_1^2) \right\} \\ &\quad \iint P(\xi_x, \xi_y) \exp \left\{ i \frac{\pi}{\lambda} \left(\frac{1}{d_1 - \mathbf{z}_1} + \frac{1}{d_2} - \frac{1}{F} \right) (\xi_x^2 + \xi_y^2) \right\} \\ &\quad \exp \left\{ -i \frac{2\pi}{\lambda} \left[\left(\frac{\mathbf{x}_1}{d_1 - \mathbf{z}_1} + \frac{\mathbf{x}}{d_2} \right) \xi_x + \left(\frac{\mathbf{y}_1}{d_1 - \mathbf{z}_1} + \frac{\mathbf{y}}{d_2} \right) \xi_y \right] \right\} d\xi_x d\xi_y \end{aligned}$$

where P is the pupil function of the objective lens and F is the focal length of the lens. The quadratic phase term inside the integral can be approximated using the

following approximation:

$$\frac{1}{d_1 - \mathbf{z}_1} = \frac{d_1 + \mathbf{z}_1}{d_1^2 - \mathbf{z}_1^2} \approx \frac{d_1 + \mathbf{z}_1}{d_1^2} = \frac{1}{d_1} + \frac{\mathbf{z}_1}{d_1^2}.$$

According to the lens law, this condition is satisfied:

$$\frac{1}{d_1} + \frac{1}{d_2} - \frac{1}{F} = 0.$$

Thus the quadratic phase term becomes

$$\exp \left\{ i \frac{\pi}{\lambda} \left(\frac{1}{d_1 - \mathbf{z}_1} + \frac{1}{d_2} - \frac{1}{F} \right) (\xi_x^2 + \xi_y^2) \right\} \approx \exp \left\{ i \frac{\pi \mathbf{z}_1}{\lambda d_1^2} (\xi_x^2 + \xi_y^2) \right\}.$$

The linear phase term inside the integral can also be approximated as follows:

$$\begin{aligned} \exp \left\{ -i \frac{2\pi}{\lambda} \left[\left(\frac{\mathbf{x}_1}{d_1 - \mathbf{z}_1} + \frac{\mathbf{x}}{d_2} \right) \xi_x + \left(\frac{\mathbf{y}_1}{d_1 - \mathbf{z}_1} + \frac{\mathbf{y}}{d_2} \right) \xi_y \right] \right\} \approx \\ \exp \left\{ -i \frac{2\pi}{\lambda d_2} [(\mathbf{x} - M\mathbf{x}_1)\xi_x + (\mathbf{y} - M\mathbf{y}_1)\xi_y] \right\} \end{aligned}$$

where the magnification M is $-\frac{d_2}{d_1}$. Following [57], we can ignore the quadratic phase terms in front of the integral and the PSF in the object beam becomes

$$\begin{aligned} h_o(\mathbf{x}, \mathbf{y}; \mathbf{x}_1, \mathbf{y}_1, \mathbf{z}_1) = & \frac{\exp\{i\frac{2\pi}{\lambda}(d_s + \mathbf{z}_1)\}}{i\lambda^3 d_1 d_2 (d_s + \mathbf{z}_1)} \iint P(\xi_x, \xi_y) \exp \left\{ i \frac{\pi \mathbf{z}_1}{\lambda d_1^2} (\xi_x^2 + \xi_y^2) \right\} \\ & \exp \left\{ -i \frac{2\pi}{\lambda d_2} [(\mathbf{x} - M\mathbf{x}_1)\xi_x + (\mathbf{y} - M\mathbf{y}_1)\xi_y] \right\} d\xi_x d\xi_y. \end{aligned} \quad (\text{B.1})$$

Each plane of a thick object indexed by \mathbf{z}_1 produces an image in the image plane, so the total field in the image plane is the superposition of the contributions from each \mathbf{z}_1 section. Therefore, we integrate u_o over \mathbf{z}_1 :

$$\begin{aligned} u_o(\mathbf{x}, \mathbf{y}; \mathbf{x}_s, \mathbf{y}_s) = & \iiint t(\mathbf{x}_1, \mathbf{y}_1, \mathbf{z}_1) h_o(\mathbf{x} - M\mathbf{x}_1, \mathbf{y} - M\mathbf{y}_1, \mathbf{z}_1) \\ & \exp \left\{ i \frac{\pi}{\lambda(d_s + \mathbf{z}_1)} [(\mathbf{x}_1 - \mathbf{x}_s)^2 + (\mathbf{y}_1 - \mathbf{y}_s)^2] \right\} d\mathbf{x}_1 d\mathbf{y}_1 d\mathbf{z}_1. \end{aligned}$$

To construct a 3D holographic image, the object is moved at different depth to generate a holographic image on that plane. Let \mathbf{z} be the distance away from the

center plane of the object. Then the object field at the hologram plane corresponding to the object displacement \mathbf{z} becomes

$$u_o(\mathbf{x}, \mathbf{y}, \mathbf{z}; \mathbf{x}_s, \mathbf{y}_s) = \iiint t(\mathbf{x}_1, \mathbf{y}_1, \mathbf{z} - \mathbf{z}_1) h_o(\mathbf{x} - M\mathbf{x}_1, \mathbf{y} - M\mathbf{y}_1, \mathbf{z}_1) \exp \left\{ i \frac{\pi}{\lambda(d_s + \mathbf{z}_1)} [(\mathbf{x}_1 - \mathbf{x}_s)^2 + (\mathbf{y}_1 - \mathbf{y}_s)^2] \right\} d\mathbf{x}_1 d\mathbf{y}_1 d\mathbf{z}_1.$$

Since the reference beam propagates through the same system as the object beam but without the object, the field from the same point source through the reference beam to the hologram plane is:

$$u_{\text{ref}}(\mathbf{x}, \mathbf{y}; \mathbf{x}_s, \mathbf{y}_s) = \iiint h_{\text{ref}}(\mathbf{x} - M\mathbf{x}'_1, \mathbf{y} - M\mathbf{y}'_1, \mathbf{z}'_1) \exp \left\{ i \frac{\pi}{\lambda(d_s + \mathbf{z}'_1)} [(\mathbf{x}'_1 - \mathbf{x}_s)^2 + (\mathbf{y}'_1 - \mathbf{y}_s)^2] \right\} d\mathbf{x}'_1 d\mathbf{y}'_1 d\mathbf{z}'_1$$

where the PSF of the reference beam h_{ref} is the same as (B.1). At the hologram plane, the object and reference beams are interfered and the corresponding field due to a point source is

$$u(\mathbf{x}, \mathbf{y}, \mathbf{z}; \mathbf{x}_s, \mathbf{y}_s) = u_o(\mathbf{x}, \mathbf{y}, \mathbf{z}; \mathbf{x}_s, \mathbf{y}_s) + u_{\text{ref}}(\mathbf{x}, \mathbf{y}; \mathbf{x}_s, \mathbf{y}_s).$$

The total intensity recorded as a hologram when the object is displaced by \mathbf{z} is obtained by integrating over the source of uniform irradiance as follows:

$$\begin{aligned} I(\mathbf{x}, \mathbf{y}; \mathbf{z}) &= \int_{-\frac{D}{2}}^{\frac{D}{2}} \int_{-\frac{D}{2}}^{\frac{D}{2}} |u(\mathbf{x}, \mathbf{y}, \mathbf{z}; \mathbf{x}_s, \mathbf{y}_s)|^2 d\mathbf{x}_s d\mathbf{y}_s \\ &= \int_{-\frac{D}{2}}^{\frac{D}{2}} \int_{-\frac{D}{2}}^{\frac{D}{2}} [|u_o(\mathbf{x}, \mathbf{y}, \mathbf{z}; \mathbf{x}_s, \mathbf{y}_s)|^2 + |u_{\text{ref}}(\mathbf{x}, \mathbf{y}; \mathbf{x}_s, \mathbf{y}_s)|^2 \\ &\quad + u_o(\mathbf{x}, \mathbf{y}, \mathbf{z}; \mathbf{x}_s, \mathbf{y}_s) u_{\text{ref}}^*(\mathbf{x}, \mathbf{y}; \mathbf{x}_s, \mathbf{y}_s) \\ &\quad + u_o^*(\mathbf{x}, \mathbf{y}, \mathbf{z}; \mathbf{x}_s, \mathbf{y}_s) u_{\text{ref}}(\mathbf{x}, \mathbf{y}; \mathbf{x}_s, \mathbf{y}_s)] d\mathbf{x}_s d\mathbf{y}_s \end{aligned} \quad (\text{B.2})$$

where u^* represents the complex conjugate of u . Since the term relating to the field of the object wave is of interest, we consider only the third term for holographic

reconstruction. Thus, the reconstructed wave is

$$\begin{aligned}
u_R(\mathbf{x}, \mathbf{y}, \mathbf{z}) &= \int_{-\frac{D}{2}}^{\frac{D}{2}} \int_{-\frac{D}{2}}^{\frac{D}{2}} u_o(\mathbf{x}, \mathbf{y}, \mathbf{z}; \mathbf{x}_s, \mathbf{y}_s) u_{\text{ref}}^*(\mathbf{x}, \mathbf{y}; \mathbf{x}_s, \mathbf{y}_s) d\mathbf{x}_s d\mathbf{y}_s \\
&= \int_{-\frac{D}{2}}^{\frac{D}{2}} \int_{-\frac{D}{2}}^{\frac{D}{2}} \left(\iiint t(\mathbf{x}_1, \mathbf{y}_1, \mathbf{z} - \mathbf{z}_1) h_o(\mathbf{x} - M\mathbf{x}_1, \mathbf{y} - M\mathbf{y}_1, \mathbf{z}_1) \right. \\
&\quad \left. \exp \left\{ i \frac{\pi}{\lambda(d_s + \mathbf{z}_1)} [(\mathbf{x}_1 - \mathbf{x}_s)^2 + (\mathbf{y}_1 - \mathbf{y}_s)^2] \right\} d\mathbf{x}_1 d\mathbf{y}_1 d\mathbf{z}_1 \right) \\
&\quad \left(\iiint h_{\text{ref}}^*(\mathbf{x} - M\mathbf{x}'_1, \mathbf{y} - M\mathbf{y}'_1, \mathbf{z}'_1) \right. \\
&\quad \left. \exp \left\{ -i \frac{\pi}{\lambda(d_s + \mathbf{z}'_1)} [(\mathbf{x}'_1 - \mathbf{x}_s)^2 + (\mathbf{y}'_1 - \mathbf{y}_s)^2] \right\} d\mathbf{x}'_1 d\mathbf{y}'_1 d\mathbf{z}'_1 \right) d\mathbf{x}_s d\mathbf{y}_s
\end{aligned}$$

Since both beams propagate through the same system and the planes in the object and reference beams with the same distance from the source interfere only with each other, we can assume that $\mathbf{z}_1 = \mathbf{z}'_1$ and thus

$$\begin{aligned}
u_R(\mathbf{x}, \mathbf{y}, \mathbf{z}) &= \iiint \iiint t(\mathbf{x}_1, \mathbf{y}_1, \mathbf{z} - \mathbf{z}_1) h_o(\mathbf{x} - M\mathbf{x}_1, \mathbf{y} - M\mathbf{y}_1, \mathbf{z}_1) \\
&\quad h_{\text{ref}}^*(\mathbf{x} - M\mathbf{x}'_1, \mathbf{y} - M\mathbf{y}'_1, \mathbf{z}_1) \exp \left\{ i \frac{\pi}{\lambda(d_s + \mathbf{z}_1)} [(\mathbf{x}_1 - \mathbf{x}'_1)^2 + (\mathbf{y}_1 - \mathbf{y}'_1)^2] \right\} \\
&\quad \text{sinc} \left(\frac{D}{\lambda(d_s + \mathbf{z}_1)} (\mathbf{x}_1 - \mathbf{x}'_1) \right) \text{sinc} \left(\frac{D}{\lambda(d_s + \mathbf{z}_1)} (\mathbf{y}_1 - \mathbf{y}'_1) \right) \\
&\quad d\mathbf{x}_1 d\mathbf{y}_1 d\mathbf{z}_1 d\mathbf{x}'_1 d\mathbf{y}'_1
\end{aligned} \tag{B.3}$$

If the source size is very large, then the coherence area will be very small and the following approximation can be assumed:

$$\text{sinc} \left(\frac{D}{\lambda(d_s + \mathbf{z}_1)} (\mathbf{x}_1 - \mathbf{x}'_1) \right) \text{sinc} \left(\frac{D}{\lambda(d_s + \mathbf{z}_1)} (\mathbf{y}_1 - \mathbf{y}'_1) \right) \approx \delta(\mathbf{x}_1 - \mathbf{x}'_1) \delta(\mathbf{y}_1 - \mathbf{y}'_1).$$

This implies that one point in the object beam is coherent with only one point in the reference beam. Therefore the reconstructed field is:

$$\begin{aligned}
u_R(\mathbf{x}, \mathbf{y}, \mathbf{z}) &= \iiint [t(\mathbf{x}_1, \mathbf{y}_1, \mathbf{z} - \mathbf{z}_1) h_o(\mathbf{x} - M\mathbf{x}_1, \mathbf{y} - M\mathbf{y}_1, \mathbf{z}_1) \\
&\quad h_{\text{ref}}^*(\mathbf{x} - M\mathbf{x}_1, \mathbf{y} - M\mathbf{y}_1, \mathbf{z}_1)] d\mathbf{x}_1 d\mathbf{y}_1 d\mathbf{z}_1.
\end{aligned}$$

By changing variables, we can express the reconstructed field in terms of convolution between the object and the PSF of the system as follows:

$$\begin{aligned} u_R(\mathbf{x}, \mathbf{y}, \mathbf{z}) &= \iiint t'(\mathbf{x}', \mathbf{y}', \mathbf{z} - \mathbf{z}_1) h(\mathbf{x} - \mathbf{x}', \mathbf{y} - \mathbf{y}', \mathbf{z}_1) d\mathbf{x}' d\mathbf{y}' d\mathbf{z}_1 \\ &= t'(\mathbf{x}, \mathbf{y}, \mathbf{z}) *** h(\mathbf{x}, \mathbf{y}, \mathbf{z}) \end{aligned}$$

where the scaled version of the object $t'(\mathbf{x}, \mathbf{y}, \mathbf{z})$ is

$$t'(\mathbf{x}, \mathbf{y}, \mathbf{z}) = \frac{1}{M^2} t\left(\frac{\mathbf{x}}{M}, \frac{\mathbf{y}}{M}, \mathbf{z}\right)$$

and the system PSF $h(\mathbf{x}, \mathbf{y}, \mathbf{z})$ when assuming an ideal large source is

$$h(\mathbf{x}, \mathbf{y}, \mathbf{z}) = h_o(\mathbf{x}, \mathbf{y}, \mathbf{z}) h_{\text{ref}}^*(\mathbf{x}, \mathbf{y}, \mathbf{z}).$$

If the source size is not sufficiently large to be considered as an infinite source, then it will affect the system PSF. By substituting $t(\mathbf{x}_1, \mathbf{y}_1, \mathbf{z} - \mathbf{z}_1)$ in (B.3) with $\delta(\mathbf{x}_1, \mathbf{y}_1, \mathbf{z} - \mathbf{z}_1)$, the PSF of the system is

$$\begin{aligned} h(\mathbf{x}, \mathbf{y}, \mathbf{z}) &= h_o(\mathbf{x}, \mathbf{y}, \mathbf{z}) \iint h_{\text{ref}}^*(\mathbf{x} - M\mathbf{x}', \mathbf{y} - M\mathbf{y}', \mathbf{z}) \exp\left\{i\frac{\pi}{\lambda(d_s + \mathbf{z})}[\mathbf{x}'^2 + \mathbf{y}'^2]\right\} \\ &\quad \text{sinc}\left(\frac{D\mathbf{x}'_1}{\lambda(d_s + \mathbf{z})}\right) \text{sinc}\left(\frac{D\mathbf{y}'_1}{\lambda(d_s + \mathbf{z})}\right) d\mathbf{x}'_1 d\mathbf{y}'_1 \\ &= h_o(\mathbf{x}, \mathbf{y}, \mathbf{z}) \iint h_{\text{ref}}^*(\mathbf{x} - \xi, \mathbf{y} - \eta, \mathbf{z}) \frac{1}{M^2} \exp\left\{i\frac{\pi}{\lambda(d_s + \mathbf{z})}\left[\left(\frac{\xi}{M}\right)^2 + \left(\frac{\eta}{M}\right)^2\right]\right\} \\ &\quad \text{sinc}\left(\frac{D\xi}{M\lambda(d_s + \mathbf{z})}\right) \text{sinc}\left(\frac{D\eta}{M\lambda(d_s + \mathbf{z})}\right) d\xi d\eta \\ &= h_o(\mathbf{x}, \mathbf{y}, \mathbf{z}) [h_{\text{ref}}^*(\mathbf{x}, \mathbf{y}, \mathbf{z}) ** \mathcal{D}(\mathbf{x}, \mathbf{y})] \end{aligned}$$

where $\mathcal{D}(\mathbf{x}, \mathbf{y})$ can be expressed as

$$\mathcal{D}(\mathbf{x}, \mathbf{y}) = \frac{1}{M^2} \text{sinc}\left(\frac{D\mathbf{x}}{\lambda M(d_s + \mathbf{z})}\right) \text{sinc}\left(\frac{D\mathbf{y}}{\lambda M(d_s + \mathbf{z})}\right) \exp\left\{i\frac{\pi}{\lambda M^2(d_s + \mathbf{z})}[\mathbf{x}^2 + \mathbf{y}^2]\right\}.$$

APPENDIX C

The Grouped Coordinated Ascent Algorithm (GCA)

The grouped coordinated ascent (GCA) algorithm was developed in [42, 43, 99] to enable parallelization. In this algorithm, pixels are divided into a typically small number of groups. The pixels in the same group are chosen to be spatially separated so that they are approximately decoupled from each other. All pixels within each group are updated simultaneously using up to as many processors as there are pixels within the group. One iteration consists of cycling sequentially through all groups.

1	2	1	2	1	2
3	4	3	4	3	4
1	2	1	2	1	2
3	4	3	4	3	4

Figure C.1: Example of groups in GCA algorithm. Pixels with the same group index are updated simultaneously.

In Figure C.1, the same number corresponds to the same group which is assigned to different processors. Thus the total of 4 groups can be performed on up to 6 processors.

The idea of GCA-PS algorithm is to first separate pixels into groups and then find a separable paraboloidal surrogate function for each group.

$$\Phi(x_{S^n}, x_{\bar{S}^n}^n) \geq \Phi(x_{S^n}; x^n) \geq \phi(x_{S^n}; x^n) = \sum_{j \in S^n} Q_j(x_j; x^n)$$

where S^n denotes the group at the n th iteration and

$$\begin{aligned}\Phi(x_{S^n}; x^n) &= \sum_i \sum_{j \in S^n} \alpha_{ij} \psi_i \left(\frac{b_{ij}}{\alpha_{ij}} (x_j - x_j^n) + [Bx^n]_i \right), \\ Q_j(x_j; x^n) &= \sum_i \alpha_{ij} q_i \left(\frac{b_{ij}}{\alpha_{ij}} (x_j - x_j^n) + [Bx^n]_i; [Bx^n] \right).\end{aligned}$$

Since $\sum_{j \in S^n} \alpha_{ij} = 1$, one choice of α_{ij} is $\frac{|b_{ij}|}{\sum_{k \in S^n} |b_{ik}|}$. Thus the update x is obtained by:

$$\begin{aligned}x_j^{n+1} &= \arg \max_{x_j \geq 0} Q_j(x_j; x^n) \\ &= \left[x_j^n + \frac{\frac{\partial}{\partial x_j} Q_j(x_j; x^n) \Big|_{x_j=x_j^n}}{-\frac{\partial^2}{\partial x_j^2} Q_j(x_j; x^n) \Big|_{x_j=x_j^n}} \right]_+, \quad \forall j \in S^n\end{aligned}$$

where

$$\begin{aligned}\frac{\partial}{\partial x_j} Q_j(x_j; x^n) \Big|_{x_j=x_j^n} &= \sum_i b_{ij} \dot{q}_i([Bx^n]_i) = \frac{\partial}{\partial x_j} \Phi(x) \Big|_{x=x^n} \\ -\frac{\partial^2}{\partial x_j^2} Q_j(x_j; x^n) \Big|_{x_j=x_j^n} &= \sum_i b_{ij}^2 \frac{c_i^n}{\alpha_{ij}}\end{aligned}$$

For $j \notin S^n$, $x_j^{n+1} = x_j^n$. Note that to derive the GCA-PS algorithm, we must have a concave function of the objective function so that the concavity technique is feasible.

The PS-GCA algorithm is derived in a similar way; however, the paraboloidal surrogate function is obtained first and then the GCA algorithm is applied on the parabola. This allows application of the approach even to nonconcave objective functions. Here are the surrogates for the PS-GCA algorithm:

$$\Phi(x) \geq \tilde{Q}(x; x^n) \geq \tilde{\phi}(x; x^n) = \sum_{j \in S^n} \tilde{Q}_j(x; x^n)$$

where

$$\begin{aligned}\tilde{Q}(x; x^n) &= \sum_i q_i([Bx]_i; [Bx^n]_i) \\ \tilde{\phi}(x; x^n) &= \sum_i \sum_{j \in S} \alpha_{ij} q_i \left(\frac{b_{ij}}{\alpha_{ij}} (x_j - x_j^n) + [Bx^n]_i; [Bx^n] \right) \\ \tilde{Q}_j(x_j; x^n) &= \sum_i \alpha_{ij} q_i \left(\frac{b_{ij}}{\alpha_{ij}} (x_j - x_j^n) + [Bx^n]_i; [Bx^n] \right).\end{aligned}$$

Without sub-iterations for maximizing x in each group, the GCA-PS and PS-GCA algorithms yield the same results for concave objective functions.

APPENDIX D

Curvature Proof

For simplicity, we drop the subscript “ i ” in this appendix and the following proofs consider only the real or imaginary part.

Lemma 1: If $h(l)$ and $q(l)$ are differentiable and the following three conditions are satisfied:

$$(C1) \quad h(m) = q(m) \text{ for some } m$$

$$(C2) \quad \dot{q}(l) \geq \dot{h}(l), \forall l \geq m$$

$$(C3) \quad \dot{q}(l) \leq \dot{h}(l), \forall l \leq m$$

Then it follows that $q(l) \geq h(l), \forall l$ and thus $q(l)$ is a surrogate for $h(l)$, i.e., $q(l) \geq h(l), \forall l$.

Proof: For $l \geq m$, then

$$\begin{aligned} q(l) &= q(m) + \int_m^l \dot{q}(t) dt \\ &\geq h(m) + \int_m^l \dot{h}(t) dt = h(l) \end{aligned}$$

For $l \leq m$, then

$$\begin{aligned} q(l) &= h(m) + \int_l^m [-\dot{q}(t)] dt \\ &\geq h(m) + \int_l^m [-\dot{h}(t)] dt = h(l) \end{aligned}$$

Thus, $q(l) \geq h(l), \forall l$ under the above conditions. \square

Lemma 2: If $h(l)$ is differentiable and the following maximum is finite and non-negative,

$$c(m) = \max_{l \neq m} \frac{\dot{h}(l) - \dot{h}(m)}{l - m},$$

then

$$q(l) = h(m) + \dot{h}(m)(l - m) + \frac{1}{2}c(m)(l - m)^2 \quad (\text{D.1})$$

is a parabolic surrogate for h , i.e., $q(l) \geq h(l), \forall l$.

Proof: Condition (C1) of Lemma 1 is clearly satisfied by q when $l = m$. To prove Condition (C2), for $l \geq m$, we differentiate (D.1) with respect to l and substitute $c(m)$ with the proposed curvature as follows:

$$\begin{aligned} \dot{q}(l) &= \dot{h}(m) + c(m)(l - m) \\ &\geq \dot{h}(m) + \frac{\dot{h}(l) - \dot{h}(m)}{l - m}(l - m) = \dot{h}(l). \end{aligned}$$

Similarly, $\dot{q}(l) \leq \dot{h}(l)$, for $l \leq m$, so Condition (C3) is satisfied. Because all three conditions of Lemma 1 are satisfied, $q(l)$ is a parabolic surrogate for $h(l)$. \square

APPENDIX E

Derivation of a Closed-Form Curvature

The first derivative of h in (7.12) or (7.13) is

$$\dot{h}^o(l; l^n) = \frac{-2y(l + u^o)[(l^{o,n} + u^o)^2 + b/2]}{k^n[(l + u^o)^2 + b/2]} + 2(l + u^o). \quad (\text{E.1})$$

Thus we define

$$f(l) \triangleq \frac{\dot{h}^o(l; l^n) - \dot{h}^o(l^{o,n}; l^n)}{l - l^{o,n}} = \frac{2y}{k^n} \left[\frac{(l + u^o)(l^{o,n} + u^o) - b/2}{(l + u^o)^2 + b/2} \right] + 2. \quad (\text{E.2})$$

To obtain the maximum of the above continuous function, we equate the first derivative to zero:

$$\dot{f}(l) = \frac{2y}{k^n} \left[\frac{-(l^{o,n} + u^o)(l + u^o)^2 + b(l + u^o) + \frac{b}{2}(l^{o,n} + u^o)}{[(l + u^o)^2 + b/2]^2} \right] = 0. \quad (\text{E.3})$$

Then the optimal l^* that yields the maximum is

$$l^* = \frac{b + \sqrt{b^2 + 4(l^{o,n} + u^o)^2}}{2(l^{o,n} + u^o)} - u^o \quad (\text{E.4})$$

and

$$f(l^*) = \frac{2y\sqrt{b^2 + 4(l^{o,n} + u^o)^2}(l^{o,n} + u^o)^2}{k^n \left\{ (l^{o,n} + u^o)^2(b + 2) + b \left[b + \sqrt{b^2 + 4(l^{o,n} + u^o)^2} \right] \right\}} + 2 \quad (\text{E.5})$$

is the curvature of the parabolic surrogate function.

BIBLIOGRAPHY

BIBLIOGRAPHY

- [1] The XCOSM deconvolution package [Online]. Available: <http://3dmicroscopy.wustl.edu/~xcosm/>.
- [2] D. A. Agard. Optical Sectioning Microscopy: Cellular Architecture in Three Dimensions. *Annu. Rev. Biophys. Bioeng.*, 13:191–219, 1984.
- [3] D. A. Agard, Y. Hiraoka, P. Shaw, and J. W. Sedat. Fluorescence Microscopy in Three Dimensions. In D. L. Taylor and Y. Wang, editors, *Fluorescence Microscopy of Living Cells in Culture*, pages 353–377. Academic Press, San Diego, 1989.
- [4] S. Ahn and J. A. Fessler. Globally Convergent Ordered Subsets Algorithms: Application to Tomography. In *Proc. IEEE Nuc. Sci. Symp. Med. Im. Conf.*, pages 1064–1068, 2001.
- [5] S. Ahn and J. A. Fessler. Globally convergent image reconstruction for emission tomography using relaxed ordered subsets algorithms. *IEEE Trans. Med. Imaging*, 2003. To appear.
- [6] G. M. Amdahl. Validity of the single-processor approach to achieving large scale computing capabilities. In *AFIPS Conference Proceedings*, volume 30, pages 483–485. AFIPS Press, 1967.
- [7] E. Arons and E. Leith. Coherence confocal-imaging system for enhanced depth discrimination in transmitted light. *Applied Optics*, 35(14):2499–2506, May 1996.
- [8] M. R. Banham and A. K. Katsaggelos. Digital Image Restoration. *IEEE Signal Processing Magazine*, pages 24–41, March 1997.
- [9] L. Bedini, I. Gerace, A. Tonazzini, and P. Gualtieri. Edge-preserving Restoration in 2-D Fluorescence Microscopy. *Micron*, 27(6):431–447, 1996.
- [10] M. Bertero and P. Boccacci. Application of the OS-EM method to the restoration of LBT images. *Astron. Astrophys. Suppl. Ser.*, 144(1):181–186, May 2000.
- [11] D. P. Bertsekas. A new class of incremental gradient methods for least squares problems. *SIAM J. Optim.*, 7(4):913–926, November 1997. <http://epubs.siam.org/sam-bin/dbq/article/28702>.

- [12] M. Born and E. Wolf. *Principles of Optics*. Pergamon Press, New York, 6 edition, 1980.
- [13] C. Bouman and K. Sauer. A generalized Gaussian image model for edge-preserving MAP estimation. *IEEE Tr. Im. Proc.*, 2(3):296–310, July 1993.
- [14] C. A. Bouman and K. Sauer. A Unified Approach Statistical Tomography Using Coordinate Descent Optimization. *IEEE Trans. Image Processing*, 5(3):480–492, March 1996.
- [15] G. J. Brakenhoff, P. Blom, and P. Barends. Confocal scanning light microscopy with high aperture immersion lenses. *J. Microscopy*, 117:219–232, November 1979.
- [16] G. J. Brakenhoff, E. A. van Spronsen, H. T. M. van der Voort, and N. Nanninga. Three-Dimensional Confocal Fluorescence Microscopy. In D. L. Taylor and Y. Wang, editors, *Fluorescence Microscopy of Living Cells in Culture*, pages 379–398. Academic Press, San Diego, 1989.
- [17] J. A. Browne and A. R. De Pierro. A row-action alternative to the EM algorithm for maximizing likelihoods in emission tomography. *IEEE Trans. Med. Imaging*, 15(5):687–699, October 1996.
- [18] C. L. Byrne. Convergent Block-Iterative Algorithms for Image Reconstruction from Inconsistent Data. *IEEE Trans. Image Processing*, 6(9):1296–1304, September 1997.
- [19] C. L. Byrne. Accelerating The EMLL Algorithm and Related Iterative Algorithms by Rescaled Block-Iterative Methods. *IEEE Trans. Image Processing*, 7(1):100–109, January 1998.
- [20] M. Çetin, W. C. Karl, and A. S. Willsky. Edge-preserving image reconstruction for coherent imaging applications. In *Proc. IEEE Int'l Conf. on Image Processing*, volume 2, pages 481–484, 2002.
- [21] P. Charbonnier, L. Blanc-Féraud, G. Aubert, and M. Barlaud. Deterministic Edge-Preserving Regularization in Computed Imaging. *IEEE Trans. Image Processing*, 6(2):298–311, February 1997.
- [22] H. Chen, M. Shih, E. Arons, E. Leith, J. Lopez, D. Dilworth, and P. C. Sun. Electronic holographic imaging through living human tissue. *Applied Optics*, 33(17):3630–3632, June 1994.
- [23] P. C. Cheng, T. H. Lin, W. L. Wu, and J. L. Wu. *Multidimensional Microscopy*. Springer-Verlag, New York, 1994.
- [24] J. A. Conchello. Tutorials: Image Resotration for 3-D Microscopy.

- [25] J. A. Conchello. Superresolution and convergence properties of the expectation-maximization algorithm for maximum-likelihood deconvolution of incoherent images. *J. Opt. Soc. Am. A*, 15(10):2609–2619, October 1998.
- [26] J. A. Conchello and E. W. Hansen. Enhanced 3-D reconstruction from confocal scanning microscope images. 1: Deterministic and maximum likelihood reconstructions. *Applied Optics*, 29(26):3795–3804, September 1990.
- [27] J. A. Conchello, J. J. Kim, and E. W. Hansen. Enhanced three-dimensional reconstruction from confocal scanning microscope images. ii. Depth discrimination versus signal-to-noise ratio in partially confocal images. *Applied Optics*, 33(17):3740–3750, June 1994.
- [28] J. A. Conchello and J. G. McNally. Fast regularization technique for expectation maximization algorithm for computational optical sectioning microscopy. In C. J. Cogswell, G. S. Kino, and T. Wilson, editors, *Three-dimensional and multidimensional microscopy: Image Acquisition and Processing*, pages 199–208. Proc. SPIE 2655, 1996.
- [29] J. A. Conchello and Q. Yu. Parametric blind deconvolution of fluorescent microscopy images: Preliminary results. In C. J. Cogswell, G. Kino, and T. Wilson, editors, *Three-dimensional and multidimensional microscopy: Image Acquisition and Processing III*, pages 164–174. Proc. SPIE 2655, 1996.
- [30] T. R. Corle and G. S. Kino. *Confocal Scanning Optical Microscope and Related Imaging Systems*. Academic Press, 1996.
- [31] G. Cox and C. Sheppard. Effects of image deconvolution on optical sectioning in conventional and confocal microscopes. *Bioimaging*, 1(2):82–95, June 1993.
- [32] E. Cuche, F. Bevilacqua, and C. Depeursinge. Digital holography for quantitative phase-contrasting imaging. *Optics Letters*, 24(5):291–293, March 1999.
- [33] E. Cuche, P. Marquet, and C. Depeursinge. Spatial filtering for zero-order and twin-image elimination in digital off-axis holography. *Applied Optics*, 39(23):4070–4075, August 2000.
- [34] J. C. D. de Melo. Partial FFT Evaluation. In *Int'l Conf. on Signal Processing Application and Technology*, volume 1, pages 134–141, 1996. Available: <http://www.icspat.com/papers/234amfi.pdf>.
- [35] S. De Nicola, P. Ferraro, A. Finizio, and G. Pierattini. Wave front reconstruction of fresnel off-axis holograms with compensation of aberrations by means of phase-shifting digital holography. *Optics and Lasers in Engineering*, 37(4):331–340, April 2002.
- [36] A. R. De Pierro. A modified expectation maximization algorithm for penalized likelihood estimation in emission tomography. *IEEE Trans. Med. Imaging*, 14(1):132–137, March 1995.

- [37] A. R. De Pierro and M. E. B. Yamagishi. Fast EM-like methods for maximum 'a posteriori' estimates in emission tomography. *IEEE Trans. Med. Imaging*, 20(4):280–288, April 2001.
- [38] A. H. Delaney and Y. Bresler. Globally convergent edge-preserving regularized reconstruction: an application to limited-angle tomography. *IEEE Trans. Image Processing*, 7(2):204–221, February 1998.
- [39] A. P. Dempster, N. M. Laird, and D. B. Rubin. Maximum Likelihood from Incomplete Data via the EM Algorithm. *J. Roy. Stat. Soc. B*, 39:1–38, 1977.
- [40] H. Erdoğan and J. A. Fessler. Monotonic Algorithms for Transmission Tomography. *IEEE Trans. Med. Imaging*, 18(9):801–814, September 1999.
- [41] H. Erdoğan and J. A. Fessler. Ordered subsets algorithm for transmission tomography. *Phys. Med. Biol.*, 44(11):2835–2851, November 1999.
- [42] J. A. Fessler. Grouped-coordinate ascent algorithms for penalized-likelihood transmission image reconstruction. *IEEE Trans. Med. Imaging*, 16(2):166–175, April 1997.
- [43] J. A. Fessler. Grouped Coordinate Descent Algorithms for Robust Edge-Preserving Image Restoration. In T. J. Schulz, editor, *Image reconstruction and restoration II*, pages 184–194. Proc. SPIE 3170, July 1997.
- [44] J. A. Fessler and S. D. Booth. Conjugate-gradient preconditioning methods for shift-variant PET image reconstruction. *IEEE Tr. Im. Proc.*, 8(5):688–99, May 1999.
- [45] J. A. Fessler and N. Clinthorne. Statistical Methods for Image Reconstruction and Medical Imaging System Design. In *Proc. IEEE Nuc. Sci. Symp. and Med. Im. Conf.*, November 1998.
- [46] J. A. Fessler and H. Erdoğan. A Paraboloidal Surrogates Algorithm for Convergent Penalized-Likelihood Emission Image Reconstruction. In *Proc. IEEE Nuc. Sci. Symp. and Med. Im. Conf.*, volume 2, pages 1132–1135, 1998.
- [47] J. A. Fessler and E. P. Ficaro. Fully 3D PET image reconstruction using a Fourier preconditioned conjugate-gradient algorithm. In *Proc. IEEE Nuc. Sci. Symp. Med. Im. Conf.*, volume 3, pages 1599–1602, 1996.
- [48] J. A. Fessler and A. O. Hero. Space-Alternating Generalized Expectation-Maximization Algorithm. *IEEE Trans. Signal Processing*, 42(10):2664–2677, October 1994.
- [49] J. A. Fessler and A. O. Hero. Penalized Maximum-Likelihood Image Reconstruction Using Space-Alternating Generalized EM Algorithms. *IEEE Trans. Image Processing*, 4(10):1417–1429, October 1995.

- [50] D. Gabor. A New microscope Principle. *Nature*, 161:777–778, 1948.
- [51] D. Gabor. Microscopy by Reconstructed Wave-Fronts. *Proc. Roy. Soc.*, A197:454–487, 1949.
- [52] D. Gabor. Microscopy by Reconstructed Wave Fronts II. *Proc. Phys. Soc.*, B64:449–469, 1951.
- [53] D. Geman and G. Reynolds. Constrained restoration and the recovery of discontinuities. *IEEE Trans. Patt. Anal. Mach. Int.*, 14(3):367–383, March 1992.
- [54] D. Geman and C. Yang. Nonlinear Image Recovery with Half-Quadratic Regularization. *IEEE Trans. Image Processing*, 4(7):932–946, July 1995.
- [55] S. Geman and D. Geman. Stochastic relaxation, Gibbs distributions, and Bayesian restoration of images. *IEEE Tr. Patt. Anal. Mach. Int.*, 6(6):721–41, November 1984.
- [56] R. C. Gonzalez and R. E. Woods. *Digital Image Processing*. Addison-Wesley, Massachusetts, 1992.
- [57] J. W. Goodman. *Introduction to Fourier Optics*. McGraw-Hill, New York, 1996.
- [58] P. J. Green. Bayesian reconstructions from emission tomography data using a modified EM algorithm. *IEEE Tr. Med. Im.*, 9(1):84–93, March 1990.
- [59] P. J. Green. On use of the EM algorithm for penalized likelihood estimation. *J. Royal Stat. Soc. Ser. B*, 52(3):443–452, 1990.
- [60] M. Gu. *Principles of Three-Dimensional Imaging in Confocal Microscopes*. World Scientific, New Jersey, 1996.
- [61] G. Harikumar and Y. Bresler. Perfect Blind Restoration of Images Blurred by Multiple Filters: Theory and Efficient Algorithms. *IEEE Trans. Image Processing*, 8(2):202–219, February 1999.
- [62] T. Hebert and R. Leahy. A Bayesian reconstruction algorithm for emission tomography using a Markov random field prior. In *Proc. SPIE 1092, Med. Im. III: Im. Proc.*, pages 458–466, 1989.
- [63] T. Hebert and R. Leahy. A generalized EM algorithm for 3-D Bayesian reconstruction from Poisson data using Gibbs priors. *IEEE Tr. Med. Im.*, 8(2):194–202, June 1989.
- [64] T. J. Hebert. Statistical stopping criteria for iterative maximum likelihood reconstruction of emission images. *Phys. Med. Biol.*, 35(9):1221–32, September 1990.

- [65] T. J. Holmes. Maximum-likelihood image restoration adapted for noncoherent optical imaging. *J. Opt. Soc. Am. A*, 5(5):666–673, May 1988.
- [66] T. J. Holmes. Blind deconvolution of quantum-limited incoherent imagery: maximum-likelihood approach. *J. Opt. Soc. Am. A*, 9(7):1052–1061, July 1992.
- [67] T. J. Holmes and Y. H. Liu. Image Restoration for 2-D and 3-D Fluorescence Microscopy. In A. Kriete, editor, *Visualization in Biomedical Microscopies*, pages 283–327. VCH, New York, 1992.
- [68] P. J. Huber. *Robust Statistics*. Wiley, New York, 1981.
- [69] H. M. Hudson and R. S. Larkin. Accelerated image reconstruction using ordered subsets of projection data. *IEEE Trans. Med. Imaging*, 13(4):601–609, December 1994.
- [70] B. R. Hunt. The Application of Constrained Least Squares Estimation to Image Restoration by Digital Computer. *IEEE Trans. Computers*, C-22(9):805–812, September 1973.
- [71] A. K. Jain. *Fundamentals of digital image processing*. Prentice-Hall, New Jersey, 1989.
- [72] P. A. Jansson, R. H. Hunt, and E. K. Plyler. Resolution enhancement of spectra. *J. Opt. Soc. Am. A*, 60(5):596–599, May 1970.
- [73] S. Joshi and M. I. Miller. Maximum a posteriori estimation with Good’s roughness for three-dimensional optical-sectioning microscopy. *J. Opt. Soc. Am. A*, 10(5):1078–1085, May 1993.
- [74] W. Kim and M. H. Hayes. Phase retrieval using two Fourier-transform intensities. *J. Opt. Soc. Am. A*, 7(3):441–449, March 1990.
- [75] S. Kimura and C. Munakata. Calculation of three-dimensional optical transfer function for a confocal scanning fluorescent microscope. *J. Opt. Soc. Am. A*, 6(7):1015–1019, July 1989.
- [76] S. Kimura and C. Munakata. Dependence of 3-d optical transfer functions on the pinhole radius in a fluorescent confocal optical microscope. *Applied Optics*, 29(20):3007–3011, July 1990.
- [77] D. Kundur and D. Hatzinakos. Blind image deconvolution. *IEEE Signal Processing Magazine*, 13(3):43–64, May 1996.
- [78] R. L. Lagendijk, J. Biemond, and D. E. Boeke. Regularized Iterative Image Restoration with Ringing Reduction. *IEEE Trans. Acoustics, Speech and Signal Processing*, 36(12):1874–1887, December 1988.
- [79] E. Y. Lam and J. W. Goodman. Iterative statistical approach to blind image deconvolution. *J. Opt. Soc. Am. A*, 17(7):1177–1184, July 2000.

- [80] R. G. Lane. Methods for maximum-likelihood deconvolution. *J. Opt. Soc. Am. A*, 13(10):1992–1998, October 1996.
- [81] K. Lange. Convergence of EM Image Reconstruction Algorithms with Gibbs Smoothing. *IEEE Trans. M. Imaging*, 9(4):439–446, December 1990.
- [82] E. Leith, H. Chen, Y. Chen, D. Dilworth, J. Lopez, R. Masri, J. Rudd, and J. Valdmanis. Electronic holography and speckle methods for imaging through tissue using femtosecond gated pulses. *Applied Optics*, 30(29):4204–4210, October 1991.
- [83] E. N. Leith, W.-C. Chien, K. D. Mills, B. D. Athey, and D. S. Dilworth. Optical sectioning by holographic coherence imaging: a generalized analysis. *J. Opt. Soc. Am. A*, 20(2):380–387, February 2003.
- [84] E. N. Leith and G. J. Swanson. Recording of phase-amplitude images. *Applied Optics*, 20(17):3081–3084, September 1981.
- [85] E. N. Leith and J. Upatnieks. Reconstructed Wavefronts and Communication Theory. *J. Opt. Soc. Am. A*, 52(10):1123–1130, October 1962.
- [86] E. N. Leith and G. C. Yang. Interferometric spatial formation with an extended source. *Applied Optics*, 20(22):3819–3821, November 1981.
- [87] M. Liebling, T. Blu, E. Cuche, P. Marquet, C. Depeursinge, and M. Unser. A novel non-diffractive reconstruction method for digital holographic microscopy. In *Proc. IEEE Int'l Symp. on Biomedical Imaging*, pages 625–628, 2002.
- [88] J. S. Lim. *Two-dimensional signal and image processing*. Prentice-Hall, New Jersey, 1990.
- [89] L. B. Lucy. An iterative technique for the rectification of observed distributions. *Astronomical Journal*, 79(6):745–754, June 1974.
- [90] J. Markham and J. A. Conchello. Parametric blind deconvolution of microscopic images: Further results. In C. J. Cogswell, J. A. Conchello, J. M. Lerner, T. Lu, and T. Wilson, editors, *Three-dimensional and multidimensional microscopy: Image Acquisition and Processing V*, pages 38–49. Proc. SPIE 3261, 1998.
- [91] J. Markham and J. A. Conchello. Parametric blind deconvolution: a robust method for the simultaneous estimation of image and blur. *J. Opt. Soc. Am. A*, 16(10):2377–2391, October 1999.
- [92] J. L. Marroquin and M. Tapia. Parallel algorithms for phase unwrapping based on markov random field models. *J. Opt. Soc. Am. A*, 12(12):2578–2585, December 1995.

- [93] M. Minsky. Microscopy Apparatus. U.S. Patent #3013467, 1957.
- [94] M. Minsky. Memoir on inventing the confocal scanning microscope. *Scanning*, 10:128–138, 1988.
- [95] S. K. Mitra. *Digital signal procesing: A computer-based approach*. McGraw-Hill, New York, 2 edition, 2001.
- [96] E. Ü Mumcuoğlu, R. M. Leahy, and S. R. Cherry. Bayesian reconstruction of PET images: methodology and performance analysis. *Phys. Med. Biol.*, 41(9):1777–1807, September 1996.
- [97] P. B. Pawley, editor. *Handbook of Biological Confocal Microscopy*. Plenum Press, New York, 2 edition, 1995.
- [98] R. Richardson. Bayesian-based iterative method of image restoration. *J. Opt. Soc. Am.*, 62(1):55–59, January 1972.
- [99] K. D. Sauer, S. Borman, and C. A. Bouman. Parallel Computation of Sequential Pixel Updates in Statistical Tomographic Reconstruction. In *Proc. IEEE Int'l Conf. on Image Processing*, volume 2, pages 93–96, 1995.
- [100] P. J. Shaw and D. J. Rawlins. The point-spread function of a confocal microscope: its measurement and use in deconvolution of 3-D data. *J. Microscopy*, 163:151–165, August 1991.
- [101] C. J. R. Sheppard and A. Choudhury. Image formation in the scanning microscope. *Optica*, 24(10):1051–1073, October 1977.
- [102] C. J. R. Sheppard and D. M. Shotton. *Confocal laser scanning microscopy*. BIOS Scientific, Oxford, 1997.
- [103] C. J. R. Sheppard and T. Wilson. Depth of field in the scanning microscope. *Opt. Lett.*, 3(3):115–117, September 1978.
- [104] D. L. Snyder, A. M. Hammoud, and R. L. White. Image recovery from data acquired with a charge-coupled-device camera. *J. Opt. Soc. Am. A*, 10(5):1014–1023, May 1993.
- [105] D. L. Snyder, C. W. Helstrom, A. D. Lanterman, M. Faisal, and R. L. White. Compensation for readout noise in CCD images. *J. Opt. Soc. Am. A*, 12(2):272–283, February 1995.
- [106] D. L. Snyder and M. I. Miller. The use of sieves to stabilize images produced with the EM algorithm for emission tomography. *IEEE Tr. Nuc. Sci.*, 32(5):3864–71, October 1985.
- [107] D. L. Snyder, M. I. Miller, L. J. Thomas, and D. G. Politte. Noise and edge artifacts in maximum-likelihood reconstructions for emission tomography. *IEEE Tr. Med. Im.*, 6(3):228–38, September 1987.

- [108] S. Sotthivirat and J. A. Fessler. Partitioned Separable Paraboloidal Surrogate Coordinate Ascent Algorithm for Image Restoration. In *Proc. IEEE Int'l Conf. on Image Processing*, volume 1, pages 109–112, 2000.
- [109] S. Sotthivirat and J. A. Fessler. Image Recovery Using Partitioned-Separable Paraboloidal Surrogate Coordinate Ascent Algorithms. *IEEE Trans. Image Processing*, 11(3):306–317, March 2002.
- [110] S. Sotthivirat and J. A. Fessler. Relaxed ordered subsets algorithm for image restoration of confocal microscopy. In *Proc. IEEE Int'l Symp. on Biomedical Imaging*, pages 1051–1054, 2002.
- [111] S. Sotthivirat and J. A. Fessler. Relaxed Ordered-Subsets Algorithm for Penalized-Likelihood Image Restoration. *J. Opt. Soc. Am. A*, 20(3):439–449, March 2003.
- [112] S. Sotthivirat and J. A. Fessler. Statistical image reconstruction for digital holography. *J. Opt. Soc. Am. A*, 2003. Submitted.
- [113] J. W. Stayman and J. A. Fessler. Regularization for uniform spatial resolution properties in penalized-likelihood image reconstruction. *IEEE Tr. Med. Im.*, 19(6):601–15, June 2000.
- [114] E. H. K. Stelzer and F.-M. Haar. Confocal Microscopy: Recent Developments. In P. Hawkes, editor, *Advances in Imaging and Electron Physics*, pages 293–245. Academic Press, 1999.
- [115] P.-C. Sun and E. Arons. Nonscanning confocal ranging system. *Applied Optics*, 34(7):1254–1261, March 1995.
- [116] P.-C. Sun and E. N. Leith. Broad-source image plane holography as a confocal imaging process. *Applied Optics*, 33(4):597–602, February 1994.
- [117] Y. Takaki, H. Kawai, and H. Ohzu. Hybrid holographic microscopy free of conjugate and zero-order images. *Applied Optics*, 38(23):4990–4996, August 1999.
- [118] Y. Takaki and H. Ohzu. Fast numerical reconstruction technique for high-resolution hybrid holographic microscopy. *Applied Optics*, 38(11):2204–2211, April 1999.
- [119] E. Thiébaud and J.-M. Conan. Strict a priori constraints for maximum-likelihood blind deconvolution. *J. Opt. Soc. Am. A*, 12(3):485–492, 1995.
- [120] A. N. Tikhonov and V. Y. Arsenin. *Solutions of Ill-posed Problems*. Winston, Washington, DC, 1977.
- [121] L. Tong and S. Perreau. Multichannel Blind Identification: From Subspace to Maximum Likelihood Methods. *Proceedings of the IEEE*, 86(10):1951–1968, October 1998.

- [122] G. M. P. van Kempen, L. J. van Vliet, P. J. Verveer, and H. T. M. van der Voort. A quantitative comparison of image restoration methods for confocal microscopy. *J. Microscopy*, 185(3):354–365, March 1997.
- [123] Y. Vardi, L. A. Shepp, and L. Kaufman. A statistical model for positron emission tomography. *J. Am. Stat. Ass.*, 80(389):8–37, March 1985.
- [124] E. Veklerov and J. Llacer. Stopping rule for the MLE algorithm based on statistical hypothesis testing. *IEEE Tr. Med. Im.*, 6(4):313–9, December 1987.
- [125] P. J. Verveer and T. M. Jovin. Image restoration based on Good’s roughness penalty with application to fluorescence microscopy. *J. Opt. Soc. Am. A*, 15(5):1077–1083, May 1998.
- [126] C. Wagner, S. Seebacher, W. Osten, and W. Jüptner. Digital recording and numerical reconstruction of lensless fourier holograms in optical metrology. *Applied Optics*, 38(22):4812–4820, August 1999.
- [127] T. Wilson, editor. *Confocal Microscopy*. Academic Press, San Diego, CA, 1990.
- [128] T. Wilson and A. R. Carlini. Three-dimensional imaging in confocal imaging systems with finite sized detectors. *J. Microscopy*, 149(1):51–66, January 1988.
- [129] C. F. J. Wu. On the convergence properties of the EM algorithm. *Ann. Stat.*, 11(1):95–103, 1983.
- [130] D. Xie and L. Adams. New parallel SOR method by domain partitioning. *Siam J. Sci. Comput.*, 20(6):2261–2281, 1999.
- [131] I. Yamaguchi and T. Zhang. Phase-shifting digital holography. *Optics Letters*, 22(16):1268–1270, August 1997.
- [132] G. G. Yang, H. S. Chen, and E. Leith. Volume reflection holographic confocal imaging. *Applied Optics*, 39(23):4076–4079, August 2000.
- [133] Y. You and M. Kaveh. Blind Image Restoration by Anisotropic Regularization. *IEEE Trans. Image Processing*, 8(3):396–407, March 1999.

ABSTRACT

Statistical Image Recovery Techniques for Optical Imaging Systems

by

Saowapak Sotthivirat

Chair: Jeffrey A. Fessler

Statistical techniques are very attractive for image recovery because they can incorporate the physical model of imaging systems, thus improving the quality of recovered images. To overcome the ill-posed nature of image recovery, one often uses penalized-likelihood estimation. Since closed-form solutions for these statistical techniques are unavailable, iterative algorithms are needed. However, existing algorithms lack one or more desirable properties, such as the guarantee of convergence, rapid convergence, and efficient computation.

In the first part of the dissertation, we present a new, fast-converging algorithm called partitioned-separable paraboloidal surrogate coordinate ascent (PPCA). This algorithm captures the fast convergence of iterative coordinate ascent algorithms, while remaining parallelizable to reduce computation time. The PPCA algorithm is based on paraboloidal surrogate functions and a concavity technique. It is most

beneficial when applied to space-variant systems for which the fast Fourier transform (FFT) is inapplicable.

Because our primary applications are confocal microscopy and image plane holography, for which space-invariance of the systems is usually assumed, in the second part of the dissertation, we develop another algorithm that can be used with the FFT for fast computation time. We adapt the relaxed ordered-subset separable paraboloidal surrogate (OS-SPS) algorithm, which was originally invented for projection-based tomographic reconstruction, to pixel-based image restoration. The relaxed OS-SPS algorithm provides very fast initial convergence and is guaranteed to converge to the optimal solution. Furthermore, we develop different strategies for choosing subsets and efficient implementation. Both the PPCA and relaxed OS-SPS algorithms can be applied to many imaging problems; here we demonstrate their use for confocal microscopy problems.

In the third and last part of the dissertation, we develop a new statistical image reconstruction technique for digital holography including image plane holography. This approach reconstructs the complex object field from real-valued hologram intensity data. We develop a Poisson statistical model for this problem and derive an optimization transfer algorithm that monotonically decreases the cost function at each iteration and ensures convergence to a local minimum. Our statistical technique is shown to improve image quality in simulated digital holography relative to conventional numerical reconstruction using a filter applied in the frequency domain.